Inner structure, turbulent transfer and cascade properties of the turbulent/non-turbulent interface of a turbulent jet

Sarp Er

Thèse de Doctorat de l'Université de Lille

Spécialité: Mécanique des fluides

Structure interne, transfert turbulent et propriétés de cascade de l'interface turbulent/non-turbulent d'un jet turbulent

présentée et soutenue le 15 décembre 2023 publiquement par

Sarp ER

pour obtenir le grade de *Docteur* de l'Université de Lille

Soutenue le — devant le jury composé de:

Président	**Martin OBLIGADO**	Professor, École Centrale de Lille
Rapporteur	**Carlos Bettencourt DA SILVA**	Professor, Universidade de Lisboa
Rapporteur	**Oliver BUXTON**	Reader, Imperial College London
Examinatrice	**Elisabetta DE ANGELIS**	Assoc. Prof., Università di Bologna
Directeur de thèse	**J. Christos VASSILICOS**	Director of Research, CNRS, LMFL
Co-Directeur de thèse	**Jean-Philippe LAVAL**	Director of Research, CNRS, LMFL

Thèse préparée au Laboratoire de Mécanique des Fluides de Lille - Kampé de Fériet

Ecole Doctorale Sciences de l'Ingénierie et des Systèmes (ENGSYS-632)

Ph.D. Thesis at University of Lille

Speciality: Fluid mechanics

Inner structure, turbulent transfer and cascade properties of the turbulent/non-turbulent interface of a turbulent jet

publicly presented and defended on 15 December 2023 by

Sarp ER

to obtain the degree of *Doctor of Philosophy*

in front of the jury:

President	**Martin OBLIGADO**	Professor, École Centrale de Lille
Reviewer	**Carlos Bettencourt DA SILVA**	Professor, Universidade de Lisboa
Reviewer	**Oliver BUXTON**	Reader, Imperial College London
Examiner	**Elisabetta DE ANGELIS**	Assoc. Prof., Università di Bologna
Director	**J. Christos VASSILICOS**	Director of Research, CNRS, LMFL
Co-Director	**Jean-Philippe LAVAL**	Director of Research, CNRS, LMFL

Ph.D. thesis prepared at Lille Fluid Mechanics Laboratory - Kampé de Fériet

Ecole Doctorale Sciences de l'Ingénierie et des Systèmes (ENGSYS-632)

Declaration

I hereby declare that except where specific reference is made to the work of others, the contents of this dissertation are original and have not been submitted in whole or in part for consideration for any other degree or qualification in this, or any other university. This dissertation is my own work and contains nothing which is the outcome of work done in collaboration with others, except as specified in the text and Acknowledgements.

Sarp ER

Acknowledgements

First, I would like to express my gratitude to my supervisors Prof. Christos Vassilicos and Dr. Jean-Philippe Laval, who guided me through this journey. Their knowledge and experience shed light on the path I walked and their support gave me the power to continue until the end. It has always been a great pleasure to discover new questions and ideas with them, and it was a great chance to observe their expertise at work when thinking on a problem together, occasionally drifting into the subjects of philosophy from the turbulent/non-turbulent interface. I learned so much from them, both from their scientific knowledge and from their skills of guidance with patience.

Then I would like to mention my friends and colleagues at LMFL. Starting with Felipe, with whom we shared great memories not only in France but also in the US, and Greece; and who has always been there at the hardest times, with great empathy and kindness, and Argyris with whom we started this journey and walked through all the hardships together. Paul, Marcello, Christopher, Rakesh, Tarek, Oğuzhan, and Vinicius with whom we have consumed a considerable amount of Flanders beer, shared a great amount of laughter and beautiful memories. Without the companionship and friendship of all these people, it wouldn't be possible to complete this journey.

I am also deeply thankful to my family, who give me their unconditional support and encouragement with every step I take in my journey of self-discovery. Their love is invaluable to me. Without a doubt, I wouldn't be the person I am today, without their support.

Also, I am grateful to have Antoine, Cédric, Bruno, Chloé, Marine, Keith and many other lovely people who accompanied me through the voyage of exploring the beautiful French language and culture and especially Anne, for all the beautiful moments we shared together.

Finally, Ezgi, Çağatay, Didem, Semih, Taygun and Tuğberk whose friendship I felt close and profound, despite being in different corners of the world.

I would also like to acknowledge the financial support from the I-SITE Université Lille Nord-Europe, Métropole Européenne de Lille and Région Hauts de France, in collaboration with CNRS. This work was granted access to the HPC resources of IDRIS for performing numerical simulations and post-processing of high-fidelity data.

Abstract

The turbulent/non-turbulent interface (TNTI) is a very sharp interface layer between turbulent and non-turbulent regions of the flow. This study aims to gain insight into the kinetic energy balance in the vicinity of the TNTI. The Kármán-Howarth-Monin-Hill equation (KHMH) is used to characterize the local kinetic energy balance including interscale/interspace energy transfers. The analysis is conducted by using a data set obtained by highly resolved direct numerical simulation (DNS) of a temporally developing turbulent planar jet.

The scalings for the velocity and length scales of the temporally developing turbulent planar jet are shown to be different from its spatially developing counterpart in the sense that these scalings are independent of the turbulent dissipation scaling, whether equilibrium or non-equilibrium. The variation of the mean propagation velocity across the thickness of the TNTI is shown as a function of the fractal dimension of the surface at each location.

Furthermore, a methodology based on a TNTI-averaging operation is used for the analysis of the local flow field in the vicinity of the TNTI. The analysis of the normal vector associated with the local facing direction of the TNTI provides valuable insights into the predominant geometric characteristics of the interface. The TNTI-averaged statistics are further conditioned on the mean curvature and the local propagation velocity of the interface, in order to characterize the variation of the local flow field and KHMH balance in various regions of the interface.

The thickness of the TNTI and its sublayers are shown to reduce significantly in regions of fast entrainment. The interscale/interspace transfer terms are decomposed into solenoidal/irrotational parts showing the central importance at the TNTI of the irrotational interscale/interspace transfers of kinetic energy associated with pressure-velocity correlation. Compression and stretching are observed on average at the TNTI location, in the normal and tangential directions of the interface respectively. Investigation of the interscale transfer term shows the presence of a forward cascade in the normal direction and an inverse cascade in the tangential direction.

In regions of detrainment, the local statistics display stretching in the normal direction and compression in the tangential direction, which is in contrast with the statistics observed for the entire TNTI and the local entrainment regions. Close to the location of TNTI, on the

turbulent side, an unexpected Kolmogorov-like balance is observed between the interscale transfer and the dissipation rate for a wide range of scales. For these scales, unlike the usual Kolmogorov balance for homogeneous turbulence, the interscale transfer consists solely of the irrotational part which is directly associated with the pressure-velocity correlations.

Résumé

L'interface turbulent/non-turbulent (TNTI) est une couche très fine entre les régions turbulentes et non turbulentes de l'écoulement. Cette étude vise à mieux comprendre le bilan d'énergie cinétique au voisinage de l'interface turbulent/non-turbulent. L'équation de Kármán-Howarth-Monin-Hill (KHMH) est utilisée pour caractériser le bilan énergétique cinétique local, y compris les transferts d'énergie dans l'espace et entre les échelles. L'analyse est effectuée à l'aide de données obtenues par simulation numérique directe (DNS) finement résolue d'un jet plan turbulent se développant avec le temps. Les lois d'échelles de vitesse et de longueur du jet plan turbulent en evolution temporelle sont différentes de celles de son homologue en développement spatial, dans le sens où ces lois sont indépendantes de l'échelle de dissipation turbulente, qu'elle soit à l'équilibre ou hors équilibre. Il est montré que la variation de la vitesse moyenne de propagation à travers l'épaisseur de la TNTI est fonction de la dimension fractale de la surface à chaque position. Une méthodologie basée sur une opération de moyennage le long de la TNTI est utilisée pour l'analyse de l'écoulement local à proximité de la TNTI. L'analyse du vecteur normal associé à l'orientation locale de la TNTI fournit des informations précieuces sur les caractéristiques géométriques prédominantes de l'interface. Les statistiques moyennes de l'interface sont ensuite conditionnées par sa courbure moyenne et sa vitesse de propagation locale afin de caractériser la variation locale de l'écoulement et le bilan de l'équation KHMH dans les différentes couche de l'interface. Il est démontré que l'épaisseur de la TNTI et de ses sous-couches diminuent de manière significative dans les régions de fort entraînement. Les transferts entre échelles et en espace sont décomposés en une partie solénoïdale et une partie irrotationnelle, ce qui montre l'importance, au niveau de la TNTI, des transferts irrotationnels d'énergie cinétique entre échelles et en espace, associés à la corrélation pression-vitesse. Des phénomènes de compression et d'étirement sont observés en moyenne à proximité de la TNTI, dans les directions respectivement normale et tangentielle à l'interface. L'étude du terme de transfert inter-échelles montre la présence d'une cascade directe dans la direction normale et d'une cascade inverse dans la direction tangentielle. Dans les régions d'entraînement inverse, les statistiques locales montrent un étirement dans la direction normale et de la compression dans la direction tangentielle, ce qui contraste avec les statistiques observées pour l'ensemble de la

TNTI et les régions d'entraînement locales. Près de la TNTI, du côté turbulent, un équilibre inattendu ressemblant à celui de Kolmogorov est observé entre le transfert inter-échelle et le taux de dissipation pour une large gamme d'échelles. Pour ces échelles, contrairement à l'équilibre de Kolmogorov habituel pour la turbulence homogène, le transfert inter-échelle est constitué uniquement de la partie irrotationnelle qui est directement associée aux corrélations pression-vitesse.

Table of contents

List of figures

List of tables

Nomenclature

Roman Symbols

D_c Viscous diffusion of $|\delta \boldsymbol{u}|^2$ in physical space

D_f Fractal dimension of the TNTI

D_r Viscous diffusion of $|\delta \boldsymbol{u}|^2$ in scale space

D_t Rate of change of $|\delta \boldsymbol{u}|^2$ in time

D_{ω^2} Viscous diffusion of enstrophy

$\boldsymbol{e}_x$, $\boldsymbol{e}_y$, $\boldsymbol{e}_z$ Unit vectors of the TNTI local coordinate system

H_J Initial jet width

H_m Mean curvature of the surface

$\boldsymbol{i}$, $\boldsymbol{j}$, $\boldsymbol{k}$ Streamwise, cross-stream, spanwise unit vectors in global coordinate system

L_x, L_y, L_z DNS domain sizes in streamwise, cross-stream and spanwise directions

N_x, N_y, N_z Number of grid points in x, y, and z directions

P_{ω^2} Production of enstrophy

$\boldsymbol{r}$ Separation vector between the two-points

r_n Component of the separation vector in the interface normal direction

r_t Component of the separation vector in the tangential direction of the interface

R_{curv} Radius of curvature

Re_λ Reynolds number based on Taylor length scale

Re_G Global Reynolds number

T_p Pressure-velocity correlation term

T_r Transfer of $|\delta \boldsymbol{u}|^2$ in scale space

T_y Transfer of $|\delta \boldsymbol{u}|^2$ in physical space

T_{ref} Reference time scale

$\boldsymbol{u}$ Velocity vector

U, V, W Mean streamwise, cross-stream and spanwise velocities with respect to $(x-z)$ averaging

U_J Initial jet centre-plane velocity

v_n^l Local TNTI propagation velocity

V_J Turbulent jet volume

v_n Average TNTI propagation velocity

x, y, z Coordinates in streamwise, cross-stream and spanwise directions

Greek Symbols

δ Jet half-width

$|\delta \boldsymbol{u}|^2$ Second-order structure function

η Kolmogorov length scale

η_T Generalised Corssin length scale

ε_{ω^2} Dissipation of enstrophy

δ_I Total thickness of the TNTI

δ_{ω^2} Total thickness of the TSL

δ_ν Total thickness of the VSL

λ Taylor length scale

ν Kinematic viscosity of the fluid

ω^2 Enstrophy

ω^2_{ref} Reference enstrophy value

ω^2_{th} Enstrophy threshold value

ω Vorticity vector

Superscripts

$'$ Fluctuation with respect to $(x-z)$ average

$''$ Fluctuation with respect to TNTI-average

I Irrotational part

S Solenoidal part

Subscripts

0 Amplitude scaling parameter

c Mean centre-plane value

l Vector component in the local coordinate system

Other Symbols

$\langle\cdot\rangle$ Averaging operation in the homogeneous directions $(x-z)$

$\langle\cdot\rangle_I$ TNTI-averaging operation

Acronyms / Abbreviations

DNS Direct Numerical Simulation

IES Iso-Enstrophy Surface

IVS Intense Vortical Structure

JPDF Joint Probability Density Function

KHMH Kármán-Howarth-Monin-Hill

PDF Probability Density Function

PJx Turbulent Planar Jet Simulations

PJx-HR High Resolution Turbulent Planar Jet Simulations

TNTI Turbulent/Non-Turbulent Interface

TSL Turbulent Sublayer

VS Vortical Structure

VSL Viscous Superlayer

Chapter 1

Introduction

1.1 Turbulent/non-turbulent interface (TNTI)

Boundaries never fail to capture people's attention, whether due to the mysteries hidden behind them or the potential knowledge they hold. Interfaces in fluids have long piqued curiosity, as they manifest in natural phenomena such as clouds (Hentschel and Procaccia, 1984; Howard, 1803; Lovejoy, 1982). Similarly, the various aspects of the turbulent/non-turbulent interface (TNTI) have been investigated in numerous studies including the local mechanisms playing a role in the expansion of the turbulent volume into the outer non-turbulent fluid, geometrical properties of the interface, its fractal nature (Corrsin and Kistler, 1955; Dimotakis and Catrakis, 1999; Miller and Dimotakis, 1991; Sreenivasan, 1991; Sreenivasan et al., 1989; Watanabe et al., 2014a) and the coherent structures residing near the interface (da Silva and dos Reis, 2011; da Silva et al., 2011; Neamtu-Halic et al., 2019, 2020; Watanabe et al., 2017) and many more (Bisset et al., 2002; da Silva et al., 2014; da Silva and Pereira, 2008; Phillips, 1955).

Although interfaces are relatively easily identified visually in everyday examples such as clouds, smoke plumes, or other instances where the jets/plumes are seeded by particles or water particles, it is still useful to elaborate the concept of the interface between the turbulent and non-turbulent regions for the sake of clarity.

The turbulent region is characterized by vorticity, defined as the curl of the velocity field $\omega = \nabla \times u$. In contrast, the non-turbulent region is where the flow is irrotational. The existence of a very thin fluid layer as a frontier of the turbulent fluid has been proposed and justified in the seminal work by Corrsin and Kistler (1955).

A generalization of the concept of the interface layer can be extended to include turbulent-turbulent interfaces where both regions can be turbulent, at least up to some extent, while still having a significant difference in enstrophy ($\omega^2 = \omega \cdot \omega$) on each side of the interface

(Kankanwadi and Buxton, 2020). In the present study, we limit our interest only to the TNTI which is characterized by the complete lack of enstrophy on one side.

In their report, Corrsin and Kistler (1955) highlighted the central role of the viscosity in the process of the irrotational fluid acquiring vorticity while crossing the sharp interface layer, referred to as the *laminar superlayer* in the original text (Corrsin and Kistler, 1955). In their study, they have conducted a comprehensive investigation into various aspects of this layer such as the surface's wrinkling, the propagation of the interface in the normal direction, and the assertion that the interface thickness is influenced by both the viscous diffusion of vorticity and the straining due to the turbulence (Corrsin and Kistler, 1955).

They proposed a model for the thickness and the propagation velocity of the interface. They have concluded that the thickness of the *laminar superlayer* is of the order of Kolmogorov length scale $\eta = (\nu^3/\varepsilon)^{1/4}$, where ε stands for the turbulent dissipation rate and ν is the kinematic viscosity of the fluid (Corrsin and Kistler, 1955).

Further analytical investigations on the interface have been carried out in other studies (Phillips, 1955, 1972; Reynolds, 1972). Phillips (1955) focused on the irrotational fluctuations in the non-turbulent side of the interface, examining the kinetic energy associated with normal and tangential oscillations of the interface, as well as the distribution of energy across the spectrum at various distances from the interface. In the study by Phillips (1972), the evolution of the interface is explored using both pseudo-Lagrangian and Eulerian descriptions of the surface. Conclusions regarding the entrainment velocity at the interface in turbulent boundary layer flows are drawn based on experimental data from the literature. Notably, it is found that the advancement speed of the interface greatly exceeded the Kolmogorov velocity u_η (of the order of 15 times), although potential limitations of the model employed by Phillips (1972) are acknowledged, including the assumption of time independence of large-scale motions.

In contrast, Reynolds (1972) conducted a control volume analysis at the interface location, with the assumption of the interface being an infinitesimally thin layer. This analysis led to the proposal of a relationship between the jump in vorticity and the Reynolds stresses across the interface. Additionally, Reynolds (1972) suggested the existence of a jump for the tangential component of the velocity across the thickness of the interface, a concept that has been referenced in later studies on the TNTI (da Silva and Pereira, 2008; Hunt et al., 2008; Westerweel et al., 2009).

1.1.1 Entrainment and the underlying processes

A central subject that is closely related to the TNTI is the entrainment and detrainment processes, which can be associated with the incorporation of the outer non-turbulent fluid

into the turbulent volume or the loss of a portion of the turbulent fluid into the outer non-turbulent external flow respectively.

Various methods have been employed in the literature to detect the bounding surface of the turbulent volume. Enstrophy, denoted as $\omega^2 = \omega \cdot \omega$ (or the norm of vorticity, related to enstrophy as $|\omega| = (\omega \cdot \omega)^{1/2}$), is the most widely used marker for delineating the turbulent volume (Bisset et al., 2002; da Silva and Pereira, 2008; Holzner et al., 2008; Holzner and Lüthi, 2011; Krug et al., 2017; Taveira et al., 2013; van Reeuwijk and Holzner, 2014; Wolf et al., 2012). In some experimental studies where velocity gradients may not be readily available, a passive scalar with a high Schmidt number is also commonly employed for this purpose (Gampert et al., 2014; Mistry et al., 2016; Sandham et al., 1988; Westerweel et al., 2009).

Over time, numerous studies have focused on gaining a deeper understanding of the entrainment process and how turbulent volumes expand by incorporating outer irrotational fluid. This phenomenon has been investigated in various flow configurations, including jets (Mathew and Basu, 2002; Mistry et al., 2019, 2016; Taveira et al., 2013; Watanabe et al., 2016a; Westerweel et al., 2005), mixing layers (Jahanbakhshi and Madnia, 2016; Watanabe et al., 2016a), wakes (Kankanwadi and Buxton, 2020; Philip and Marusic, 2012; Zhou and Vassilicos, 2017) plumes (Krug et al., 2017; Turner, 1986) and shear-free turbulence (Holzner et al., 2008; Holzner and Lüthi, 2011).

As has been pointed out in the literature, there have been different definitions of the entrainment velocity that emerged in time (Hunt et al., 1984; Jahanbakhshi and Madnia, 2016; Turner, 1986). This conceptual variance, as discussed by Turner (1986), may lead to quantitative differences under specific flow conditions or at different interfaces. Turner (1986) outlines three distinct definitions of entrainment velocity: the velocity of external fluid flowing into the turbulent region, the velocity at which the turbulent flow boundary expands into the external flow, and the entrainment velocity relative to the local mean flow. These definitions can also be categorized into two main approaches: the global approach and the local approach for defining entrainment.

Examples of studies employing the global approach to determine entrainment velocity include the works of van Reeuwijk and Holzner (2014), Zhou and Vassilicos (2017), and Krug et al. (2017). In these studies, entrainment velocity is derived from the global rate of change of turbulent volume.

Conversely, the local entrainment velocity is defined at each location along the boundary in some other studies (Holzner and Lüthi, 2011; van Reeuwijk and Holzner, 2014; Watanabe et al., 2015; Wolf et al., 2012). Holzner and Lüthi (2011) derives an expression for the local propagation velocity v_n^l of an iso-enstrophy surface element by considering that $D\omega^2/Dt = 0$

in the reference frame following the iso-enstrophy surface element. This expression is derived by employing the transport equation for the enstrophy (Holzner and Lüthi, 2011; van Reeuwijk and Holzner, 2014) (see section 4.10 for the definition of the local propagation velocity v_n^l). A direct relation exists between these two approaches for the propagation velocity which is also shown by van Reeuwijk and Holzner (2014) and Jahanbakhshi and Madnia (2018) when the turbulent volume and its boundary are consistently defined.

In the current study, we utilize a condition on ω^2 for the detection of the turbulent volume and the associated boundary. Consequently, the boundary that separates the turbulent volume from the external fluid corresponds to an iso-enstrophy surface defined by a threshold value ω_{th}^2 employed for the field of ω^2. Both the global and the local approaches are employed in the current study for the characterization of the entrainment and the expansion of the turbulent volume.

Many studies have delved into the intricacies of the entrainment mechanism to determine whether it is primarily driven by the large scales or the smaller scales of motion. Several examples to these studies are (Brown and Roshko, 1974; Mathew and Basu, 2002; Sreenivasan et al., 1989; Taveira et al., 2013; Westerweel et al., 2009). The entrainment mechanisms are distinguished into two main categories in relation to their association with large or small-scale motions and are referred to as "engulfment" and "nibbling" respectively.

Nibbling is linked to small-scale motions, as it involves the expansion of the turbulent volume through the viscous diffusion of vorticity and momentum into the non-turbulent region (Bisset et al., 2002; Corrsin and Kistler, 1955; Mathew and Basu, 2002; Taveira et al., 2013; Westerweel et al., 2009, 2005; Wolf et al., 2013a) occurring along a highly contorted surface due to the small scale motions (Sreenivasan et al., 1989). This mechanism can be associated with the viscous process described by Corrsin and Kistler (1955), which is emphasized as being critical for the acquisition of vorticity by the irrotational fluid as it crosses the TNTI.

In contrast, engulfment is predominantly linked to large-scale motions in the literature (Brown and Roshko, 1974; Dahm and Dimotakis, 1987; Jahanbakhshi and Madnia, 2016; Liepmann and Gharib, 1992; Mathew and Basu, 2002; Philip and Marusic, 2012; Westerweel et al., 2009, 2005). It is worth noting that the definition of engulfment varies among studies investigating entrainment phenomena. In some studies, engulfment is described as a volume of irrotational fluid completely surrounded by turbulent flow, entirely separated from the outer non-turbulent flow (Jahanbakhshi and Madnia, 2016; Mathew and Basu, 2002; Taveira et al., 2013; Westerweel et al., 2009, 2005) while still being irrotational. An alternative use of engulfment is also suggested, where it corresponds to the enhancement of the entrainment

due to the large-scale motions by means such as amplifying the interface surface area by contorting it (de Silva et al., 2013; Krug et al., 2017; Philip et al., 2014).

Determining the driving mechanism of entrainment holds significance because it can impact the resolution requirements for numerical simulations and the choice of modelling approaches for flows involving a TNTI. Improved modelling can lead to a more accurate representation of large-scale quantities, including jet expansion rate and entrainment, especially in situations where highly resolved simulations are not available.

Since 1970's, with the discovery of the coherent structures and their significance in turbulent shear flows (Brown and Roshko, 1974; Crow and Champagne, 1971; Kline et al., 1967), the importance of the large-scale motions is pointed out as being the main contributors for the outer, non-turbulent flow to be entrained into the turbulent volume (Bisset et al., 2002; Brown and Roshko, 1974; Dahm and Dimotakis, 1987; Liepmann and Gharib, 1992).

On the other hand, in more recent studies, the amount of entrainment due to the nibbling process associated with the small-scale motions is shown to be much more significant in studies analyzing the free-shear flows numerically both in the presence of mean shear Bisset et al. (2002); Mathew and Basu (2002); Taveira et al. (2013) in the absence of mean shear (Holzner and Lüthi, 2011), and also experimentally Westerweel et al. (2009, 2005). These findings are directly related to the conclusions given in the seminal study by Corrsin and Kistler (1955), where the critical role of viscosity is pointed out for the entrainment which has a dominant effect at the smallest scales.

Providing a complete picture of the entrainment phenomena is undoubtedly a complex endeavour. It is likely that entrainment is not solely attributable to either large-scale or small-scale motions but rather emerges as a result of a process in which both scales, as well as intermittent ones, play roles. Numerous studies have underscored the significance of both large and small scales, particularly in the context of the latter definition of engulfment (Bisset et al., 2002; Chauhan et al., 2014; Krug et al., 2017; Mathew and Basu, 2002; Philip and Marusic, 2012; Philip et al., 2014; Sreenivasan et al., 1989). In this framework, large-scale motions contribute to entrainment by modulating the interface's surface area. Simultaneously, viscous diffusion, occurring at smaller scales, is solely responsible for transforming the initially irrotational external fluid into rotational fluid, consequently leading to the expansion of the turbulent volume defined by vorticity/enstrophy conditions into the external region (Bisset et al., 2002; Chauhan et al., 2014; Krug et al., 2017; Mathew and Basu, 2002; Philip and Marusic, 2012; Philip et al., 2014; Sreenivasan et al., 1989).

An important study pointing out both ends of the entrainment process is conducted by Sreenivasan et al. (1989). This study highlights the connection between the large-scale end of the process, where the entrainment is associated with the large eddies, and the small-scale

end, where the diffusive action happens at the molecular level. In order to characterize the entrainment process, they opt for the latter approach due to an approximation of small scales being more independent from the flow configuration, thus being more potent to arrive at a more universal result, which can be valid for various flows (Sreenivasan et al., 1989).

A crucial point is made by Sreenivasan et al. (1989) on why the earlier attempts have been unsuccessful in modelling the entrainment process by the small-scale motions and the diffusion mechanism. They highlight the fact that these prior studies have failed to account for the fractal nature of the interface, which is important for the surface across which the diffusion occurs (Sreenivasan et al., 1989). They proceed by presenting an argument and experimental results supporting the conclusion that the interface indeed exhibits fractal properties with a fractal dimension of $7/3$ and suggesting that the large-scale fluxes become independent of viscosity by the specific adjustment of the small scales (Sreenivasan et al., 1989).

1.1.2 Local analysis of the interface

Another milestone for the analysis of the TNTI is the methodology introduced by Bisset et al. (2002). This approach involves directly analyzing flow field statistics at the TNTI location through a specialized averaging operation conditioned on the interface's position. Subsequently, this methodology has been widely adopted in numerous studies to investigate local profiles of vorticity (da Silva and dos Reis, 2011; Taveira and da Silva, 2013), velocity (Westerweel et al., 2009, 2005), and terms of the enstrophy balance equation (Holzner et al., 2008; Silva et al., 2018; Taveira and da Silva, 2014a; Watanabe et al., 2015) and many more.

Bisset et al. (2002) has conducted their analysis by conditioning the statistics further on the local orientation of the interface, which is useful to see the variation of the 1D profiles of various flow quantities in the normal direction of the interface in specific regions of the TNTI. A similar conditioning has been carried out also in the work by (Watanabe et al., 2014a) which draws detailed conclusions about the enstrophy balance at the leading edge, trailing edge, and the cross-stream facing parts of the TNTI.

Wolf et al. (2013a), analyzes the PDFs of the local propagation velocity of the TNTI and the local shape of the interface characterized by the mean and Gaussian curvature parameters. They report a significant variation of the local propagation velocity between the regions with different geometrical characteristics, especially with different mean curvature values (Wolf et al., 2013a).

In the present study, we adopt a similar methodology to the one mentioned above, in chapters 4 and 5 for the analysis of the flow field near the TNTI. Different from the previously mentioned studies in the literature, we apply the TNTI-averaging procedure to a 3D local field

because of the 3D nature of the analysis conducted with the Kármán-Howarth-Monin-Hill equation employed in chapter 5 (Hill, 2002). Taking the findings in the literature into account, which highlight the variation of the local balance along the surface of the interface (Watanabe et al., 2014a; Wolf et al., 2013a), the TNTI-averaged statistics are further conditioned on the local quantities such as the local mean curvature and the local propagation velocity.

1.1.3 Physical properties of the TNTI and its sublayers

Following the study by Sreenivasan and Meneveau (1986), numerous works have investigated the fractal properties of the interface (Dimotakis and Catrakis, 1999; Flohr and Olivari, 1994; Lane-Serff, 1993; Miller and Dimotakis, 1991; Mistry et al., 2018, 2016; Sreenivasan, 1991; Sreenivasan et al., 1989). The fractal nature of the TNTI is widely acknowledged in the literature, although there have been differing opinions regarding whether the fractal dimension of the interface is constant $7/3$ (de Silva et al., 2013; Mistry et al., 2018; Sreenivasan, 1991; Sreenivasan et al., 1989), if it varies with threshold and Reynolds number (Flohr and Olivari, 1994; Lane-Serff, 1993; Miller and Dimotakis, 1991), or if it can even be expressed with a constant value or it is scale-dependent (Miller and Dimotakis, 1991) (see also (Catrakis and Dimotakis, 1999), (Dimotakis and Catrakis, 1999) and references therein).

Some studies have explored the relationship between TNTI properties, entrainment, and coherent structures in various flows, including jets (da Silva and dos Reis, 2011; da Silva et al., 2011; da Silva and Taveira, 2010) and gravity currents (Neamtu-Halic et al., 2019, 2020, 2021). Considering the conditional profiles at the TNTI location, these studies have suggested the possible effects of different vortical structures, such as vortex tubes and vortex sheets, as noted by Westerweel et al. (2009) and da Silva and dos Reis (2011). da Silva and dos Reis (2011) also emphasize the difference in the longevity of these structures, with vortex tubes having a longer lifespan, suggesting that these tube-like structures have a greater influence on determining the features of the TNTI such as its thickness.

In their study, da Silva and Taveira (2010) introduce a procedure to detect vortical structures, categorizing them into two distinct groups: large vortical structures (LVS) and intense vortical structures (IVS). They propose that LVSs are associated with remnants of the Kelvin-Helmholtz instability and secondary instabilities. They note that these structures primarily exhibit spatial orientations in the spanwise and streamwise directions. The description of LVS presented by da Silva and Taveira (2010) encompasses both primary and secondary (coherent) structures described by Fiedler (1988) for free-shear flows. Primary and secondary coherent structures are suggested to be responsible for the exchange of mass, momentum, etc. across the whole flow and the production of turbulent kinetic energy respectively (Fiedler, 1988). The radius of the LVSs is being measured by da Silva and Taveira (2010) along

with the thickness of the TNTI which are shown to follow closely each other in planar jet simulations having a Reynolds number based on the Taylor length scale between $Re_\lambda = 30$ to $Re_\lambda = 160$.

In the same study, da Silva and Taveira (2010) introduce an argument regarding the lifespan of vortical structures, based on the balance between radial viscous diffusion of vorticity and axial stretching, akin to a Burgers vortex. This analysis suggests that the thickness of the TNTI would be influenced by the shear acting on the vortical structures and would differ between flows with mean shear and shear-free turbulence. Consequently, they propose that the mean thickness of the TNTI is linked to the radius of the largest vortices near the interface, which is λ for flows with mean shear and η for shear-free flows. This argument aligns with measurements in the literature for shear-free flows (Holzner et al., 2007, 2008) and jets (da Silva and Pereira, 2004, 2008; Westerweel et al., 2009, 2005), as pointed out by da Silva and dos Reis (2011).

On the other hand, the IVSs in da Silva and dos Reis (2011); da Silva and Taveira (2010), and da Silva et al. (2011) are depicted as worms described in the studies of homogeneous isotropic turbulence (Jimenez et al., 1993; Jiménez and Wray, 1998). These IVSs lack a preferential orientation and are associated with very high enstrophy values.

In da Silva et al. (2011), a comprehensive investigation of these IVSs near the TNTI is conducted. They characterize various aspects of these structures, such as the probability density function (PDF) of the radius, axial vorticity of these vortical structures, and strain acting on them at different distances from the interface. They report a significant drop in the stretching of IVSs at the jet edge, which they attribute to the absence of background vorticity near the TNTI, as the large vortical structures (LVS) are bounded by the interface (da Silva et al., 2011). This led da Silva et al. (2011) to conclude that the radius of IVSs near the interface tends to increase over time due to the dominance of vortex diffusion over stretching, indicating that these IVSs are not equilibrium Burgers vortices.

Additionally, Taveira and da Silva (2014a,b) point out a relationship between the local thickness of the outer, viscous layer of the TNTI, (viscous superlayer) and the radius of IVSs near the TNTI. However, they noted that this relationship may not explain all regions of the VSL, as IVSs are found only near some parts of the interface.

With the increase of the computing resources at disposal and the development of measurement techniques such as particle image velocimetry (PIV), particle tracking velocimetry (PTV), and planar laser-induced fluorescence (PLIF), the inner structure of the TNTI has been analyzed in more detail along with its shape and its local propagation velocity in various free-shear flows both numerically (da Silva et al., 2011, 2014; da Silva and Pereira, 2008; da Silva and Taveira, 2010; Krug et al., 2017; Neamtu-Halic et al., 2020; Silva et al., 2018;

Taveira and da Silva, 2014a; van Reeuwijk and Holzner, 2014; Watanabe et al., 2019, 2020, 2017, 2016a, 2014a; Zecchetto and da Silva, 2021) and experimentally (Balamurugan et al., 2020; Holzner et al., 2008; Holzner and Lüthi, 2011; Mistry et al., 2018, 2019; Neamtu-Halic et al., 2019; Wolf et al., 2012).

Higher-resolution studies of the TNTI have led to a significant change in how it is conceptualized, with the identification of distinct sublayers within the TNTI itself (Bisset et al., 2002; da Silva et al., 2014; Taveira and da Silva, 2014a). These sublayers are commonly referred to as the viscous superlayer (VSL) and the turbulent sublayer (TSL) (da Silva et al., 2014; Taveira and da Silva, 2014a), although the latter is also referred to as the buffer layer in the work of van Reeuwijk and Holzner (2014). The differentiation between these layers is based on the observation of different dominant mechanisms in the enstrophy balance in various regions across the thickness of the TNTI (da Silva et al., 2014; Silva et al., 2018; Taveira and da Silva, 2014a; Watanabe et al., 2015).

The VSL is primarily associated with the dominant viscous mechanism responsible for the diffusion of vorticity into the outer, non-turbulent region of the flow. This layer is conceptually related to the "laminar superlayer" described by Corrsin and Kistler (1955) (Bisset et al., 2002; da Silva et al., 2014). In contrast, the TSL is characterized as a layer where the flow is already turbulent, and there is significant turbulent production of vorticity, distinct from the external VSL (Bisset et al., 2002; da Silva et al., 2014; Taveira and da Silva, 2014a).

In the studies conducted by Silva et al. (2018); Taveira and da Silva (2014a); Watanabe et al. (2015), a methodology for distinguishing these sublayers has been provided. The extent of these sublayers is determined by examining the magnitudes of various terms in the enstrophy balance equation. The VSL is identified by recognizing that the dominant mechanism in this region is the viscous diffusion of vorticity/enstrophy. Starting from the external regions of the TNTI and moving towards the turbulent core, the non-linear production of enstrophy gradually increases and reaches a magnitude comparable to that of viscous diffusion, which marks the boundary separating the VSL from the TSL in this methodology (Silva et al., 2018; Taveira and da Silva, 2014a; Watanabe et al., 2015). Therefore, the VSL can be characterized as the external region of the interface where enstrophy is diffused primarily due to viscosity, while in the TSL, non-linear mechanisms such as vortex stretching become increasingly important and contribute to the increase of enstrophy within this sublayer.

Another approach to distinguishing the sublayers within the TNTI is proposed by van Reeuwijk and Holzner (2014). In their study, they treat the TNTI as a continuous phenomenon and investigate the local propagation velocity of the interface and its constituent enstrophy isosurfaces for a wide range of enstrophy threshold values. By calculating the mean propagation

velocity for this broad range of threshold values, they observe that the external iso-enstrophy surfaces (associated with low ω^2 threshold values) propagate towards the non-turbulent region. However, this velocity decreases as the threshold value increases, eventually reaching zero and changing sign for the iso-surfaces corresponding to higher ω^2 threshold values (van Reeuwijk and Holzner, 2014). The variation in propagation velocity is linked to the constancy of flux through the interface and the increase in surface area for higher threshold values (van Reeuwijk and Holzner, 2014). Based on this observation, van Reeuwijk and Holzner (2014) suggest that the point where the propagation velocity crosses zero can be considered as the boundary marking the extent of the VSL in the turbulent direction across the thickness of the TNTI.

In a study by Silva et al. (2018), the scaling of the TNTI thickness and the thicknesses of its sublayers in flows with and without shear, specifically turbulent planar jets and shear-free turbulence, are investigated. This study is notable for its extensive range of Reynolds numbers (Re_λ) covered by the DNS dataset used for systematic analysis. They report the probability density functions (PDFs) of the local thicknesses of TNTI, TSL, and VSL, along with their mean values (Silva et al., 2018). The results show that the mean values of these thicknesses follow a similar trend, scaling with the Kolmogorov length scale (η) rather than the Taylor length scale (λ) for Re_λ values exceeding 200. The differences between these findings and those reported by da Silva and Taveira (2010) and da Silva and dos Reis (2011) are suggested to be due to the lower Re_λ values in the flows considered in the former studies (for a detailed discussion on the implications of low Re_λ, refer to Silva et al. (2018)).

Another important result presented by Silva et al. (2018) is the PDF of the local thicknesses of TNTI and its layers. These PDFs reveal that, for $Re_\lambda \gtrsim 200$, the PDFs of local VSL thickness have peaks between 2.3η and 3.1η, and a very limited range of values makes up the majority of the local VSL thickness for planar jet TNTI (Silva et al., 2018). This highlights the sharpness of the layers under investigation and underscores the importance of simulation resolution to capture the internal structure of TNTI accurately.

Apart from the thickness of the TNTI, and its sublayers, some studies have investigated the effects of surface characteristics, including its orientation (Watanabe et al., 2017, 2014b) and its local curvature (Wolf et al., 2013a, 2012, 2013b).

The studies conducted by Wolf et al. (2012, 2013b) involve conditional average values of the entrainment velocity, further conditioned on the mean and Gaussian curvatures of the interface. Their findings reveal significant variations in the entrainment velocity at regions with different mean curvature characteristics of the interface, while no notable correlation is observed between the local Gaussian curvature and the entrainment velocity. These observations are further supported by the results obtained by Wolf et al. (2013a)

in experimental cases of spatially developing jets with Reynolds numbers of $Re = 2000$ ($Re_\lambda = 60$), $Re = 5000$ ($Re_\lambda = 80$), and $Re = 8000$ ($Re_\lambda = 100$), as well as DNS results of shear-free turbulence with $Re_\lambda = 50$.

In the study conducted by Watanabe et al. (2014b), regions associated with enstrophy production and reduction are identified. The analysis involves examining the alignment between the interface normal, vorticity, and strain rate eigenvectors to gain insights into the details of vortex stretching and compression events near the interface. The results indicate that predominant vortex stretching occurs in regions where the fluid velocity is directed towards the interface, while predominant vortex compression occurs in regions where the velocity field is moving away from the interface.

Additionally, in the work of Watanabe et al. (2017), an analysis of the relative motion of the fluid with respect to the interface is conducted, conditional on the orientation of the interface normal vector. This analysis is carried out for the TNTI of shear-free turbulence and a turbulent planar jet. The study reveals that the velocity of the fluid with respect to the interface varies depending on the presence of mean shear. In the case of a planar jet, the fluid velocity is directed towards the interface in regions facing downstream, whereas the opposite is observed in regions where the interface is oriented towards the upstream direction.

1.1.4 Local energy/enstrophy budgets and their cascade in the vicinity of the TNTI

As previously mentioned, the TNTI is a highly localized phenomenon in space, which brings certain challenges for its analysis. Additionally, the budgets of kinetic energy, enstrophy, and other relevant quantities involve various processes such as transport, diffusion, production, and dissipation, all of which are scale-dependent. There are studies in the literature where these multidimensional processes are investigated in the presence of the TNTI, in flows with mean shear (Cimarelli et al., 2021; da Silva, 2009; Zhou and Vassilicos, 2020) and without mean shear (Cimarelli et al., 2015; Watanabe et al., 2020).

In the studies by Cimarelli et al. (2015) and Cimarelli et al. (2021) the shear-free turbulence and temporally developing planar jet flows are studied respectively. In these studies, the respective flow fields are divided into layers along the axis, which the TNTI propagates and the extents of these layers are given with respect to the mean location of the interface along this axis (Cimarelli et al., 2015, 2021). The details of the enstrophy/energy budgets and associated fluxes are analyzed in and across these layers, in a multiscale framework.

From this perspective, the methodology employed in these studies (Cimarelli et al., 2015, 2021) differs from the local analysis conducted in the present study, where we employ a

TNTI-averaging operation, carried out at the exact location of the TNTI and by also taking into account its local orientation. This allows us to account for the local inhomogeneous direction associated with the presence of the TNTI, which has been proven to be crucial for the analysis of the TNTI layer (Bisset et al., 2002; da Silva and dos Reis, 2011; Holzner et al., 2008; Silva et al., 2018; Taveira and da Silva, 2013, 2014a; Watanabe et al., 2015; Westerweel et al., 2009).

Cimarelli et al. (2015) investigate the enstrophy budget in shear-free turbulence with a TNTI propagating towards the non-turbulent region. The various layers are defined within the flow as the bulk turbulent region, the inhomogeneous turbulent layer, and the interfacial layer. In order to understand the balance of enstrophy in the turbulent region, both the one-point equation and an equation for the evolution of spectral enstrophy in the wavenumber space are employed by Cimarelli et al. (2015), providing insights into the mechanisms acting on this balance in a multiscale framework in the various regions of the flow.

They report a spatial transport of enstrophy from the bulk turbulent region towards the interfacial layer by the inviscid turbulent transport mechanism and they highlight the role of viscous diffusion in the increase of enstrophy, particularly in the external part of the interfacial layer, although its contribution in the other regions is negligible (Cimarelli et al., 2015).

In the multiscale framework, Cimarelli et al. (2015) conclude that the large scales are responsible for carrying enstrophy from the bulk turbulent region to the interfacial layer. Going in the direction of the non-turbulent region, enstrophy is observed to be transferred from the large scales to the smaller scales. In the interfacial layer, the enstrophy cascade is reported to become anisotropic, with the cascade shifting from large to small scales in the tangent plane to the small scales in the interface normal direction (Cimarelli et al., 2015).

A region-by-region analysis, similar to the one conducted by Cimarelli et al. (2015), is applied to the temporal planar jet flow by Cimarelli et al. (2021) for the analysis of the evolution of the cascade at and across the various regions of a temporal planar jet. In this study, they employ an equation based on the exact equation for the second order structure function given by Hill (2002) applied to the symmetries of the temporally developing planar jet flow (Cimarelli et al., 2021). They document separate families of fluxes responsible for the transfer of turbulent kinetic energy in both physical and scale space (across the spatial layers and across the scales). One family of fluxes is shown to distribute the energy from the large scales in the region associated with the production of the turbulent kinetic energy along the cross-stream axis in both directions i.e., towards the non-turbulent region and the centre-plane of the jet (Cimarelli et al., 2021). Meanwhile, the kinetic energy cascades from larger towards smaller scales in the scale space. Another family of fluxes is reported to feed

the inner region of the jet (close to centre-plane) with the kinetic energy transferred from the production region, while this time the kinetic energy cascades not only towards the small scales but to both small and large scales (Cimarelli et al., 2021). Lastly, another family of fluxes is described by Cimarelli et al. (2021) which, again transports the energy originating from the production region, but this time in the direction of the interfacial region. Moreover, this last family of fluxes is also associated with a reverse cascade towards the larger scales as it feeds larger streamwise scales. As a result, a detailed picture of the various paths taken by the turbulent kinetic energy, both in physical and scale space, are depicted by Cimarelli et al. (2021) in and across the layers defined for the temporally developing planar jets.

Differently from the region-by-region analysis by Cimarelli et al. (2015) and Cimarelli et al. (2021), Zhou and Vassilicos (2020) conduct a study centred on the interscale energy transfer at the location of the TNTI of a spatially developing wake. They make the connection between the forward/backwards energy cascade and the compression/stretching events and they report weak backwards interscale transfers due to straining motions in the interface tangential direction and forward interscale transfer in the other directions due to compressing motions (Zhou and Vassilicos, 2020). In their analysis, they focus on the interscale energy transfer and the associated term in the KHMH equation by decomposition of the interscale energy transfer into the transfers of longitudinal and rotational energy. Also by analysing the higher-order moments of the term associated with the compression/stretching events, they observe that extreme compression events are more likely to occur compared to the extreme stretching events. Apart from this, it can be noted that they do not study the other mechanisms acting on the local scale-by-scale energy balance which are described by the various terms of the KHMH equation, except the spatial turbulent transfer rate.

On the other hand, Watanabe et al. (2020) investigate the scale-by-scale kinetic energy balance near the TNTI of a shear-free turbulence. They employ a methodology based on local volume averaging for the decomposition of the kinetic energy into parts associated with the large and small scales near the TNTI layer and report the terms for the sub-grid scale (SGS) energy budget equation. They extend the analysis by investigating the contributions of the interface normal and tangential velocities and their derivatives in the normal/tangential directions, to the kinetic energy transfer towards the SGSs. Similarly to the findings by Zhou and Vassilicos (2020), they report energy transfer from large to small scales in the interface normal direction due to the velocity gradients in that direction (fluid compression in the normal direction) and a shearing motion due to the interface-tangential velocity (Watanabe et al., 2020). They also analyze the contributions of the viscous diffusion and the pressure diffusion near the TNTI, where the former is reported to increase the small-scale kinetic

energy and the latter is suggested to be associated with the small-scale vortices possibly present near the TNTI.

1.2 Objectives

In the early studies, the TNTI has been modelled as a finite thickness surface (Corrsin and Kistler, 1955; Reynolds, 1972). This paradigm of TNTI has evolved throughout time, with the improving abilities of numerical and experimental capabilities and the finer resolution of this sharp interface. The term TNTI now describes an interface layer which contains various sublayers with distinct properties (da Silva et al., 2014). Still, many questions remain for a deeper understanding of the structure of the TNTI, its local properties and the relation between the entrainment mechanisms. In this study, we aim to gain more insight into the following questions:

- What are the fractal properties of the TNTI? Does it remain constant across the interface or does it vary due to the inner structure of the TNTI? The more accurate resolution of the TNTI with its inner structure raises the question of whether the fractal nature of the surface can be determined by a single fractal dimension $7/3$ or by a range of fractal dimensions due to the varying inner structure of the interface layer.

- The variation of the mean propagation velocity of the iso-enstrophy surfaces across the TNTI thickness has been shown by van Reeuwijk and Holzner (2014). Taking into account the fractal properties of the TNTI, is it possible to gain more insight into the mean propagation velocity of the TNTI from a global perspective?

- Different scalings for the length and velocity scales of the flow have been shown for spatially developing wakes by Obligado et al. (2016) and Ortiz-Tarin et al. (2021), and for spatially developing planar jets by Cafiero and Vassilicos (2019). What are the implications of the non-equilibrium dissipation scaling for the temporally developing turbulent planar jet and is it possible to make a connection between various dissipation scaling regimes and the local mechanisms at the TNTI, playing a role in the entrainment process?

- What are the mechanisms acting on the local kinetic energy balance at the TNTI location and what are the properties of the local cascade? The Kármán-Howarth-Monin-Hill equation (KHMH) allows an effective distinction between various transfer mechanisms of the kinetic energy in both physical and scale spaces (Hill, 2002). In the present study, we employ KHMH in the vicinity of the TNTI, which permits us to

investigate the local kinetic energy balance at the TNTI, and whether the individual sublayers have specific characteristics in terms of various mechanisms acting in this balance.

- Do the roles of these kinetic energy mechanisms vary at the TNTI location in the regions of local entrainment and detrainment along the interface?
- What are the implications of the local geometry and the orientation of the TNTI surface on the topology of the local flow field and on the terms acting in the KHMH balance?

1.3 Organization of the Thesis

The present study is organized into five chapters following this introduction chapter, mainly by considering the different approaches being employed for the analysis of various aspects of the TNTI. These chapters can be briefly summarized as follows:

- The details of the datasets produced by direct numerical simulation of temporally developing turbulent planar jets are presented in chapter 2. These include the details of the numerical method used, the initial conditions, the evaluation of the quality of the produced dataset, and a discussion of the various constraints such as for the grid resolution or on the Reynolds number. The two datasets with different numerical resolutions are presented along with a discussion of the importance of the resolution for the analysis we have conducted. The TNTI detection method is also given in this chapter along with the detection and labelling procedure for the turbulent, non-turbulent, and engulfed volumes.
- Chapter 3 employs a global approach to investigate the details of the mean propagation velocity across the thickness of the interface. This global approach relates the rate of increase of the turbulent volume with the surface area of the various enstrophy iso-surfaces constituting the TNTI and the mean propagation velocity at each iso-surface. The fractal characteristics of the interface are presented in this chapter by the investigation of its variation across the thickness of the TNTI layer. The results presented in this chapter are published in the *Journal of Fluid Mechanics* (Er et al., 2023).
- In chapter 4 a local approach is introduced based on a TNTI-averaging operation for the analysis of the local flow field in the vicinity of the TNTI. The enstrophy balance is investigated in terms of various contributing terms. Alignment of the velocity

and vorticity vectors are investigated, which has implications for the production of enstrophy. The local propagation velocity of the iso-enstrophy surface elements and the local curvature are used for the conditioning of the statistics. The pictures of the local flow field and the local enstrophy balance are obtained for each of these conditions. A general sketch is given depicting the TNTI of the temporally developing turbulent planar jet.

- Chapter 5 is devoted to the analysis of the various mechanisms in the KHMH equation and the characterization of interscale/interspace transfer of the kinetic energy near the TNTI location. The analysis is further detailed by the decomposition of the interscale/interspace terms into solenoidal and irrotational parts. Furthermore, the KHMH balance is analyzed close to the interface, on the turbulent side where significant non-linear production of enstrophy is present.

- In chapter 6, the main conclusions of the thesis are given with the perspectives for future works.

Chapter 2

Simulations

2.1 Parameters of the simulation and details of the solver

DNS of a temporally evolving turbulent jet is conducted similarly to those described in the studies of (da Silva and Pereira, 2008; Silva et al., 2018; van Reeuwijk and Holzner, 2014). The global Reynolds number is $Re_G \equiv \frac{U_J H_J}{\nu} = 3200$, where U_J is the initial streamwise velocity at the center-plane, H_J is the initial jet width and ν is the kinematic viscosity of the fluid. The reference time scale $T_{ref} = H_J/(2U_J)$ is used for the normalization of time when presenting the results.

The initial mean velocity profile of the jet is defined by (da Silva and Pereira, 2008; van Reeuwijk and Holzner, 2014);

$$U(y,t=0) = \frac{U_J}{2} - \frac{U_J}{2}\tanh\left[\frac{H_J}{4\theta_0}\left(1-\frac{2|y|}{H_J}\right)\right], \tag{2.1}$$

where $y = 0$ is the centre-plane of the planar jet and θ_0 is the initial momentum thickness. We take $H_J/\theta_0 = 35$ as in other studies since this value was reported to lead to faster transition compared to lower H_J/θ_0 values when perturbed (da Silva and Pereira, 2008). A high-frequency white noise is added on top of the mean velocity profile to accelerate the transition to turbulent flow. To confine the added noise inside the jet region, $y = [-H_J/2, H_J/2]$, the hyperbolic tangent velocity profile is used (i.e., eq. 2.1) by taking $U_J = 1$. The initial noise is multiplied by this function which is equal to one at the centre-plane and goes smoothly to zero at the border of the jet. The added noise is made divergence-free and the resulting total velocity field satisfies the continuity equation.

The energy spectrum of the random velocity field is $E_{noise}(k) = C_{noise}\exp(-(k-k_0)^2)$ where C_{noise} is the constant controlling the amplitude and k_0 is the wavenumber of the energy

peak. This peak of the excited wavenumber is chosen to be 1.5 times the wavenumber corresponding to the initial shear layer thickness, which corresponds to $k_0 = 75$. The shear layer thickness is determined by the difference between the value of y where $dU/dy = 0.95max(dU/dy)$ and the value of y where $dU/dy = 0.05max(dU/dy)$, $max(dU/dy)$ being the maximum velocity gradient on the initial mean profile. The amplitude C_{noise} is tuned so that the mean enstrophy value of the random fluctuations at the centre-plane $y/H_J = 0$ is approximately 4% of the maximum value of the initial mean enstrophy profile. This corresponds to velocity fluctuations at the centre of the jet which are 2.45% of the initial mean stream-wise velocity U_J.

The domain size of the DNS is ($8H_J$, $12H_J$, $8H_J$). The current domain size is two times larger on each side compared to the domain used in da Silva and Pereira (2008) where the streamwise extent of the domain is evaluated by taking into account the length scale associated with the Kelvin-Helmholtz (KH) instability in this direction. Following the discussion by da Silva and Pereira (2008), the streamwise extent of the current simulation domain corresponds to $L_x = 9.2\ell_{KH}$, where ℓ_{KH} corresponds to the length scale for the KH instability in the streamwise direction. For the cross-stream extent of the domain L_y is larger than numerous studies reporting the details of the DNS of temporally developing planar jet, where $6H_J$ is used in the studies of da Silva and Pereira (2008) and da Silva and dos Reis (2011), while $10H_J$ is used by Watanabe et al. (2019) and Hayashi et al. (2021). On the other hand, a significantly large L_y is used in the study of van Reeuwijk and Holzner (2014) as large as $18H_J$ in order to extend the window for time integration, before the expansion of the jet is affected by the boundary conditions in the cross-stream direction. In the present study, we do not have a specific reason to extend the simulation time and thus $L_y = 12H_J$ is chosen. The spanwise extent of the domain is mainly related to the convergence of the results, which is observed to be particularly important for the TNTI local analysis conducted in chapters 4 and 5 and thus the domain size in the spanwise direction is chosen as $L_z = L_x = 8H_J$, similar to the stream-wise extent. Of course, the extent of the simulation domain has been thought by taking into account the desired resolution and also the limits of the computational tools/resources in use.

The corresponding grid size is $(1024 \times 1536 \times 1024)$ in directions x, y, and z respectively, which leads to a homogeneous grid size in every direction. For ensemble averaging, five DNS were run, referred to as $PJ1$, $PJ2$, $PJ3$, $PJ4$, and $PJ5$ to improve the convergence of the results. The governing equations are solved with a pseudo-spectral solver and a second-order Runge-Kutta time stepping scheme. Periodic boundary conditions in all directions are compatible with $V = 0$ and $\partial\langle p\rangle/\partial x = 0$, in agreement with the theory in section 3.2. Apart from the $2/3$ truncation de-aliasing method, a filtering function effective at the very high end

of the resolved wavenumbers is also applied to reduce the oscillations appearing in the outer edge of the TNTI layer and the irrotational region outside of the turbulent bulk of the jet.

Figure 2.1a shows the Reynolds number defined in terms of the Taylor length scale $\lambda = \sqrt{10\nu K_0/\varepsilon_0}$, where the K_0 and ε_0 are the kinetic energy and dissipation averaged over the centre-plane ($y = 0$). $Re_\lambda = (\sqrt{2/3K_0}\lambda)/\nu$ remains constant at about $Re_\lambda \sim 45 - 65$ throughout the time evolution of the jet after the transition to a fully turbulent regime.

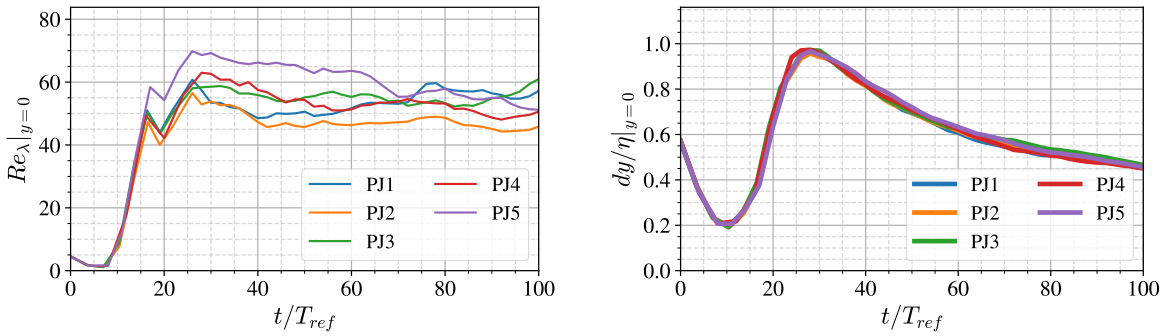

(a) Taylor Reynolds number

(b) Grid resolution

Fig. 2.1 Taylor Reynolds number, Re_λ and spatial resolution $dx = dz = dy = H_J/128$, normalized by the Kolmogorov scale at the centre-plane of the jet ($y = 0$). The five different curves correspond to five DNS realizations.

Given that $\nu/\sqrt{K_c} \sim \eta(\eta/\delta)^{1/3}$, the constancy of Re_λ in time is one indication that the turbulent length scales of the flow evolve similarly in time as expected from the previous section. Figure 2.1b shows that the spatial resolution $dx = dy = dz$ remains at all times smaller than the Kolmogorov length calculated in the centre-plane $y = 0$. This resolution is observed to be critical for post-processing in this study as it is directly related to the accurate resolution of the geometrical properties of the TNTI. Results for the simulations with higher Reynolds numbers on the same grid will be presented later in section 2.3 and the necessity for the high grid resolution favoured in the present study will be demonstrated.

2.2 Modified de-aliasing method

We are interested in fine details of iso-enstrophy surfaces (IES)s which are part of the TNTI layer and located at the boundary of the turbulent volume. At the outer edge of the TNTI, the enstrophy value decays quickly to zero. In chapter 3 we investigate how quantities such as the fractal dimension of the interface D_f, and local propagation velocity of the TNTI v_n vary across the thickness of the TNTI, for various IESs. A wide range of enstrophy threshold values $\omega_{th}^2/\omega_{ref}^2$ are considered, in a range where the sensitivity of the detected turbulent

volume to the value of $\omega_{th}^2/\omega_{ref}^2$ is low (see figure 2.7). The lowest threshold considered in chapter 3 is $\omega_{th}^2/\omega_{ref}^2 = 10^{-6}$.

In order to obtain relevant TNTI statistics at such very low enstrophy levels, the DNS solution must be smooth and free of oscillations. When using a classical $2/3$ truncation de-aliasing method for the simulations with the pseudo-spectral code, we observe numerical oscillations at these low enstrophy values which makes it impossible to investigate this outer part of the TNTI layer. The limiting effects of these oscillations have been mentioned also in the study of Krug et al. (2017) at the non-turbulent side of the interface layer. Some trials with (i) a posteriori filtering of the velocity field by spectral filter and (ii) modification of the $2/3$ truncation de-aliasing method acting during the simulation, lead to the conclusion that the latter is much more effective for the elimination of the weak numerical oscillations for very low ω^2 threshold values and the accurate resolution of the geometrical features of these IES. Thus the modified de-aliasing approach has been chosen to be applied in the present study.

For the modified de-aliasing method, a filter function $R(|\vec{k}|)$ (where $\vec{k} = (k_x, k_y, k_z)$) has been applied in the form $R(|\vec{k}|) = 2 - \exp(c_1(|\vec{k}| - k_{filter})^2)$ where c_1 is a coefficient chosen to fix the value $R(k_{cut-off}) = 0.01$. The wavenumbers with $|\vec{k}| < k_{filter}$ are completely unaffected by the filtering and the wavenumbers with at least one component greater than the cut-off wavenumber, i.e. $max[(k_x, k_y, k_z)] > k_{cut-off}$, are truncated. The wavenumbers with $|\vec{k}| > k_{filter}$ but $max[(k_x, k_y, k_z)] < k_{cut-off}$ are then filtered by using the function $R(|\vec{k}|)$. Due to the shape of $R(|\vec{k}|)$, the effect of this modified de-aliasing is only limited to the wavenumbers very close to the cut-off wavenumbers.

A similar procedure is applied in Krug et al. (2017) with their choice of a pth-order Fourier exponential filter for the de-aliasing. Our method, which has no effect on the modes unaffected by the aliasing, is able to suppress the oscillations within the useful range of enstrophy. As we are dealing with a very sharp interface and need to reduce our enstrophy thresholds to extremely low values, the numerical oscillations naturally become observable at some point, particularly without a special treatment being employed. This is due to the fact that the spectral method does not underestimate the derivatives and does not smooth out sharp gradients as is the case with finite difference methods for example.

In order to demonstrate how the classical sharp de-aliasing leads to some oscillations and the effectiveness of our modified de-aliasing method, we compare the results of two simulations starting from identical initial conditions (even the same random noise phase distribution), solved by the same pseudo-spectral solver. The first simulation was performed with the classical sharp de-aliasing method which truncates the solution at all wavenumbers with a modulus larger than $2/3k_{max} = N/3$, and the second simulation uses our modified

de-aliasing method. As can be observed in figure 2.1b, the minimum value of the mean Kolmogorov scale η on the centreline appears just after the transition, and we therefore compare the solutions of the two simulations at $t/T_{ref} = 26$ where the grid resolution is most problematic. We also consider the simulation $PJ5$ which has the highest Re_λ peak.

Figures 2.2a and 2.2b show the enstrophy in a normal streamwise plane for the two simulations at $t/T_{ref} = 26$. Figure 2.2a corresponds to the simulation with the modified de-aliasing and figure 2.2b is the case where the classical $2/3$ truncation method is used. Oscillations are clearly visible in the case of classical de-aliasing even for normalized enstrophy levels higher than 10^{-3} whereas the solution is smooth for all investigated enstrophy levels with our modified de-aliasing method.

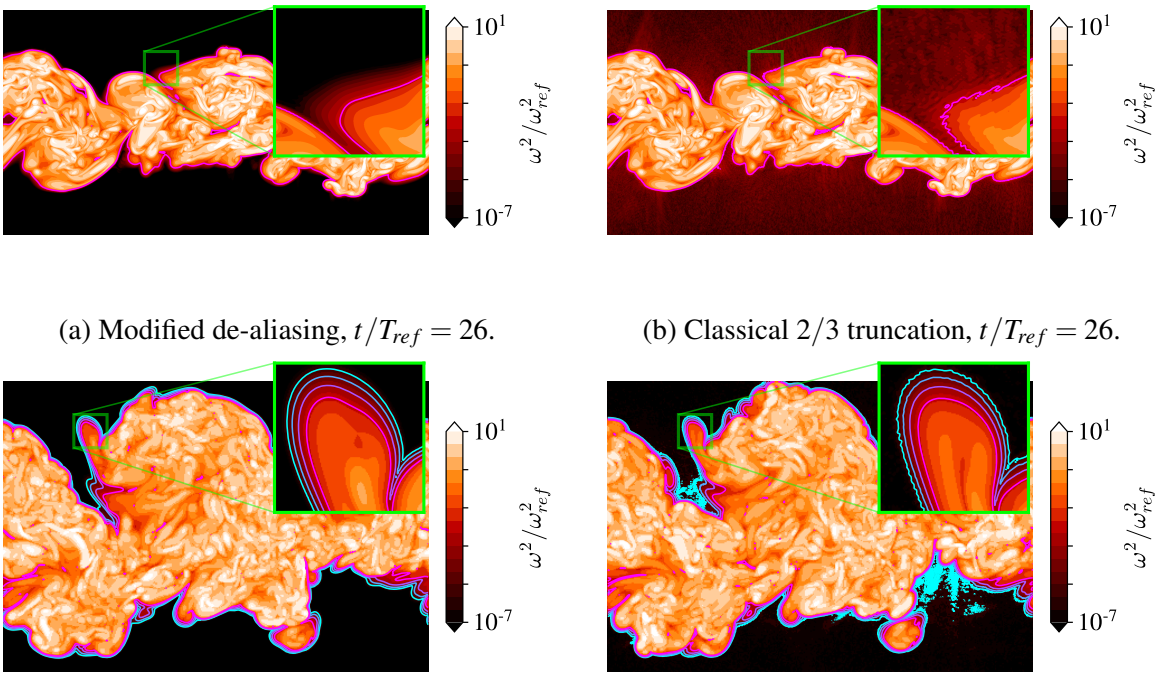

(a) Modified de-aliasing, $t/T_{ref} = 26$.

(b) Classical $2/3$ truncation, $t/T_{ref} = 26$.

(c) Modified de-aliasing, $t/T_{ref} = 50$.

(d) Classical $2/3$ truncation, $t/T_{ref} = 50$.

Fig. 2.2 Contour fields of ω^2/ω^2_{ref}, on the mid-section along the z-axis, for two identical simulations PJ5 (a,c) with modified de-aliasing (used in the present study) (b,d) classical $2/3$ truncation. (a,b) at $t/T_{ref} = 26$ and (c,d) at $t/T_{ref} = 50$. Contours showing IES associated with $\omega^2_{th}/\omega^2_{ref}$ from 10^{-3} to 10^{-6}, by colours magenta to cyan with an interval of one order of magnitude in between the values of ω^2_{th}. Magenta and cyan correspond to $\omega^2_{th}/\omega^2_{ref} = 10^{-3}$ and 10^{-6} respectively.

It should be noted that the oscillations are visible at fairly high enstrophy thresholds at this instant and that these oscillations gradually reduce with time, but do not disappear at

the targeted enstrophy thresholds $\omega_{th}^2/\omega_{ref}^2 > 10^{-6}$ for $t/T_{ref} > 30$ with the classical $2/3$ truncation method. In figure 2.2c and 2.2d, enstrophy contours are given for $t/T_{ref} = 50$, which is in the time range we will investigate in chapter 3 and conduct the local analysis of the TNTI in chapters 4 and 5. Although some IES appear smooth, local regions where the oscillations are present may introduce significant problems. For example, the computation of the fractal dimension of the IES D_f would be affected by these oscillations, as the IES becomes more volume-filling in the presence of these numerical artifacts.

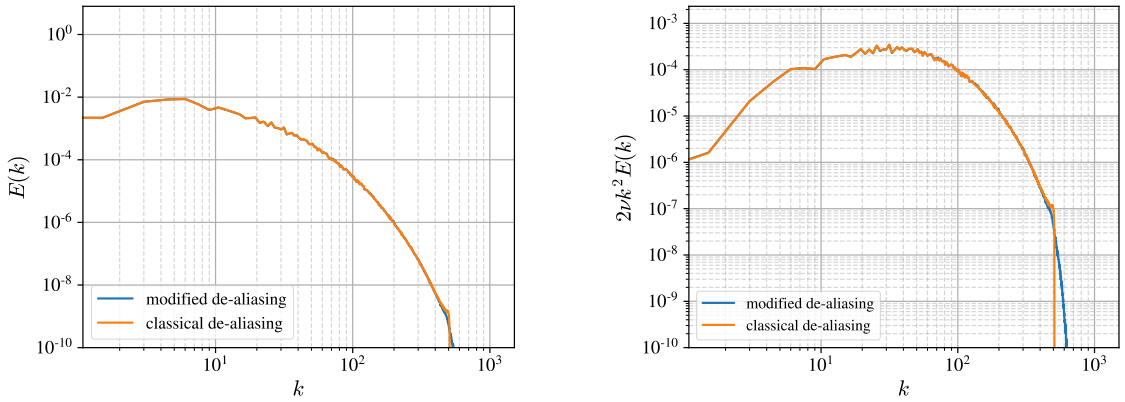

(a) 2D energy spectra

(b) 2D dissipation spectra

Fig. 2.3 (a) Energy and (b) dissipation spectra at the centre-plane of two identical simulations in terms of flow parameters and initial conditions, one with modified de-aliasing and the other one with classical $2/3$ truncation method. Results are from the simulation PJ5 at $t/T_{ref} = 26$.

To quantify the energy content of these oscillations, the energy and dissipation spectra on the centre-plane are compared for the two simulations in figure 2.3. The spectra look identical for both cases, apart from the small peak at the very end of the resolved wave numbers which is present for the classical $2/3$ truncation method. This shows how difficult it is to assess the smoothness of the irrotational region and the external part of the TNTI from energy and dissipation spectra.

In figure 2.4, the jet volume as a function of the enstrophy threshold is plotted at $t/T_{ref} = 26$ for the two simulations with classical and modified de-aliasing methods. A clear extension of the plateau towards lower values of $\omega_{th}^2/\omega_{ref}^2$ is seen when the modified de-aliasing method is used. Meanwhile, the high threshold regions remain unaffected by the modification, showing that the de-aliasing method works as planned. It suppresses the weak oscillations at the outer regions of the TNTI but the evolution of the turbulent region is similar in both cases.

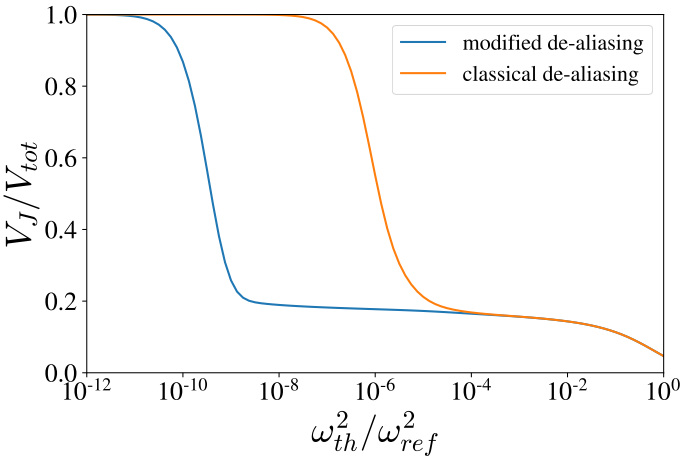

Fig. 2.4 The jet volume defined as $\omega^2 > \omega^2_{th}$ for the two simulations PJ5 at $t/T_{ref} = 26$ with modified de-aliasing (blue) and classical $2/3$ truncation (orange).

2.3 Limitations on the Reynolds number

Despite the success of the modified de-aliasing method for the accurate resolution of the IESs associated with low values of ω^2, there exists a limitation in terms of the Reynolds number Re_G of the simulations, as increasing values of Re_G leads to smaller turbulent scales, which in turn means a drop in the resolution of the simulation in terms of the smallest turbulent length scales. Dissipation of the turbulent kinetic energy is mainly associated with these small scales and their under-resolution leads to a build-up of turbulent kinetic energy at the highest wavenumbers, which leads to the weak oscillations that are documented in section 2.2.

In an attempt to demonstrate the limitations in Reynolds number, additional simulations have been conducted with $Re_G = 6400$ and $Re_G = 9600$ which are referred to as PJ-Re6400 and PJ-Re9600 respectively. The initial conditions and the solver properties remain the same as described in section 2.1. The computational grid also remains the same as the PJx simulations, due to the computational constraints and the modified de-aliasing method is also employed.

With the increase of Re_G, the Reynolds number based on Taylor length scale Re_λ at the centre-plane of the jet becomes $Re_\lambda \approx 70$ and $Re_\lambda \approx 80$ for the simulations PJ-Re6400 and PJ-Re9600, compared to $Re_\lambda \approx 50$ for PJ1 simulation (labelled as $Re_G = 3200$), which can be seen in figure 2.5a. Figure 2.5b shows the time evolution of the spatial resolution normalized by the Kolmogorov scale at the centre-plane after the transition of the planar jet into the fully turbulent regime.

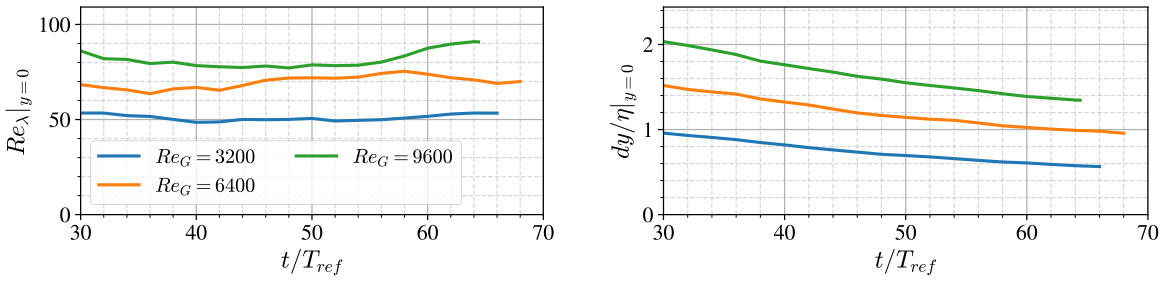

(a) Variation of Re_λ in time.

(b) Variation of resolution dy/η at the centre-plane of the planar jet.

Fig. 2.5 Re_λ and dy/η at the centre-plane of the planar jet for $Re_G = 3200$ (PJ1 simulation), $Re_G = 6400$ and $Re_G = 9600$.

Following section 2.2, a comparison at $t/T_{ref} = 50$ is chosen as this time is in the middle of the investigated time range in chapter 3. Figure 2.6 shows the enstrophy contours at the cut section of the PJ-Re6400 simulation along with the IES marked at the TNTI.

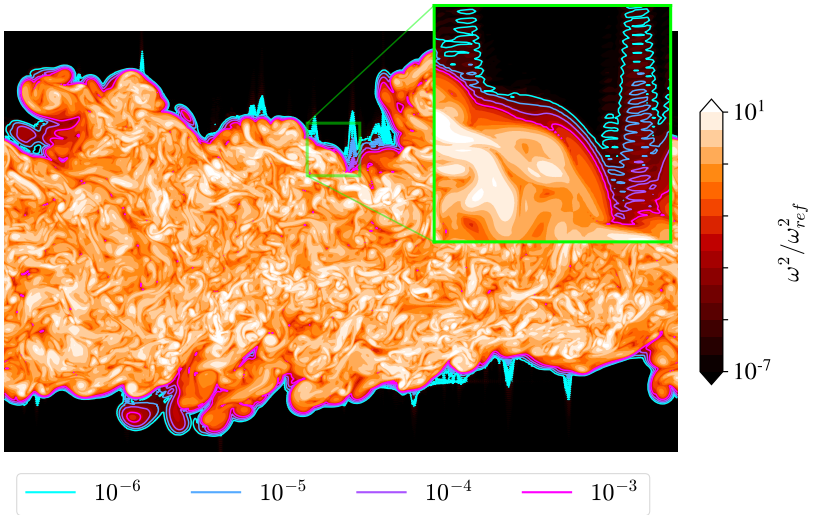

Fig. 2.6 Enstrophy contour field at a cut-section of the simulation PJ-Re6400 at $t/T_{ref} = 50$, with the IES from $\omega^2_{th}/\omega^2_{ref} = 10^{-6}$ to 10^{-3} are shown as contours at the TNTI.

It is observed that numerical oscillations are present in the IESs due to the reduction of the resolution of the simulations. The oscillations are present even at the IES of thresholds up to $\omega^2_{th}/\omega^2_{ref} = 10^{-4}$. In chapter 3, the box-counting algorithm is applied in order to get information about the fractal properties of each IES. Under these conditions, the application of the box-counting algorithm at these thresholds ($\omega^2_{th}/\omega^2_{ref} \lesssim 10^{-3}$) is not possible.

This analysis shows that $Re_G = 3200$ is the maximum Reynolds which can be achieved keeping the resolution $(1024 \times 1536 \times 1024)$ used for the simulation PJx without compromising the accurate resolution of the wide range of IESs constituting the TNTI.

2.4 Identification of the turbulent jet and locating the TNTI

The procedure for the detection of the TNTI starts with the identification of the turbulent jet. As it has been mentioned above, TNTI is a spatially local region associated with very high gradients of ω^2. In relation to IESs being located extremely close to each other, the identified turbulent jet volume does not depend much on the threshold value of enstrophy ω^2_{th} being used, if the threshold value is chosen from the range of ω^2 values which fall into the TNTI layer. In figure 2.7 we plot the turbulent jet volume V_J identified by the condition $\omega^2 \geq \omega^2_{th}$. In this figure, V_J is normalized by the volume of the simulation domain V_{tot} and plotted as a function of the normalized enstrophy threshold values $\omega^2_{th}/\omega^2_{ref}$, where the ω^2_{ref} is the ω^2 averaged over the centre-plane of the jet (Note that ω^2_{ref} evolves in time).

Figure 2.7 reveals the presence of a plateau over a very wide range of threshold values at any time between $t/T_{ref} = 30$ and $t/T_{ref} = 90$. This is the range of ω^2 packed tightly together within the TNTI, leading to V_J/V_{tot} being approximately constant for a wide range of $\omega^2_{th}/\omega^2_{ref}$ values and thereby reflecting the sharp demarcation between the turbulent region and the outer non-turbulent region.

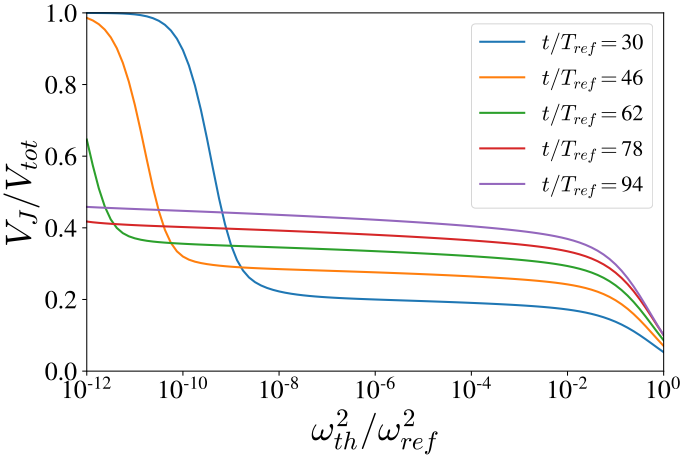

Fig. 2.7 Detected turbulent volume V_J/V_{tot} obtained by varying the threshold values $\omega^2_{th}/\omega^2_{ref}$ for the PJ1 simulation.

The left side of the plateau, corresponding to low enstrophy threshold values, is limited by the numerical noise. These numerical oscillations get significant as the threshold value goes

to zero. Also, it has been shown in section 2.2 that the modified de-aliasing method which has been employed in the current study reduces the numerical oscillations and increases the $\omega_{th}^2/\omega_{ref}^2$ range of the plateau by extending its left side to values closer to $\omega_{th}^2/\omega_{ref}^2 = 0$.

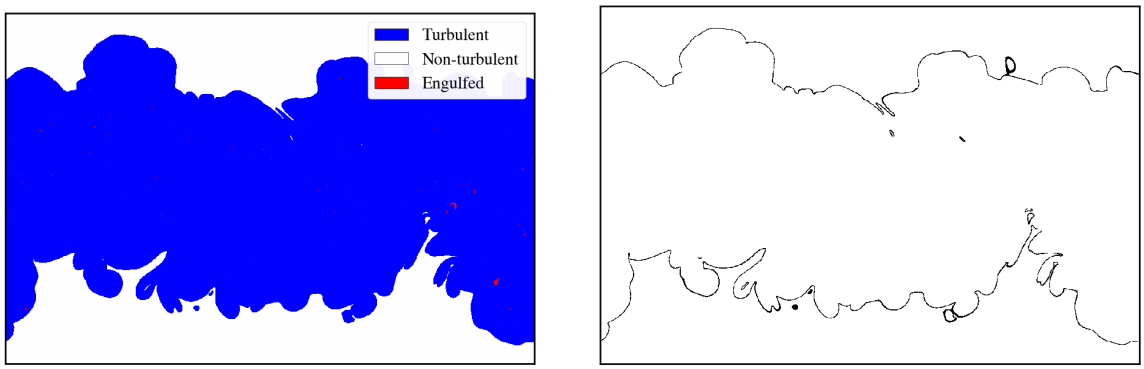

(a) Labelled turbulent, non-turbulent and engulfed volumes.

(b) Cut-section of the detected IES defined by $\omega_{th}^2/\omega_{ref}^2 = 10^{-3}$.

Fig. 2.8 Labelling of the volume and the detected IES at time $t/T_{ref} = 50$ for simulation PJ1, by using the threshold $\omega_{th}^2/\omega_{ref}^2 = 10^{-3}$.

Following the determination of the $\omega_{th}^2/\omega_{ref}^2$ range defining the TNTI, we now determine the TNTI as shown in figure 2.8. The procedure starts by labelling the turbulent volume by the condition $\omega^2(x,y,z) \geq \omega_{th}^2$ and obtaining the binary field. The turbulent region corresponds to blue marked region in figure 2.8a and the non-turbulent regions correspond to the white and red marked regions, where the engulfed regions (shown with red) are still present. The non-turbulent volumes are labelled in 3D by using the labelling function from the open-source SciPy library (Virtanen et al., 2020) so that all independent non-turbulent volumes have their individual label number. At this stage, the connectivity of the non-turbulent regions is checked leading to the detection of engulfed non-turbulent volumes. Engulfed volumes are the chunks of irrotational fluid surrounded totally by the turbulent volume and they have no connection in 3D with the external irrotational region. Some examples of these detected engulfed volumes can be seen in figure 2.8a, marked in red. The white detached regions inside the turbulent area 2.8a (blue) are connected to the outer non-turbulent region in the 3D field (out of the figure's plane). In order to consider only the outer surface for the TNTI, the engulfed volumes are suppressed in this study. To get the surface corresponding to a chosen $\omega_{th}^2/\omega_{ref}^2$ in 3D, a dilation procedure is used in 3-dimensions to expand the non-turbulent region into the turbulent region by one data point. Then by subtracting the original field from the dilated field, we end up with a field where the 3D jet envelope is marked by the number one, and all other data points are marked zero in the entire simulation domain. A cut-section

of the resulting field is shown in 2.8b, as the dark line showing the cut-section of the detected IES of $\omega^2_{th}/\omega^2_{ref}$. This detection procedure is applied for various $\omega^2_{th}/\omega^2_{ref}$ values to obtain the interface characteristics at different locations throughout the TNTI layer as in Krug et al. (2017); van Reeuwijk and Holzner (2014).

2.5 Highly resolved simulations

Even though the resolution of the PJx simulations, obtained with a dedicated modified de-aliasing method is observed to be enough to conduct a global study of the TNTI which is presented in chapter 3, different methods of analysis are employed for the investigation of the flow field at the vicinity of the TNTI in chapters 4 and 5. An important local property that will be used widely in chapter 4 and 5 is the mean curvature H_m computed at any location on detected IESs by using the relation,

$$H_m = \frac{1}{2}\nabla \cdot \boldsymbol{n} = \frac{1}{2}(\kappa_1 + \kappa_2). \tag{2.2}$$

Here, κ_1 and κ_2 are the curvatures on the two principal axes and $\boldsymbol{n}$ is the enstrophy normal vector defined as,

$$\boldsymbol{n} = \frac{\nabla\omega^2}{|\nabla\omega^2|}. \tag{2.3}$$

According to this definition, the vector $\boldsymbol{n}$ points towards the turbulent core of the jet. Another physical interpretation for H_m is that $H_m = 1/R_{curv}$ where R_{curv} is the radius of the curvature of the surface. Figure 2.9b shows the PDF of the H_m normalized by the turbulent length scales at the centre-plane, η and λ. It is seen from the figure that a sharp peak is present at the low-negative values of H_m. This is related to the concave surfaces at the interface, showing that the interface is mainly constituted by concave regions with low curvature values. The peak is located at $H_m\lambda \approx 0.5$ meaning the radius of curvature is $R_{curv} \approx 2\lambda$ for these regions. Despite the negative side of the PDF going rapidly to very low probability values, a second peak is present for the positive values of H_m. This second peak is located roughly at $H_m\eta \approx 1$ meaning some parts of the interface have a curvature with a radius of approximately η. Naturally, the question arises about this particular feature, whether these values of H_m are physical or do they occur due to numerical oscillations and what is the extent of H_m which is physical?

Although great care has been taken to reduce the numerical oscillations in the data, mainly to eliminate any numerical effect on the topology of the interface, for the wide range of IESs

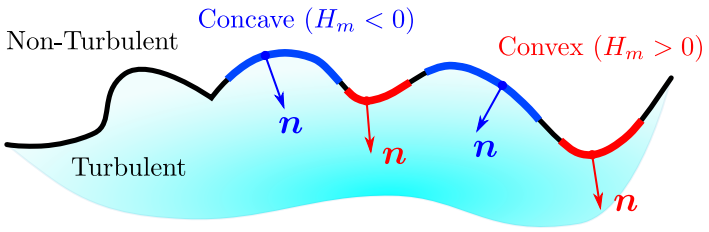

(a) Schematic of TNTI showing the enstrophy normal vector $\boldsymbol{n}$ defined by the eq. 2.3 and examples of concave and convex regions.

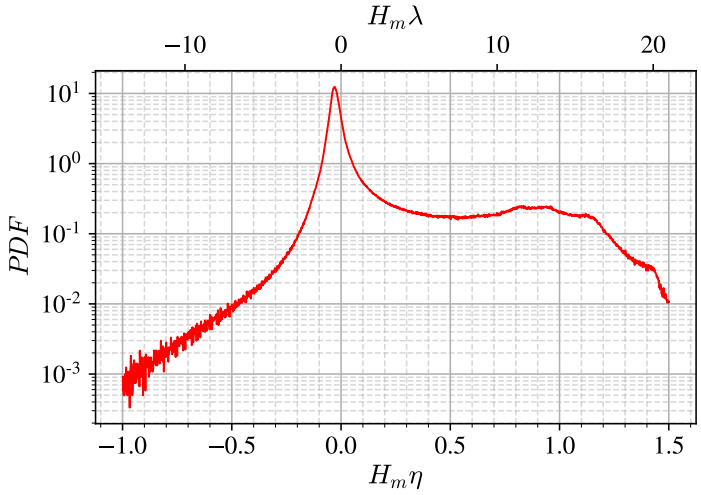

(b) PDF of H_m for the IES of $\omega_{th}^2/\omega_{ref}^2 = 10^{-3}$ for the simulation PJ1.

Fig. 2.9 Schematic of the TNTI showing the concave/convex regions and the PDF of $H_m\eta$ for the IES of $\omega_{th}^2/\omega_{ref}^2 = 10^{-3}$ for the simulation PJ1.

considered in chapter 3, the accurate computation of H_m imposes a more strict constraint as it contains second order derivatives of ω^2 (see eq. 2.2 and 2.3).

In order to investigate the effects of numerical noise on the field of H_m, a series of tests are conducted with a posteriori filtering of the ω^2 field by using a Gaussian filter. Then H_m is calculated to see the effects of the filtering of ω^2 field on the H_m values at the IES. The standard deviation of the filter kernel σ is also varied to see its effect. Figure 2.10 shows again the PDF of the H_m values at the IES of $\omega_{th}^2/\omega_{ref}^2 = 10^{-3}$, this time along with the H_m values computed by the filtered $\widetilde{\omega^2}$ field. A variation in the PDF of H_m is observed mostly in the high curvature regions of the PDF in the case of the application of the a posteriori filter. The distribution at the lower values of H_m remained unchanged by this operation.

These findings suggest that even though the numerical oscillations are pretty weak and their effect is small enough not to interfere with the resolution of the general shape of the

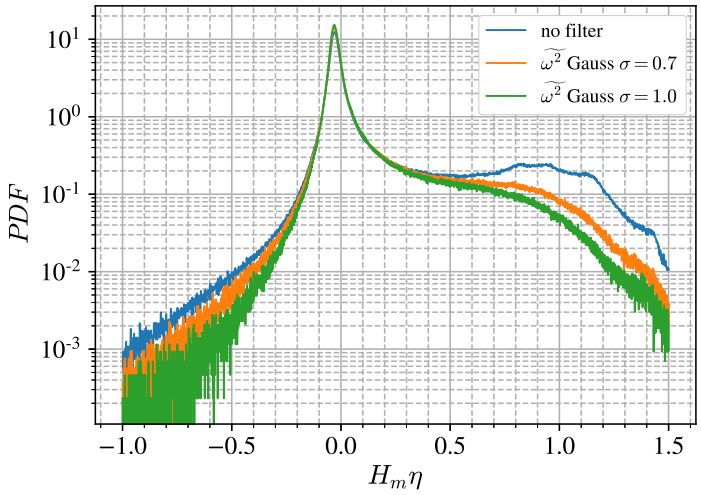

Fig. 2.10 PDF of H_m for the IES of $\omega_{th}^2/\omega_{ref}^2 = 10^{-3}$ detected from the ω^2 field and a posteriori filtered enstrophy fields $\widetilde{\omega^2}$, for the simulation PJ1.

IESs, the computed quantities containing high order derivatives or ω^2 can still be affected. On the other hand, applying an a posteriori filter opens new questions such as at which stage the filter should be applied (filtering the field of $\boldsymbol{u}$, $\boldsymbol{\omega}$ or ω^2) for the consistency of the variables at the TNTI location? What should be the properties of the filter used? What will be the eventual effects of the filter on the nature of the TNTI? All these points being important, the latter question is the most concerning one. TNTI being a very local phenomenon with sharp gradients of flow variables, can be altered by the filtering operation. On top of that, the thickness of the TNTI varies at different locations of the interface, thus the effects of the filter will depend on the local structure of the TNTI.

In order to avoid the introduction of these new questions which may lead to serious doubts about the data being used, the quality of the data is chosen to be improved by further increasing the resolution of the simulation, thus resolving the dissipation scales more accurately. Energy reduces very sharply in the dissipative range, thus any increase of the resolved wavenumber will have a significant effect on the energy content of these oscillations.

Due to the computational limits of the solver being used, the flow fields from PJ1 - PJ5 simulations are being interpolated, in Fourier space, into a finer grid which consists of $N_x \times N_y \times N_z = (1536 \times 2304 \times 1536)$ elements in each direction. All simulations are run for $t = 2T_{ref}$ so that the oscillations are damped naturally by the dissipative term of NS equations and the PJx-HR data set is produced. For example in order to obtain PJ1-HR data, the velocity field of PJ1 at $t/T_{ref} = 48$ is interpolated to a fine grid and then run with exact same parameters for $2T_{ref}$ which becomes the highly resolved case of PJ1 simulation at the

instant of $t/T_{ref} = 50$. The resolution increases from $dy/\eta = 0.7$ to $dy/\eta = 0.47$ for the instant of $t/T_{ref} = 50$ for the PJx-HR data set.

Figure 2.11 shows the PDF of H_m on the IES of $\omega_{th}^2/\omega_{ref}^2 = 10^{-3}$, for the simulations PJ1 and PJ1-HR. As PJ1-HR has been obtained by using the flow field of PJ1 at a previous instant, they have nearly exact same flow structures. The difference comes from the fact that the finer grid used for PJ1-HR simulation leads to a more accurate resolution of the very small scales and that the dissipation range is better captured. Without an energy build-up at small scales, the numerical oscillations at very high wavenumbers are significantly reduced.

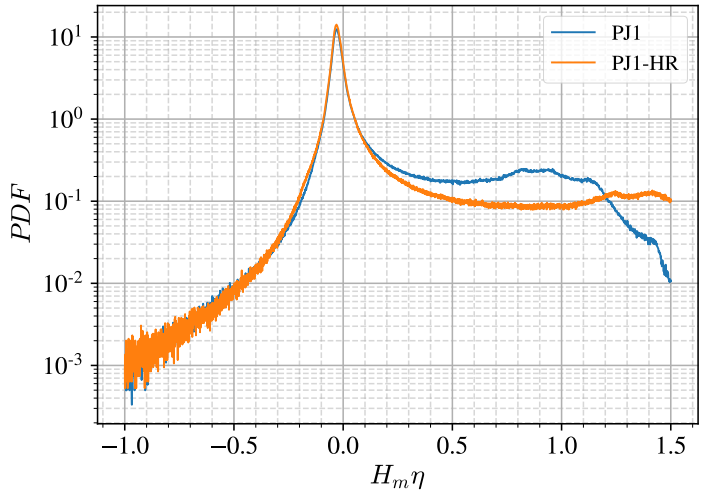

Fig. 2.11 PDF of H_m at the IES of $\omega_{th}^2/\omega_{ref}^2 = 10^{-3}$ for the simulations PJ1 and PJ1-HR.

For the small values of H_m, both cases correspond to each other but for the positive branch of the PDF, they start deviating from each other at $H_m\eta \approx 0.15$. The second peak observed in figure 2.9b at $H_m\eta \approx 1$ is shifted to higher $H_m\eta$ values (clearly larger than 1) by the increase of the resolution of the simulation. This shows that the increase in the resolution is still beneficial to capture the very fine details of the IESs more accurately. It should be noted again that the amplitudes of oscillations of PJx simulations are extremely small, they do not affect any quantities being investigated in chapter 3, as a global approach has been employed in this chapter for the investigation of the properties of the temporally developing turbulent jet and the mean propagation velocity of the interface.

On the other hand, in chapter 4 and 5, a different methodology is used for the analysis of the interface locally, where the accurate computation of the high order derivatives of flow variables is becoming crucial as it has direct effects on the local properties at the detected IESs such as H_m. For this reason, the data set of PJx-HR is used in chapters 4 and 5.

2.6 Improved TNTI detection

In addition to enhancing the resolution of the dataset for the local analysis of flow parameters at the TNTI, we have also improved the accuracy of TNTI detection. The classification of the turbulent jet volume, non-turbulent region, and engulfed regions is detailed in Section 2.4. This methodology yields a set of points representing the Interface of Entrainment Structure (IES), corresponding to the closest grid points that satisfy the condition $\omega^2 > \omega_{th}^2$ on the turbulent side of the IES, defined by $\omega^2 = \omega_{th}^2$. Given the high resolution of our simulations, these detected points are already precise enough to capture the fine geometrical details of the interface.

However, it is essential to note that the TNTI is associated with a thin layer characterized by very high gradients. Therefore, a slight error in the exact location of the detected points on the IES can lead to inaccuracies in some statistics. In Chapters 4 and 5, we consider local variables at the TNTI location, such as H_m over the TNTI surface, and derive local statistics based on these variables. Thus, having precise values of these local variables on the detected IES is crucial for our analysis. To enhance the accuracy of TNTI location, we have applied a sub-grid correction to the coordinates of the points detected using the method described in Section 2.4. This refinement ensures the TNTI location is as precise as possible for our analysis.

To apply the correction, we process each detected point individually. For every point, we calculate the enstrophy normal vector $\boldsymbol{n}$ (eq. 2.3), which indicates the direction of the fastest growth of enstrophy. We then create a very fine 1D grid (with a resolution of $\frac{1}{10}dy$) aligned with the $-\boldsymbol{n}$ direction and we interpolate the values of enstrophy ω^2.

Following this interpolation, we examine each point on the fine 1D grid to identify the one that is closest to the specified ω_{th}^2 value. Subsequently, we update the coordinates of the detected point and the enstrophy normal vector $\boldsymbol{n}$ at this new location.

Since the condition for the identification of the point where the enstrophy value is closest to ω_{th}^2 is a manual process, in the regions where the TNTI normal axis crosses the same IES multiple times, it may lead to a jump of the point to another location along the IES. In order to avoid this, we implement an additional condition that prevents the coordinate correction if the correction distance is greater than dy.

The contour plot given in figure 2.12 illustrates the improvement of the locations of points by showing the probability density of the enstrophy values of all the points before and after the correction operation i.e., ω_{before}^2, ω_{after}^2. The contour plot in figure 2.12 is generated by the application of the coordinate correction process to $22M$ points detected by the procedure described in section 2.4, for the IES of $\omega_{th}^2/\omega_{ref}^2 = 10^{-3}$ for the PJ4-HR simulation at $t/T_{ref} = 50$. The magenta line shows the perfect initial value of enstrophy corresponding to

$\omega^2_{before}/\omega^2_{th} = 1$, at which the enstrophy was equal to ω^2_{th} before the correction. Similarly, the red line corresponds to the perfect correction where the enstrophy value is exactly ω^2_{th} after the application of the correction.

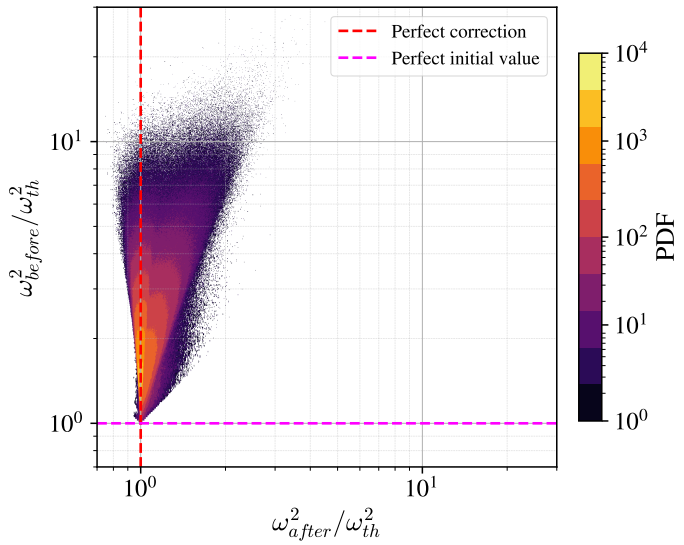

Fig. 2.12 Contour plot of the joined probability of enstrophy values at the detected points on the IES before and after the coordinate correction operation. Plot generated for the IES of $\omega^2_{th}/\omega^2_{ref} = 10^{-3}$ for the PJ4-HR simulation at $t/T_{ref} = 50$.

The improvement can be observed clearly as there is a significant difference for all the points where they are positioned much more accurately on the IES defined by ω^2_{th}, resulting in a narrower distribution of points along the $\omega^2_{after}/\omega^2_{th}$ axis. The majority of the points are observed to be positioned close to the line for the perfect correction and the maximum error on the enstrophy value along the IES decreases by a factor of approximately 5.

This sub-grid correction ensures that the locations of the points are more precise concerning the IES associated with ω^2_{th} value. This accuracy for the location of the points is crucial as the TNTI is characterized by very high gradients, meaning that even a small displacement error can have a considerable impact on the values of local variables.

Chapter 3

Scaling of the Jet and the Mean Propagation Velocity of the Interface

Preface to the chapter

The results given in this chapter are published in *Journal of Fluid Mechanics*, with the title "Length scales and the turbulent/non-turbulent interface of a temporally developing turbulent jet" (Er et al., 2023). The appendices and the sections of the paper where the simulation details are given, including modified de-aliasing and TNTI detection are moved to chapter 2 for the completeness of the current manuscript.

Abstract

The temporally developing self-similar turbulent jet is fundamentally different from its spatially developing namesake because the former conserves volume flux and has zero cross-stream mean flow velocity whereas the latter conserves momentum flux and does not have zero cross-stream mean flow velocity. It follows that, irrespective of the turbulent dissipation's power law scalings, the time-local Reynolds number remains constant and the jet half-width δ, the Kolmogorov length η and the Taylor length λ grow identically as the square root of time during the temporally developing self-similar planar jet's evolution. We predict theoretically and confirm numerically by Direct Numerical Simulation that the mean centre-line velocity, the Kolmogorov velocity and the mean propagation speed of the Turbulent/Non-Turbulent Interface (TNTI) of this planar jet decay identically as the inverse square root of time. The TNTI has an inner structure over a wide range of closely spatially packed iso-enstrophy surfaces with fractal dimensions that are well defined over a range

of scales between λ and δ and that decrease with decreasing iso-enstrophy towards values close to 2 at the viscous superlayer. The smallest scale on these iso-surfaces is around η and the length scales between η and λ contribute significantly to the surface area of the iso-enstrophy surfaces without being characterized by a well-defined fractal dimension. A simple model is sketched for the mean propagation speeds of the iso-enstrophy surfaces within the TNTI of temporally developing self-similar turbulent planar jets. This model is based on a generalized Corrsin length, on the multiscale geometrical properties of the TNTI and on a proportionality between the turbulent jet volume's growth rate and the growth rate of δ. A prediction of this model is that the mean propagation speed at the outer edge of the viscous superlayer is proportional to the Kolmogorov velocity multiplied by the $1/4$th power of the global Reynolds number.

3.1 Introduction

The Turbulent/Non-Turbulent Interface (TNTI) is a thin layer which sharply demarcates between turbulent vortical flow and non-vortical flow at the turbulent edge of a wide variety of turbulent flows such as turbulent boundary layers, mixing layers, jets and wakes (Corrsin and Kistler, 1955; da Silva et al., 2014). The TNTI propagates relative to the fluid and thereby controls entrainment and resulting in transfers across it of mass, momentum and various scalar quantities such as heat. Determining the local propagation velocity of the TNTI, and in particular its scalings, is therefore of central importance.

The TNTI's local propagation velocity is often thought of as related to a length scale such as a thickness pertaining to the TNTI or/and a turbulence inner length scale such as the Kolmogorov or the Taylor lengths. The question of determining the scalings of local TNTI thicknesses is therefore closely related to the question of determining the scalings of local TNTI propagation velocities. Cafiero and Vassilicos (2020) and Zhou and Vassilicos (2017) have argued, with support from Direct Numerical Simulations (DNS) and laboratory experiments of self-similar turbulent wakes and jets, that the average TNTI propagation velocity scales as the fluid's kinematic viscosity divided by a length which is the Kolmogorov length in the presence of the classical equilibrium turbulence dissipation scaling but is the Taylor length in the presence of the non-equilibrium dissipation scaling (Vassilicos, 2015).

The turbulent wakes and jets considered by Cafiero and Vassilicos (2020) and Zhou and Vassilicos (2017) are spatially developing wakes and jets whereas many DNS studies of turbulent wakes and jets in the literature are concerned with temporally developing wakes and jets (e.g. da Silva and Pereira (2008); Silva et al. (2018); van Reeuwijk and Holzner (2014) and references therein). The presence of non-equilibrium turbulence dissipation scalings

have been established in important regions of significant extent in spatially developing self-similar turbulent axisymmetric wakes (Obligado et al. (2016); Ortiz-Tarin et al. (2021) and references therein) and spatially developing self-similar turbulent planar jets (Cafiero and Vassilicos, 2019). It is in these spatially developing self-similar flow regions that the scaling of the average TNTI propagation velocity as the inverse Taylor length has been argued by theory and supported by laboratory and DNS data of turbulent planar jets and turbulent bluff body wakes (Cafiero and Vassilicos, 2019; Zhou and Vassilicos, 2017). However, Silva et al. (2018) have found that the average thicknesses of the TNTI and of its viscous superlayer both scale with the Kolmogorov rather than the Taylor length in temporally developing self-similar turbulent planar jets. Is it that there is no non-equilibrium turbulent dissipation scaling, i.e. that the turbulence dissipation scaling is classical, in temporally developing self-similar planar jets? Or is it that the average TNTI thickness does not trivially relate to the average TNTI propagation speed even in self-similar turbulent shear flows? Or is it both, or something else?

In spatially developing self-similar turbulent jets and wakes, the turbulence dissipation scaling impacts the TNTI propagation speed via its relation to the jet/wake width growth (Cafiero and Vassilicos, 2020; Zhou and Vassilicos, 2017), and the jet/wake width growth rate is obtained from mass, momentum and turbulent kinetic energy balances (Cafiero and Vassilicos, 2019; Dairay et al., 2015; George, 1989; Townsend, 1976). This approach to the estimation of the jet/wake width does not seem to have ever been applied to temporally developing turbulent flows even though Gauding et al. (2021) did apply to temporally developing turbulent planar jets the self-similar theory of Townsend (1949) (see also Tennekes and Lumley (1972)) which uses only momentum balance (but no mass and turbulent kinetic energy balances) and a hypothesis on the relation between mean flow and Reynolds shear stress profiles which is now known not to be generally true (e.g. Cafiero and Vassilicos (2019); Dairay et al. (2015)). To answer the questions at the end of the previous paragraph we therefore start by applying the mass-momentum-energy approach of Townsend (1976), George (1989), Dairay et al. (2015) and Cafiero and Vassilicos (2019) to temporally developing self-similar turbulent planar jets in section 3.2. This allows us to see how the turbulence dissipation scaling impacts the jet width and the mean flow velocity of temporally evolving self-similar turbulent planar jets. In section 3.3 we derive a formula for the TNTI's mean propagation velocity in terms of the jet width growth rate and the fractal/multiscale nature of the TNTI. The details of our pseudo-spectral DNS with particular attention paid to spatial resolution and control of numerical oscillations were presented in 2.1, and in section 3.4 we use this DNS to critically examine the assumptions and results of our theoretical approach. We report the strengths and failings of our formula for the TNTI's mean propagation velocity

and conclude with a suggestion for how to overcome the failings. We summarise our results in section 3.5.

3.2 Mean flow scalings

The temporally developing planar jet is often favoured in numerical studies because of the advantage that the boundary conditions in the streamwise and spanwise directions can be taken to be periodic. The initial condition of the planar jet is defined in terms of an initial streamwise velocity U_J and an initial jet width H_J and the global Reynolds number is $Re_G = U_J H_J/\nu$ (see section 2.1 for further details on the initial condition and the DNS of the temporally developing planar jet). The transition to the turbulent regime starts with shear layer instabilities present on both sides of the jet. After the jet has become fully turbulent, the turbulent jet volume expands with time into the irrotational surrounding volume.

In this section, the time and Re_G dependencies of the parameters related to the mean flow and turbulence are investigated. The growth of the mean flow profile is of interest because it relates to the outward spread of the TNTI, a point at which is given quantitative expression in the next section. Following Cafiero and Vassilicos (2019); George (1989); Townsend (1976) we start the analysis with the Reynolds averaged continuity and momentum equations, where averaging is over the two homogeneous/periodic spatial directions and/or over realizations:

$$\boldsymbol{\nabla} \cdot \langle \boldsymbol{u} \rangle = 0, \tag{3.1}$$

$$\frac{\partial \langle \boldsymbol{u} \rangle}{\partial t} + \langle \boldsymbol{u} \rangle \cdot \nabla \langle \boldsymbol{u} \rangle = -\frac{1}{\rho} \nabla \langle p \rangle + \nu \nabla^2 \langle \boldsymbol{u} \rangle - \langle \boldsymbol{u'} \cdot \nabla \boldsymbol{u'} \rangle. \tag{3.2}$$

where the vector $\boldsymbol{u}$ is the instantaneous velocity field and the brackets signify averaging.

Homogeneity/periodicity along x (streamwise) and z (spanwise) coordinates implies $\partial \langle .. \rangle / \partial x = \partial \langle .. \rangle / \partial z = 0$. Defining $\langle \boldsymbol{u} \rangle = (U, V, W)$, these being the mean flow components in the streamwise, cross-stream and spanwise directions respectively, the relation $\partial V / \partial y = 0$ is reached from eq. (3.1). Because of reflectional symmetry with respect to $y = 0$, y being the cross-stream coordinate, we are led to $V = 0$. The immediate result $V = 0$ is a very significant difference between temporally and spatially developing turbulent jets as $V \neq 0$ in the spatially developing case.

For high Reynolds number temporally evolving $x-$ and $z-$periodic/homogeneous turbulent jets the momentum equation in the streamwise direction is well approximated by

$$\frac{\partial U}{\partial t} \approx -\frac{\partial \langle u'v' \rangle}{\partial y} \tag{3.3}$$

where u' and v' are the streamwise and cross-stream fluctuating velocities.

Integrating eq. (3.3) within one period along y, the following constraint is obtained;

$$\frac{\partial}{\partial t} \int U dy = 0, \tag{3.4}$$

implying that the volume flux is conserved throughout the time evolution of the jet. The conservation of the volume flux is another important difference between the temporally developing jet and its spatially developing counterpart where it is the momentum flux that is conserved (momentum deficit for the spatially developing wakes) instead of the volume flux throughout the streamwise direction (Tritton, 1988).

At this point, the self-similarity assumption for the mean streamwise velocity U is introduced:

$$U(y,t) = u_0(t) f(y/\delta) \tag{3.5}$$

where $\delta(t)$ is the instantaneous jet half-width, $u_0(t)$ is the centre-line ($y = 0$) mean flow velocity of the jet and both are time-dependent. Plugging eq. (3.5) for the mean streamwise velocity into eq. (3.4) yields the following result;

$$u_0(t)\delta(t) = const \sim U_J H_J. \tag{3.6}$$

A popular way to obtain $\delta(t)$ and $u_0(t)$ for the temporally evolving jet is by dimensional analysis based on volume flux conservation. The volume flux is constant in time and therefore proportional to $U_J H_J$, one is tempted to argue that δ and u_0 are functions of $U_J H_J$ and time t only, in which case dimensional analysis immediately implies $\delta \sim (U_J H_J)^{1/2} t^{1/2}$ and $u_0 \sim (U_J H_J)^{1/2} t^{-1/2}$. However, all power laws $\delta \sim H_J (tU_J/H_J)^a$, $u_0 \sim U_J (tU_J/H_J)^{-a}$ are consistent with the constant volume flux $u_0\delta = const. \sim U_J H_J$ and there is no a priori reason why δ and u_0 should depend on $U_J H_J$ rather than on U_J and H_J separately. In fact, Cafiero and Vassilicos (2019) have shown that different mean flow scalings exist for the spatially developing turbulent planar jet, depending on different turbulent dissipation scaling possibilities. If one were to use dimensional analysis based on the notion that δ and u_0 must depend only on the conserved momentum flux and streamwise distance in the spatially developing jet, then one would only obtain mean flow scalings compatible with one particular

turbulence dissipation scaling (the classical equilibrium dissipation scaling) and no other, in disagreement with experimental results, see Cafiero and Vassilicos (2019). Thus, in order to obtain the most general picture for the temporally developing self-similar planar jet case, which can also potentially allow for effects of non-equilibrium turbulence dissipation, we do not adopt the dimensional analysis we mentioned and continue our analysis by deriving the self-similarity of the Reynolds shear stress and by introducing the equation for the turbulent kinetic energy, a general turbulence dissipation scaling and self-similarity assumptions for the terms in the turbulent kinetic energy equation.

By inserting the self-similarity relation for U, relation 3.5, into eq. 3.3, by integrating over y both sides of eq. 3.3 from 0 to y, and by making use of $\langle u'v' \rangle = 0$ at $y = 0$, we easily show that the Reynolds stress also has a self-similar form which can be written as;

$$\langle u'v' \rangle = R_0(t) g(y/\delta), \tag{3.7}$$

where $R_0(t)$ is given by

$$R_0 \sim \delta \frac{du_0}{dt} \sim u_0 \frac{d\delta}{dt}. \tag{3.8}$$

Note that this is different from $R_0 \sim u_0^2$ which is the assumption made in Townsend (1949), Tennekes and Lumley (1972) and Gauding et al. (2021). We do not use this assumption here (but the results 3.19 and 3.20 of our analysis confirm it in this very particular flow case).

At this point, we have three unknowns, u_0, δ, R_0, and two relations, eq. 3.6 and eq. 3.8. Hence, one more relation is needed. Following Cafiero and Vassilicos (2019); George (1989); Townsend (1976) the equation for the x- and z-average turbulent kinetic energy K is therefore also incorporated into the analysis:

$$\frac{D}{Dt} K = T + P - \varepsilon \tag{3.9}$$

where T, P and ε are the x- and z-averaged turbulence transport, production and dissipation terms respectively. Due to homogeneity/periodicity in x and z and to the fact that the mean velocity component V is 0, the equation reduces to the form

$$\frac{\partial}{\partial t} K = T + P - \varepsilon. \tag{3.10}$$

Making self-similarity assumptions for the turbulent kinetic energy K, dissipation ε and transport and production terms as one entity $T+P$, i.e.

$$K(t,y/\delta) = K_0(t)e(y/\delta), \tag{3.11}$$

$$\varepsilon(t,y/\delta) = \varepsilon_0(t)\theta(y/\delta), \tag{3.12}$$

$$(T+P)(t,y/\delta) = P_0(t)\tau(y/\delta), \tag{3.13}$$

and then plugging these expressions into the eq. 3.10, we obtain

$$\frac{\partial K_0}{\partial t}e - \frac{K_0}{\delta}\frac{d\delta}{dt}e' = P_0\tau - \varepsilon_0\theta, \tag{3.14}$$

where e' is the derivative of e with respect to y/δ. The coefficients which are only functions of t and not of y/δ must be proportional to each other, hence

$$\frac{\partial K_0}{\partial t} \sim K_0\frac{1}{\delta}\frac{\partial \delta}{\partial t} \sim P_0 \sim \varepsilon_0. \tag{3.15}$$

The first of these proportionalities simply shows that the variables K_0 and δ have power-law dependencies on time. The remaining useful proportionality relates the turbulence dissipation to the turbulent kinetic energy and the jet half-width. We isolate it below as it is one of the additional relations that we need:

$$K_0\frac{1}{\delta}\frac{\partial \delta}{\partial t} \sim \varepsilon_0. \tag{3.16}$$

To be useful, this additional relation needs to be complemented by a separate turbulence dissipation scaling for ε_0. There are two options: the classical dissipation scaling

$$\varepsilon_0 \sim \frac{K_0^{3/2}}{\delta}, \tag{3.17}$$

and the non-equilibrium dissipation scaling found in various turbulent flows including spatially developing turbulent jets and wakes, grid-generated turbulence and time-evolving periodic turbulence (both forced and decaying) (Cafiero and Vassilicos, 2019; Dairay et al., 2015; Goto and Vassilicos, 2016; Ortiz-Tarin et al., 2021; Vassilicos, 2015)

$$\varepsilon_0 \sim \left(\frac{Re_G}{Re_0}\right)^m \frac{K_0^{3/2}}{\delta}, \tag{3.18}$$

with $m = 1$ except for slender body wakes (Ortiz-Tarin et al., 2021) where $m = 2$. Unlike Re_G, which is the global Reynolds number (independent of time), Re_0 is the local Reynolds number (time-dependent) defined by $Re_0 = \sqrt{K_0}\delta/\nu$. With eq. 3.18, the dissipation scaling is actually written in a general way which also includes the classical dissipation scaling as a special case for which $m = 0$.

To complete our analysis and obtain $\delta(t)$ and $u_0(t)$, the additional relations that we use are eq. 3.16, eq. 3.18 and Townsend's assumption $K_0 \sim R_0$ (Townsend, 1976) which is only needed, in fact, if $m \neq 1$. Combining with $u_0\delta_0 \sim U_J H_J$ (eq. 3.6) and $R_0 \sim u_0 \frac{d\delta}{dt}$ (eq. 3.8), one obtains the following scalings (where t_0 is a virtual time origin):

$$u_0 \sim (U_J H_J)^{1/2}(t - t_0)^{-1/2}, \tag{3.19}$$

$$\delta \sim (U_J H_J)^{1/2}(t - t_0)^{1/2}, \tag{3.20}$$

irrespective of the value of m. It follows, in particular, that the local Reynolds number Re_0 is constant in time irrespective of m. This Reynolds number constancy is a consequence of our analysis, not its premise. Note also that $d\delta^2/dt$ is a constant proportional to $U_J H_J$. In terms of a dimensional constant coefficient A we write $d\delta^2/dt = AU_J H_J$.

An important observation here is that the mean flow scalings are independent of the turbulent dissipation scaling relation, contrary to the spatially developing turbulent planar jet where different centre-line mean velocity and jet width scalings are present for different turbulent dissipation regimes (Cafiero and Vassilicos, 2019). In other words, for the temporally developing turbulent planar jet, the mean flow scalings are the same for all values of m, which includes the classical dissipation ($m = 0$) and the non-equilibrium dissipation ($m = 1$) cases. It is therefore not possible to distinguish between different dissipation scaling regimes from the time evolution of the temporally developing planar jet flow.

3.3 TNTI propagation velocity

With the time dependencies of the mean flow parameters obtained, a relation for the mean propagation velocity of the TNTI can also be found. Following van Reeuwijk and Holzner (2014) and Zhou and Vassilicos (2017), a relation between the growth rate of the turbulent jet volume in time and the TNTI propagation speed can be written;

$$\frac{dV_J}{dt} = Sv_n \tag{3.21}$$

where V_J stands for the turbulent volume, S stands for the surface area of the TNTI bounding this volume and v_n stands for the mean interface propagation velocity. In this chapter we follow this global/integral approach to our theoretical and computational estimates of the propagation velocity which, as shown by van Reeuwijk and Holzner (2014), is consistent with the local approach which requires highly resolved calculations with low numerical noise of first and second-order derivatives of vorticity, particularly at the outer edge of the TNTI layer (see section 2.1 and section 2.2).

Substituting $V_J = 2a\delta L_x L_z$ where a is a dimensionless constant coefficient and L_x and L_z are the extents of the domain in the streamwise and spanwise directions respectively, the relation can be written as

$$\frac{d\delta(t)}{dt} 2aL_x L_z = Sv_n. \tag{3.22}$$

In various previous studies, the TNTI defined in terms of passive scalar fields are found to have fractal or fractal-like properties, either with a constant fractal dimension over a range of scales (Prasad and Sreenivasan, 1990; Sreenivasan et al., 1989) or with a scale-dependent fractal dimension (Dimotakis and Catrakis, 1999; Miller and Dimotakis, 1991) which may actually also vary with the threshold defining the boundary of the turbulent region (Flohr and Olivari, 1994; Lane-Serff, 1993). By taking into account an assumed fractal or fractal-like nature of the interface, the surface area of the TNTI can be estimated with the following relation;

$$S(r) \sim L_x L_z \left(\frac{r}{\delta(t)} \right)^{2-D_f}, \tag{3.23}$$

where r is the length scale with which the surface area is measured (see Mandelbrot (1982)), the outer length is assumed to be $\delta(t)$ which is of the order of the integral scale, and D_f is the fractal dimension of the interface, with a value in the range $2 \leq D_f < 3$. Considering that the interface cannot have contortions of size smaller than the thickness of the interface, the smallest length scale on the interface can be considered to be the TNTI thickness, η_I. In this section, we neglect the complex inner structure of the TNTI layer and espouse a relation between η_I and the mean propagation velocity of the type

$$\eta_I = \nu / v_n, \tag{3.24}$$

which recognizes the effect of viscous diffusion of enstrophy at the interface (Corrsin and Kistler, 1955) (In subsection 3.4.5 we modify this relation in an attempt to take into account the fact that viscous superlayer is only the outer part of the TNTI layer). We therefore

estimate S by setting r proportional to η_I in eq. 3.23 in a way which models S as

$$S = L_x L_z \left(\frac{\eta_I}{\delta(t)} \right)^{2-D_f}. \tag{3.25}$$

Using this formula eq. 3.25 for S with eqs. 3.22 and 3.24, the following relation is obtained for the TNTI's mean propagation velocity:

$$\frac{v_n}{U_J} = (Aa)^{1/(D_f-1)} \frac{H_J}{\delta} Re_G^{-(D_f-2)/(D_f-1)}, \tag{3.26}$$

where we made use of the dimensionless constant coefficient A in $d\delta^2/dt = AU_J H_J$. It can be seen from eqs. 3.26 and 3.20 that the average propagation velocity of the TNTI scales as the inverse square root of time and that it scales with the global Reynolds number raised to a power depending on the fractal dimension of the interface.

We want to compare eq. 3.26 for v_n to the scalings of the characteristic velocities of the flow, $u_0 \sim (U_J H_J)^{1/2}(t-t_0)^{-1/2}$ and $u_\eta \equiv \nu/\eta$ where η is the Kolmogorov length $\eta \equiv (\nu^3/\varepsilon_0)^{1/4}$ in terms of the centre-line ($y = 0$) turbulence dissipation rate ε_0 (averaged over x and z). Firstly, we find $v_n/u_0 \sim Re_G^{(2-D_f)/(D_f-1)}$ which means that v_n/u_0 is independent of time and depends on the initial volume flux only through Re_G as it depends on Re_G raised to a power equal to $(2-D_f)/(D_f-1)$. From $\eta \equiv (\nu^3/\varepsilon_0)^{1/4}$, eq. 3.18, $K_0 \sim R_0$ and eq. 3.20 follows

$$\eta \sim (U_J H_J)^{1/2} Re_G^{-3/4} (t-t_0)^{1/2} \tag{3.27}$$

and therefore

$$u_\eta \sim (U_J H_J)^{1/2} (t-t_0)^{-1/2} Re_G^{-1/4}. \tag{3.28}$$

Hence $v_n/u_\eta \sim Re_G^{(2-D_f)/(D_f-1)+1/4}$ meaning that v_n and u_η have the same dependence on time, but the same dependence on Re_G only if $D_f = 7/3$. Note that the maximum possible fractal dimension $D_f = 3$ corresponds to $v_n \sim u_\lambda$ where $u_\lambda \equiv \nu/\lambda$, the Taylor length λ being obtained from $\varepsilon_0 \sim \nu K_0/\lambda^2$ and scaling as

$$\lambda \sim (U_J H_J)^{1/2} Re_G^{-1/2} (t-t_0)^{1/2}. \tag{3.29}$$

It follows that u_λ scales as

$$u_\lambda \sim (U_J H_J)^{1/2} (t-t_0)^{-1/2} Re_G^{-1/2}. \tag{3.30}$$

The most important implication of these relations is that the time dependencies of all the velocities v_n, u_η, u_λ and u_0 are the same. Similarly, the turbulent length scales η, λ,

the TNTI thickness η_I and the jet half-width δ have the same time dependencies too. As a result, it is not possible to distinguish whether the average TNTI propagation velocity scales with u_η or u_λ in the temporally developing turbulent jet by just monitoring the evolution in time of these velocities. Other than that, all these three velocities scale with global Reynolds number Re_G raised to different powers except if $D_f = 7/3$ in which case v_n and u_η have the same Re_G dependence, or if $D_f = 3$ in which case v_n has the same Re_G dependence as u_λ.

The validity of the time dependencies and the fractal characteristics of the TNTI are now investigated with data from a DNS of a time-developing turbulent jet. A study of the Re_G dependencies would require many such DNS with a wide enough range of high Re_G values and remains out of our present scope.

3.4 Results

3.4.1 Self-similarity and length-scales

The analysis of the DNS data set of PJx starts with mean profiles in order to determine the self-similar time range where the investigation of the TNTI is to be conducted. In order to determine the time when the jet becomes self-similar, mean profiles of the streamwise velocity, turbulent kinetic energy and the $\langle u'v' \rangle$ component of the Reynolds stress is considered. Self-similarity means that statistics evolve with a time-local amplitude scaling and a time-local length scale, i.e. $\phi_0(t)$ and $\ell(t)$, so that the time-dependent y profile of an $x-z$ averaged quantity ϕ can be written in the form (Townsend, 1976),

$$\phi = \phi_0(t) f(y/\ell(t)). \tag{3.31}$$

For the investigation of the self-similarity of the mean flow profiles, we start by normalizing the profiles by using the jet half-width $\delta(t)$ (defined as the absolute value of y where $U(y)$ is $U(0)/2$) as time-local length-scale, see figure 3.1. In order to distinguish between self-similarity and scaling, the profiles are normalized in figure 3.1 by their maxima (Dairay et al., 2015).

With a similar DNS, da Silva and Pereira (2008) report that the self-similar regime starts at $t/T_{ref} \approx 20$ which is after the transition to turbulence has happened. In another study of the same flow, van Reeuwijk and Holzner (2014) report that the jet becomes fully turbulent at $t/T_{ref} \approx 30$. Looking at figure 3.1, it is observed that the mean flow, Reynolds stress, rms streamwise velocity and turbulent kinetic energy profiles collapse rather well as functions of $y/\delta(t)$ for $t/T_{ref} \geq 30$ in the present simulations: $t/T_{ref} = 30$ marks the beginning of the self-similar regime, and as shown in figure 2.1a, it is also when the Taylor length Reynolds

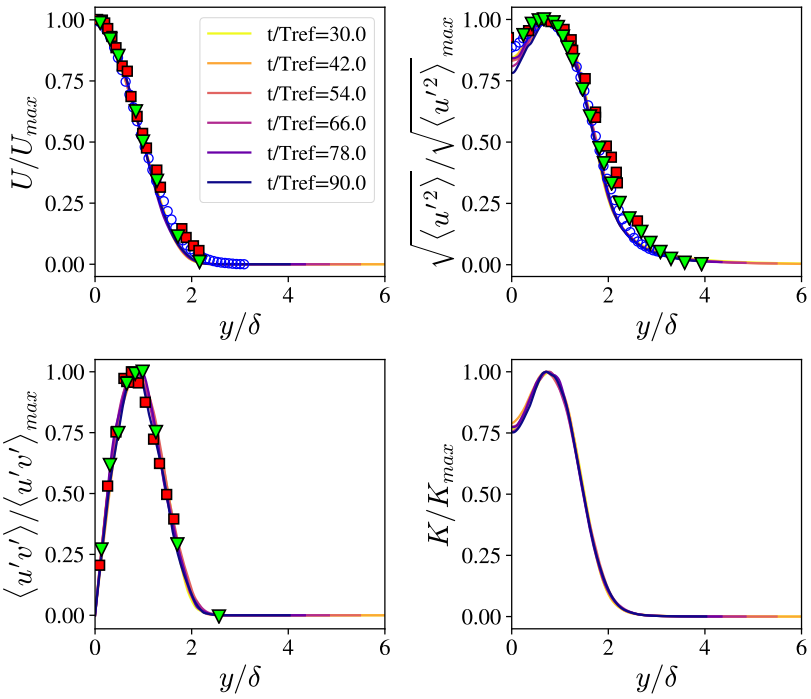

Fig. 3.1 Profiles of mean streamwise velocity U, streamwise velocity rms u_{rms}, Reynolds shear stress $\langle u'v'\rangle$, and turbulent kinetic energy K, normalized by the maximum values of the respective profiles and compared with experimental data from Cafiero and Vassilicos (2019) (○), Ramaprian and Chandrasekhara (1985) (▽) and Gutmark and Wygnanski (1976) (■).

number starts remaining about constant in time. In figure 3.1, the self-similar profiles are also compared with the experimental data of Cafiero and Vassilicos (2019); Gutmark and Wygnanski (1976); Ramaprian and Chandrasekhara (1985), showing good collapse between the present data and the profiles obtained in the experiments.

Figure 3.2a shows the time evolution of the normalized square of the jet half-width, i.e. δ^2/H_J^2.The data plotted in figures 3.1 and 3.2a are ensemble averages over the five simulations (as well as averages over the $x-z$ plane in every simulation, of course). A linear fit to the data for $t/T_{ref} \geq 30$ shows that δ^2 grows linearly with time, in agreement with the prediction in section 3.2. Figure 3.2b shows ratios of length scales, namely $\eta(t)/\lambda(t)$ and $\delta(t)/\lambda(t)$ where λ and η are calculated in terms of turbulent kinetic energy and dissipation rate at the centre-plane $y = 0$. It is observed that the turbulence length scales λ and η evolve similarly in time. In addition, the mean flow length scale $\delta(t)$ also evolves in the same way, leading to the confirmation of the conclusion in section 3.2 that all length scales grow identically with time.

To extract from the DNS data the scaling quantity R_0 of section 3.2, we identify it with $\langle u'v'\rangle_{max}$, the maximum value of the Reynolds shear stress profile in figure 3.1.

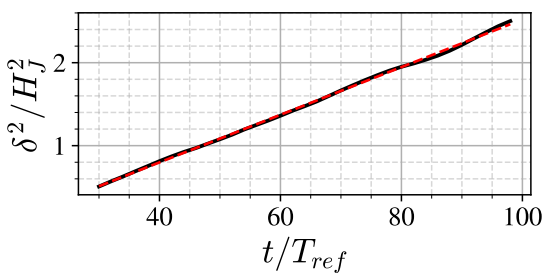

(a) δ^2. The Red dashed line is the linear fit to the data for times when the jet is fully turbulent and mean profiles are self-similar.

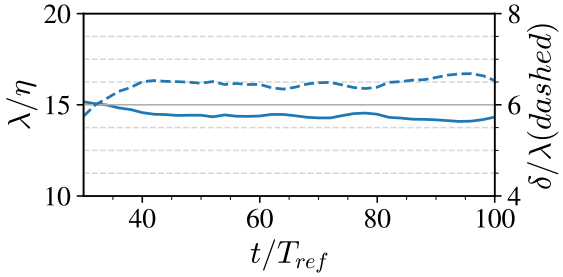

(b) Ratios λ/η (solid line) and δ/λ (dashed line).

Fig. 3.2 Time variation of the square of the jet half-width and the ratio of the length scales δ, λ and η, demonstrating the similar time evolution of all length scales of the flow between $t/T_{ref} = 30$ and $t/T_{ref} = 98$.

We find that the Townsend assumption $K_0 \sim R_0$ holds for times $t/T_{ref} = 30$ to $t/T_{ref} = 80$ (figure 3.3a). According to the scalings derived in section 3.2, K_0 should vary in time like u_0^2, where $u_0(t) \equiv U(y = 0, t)$, and this is confirmed by our DNS data as figure 3.3a makes clear over an even greater range of times than $K_0 \sim R_0$ (up to $t/T_{ref} = 100$). This range of times is greater because the effects of the boundary conditions on the time-developing jet appear to be felt first by the Reynolds shear stress and later by other quantities such as K_0 and u_0. We chose to process our data from $t/T_{ref} = 30$ to $t/T_{ref} = 100$ where self-similarity holds and where the constancy of $u_0\delta$, related to the volume flux, (eq. 3.6) is definitely respected in our DNS (figure 3.3b). With the exception of fig 3.3a where K_0/R_0 start deviating from its constancy in time after $t/T_{ref} = 80$, all the figures where we plot quantities versus time do not show a drastic change after $t/T_{ref} = 80$, which is why we chose to process our data till $t/T_{ref} = 100$ rather than $t/T_{ref} = 80$. There is no effect on our paper's conclusions.

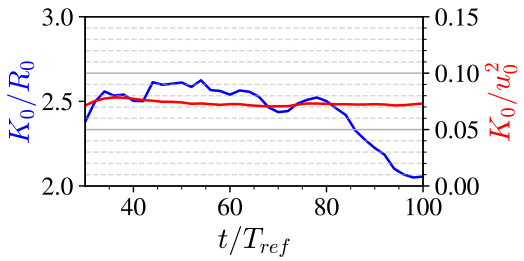

(a) Ratios K_0/R_0 and K_0/u_0^2.

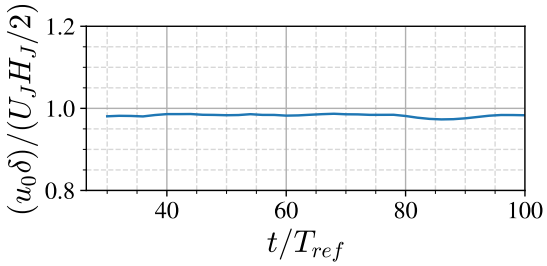

(b) Normalised volume flux.

Fig. 3.3 The ratios K_0/R_0, K_0/u_0^2 and the constancy of the normalised volume flux between $t/T_{ref} = 26$ to $t/T_{ref} = 98$.

3.4.2 Time dependence of scaling parameters and virtual origin

The time dependencies of the centreline streamwise velocity scale $u_0(t)$ and of the jet half-width $\delta(t)$, eqs. 3.19 and 3.20, are found to be power laws

$$\phi(t) = A(t - t_0)^b \tag{3.32}$$

in the theoretical analysis of section 3.2. It is important to note that these two power laws must properly combine to satisfy the governing equations and that this can only happen if the virtual origin t_0 is the exact same one in eqs. 3.19 and 3.20 (Cafiero and Vassilicos, 2019; Dairay et al., 2015; Nedić, 2013; Nedić et al., 2013).

There exist various methods for the determination of the exponent b while taking proper account of the virtual origin t_0 (Cafiero and Vassilicos, 2019; Dairay et al., 2015; Nedić et al., 2013). In the present study, the method used in Cafiero and Vassilicos (2019) is implemented on $u_0(t) \sim (t - t_0)^b$ and $\delta(t) \sim (t - t_0)^{-b}$.

The procedure starts with initial fits to the u_0 data in the form $u_0 \sim t^b$ and to the δ data in form $\delta \sim t^{-b}$ in agreement with volume flux conservation, eq. 3.6. By this step, two approximate values for the exponent b are obtained as initial guesses. Then the value of the exponent is varied in a certain range around the initial guess in order to find the corresponding t_0 values for every value of b. This procedure is carried out for both u_0 and δ separately. Plotting the resulting (b, t_0) pairs yields the plot in figure 3.4, where red and blue colours differentiate the values obtained from the u_0 and the δ data. At the point where these two lines intersect, the best fit values (b, t_0) are the ones which take into account that the virtual origin must be identical for both u_0 and δ. These values are $b = -0.51$ and $t_0 = 11.7$. The time evolutions of u_0 and δ in the time range $t/T_{ref} = 30$ to $/T_{ref} = 100$ and their power law fits with the pair ($b = -0.51$, $t_0 = 11.7$) are shown in figure 3.5.

At this point we recall our result of section 3.2 that, unlike spatially developing turbulent jets (Cafiero and Vassilicos, 2019), the evolutions (in time) of u_0 and δ_0 in temporally developing turbulent jets are independent of the exponent m in the turbulence dissipation law 3.18. The values found for b and t_0 from the DNS data are compatible with the theoretical value $b = -0.5$ obtained in section 3.2 for any exponent m.

3.4.3 Fractal dimensions of the TNTI

The theoretical analysis in section 3.2 relates the fractal dimension of the TNTI to the global Reynolds number scaling of the TNTI propagation velocity, see eq. 3.26. It is therefore important to investigate the fractal/fractal-like properties of the TNTI.

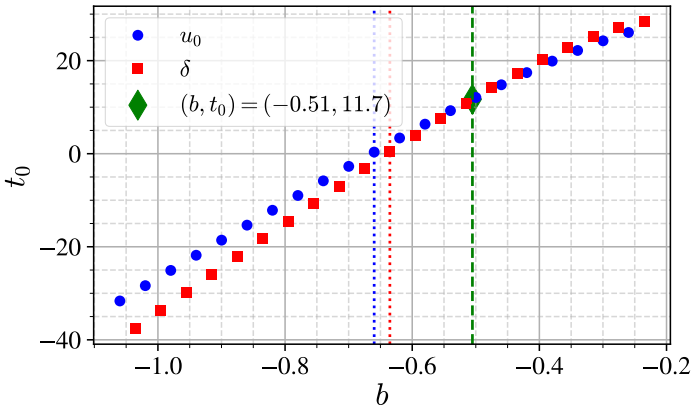

Fig. 3.4 The optimal virtual origin t_0 as a function of exponent b for the time evolutions of u_0 (blue disks) and δ (red squares). The dashed vertical lines show the best fit exponent b for $t_0 = 0$ (blue for u_0, red for δ) and the green diamond marks the one value of b for which t_0 is the same for both equations 3.19 and 3.20.

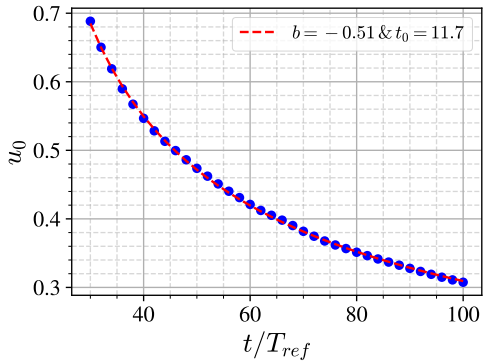

(a) Time variation of u_0.

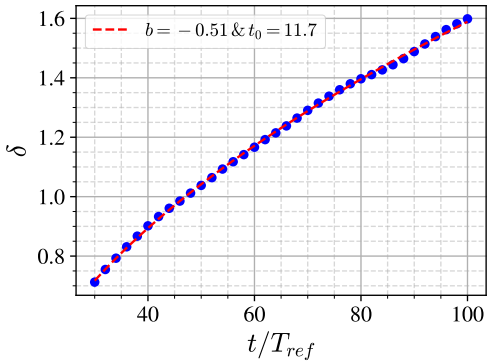

(b) Time variation of δ.

Fig. 3.5 Time variation of u_0 and δ with the best power law fits obtained by the procedure based on figure 3.4.

The fractal/fractal-like nature of scalar iso-surfaces relating to the TNTI has been reported in various studies (Dimotakis and Catrakis, 1999; Lane-Serff, 1993; Miller and Dimotakis, 1991; Mistry et al., 2018, 2016; Sreenivasan, 1991; Sreenivasan et al., 1989). However, these fractal/fractal-like characteristics are described somewhat differently in different studies. In some studies, a well-defined power-law for the scale dependence of the surface area (thus constant fractal dimension) has been reported (Mistry et al., 2018, 2016; Sreenivasan, 1991; Sreenivasan et al., 1989). This is the case where, when one covers the surface with boxes of the size of r, the number N of boxes needed to fully cover the surface scales as $N(r) \sim r^{-D_f}$ (Mandelbrot, 1982) and the fractal dimension D_f of the surface is independent of r over a significant range of scales r. In other studies of iso-surfaces, in flows such as turbulent

jets and mixing layers, a scale-dependent fractal dimension is reported, i.e. $D_f = D_f(r)$, which means that there is no constant value for the fractal dimension D_f but that the fractal dimension varies with box size r (Catrakis and Dimotakis, 1999; Dimotakis and Catrakis, 1999; Miller and Dimotakis, 1991).

There is also the question of the enstrophy threshold used to define the TNTI because a strong threshold dependence of the fractal dimension of scalar iso-surfaces has been reported in some studies (Flohr and Olivari, 1994; Lane-Serff, 1993; Miller and Dimotakis, 1991). Varying the threshold within the range of thresholds where V_J remains about constant is akin to sampling different inner iso-enstrophy surfaces within the TNTI layers inner structure (van Reeuwijk and Holzner, 2014). There may not be one single fractal dimension for the TNTI, but different fractal dimensions for different inner iso-surfaces of enstrophy within the TNTI layer, an aspect of the problem which needs to be investigated.

We apply the box-counting procedure to obtain fractal dimensions of iso-enstrophy surfaces within the TNTI. Figure 3.6 shows typical ensemble averaged box-counting results, these particular ones being for the iso-surface $\omega_{th}^2/\omega_{ref}^2 = 10^{-3}$ at time $t/T_{ref} = 50$. The plot on the left is a log-log plot of the number N of boxes needed to cover the iso-enstrophy surface versus the inverse box size $1/r$. The linear fit in orange is obtained by using all the points on the plot, and the slope of this fit is found to be $D_{f1} = 2.161$ for this particular case. On the other hand, local slopes are also calculated by fits over 9 consecutive data points on this plot. It is observed (see example in figure 3.6 (right)) that the local slope does not remain constant throughout all scales r. An approximately constant fractal dimension, seen as a plateau-like region on the right plot of Figure 3.6, appears to exist between $r = \delta$ and $r = \lambda$ for the entire range of iso-surfaces of various enstrophy threshold values within the TNTI ($\omega_{th}^2/\omega_{ref}^2$ between 10^{-6} and 10^{-3}) and for all times where the jet is fully turbulent (local slope values marked by red square markers). Note that the constancy of this local fractal dimension is affected by the fact that it is calculated by using 9 points around the value of r where the local dimension is evaluated. This means that the highly non-constant values of the fractal dimension at scales r larger than δ are responsible for deviations from constancy at scales close to but below δ; and that the progressive decrease of the local slope towards $D_f = 2$ as r decreases at scales r below λ is responsible for the systematic deviation from constancy at scales close to yet larger than λ.

Throughout this study, the fractal dimension is calculated as the average value of the local slopes between box sizes $r = \delta$ and $r = \lambda$, and this fractal dimension is denoted D_{f2}. The first point with r smaller than or equal to δ (i.e. the largest value of r in the range $\lambda \leq r \leq \delta$) is excluded from this average so as to reduce the oscillation caused by less converged values of N at larger box sizes.

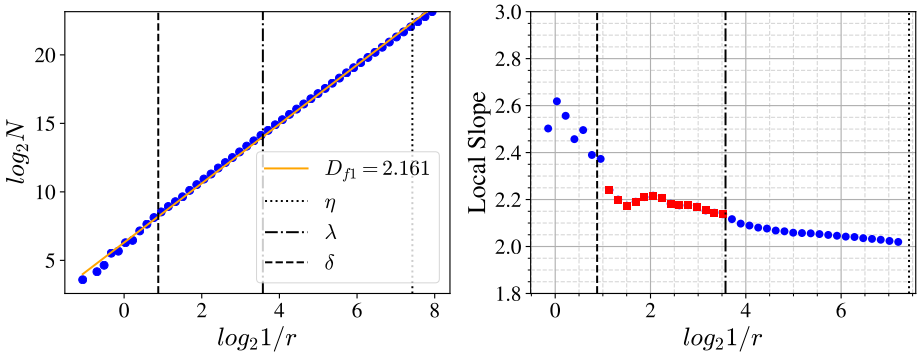

Fig. 3.6 Ensemble-averaged results of the box-counting method applied to iso-surface $\omega^2_{th}/\omega^2_{ref} = 10^{-3}$ at time $t/T_{ref} = 50$. On the left, a plot of the number of boxes N of size r versus $1/r$ is shown in log-log scale, the orange line is the linear best fit for all data points on this plot. The plot on the right shows the local slope calculated by the fits using 9 consecutive data points, the value of the local slope being attributed to the centre point. The local slopes marked as red squares (as opposed to blue disks) are the points used to calculate D_{f2}. The dashed, dot-dashed and dotted vertical lines located on the horizontal axis the length scales δ, λ and η respectively. (λ and η are calculated on the centre-plane.)

The fractal dimension D_{f2} for different enstrophy threshold values in the TNTI range $\omega^2_{th}/\omega^2_{ref} = \left[10^{-6}, 10^{-3}\right]$ is shown in figure 3.7 as a function of time. The fractal dimensions D_{f2} of the TNTI may be considered to remain approximately constant in time for all these enstrophy thresholds and the mean value around which D_{f2} appears to fluctuate is shown by the dashed lines in the figure. For the threshold values $\omega^2_{th}/\omega^2_{ref} = \left[10^{-6}, 10^{-3}\right]$, this fractal dimension value varies from $D_{f2} = 2.09$ to $D_{f2} = 2.18$. It can be observed that the values of D_{f2} for different $\omega^2_{th}/\omega^2_{ref}$ get closer to each other towards the lower values of $\omega^2_{th}/\omega^2_{ref}$. It can also be argued that an objective definition of the viscous superlayer must include within the superlayer, enstrophy iso-values for which the fractal dimension can be detected with a value larger than 2.

A significantly higher value, $D_{f2} = 2.36$, has been observed for the iso-enstrophy surface defined by the threshold $\omega^2_{th}/\omega^2_{ref} = 10^{-2}$. This value is close to the fractal dimension $7/3 \approx 2.33$ reported in various studies (Mistry et al., 2018, 2016; Sreenivasan, 1991; Sreenivasan et al., 1989). It must be noted that the enstrophy threshold $\omega^2_{th}/\omega^2_{ref} = 10^{-2}$ rests on the turbulent side of the TNTI judging from the enstrophy range of the plateau showed in figure 2.7. However, it is also observed that the $log_2 N - log_2(1/r)$ plot obtained from the box-counting algorithm for this enstrophy threshold shows no evidence of a fractal dimension that is independent of r, i.e. there is no significant plateau region in the right plot of figure 3.8 and the local slope varies significantly with r. The value $D_{f2} = 2.36$ is obtained by averaging

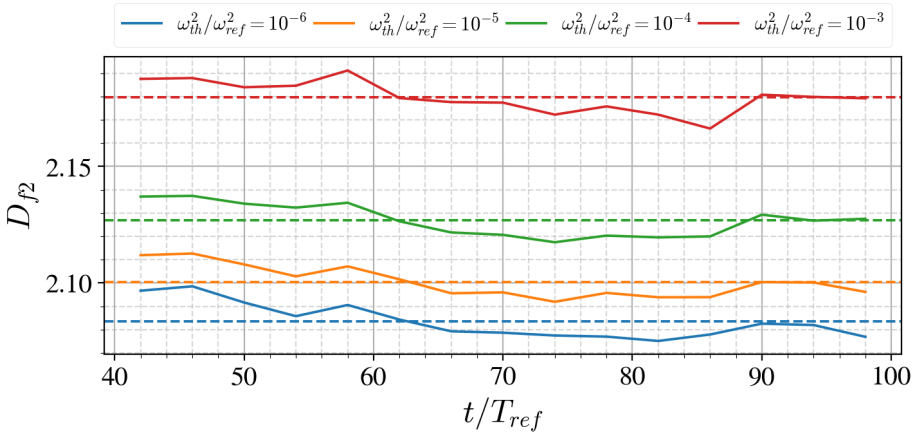

Fig. 3.7 TNTI fractal dimensions D_{f2} versus time t/T_{ref} for different normalised enstrophy thresholds within the TNTI.

over the local fractal dimensions (local slopes in the right plot of figure 3.8) from $r = \lambda$ to $r = \delta$, but these local fractal dimensions vary continuously with r from 2.2 to over 2.45.

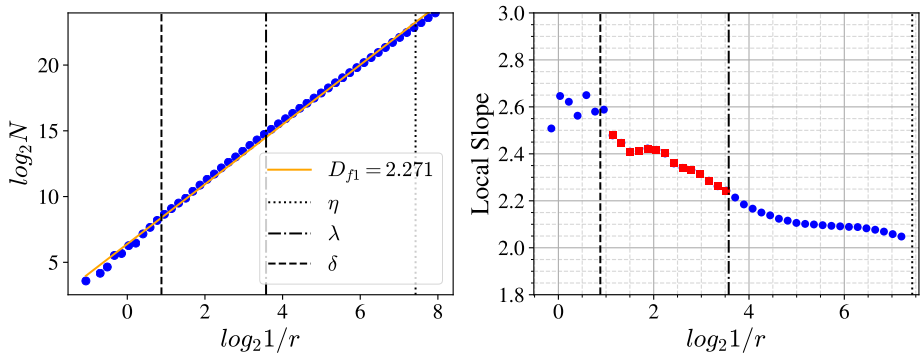

Fig. 3.8 Same as figure 3.6 but for iso-enstrophy surface $\omega^2_{th}/\omega^2_{ref} = 10^{-2}$ at same time $t/T_{ref} = 50$.

3.4.4 Propagation velocity of the interface

In section 3.2 we obtained formula 3.26 for the TNTI's mean propagation velocity on the basis of the fractal/fractal-like character of the TNTI. We now know, following the previous subsection, that the TNTI of our time-developing turbulent jet has a range of fractal dimensions D_{f2} depending on the normalised enstrophy threshold $\omega^2_{th}/\omega^2_{ref}$, and that D_{f2} is a fairly well-defined single number independent of box size r in the range $\lambda \leq r \leq \delta$ if $\omega^2_{th}/\omega^2_{ref}$ is in the range $\left[10^{-6}, 10^{-3}\right]$. The question which naturally arises now is: does formula 3.26 capture the time and enstrophy-threshold dependencies of the mean propagation velocity

v_n? More specifically, can we use $D_{f2} = D_{f2}(\omega_{th}^2/\omega_{ref}^2)$ defined in the range $\lambda \leq r \leq \delta$ as the fractal dimension in formula 3.26 to accurately capture the time and enstrophy threshold dependencies of v_n? We stress that in this formula, v_n depends on the enstrophy threshold only through D_{f2} given that A is defined in terms of quantities which are independent of enstrophy threshold and a in $V_J = 2a\delta L_x L_z$ can be expected to have a negligibly weak dependence on enstrophy threshold.

To estimate v_n independently from our formula 3.26 we use equation eq. 3.22, having first checked the validity of $\frac{d}{dt}V_J = 2aL_xL_z\frac{d}{dt}\delta$ (see figure 3.9) which is needed to go from eq. 3.21 to eq. 3.22. Figure 3.9 confirms that the dimensionless coefficient a is approximately independent of time as it oscillates around the constant value $a = 1.66$ and that it is also very weakly dependent on enstrophy threshold over at least four decades.

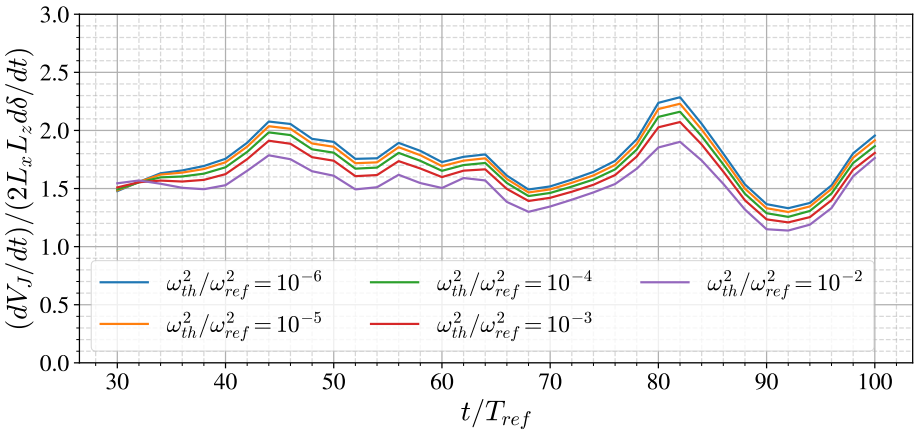

Fig. 3.9 Validity of $\frac{d}{dt}V_J \sim 2L_xL_z\frac{d}{dt}\delta$ over the time evolution of the fully turbulent jet.

To use eq. 3.22 we need a reliable estimate of the TNTI surface area S that is different from the fractal estimate 3.23. To obtain such an estimate of S we plot $r^2N(r)$: as the box-counting algorithm's box size r decreases and becomes small enough to resolve all the contortions of the iso-enstrophy surface, $r^2N(r)$ reaches a maximum and does not grow further with further decreasing r. We take this maximum as our estimate of S, i.e. $S = S_R \equiv max_r[r^2N(r)]$. Of course, S depends on the enstrophy threshold defining the chosen iso-surface within the TNTI and figure 3.10a shows an example of a $r^2N(r)$ versus $1/r$ log-log plot for $\omega_{th}^2/\omega_{ref}^2 = 10^{-3}$ at $t/T_{ref} = 50$ where the maximum $r^2N(r)$ is reached at r close to η. In fact, figure 3.10a is quite typical of normalised enstrophy thresholds in the range $\left[10^{-6}, 10^{-3}\right]$ and times t/T_{ref} in the range $[30, 100]$.

In figure 3.10b we plot $S_R \equiv max_r[r^2N(r)]$ as a function of t/T_{ref} for various normalised enstrophy thresholds. Interestingly, the TNTI surface areas S_R remain approximately constant in time for all thresholds $\omega_{th}^2/\omega_{ref}^2 = 10^{-6}$ to 10^{-4} from $t/T_{ref} = 40$ to 100 and for threshold

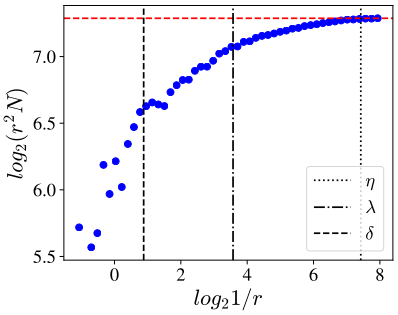

(a) log_2-log_2 plot of $r^2N(r)$ versus $1/r$, at time $t/T_{ref} = 50$, for the threshold value $\omega^2_{th}/\omega^2_{ref} = 10^{-3}$. The horizontal dotted line indicates the maximum value of $r^2N(r)$.

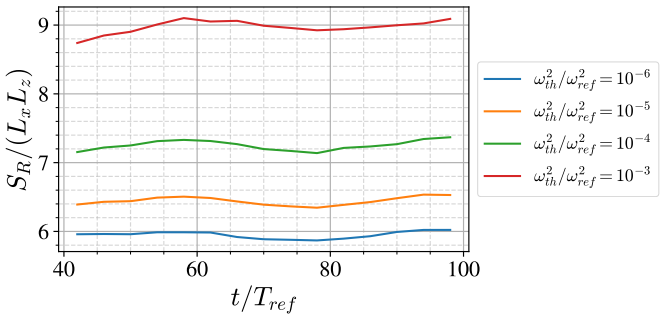

(b) S_R normalized by (L_xL_z) over time for iso-enstrophy surfaces detected by various ω^2_{th} values.

Fig. 3.10 Plot of $r^2N(r)$ versus $1/r$, at time $t/T_{ref} = 50$, for the threshold value $\omega^2_{th}/\omega^2_{ref} = 10^{-3}$ and $S_R/(L_xL_z) \equiv max_r[r^2N(r)]/(L_xL_z)$ versus time t/T_{ref} with different ω^2 thresholds.

$\omega^2_{th}/\omega^2_{ref} = 10^{-3}$ from $t/T_{ref} = 50$ to 100. This is compatible with the fact that all length scales, large and small, grow together in this flow.

We now calculate the average TNTI propagation velocity v_n by using eq. 3.22 with S obtained from $S_R \equiv max_r[r^2N(r)]$ and we compare it with formula 3.26. Firstly, in figure 3.11 we check the time-dependence of v_n which, according to formula 3.26 and $\delta \sim \sqrt{U_J H_J (t-t_0)}$, is the same as the time dependence of u_η and of u_λ. In support of this prediction, figure 3.11 shows that v_n/u_η and v_n/u_λ oscillate around a constant as time proceeds for all $\omega^2_{th}/\omega^2_{ref}$ in the range $\left[10^{-6}, 10^{-3}\right]$.

Secondly, we check the enstrophy threshold dependence of v_n which, according to formula 3.26, should be $v_n/u_\eta \sim (Aa)^{1/(D_f(\omega^2_{th}/\omega^2_{ref})-1)} Re_G^{[2-D_f(\omega^2_{th}/\omega^2_{ref})]/[D_f(\omega^2_{th}/\omega^2_{ref})-1]+1/4}$ and equivalently $v_n/u_\lambda \sim (Aa)^{1/(D_f(\omega^2_{th}/\omega^2_{ref})-1)} Re_G^{[2-D_f(\omega^2_{th}/\omega^2_{ref})]/[D_f(\omega^2_{th}/\omega^2_{ref})-1]+1/2}$. We plot v_n/u_η versus $\omega^2_{th}/\omega^2_{ref}$ for various time instants t/T_{ref} in figure 3.12a; and we take our measured $D_{f2}(\omega^2_{th}/\omega^2_{ref})$ (averaged over time for simplicity, this average being denoted $\overline{D_{f2}}$) to represent the fractal dimension D_f and plot $(v_n/u_\eta)(Aa)^{-1/(\overline{D_{f2}}-1)} Re_G^{-(2-\overline{D_{f2}})/(\overline{D_{f2}}-1)}$ versus $\omega^2_{th}/\omega^2_{ref}$ for various time instants t/T_{ref} in figure 3.12b. If our formula 3.26 is able to capture the enstrophy threshold dependence of v_n, then $(v_n/u_\eta)(Aa)^{-1/(\overline{D_{f2}}-1)} Re_G^{-(2-D_{f2})/(D_{f2}-1)}$ should be constant with varying $\omega^2_{th}/\omega^2_{ref}$ for all times t/T_{ref} between 30 and 100 with $a \approx 1.66$ (as already found from figure 3.9) and $A \approx 0.058$ from figure 3.2a.

We can clearly see in figure 3.12a that, irrespective of time, v_n decreases with increasing $\omega^2_{th}/\omega^2_{ref}$ in the TNTI normalised enstrophy range $\left[10^{-6}, 10^{-3}\right]$ which makes sense because S increases with increasing $\omega^2_{th}/\omega^2_{ref}$. Indeed, we expect Sv_n to be approximately independent

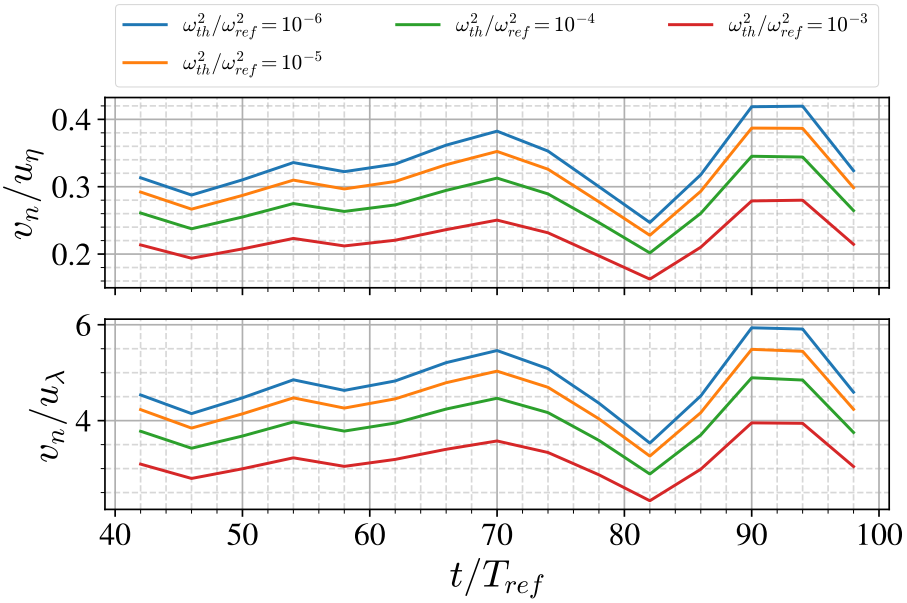

Fig. 3.11 Time dependence of v_n/u_η and v_n/u_λ.

of $\omega_{th}^2/\omega_{ref}^2$ in the TNTI range of enstrophy thresholds, judging from eq. 3.21 and the approximate constancy of V_J in that range (shown in figure 2.7).

Figure 3.12b shows that our formula 3.26 for the TNTI's mean propagation velocity v_n with D_f given by $\overline{D_{f2}}(\omega_{th}^2/\omega_{ref}^2)$, the time-averaged (from $t/T_{ref} = 30$ to 98) value of $D_{f2}(\omega_{th}^2/\omega_{ref}^2)$, captures the enstrophy threshold dependence of v_n very well over the wide range of thresholds $10^{-6} \leq \omega_{th}^2/\omega_{ref}^2 \leq 10^{-3}$ which is within the TNTI throughout the time range considered.

In the following section, we explore the inconsistencies of the simple fractal model for v_n presented in section 3.2 and investigate how they might be overcome.

3.4.5 A generalised Corrsin length for the TNTI

Our simple fractal model's formula 3.26 predicts both the time dependence of the TNTI's mean propagation velocity v_n and its enstrophy threshold dependence quite well. However, our fractal model did not foresee the complex inner structure of the TNTI where different iso-enstrophy surfaces within the TNTI have different fractal dimensions.

Our model is based on (i) $\frac{d}{dt}V_J = 2aL_xL_z\frac{d}{dt}\delta$ (needed to go from eq. 3.21 to eq. 3.22) which our simulations rather support (see figure 3.9); (ii) $S = L_xL_z(\eta_I/\delta)^{2-D_f}$ where $\eta_I = \nu/v_n$ is the Corrsin length-scale for the viscous superlayer's thickness; and (iii) a well-defined fractal dimension D_f independent of r over a significant range of r values bounded from

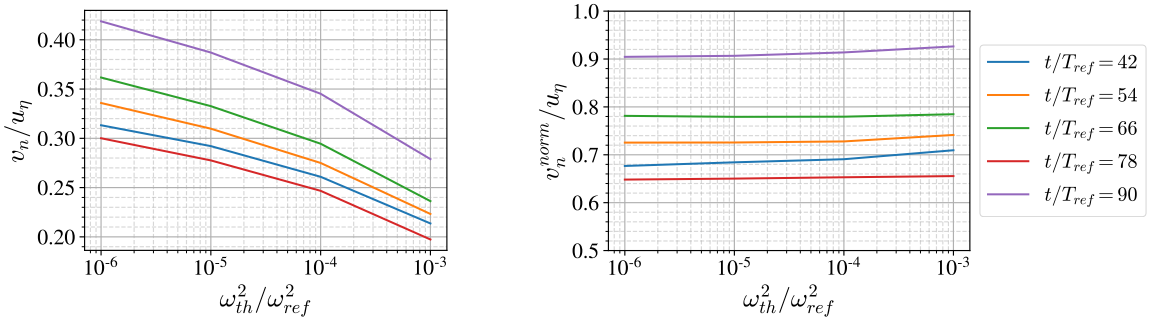

(a) Average interface propagation velocity v_n normalised by u_η versus $\omega_{th}^2/\omega_{ref}^2$ at different times t/T_{ref}.

(b) v_n divided by $(Aa)^{1/(\overline{D_{f2}}-1)} Re_G^{(2-\overline{D_{f2}})/(\overline{D_{f2}}-1)}$ according to formula 3.26 (with $A = 0.05777$ and $a = 1.6574$) normalized by u_η versus $\omega_{th}^2/\omega_{ref}^2$ at different times t/T_{ref}.

Fig. 3.12 Average TNTI propagation velocity v_n over enstrophy threshold values $\omega_{th}^2/\omega_{ref}^2$.

below by the smallest length scale on the TNTI. In the event, our DNS data have returned well-defined fractal dimensions D_{f2} independent of r in a range bounded from below by λ but not by the smallest length-scale on the TNTI, which appears to be η as the maximum of $r^2 N(r)$ is typically reached at r close to η. The number N of boxes needed to cover iso-enstrophy surfaces continues to increase faster than r^{-2} as r decreases from λ to η, implying that these scales between λ and η contribute to the surface area, but not with a well-defined r-independent fractal dimension. Furthermore, in the range where a r-independent fractal dimension may be claimed, i.e. $\lambda \leq r \leq \delta$, this fractal dimension D_{f2} is a decreasing function of enstrophy threshold $\omega_{th}^2/\omega_{ref}^2$ appearing to tend towards close to 2 as $\omega_{th}^2/\omega_{ref}^2$ tends to 0.

In figure 3.13 we plot $S(\eta) = L_x L_z (\eta/\delta)^{2-D_{f2}}$, $S(\lambda) = L_x L_z (\lambda/\delta)^{2-D_{f2}}$ and $S(\eta_I) = L_x L_z (\eta_I/\delta)^{2-D_{f2}}$, all normalised by $S_R \equiv max_r[r^2 N(r)]$. These three quantities are plotted versus time for different enstrophy thresholds within the TNTI range of thresholds, i.e. $\omega_{th}^2/\omega_{ref}^2$ within $\left[10^{-6}, 10^{-3}\right]$. The fractal dimension D_{f2} is our only possible choice of fractal dimension for the calculations of $S(\eta)$, $S(\lambda)$ and $S(\eta_I)$ if we want to be consistent with our model's requirement that the fractal dimension should be well-defined, i.e. r-independent over a significant r-range.

Firstly, figure 3.13 shows that $S(\eta)/S_R$, $S(\lambda)/S_R$ and $S(\eta_I)/S_R$ are about constant in time for all TNTI enstrophy thresholds, which is not surprising given the approximate time constancies of D_{f2} and of S_R and given that η, λ and η_I have the all same time-dependence as δ. Secondly, figure 3.13 shows that only $S(\eta)/S_R$ collapses for all enstrophy thresholds. This is not a trivial result because $S(\eta)$ is calculated in terms of a fractal dimension D_{f2} which is not well-defined at scale η. The worse collapse is returned by $S(\lambda)/S_R$; and $S(\eta_I)/S_R$ tends towards $S(\eta)/S_R$ with decreasing $\omega_{th}^2/\omega_{ref}^2$ which makes some sense because, in this limit,

D_{f2} decreases towards values close to 2 and η_I/η therefore approaches a value of order 1 extremely weakly dependent on $\omega_{th}^2/\omega_{ref}^2$ (see section 3.2). However, $S(\eta_I)/S_R$ takes values between $1/5$ and $1/4$ which is different from 1 and therefore contradicts eq. 3.25 which is a premise of our model. In fact, there is a dimensionless coefficient b in eq. 3.23, i.e. $S(r) = bL_xL_z(r/\delta)^{2-D_f}$. This coefficient b is independent of enstrophy threshold because it is set by $S(r=\delta) = bL_xL_z$. The only way to retrieve 3.25 is by writing $S = bL_xL_z(c\eta_I/\delta)^{2-D_f}$ with $bc^{2-D_f} = 1$ which requires that the dimensionless coefficient c is a function of $\omega_{th}^2/\omega_{ref}^2$. Without the arbitrary condition $bc^{2-D_f} = 1$, the formula 3.26 predicted by our simple fractal model should be replaced by

$$\frac{v_n}{U_J} = \left(\frac{c^{D_f-2}}{b}\right)^{1/(D_f-1)} (Aa)^{1/(D_f-1)} \frac{H_J}{\delta} Re_G^{-(D_f-2)/(D_f-1)}. \tag{3.33}$$

The quantity $\frac{c^{D_f-2}}{b}$ is in fact the ratio $S(\eta_I)/S_R$ (with $S(\eta_I)$ given by $L_xL_z(\eta_I/\delta)^{2-D_{f2}}$) that we plot in figure 3.13 and from our data it transpires that $(S(\eta_I)/S_R)^{1/(\overline{D_{f2}}-1)}$ is a significantly decreasing function of $\omega_{th}^2/\omega_{ref}^2$ (see figure 3.14). Without setting $\frac{c^{D_f-2}}{b} = 1$ our model does not return the right enstrophy threshold dependence of v_n, and $\frac{c^{D_f-2}}{b} = 1$ does not agree with our DNS data which show that $S(\eta_I)/S_R$ (with $S(\eta_I)$ given by $L_xL_z(\eta_I/\delta)^{2-D_{f2}}$) takes values between $1/5$ and $1/4$. We therefore need to explore how our model could be modified to be more realistic, and we do this by generalising the Corrsin length.

The Corrsin length may be considered appropriate only for the viscous superlayer at the very lowest enstrophy thresholds where the generation of vorticity is viscosity-dominated and, consistently, $S(\eta_I)/S_R$ and $S(\eta)/S_R$ appear to take similar values. To generalise this property to higher enstrophy thresholds, we introduce a generalised Corrsin length

$$\eta_T = \nu_T/v_n \tag{3.34}$$

in terms of a local turbulent viscosity ν_T (local to every iso-enstrophy surface within the TNTI) such that

$$S = bL_xL_z(c\,\eta_T/\delta)^{2-D_{f2}} \tag{3.35}$$

where b and $c = c(Re_G, \omega_{th}^2/\omega_{ref}^2)$ are dimensionless coefficients independent of time.

The simple physical idea behind eq. 3.34 is that the process of enstrophy production is increasingly dominated by vortex stretching rather than viscosity as the enstrophy threshold increases from the outer, viscous superlayer, side of the TNTI to its inner, turbulent, side. Studies over the past two decades have indeed shown that the TNTI has an inner structure which includes a viscous superlayer and a sort of buffer layer or turbulent sublayer where

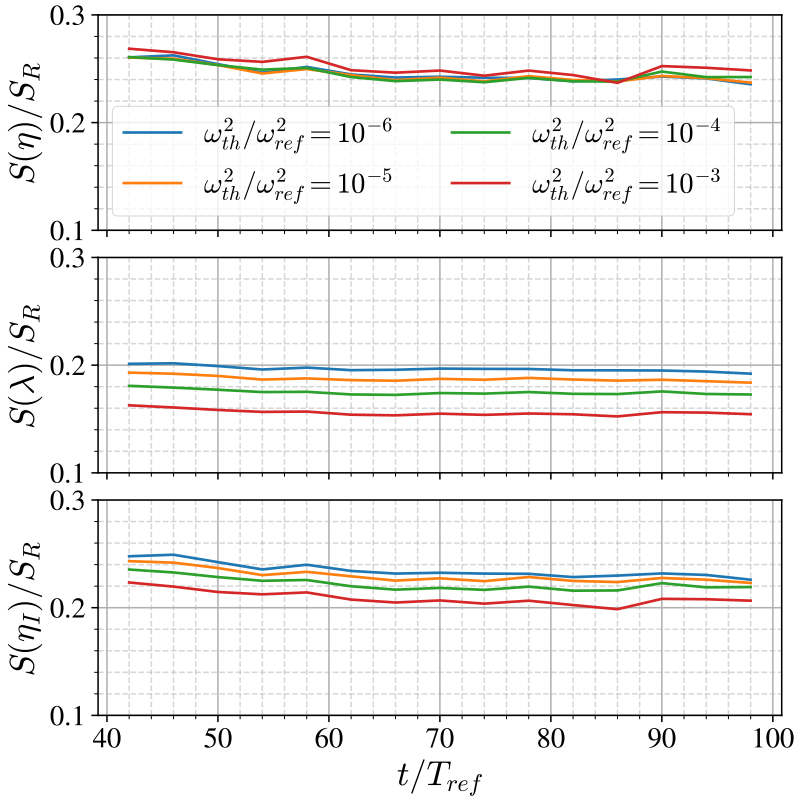

Fig. 3.13 Plots of $S(\eta) = L_x L_z(\eta/\delta)^{2-D_{f2}}$, $S(\lambda) = L_x L_z(\lambda/\delta)^{2-D_{f2}}$ and $S(\eta_I) = L_x L_z(\eta_I/\delta)^{2-D_{f2}}$ (where $\eta_I = \nu/\nu_n$ with ν_n values calculated in the previous section), all normalised by $S_R \equiv max_r[r^2 N(r)]$, versus time t/T_{ref} for various enstrophy thresholds within the TNTI.

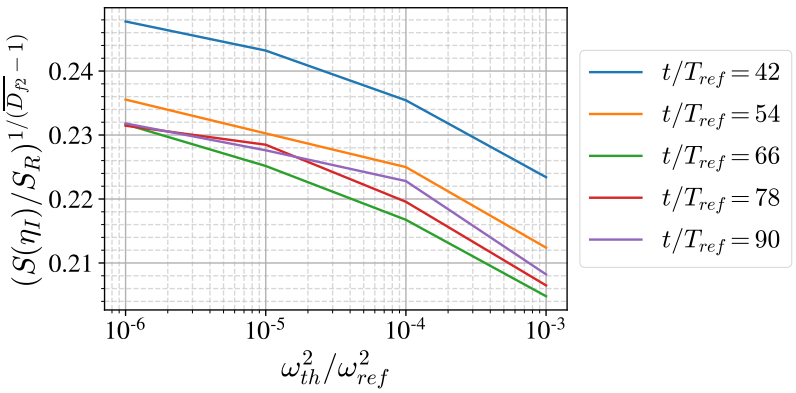

Fig. 3.14 $(S(\eta_I)/S_R)^{1/(\overline{D_{f2}}-1)}$ as a function of $\omega^2_{th}/\omega^2_{ref}$ at different times t/T_{ref}.

vorticity production dominates (da Silva et al., 2014; Nagata et al., 2018; Taveira and da Silva, 2014a). Hence, the turbulence viscosity $\nu_T = \nu_T(\omega^2_{th}/\omega^2_{ref})$ is expected to increase

and become independent of the fluid's kinematic viscosity ν with increasing $\omega_{th}^2/\omega_{ref}^2$ within the TNTI.

We now ask whether equations 3.34, 3.35 and 3.22, which represent an attempt to improve the model for v_n in section 3.2, are consistent with the requirement that ν_T must increase with $\omega_{th}^2/\omega_{ref}^2$. The three equations just mentioned imply

$$\nu_T = \frac{2a\delta}{c}\frac{d\delta}{dt}\left(\frac{S}{bL_xL_z}\right)^{-(D_{f2}-1)/(D_{f2}-2)} \tag{3.36}$$

where the dimensionless constant a is the one in $Sv_n = 2aL_xL_zd\delta/dt$. It can be seen that ν_T depends on $\omega_{th}^2/\omega_{ref}^2$ through S and D_{f2} (and also c) but does not depend on time in agreement with our observations in figures 3.2a, 3.10b and 3.7. As S/L_xL_z increases whereas $(D_{f2}-1)/(D_{f2}-2)$ decreases with increasing $\omega_{th}^2/\omega_{ref}^2$, it is not trivial to predict how $\left(\frac{S}{L_xL_z}\right)^{-(D_{f2}-1)/(D_{f2}-2)}$ behaves with varying $\omega_{th}^2/\omega_{ref}^2$. We therefore use time-averaged values of S and D_{f2} obtained in the previous section for different enstrophy thresholds and plot in figure 3.15 the turbulent viscosity ν_T given by eq. 3.36 with c set to a constant independent of $\omega_{th}^2/\omega_{ref}^2$ and $\delta\frac{d\delta}{dt} = \frac{1}{2}\frac{d\delta^2}{dt}$ given by the DNS. The result shows that ν_T with $c = Const$ is a monotonically increasing function of $\omega_{th}^2/\omega_{ref}^2$ as required for our improved model to be physically viable. This means that $\eta_T = \nu_T/v_n$ is also a monotonically increasing function of $\omega_{th}^2/\omega_{ref}^2$ because eq 3.22 implies that v_n is a decreasing function of $\omega_{th}^2/\omega_{ref}^2$. However, the result in figure 3.15 also suggests that ν_T and η_T tend to 0 as $\omega_{th}^2/\omega_{ref}^2$ decreases towards 0 whereas ν_T should be tending towards the kinematic viscosity ν in that limit. In the following paragraph, we demonstrate how the model's dimensionless coefficient $c(Re_G, \omega_{th}^2/\omega_{ref}^2)$ can ensure that ν_T tends to ν as $\omega_{th}^2/\omega_{ref}^2 \to 0$, i.e. as we move towards the outer edge of the TNTI.

We model c as being a constant independent of both Re_G and $\omega_{th}^2/\omega_{ref}^2$ for most enstrophy thresholds within the TNTI except the smallest ones where we approximate it as $c(Re_G, \omega_{th}^2/\omega_{ref}^2) \approx Re_G\tilde{c}(\omega_{th}^2/\omega_{ref}^2)$ with $\tilde{c}$ being a function of $\omega_{th}^2/\omega_{ref}^2$ but not of Re_G. Given that $\delta\frac{d\delta}{dt} = \frac{A}{2}U_JH_J$ (from eq. 3.20), we can write $2a\frac{\delta}{c}\frac{d\delta}{dt} \approx Aa\frac{\nu}{\tilde{c}}$ as $\omega_{th}^2/\omega_{ref}^2 \to 0$, i.e.

$$\nu_T \sim Aa\frac{\nu}{\tilde{c}}\left(\frac{S}{bL_xL_z}\right)^{-(D_{f2}-1)/(D_{f2}-2)}. \tag{3.37}$$

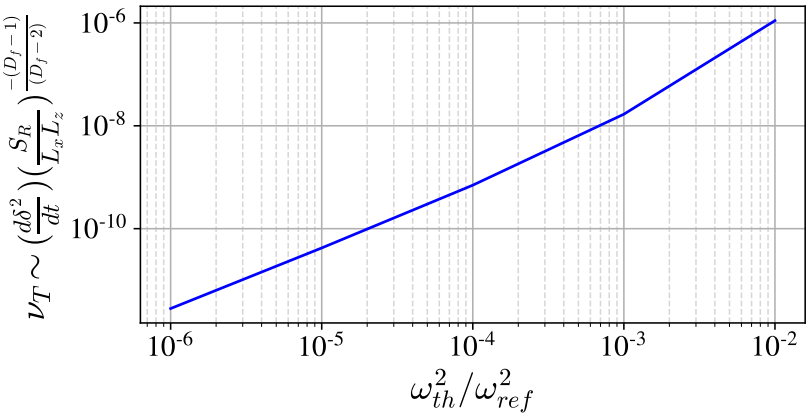

Fig. 3.15 The turbulent viscosity ν_T given by eq. 3.36 with $a/c = 1$ and $b = 1$ as a function of normalised enstrophy threshold.

in that limit. For ν_T to tend to ν as $\omega_{th}^2/\omega_{ref}^2 \to 0$, $\tilde{c}$ must tend to 0 at the same rate as $\left(\frac{S}{bL_xL_z}\right)^{-(D_{f2}-1)/(D_{f2}-2)}$, i.e.

$$\ln \tilde{c} \approx -\frac{D_{f2}-1}{D_{f2}-2} \ln\left(\frac{S}{bL_xL_z}\right) + const \tag{3.38}$$

as $\omega_{th}^2/\omega_{ref}^2 \to 0$. It is not the goal of this paper's final part to determine the functions $\nu_T(Re_G, \omega_{th}^2/\omega_{ref}^2)$ and $c(Re_G, \omega_{th}^2/\omega_{ref}^2)$ in the improved model for v_n based on eqs. 3.34, 3.35 and 3.22; the goal here is simply to demonstrate on the basis of our DNS and simple asymptotic arguments that such a model can be physically viable. The example of a choice of $c(Re_G, \omega_{th}^2/\omega_{ref}^2)$ that we made at the start of this paragraph ensures that ν_T remains a monotonically increasing function of $\omega_{th}^2/\omega_{ref}^2$ while at the same time tending to ν as $\omega_{th}^2/\omega_{ref}^2$ tends to 0. We now work out the consequences of this choice for η_T and v_n.

The formulae for v_n and η_T which can be readily derived from our improved model are

$$v_n/u_\eta \sim \left(\frac{c^{(D_{f2}-2)}}{b}\right)^{\frac{1}{D_{f2}-1}} (Aa)^{\frac{1}{D_{f2}-1}} Re_G^{-\frac{D_{f2}-2}{D_{f2}-1}+\frac{1}{4}} (\nu_T/\nu)^{\frac{D_{f2}-2}{D_{f2}-1}} \tag{3.39}$$

and

$$\eta_T/\eta \sim \left(\frac{c^{(D_{f2}-2)}}{b}\right)^{\frac{-1}{D_{f2}-1}} (Aa)^{-\frac{1}{D_{f2}-1}} Re_G^{\frac{D_{f2}-2}{D_{f2}-1}-\frac{1}{4}} (\nu_T/\nu)^{-\frac{D_{f2}-2}{D_{f2}-1}} (\nu_T/\nu) \tag{3.40}$$

Note that the original model of section 3.2 leads to $v_n/u_\eta \sim (Aa)^{\frac{1}{D_{f2}-1}} Re_G^{-\frac{D_f-2}{D_f-1}+\frac{1}{4}}$ and $\eta_I/\eta \sim (Aa)^{-\frac{1}{D_{f2}-1}} Re_G^{\frac{D_f-2}{D_f-1}-\frac{1}{4}}$ without the extra powers of $c^{D_{f2}-2}/b$ and ν_T/ν in eqs. 3.39 and 3.40.

Without these extra powers, the original model predicts the dependence of v_n on $\omega_{th}^2/\omega_{ref}^2$ very well. In our improved model, $(\nu_T/\nu)^{\frac{D_{f2}-2}{D_{f2}-1}}$ is an increasing function of enstrophy threshold because ν_T/ν is increasing and because the exponent $\frac{D_{f2}-2}{D_{f2}-1}$ is also increasing given that D_{f2} is an increasing function of $\omega_{th}^2/\omega_{ref}^2$ as observed in our DNS. Our improved model is therefore capable of maintaining the original model's good prediction for v_n if the increasing dependence of $(\nu_T/\nu)^{\frac{D_{f2}-2}{D_{f2}-1}}$ on $\omega_{th}^2/\omega_{ref}^2$ compensates the decreasing dependence of $(c^{D_{f2}-2}/b)^{1/(D_{f2}-1)}$ on $\omega_{th}^2/\omega_{ref}^2$. Indeed, $c^{D_{f2}-2}/b$ is not equal to 1 and $(c^{D_{f2}-2}/b)^{1/(D_{f2}-1)}$ is a decreasing function of enstrophy threshold, in agreement with our DNS observation in the bottom plot of figure 3.13. The entire point of our improved model has been to show that by introducing the generalised Corrsin length and the turbulent viscosity ν_T it is possible to correct our original model's wrong assumption $c^{D_{f2}-2}/b = 1$ without compromising its correct predictions.

We now show that the choice of c that we made for ν_T to tend to ν as $\omega_{th}^2/\omega_{ref}^2 \to 0$ also ensures that the generalised Corrsin length η_T tends to a finite value in that limit. As we move within the TNTI from high to low iso-enstrophy levels, i.e. as we take the limit of $\omega_{th}^2/\omega_{ref}^2$ decreasing towards very small values close to 0 and we approach the outer edge of the viscous superlayer, D_{f2} tends towards values close to 2 and ν_T tends to ν assuming $c(Re_G, \omega_{th}^2/\omega_{ref}^2) \approx Re_G \tilde{c}(\omega_{th}^2/\omega_{ref}^2)$ in that limit. We are therefore left with

$$v_n/u_\eta \sim \tilde{c}^{\frac{D_{f2}-2}{D_{f2}-1}} Re_G^{\frac{1}{4}} \tag{3.41}$$

and

$$\eta_T/\eta \sim \tilde{c}^{-\frac{D_{f2}-2}{D_{f2}-1}} Re_G^{-\frac{1}{4}} \tag{3.42}$$

as we approach the outer edge of the viscous superlayer (we have omitted the unimportant factor Aa/b). Finally, eq. 3.38 implies $\tilde{c}^{\frac{D_{f2}-2}{D_{f2}-1}} \sim L_x L_y/S$, and therefore our generalised model's predictions for the viscous superlayer where D_{f2} is very close to 2 and $\omega_{th}^2/\omega_{ref}^2$ is extremely small are

$$v_n/u_\eta \sim \frac{L_x L_z}{S_\nu} Re_G^{\frac{1}{4}} \tag{3.43}$$

and

$$\eta_T/\eta \sim \frac{S_\nu}{L_x L_z} Re_G^{-\frac{1}{4}} \tag{3.44}$$

where S_ν is the finite surface area of the effectively smooth viscous superlayer of the TNTI. Our generalised model with $c(Re_G, \omega_{th}^2/\omega_{ref}^2) \approx Re_G \tilde{c}(\omega_{th}^2/\omega_{ref}^2)$ and eq. 3.38 at the very smallest enstrophy levels and $c = 1$ above those enstrophy levels implies that η_T is a monotonically increasing function of $\omega_{th}^2/\omega_{ref}^2$ with a finite value different from η by a factor $Re_G^{-1/4}$ at the very smallest enstrophy thresholds. The exponent $1/4$ being small, this prediction is not easy to check as it requires numerical oscillation-free calculations at low enstrophy thresholds for many highly resolved DNS of temporally developing turbulent jets over a wide range of Reynolds numbers Re_G (see section 2.3 for some details about higher Reynolds number simulations and the importance of spatial resolution). This is at, and perhaps even beyond, the very limit of the most powerful current computational capabilities and therefore beyond the present paper's scope. Such a computational check would also require a computable definition or surrogate for η_T which we make a first attempt to give in the following couple of paragraphs. Before doing so, however, we point out that Silva et al. (2018) argued that the viscous superlayer thickness scales with the Kolmogorov length if Re_λ is larger than about 200 and that the TNTI layer's characteristic sizes may have different scalings at smaller values of Re_λ depending on presence or absence of mean shear (see (da Silva and Taveira, 2010) and references therein). It must be stressed that the definition of the viscous superlayer used by Silva et al. (2018) does not necessarily include some low iso-enstrophy surfaces with fractal dimensions clearly larger than 2 (see discussion around figure 3.7 in subsection 3.4.3) and, more importantly, is not local in enstrophy threshold (i.e. it does not depend on the local position within the TNTI) and is therefore different from η_T which is local in enstrophy threshold. The scaling 3.44 does not necessarily contradict the scalings in Silva et al. (2018) as they concern different quantities.

We close this section with an interpretation of the generalised Corrsin length η_T. As η_T is local in terms of iso-enstrophy levels within the TNTI and as it expresses some kind of thickness of iso-enstrophy surfaces, it appears natural to compare it with some average enstrophy length scale on the TNTI. To this end, we use enstrophy profiles conditioned on the interface location similar to Bisset et al. (2002). We define a local coordinate system with local coordinate y_I chosen along the local normal unit $\mathbf{n} = -\frac{\nabla\omega^2}{|\nabla\omega^2|}$ which is pointing towards the non-turbulent region. The origin $y_I = 0$ of this local coordinate system is placed at a given location within the TNTI, for example on the iso-surface defined by $\omega_{th}^2/\omega_{ref}^2 = 10^{-6}$, located at the very edge of the TNTI neighbouring the non-turbulent region. This way, positive values of y_I correspond to the very edge of the viscous superlayer and the non-turbulent region whereas negative values of y_I are within the TNTI and the turbulent region. Given

such local coordinate systems on the TNTI, we calculate averages of any quantity ϕ at a given y_I over all locations on the TNTI where the local y_I axis does not cross the TNTI more than once in the range $y_I = [-27\eta, +27\eta]$. We use the notation ϕ_I to denote these average quantities, averaged conditionally on the specified iso-surface location.

Figure 3.16 shows the vorticity magnitude and the enstrophy profile, averaged conditionally on the distance from the enstrophy iso-surface $\omega_{th}^2/\omega_{ref}^2 = 10^{-6}$: the profiles are normalized by the average values of the respective quantities at the centre-plane. The drastic change of both vorticity and enstrophy values in a very short distance is visible as shown previously in studies using similar methods e.g. Nagata et al. (2018); Silva et al. (2018); Watanabe et al. (2019).

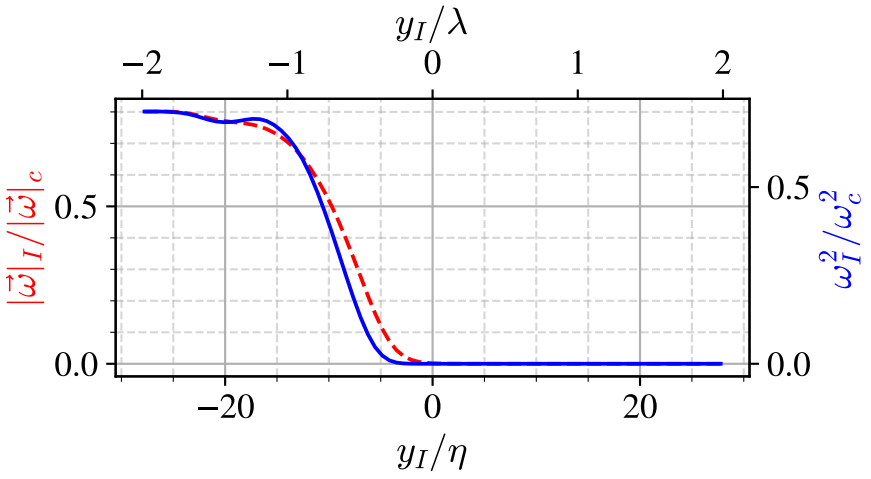

Fig. 3.16 Vorticity magnitude and enstrophy values averaged conditionally on the distance from the iso-enstrophy surface defined by $\omega_{th}^2/\omega_{ref}^2 = 10^{-6}$ for the simulation PJ1.

We define the local length $\eta_\omega \equiv \left(\frac{d\omega_I^2}{dy_I}\frac{1}{\omega_I^2}\right)^{-1}$. In figure 3.17a we plot η_ω/η versus $\omega_I^2/\omega_{ref}^2$. In agreement with η_T, η_ω is an increasing function of enstrophy, $\omega_I^2/\omega_{ref}^2$ in this case: iso-enstrophy surfaces get further away from each other on average as $\omega_I^2/\omega_{ref}^2$ increases within the TNTI. At the very smallest enstrophy thresholds, η_ω appears to tend to a finite value that is significantly smaller than η, which is also in agreement with η_T at high enough Re_G (see eq. 3.44)

We also plot η_ω/η versus y_I/η in figure 3.17b. In this figure $y_I = 0$ corresponds to the iso-enstrophy surface $\omega_{th}^2/\omega_{ref}^2 = 10^{-6}$. We see that the profile of η_ω along y_I is exponentially decreasing with increasing y_I. The linear region ends near $y_I/\eta \approx -2.5$. This is due to some points where the normal enstrophy profiles do not decrease monotonically to zero when going towards the non-turbulent region, even though the local enstrophy values always remain lower than the threshold value.

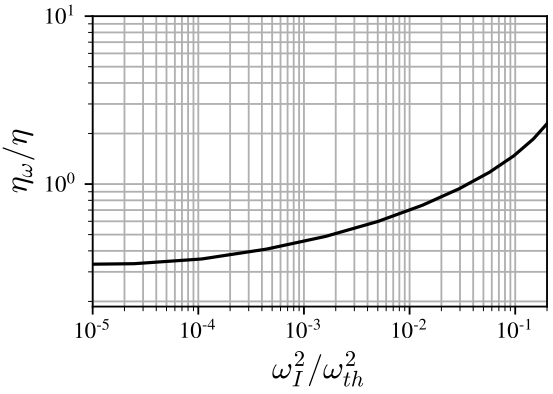

(a) Plot of η_ω/η versus $\omega_I^2/\omega_{ref}^2$ for $t/T_{ref} = 50$, PJ1 simulation. This plot is typical for all times t/T_{ref} between 30 and 100.

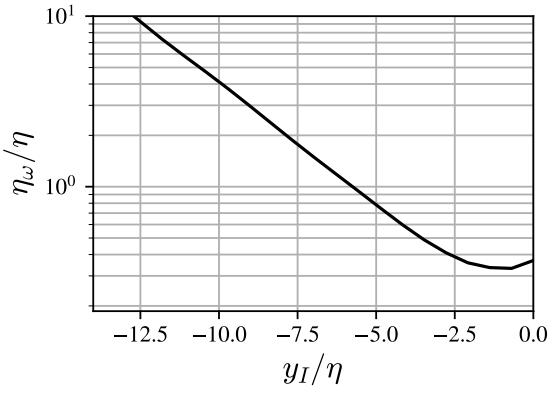

(b) Profile of η_ω along y_I/η, for the isoenstrophy surface detected by $\omega_{th}^2/\omega_{ref}^2 = 10^{-6}$.

Fig. 3.17 Variation of η_ω/η with $\omega_I^2/\omega_{ref}^2$ and y_I/η at $t/T_{ref} = 50$, in PJ1 simulation.

3.5 Conclusion

To determine the mean flow profile evolution, we have applied to the temporally developing turbulent planar jet the approach typically applied to spatially developing free turbulent shear flows. This approach is based on self-similarity and on mass, momentum and turbulent kinetic energy balance equations (Cafiero and Vassilicos, 2019; George, 1989; Townsend, 1976). The turbulent kinetic energy equation involves the turbulence dissipation rate and one needs to specify the turbulence dissipation rate's scalings in order to close the problem. While dissipation of the turbulent kinetic energy takes place exclusively at the smallest scales in the flow, there are different ways through which the energy may be transferred to those scales, that is, different types of turbulence cascades (e.g. equilibrium, non-equilibrium, balanced non-equilibrium, see Cafiero and Vassilicos (2019); Dairay et al. (2015); Goto and Vassilicos (2016); Vassilicos (2015)). The presence of different types of large-scale coherent structures can lead to different turbulence dissipation scalings due to different turbulent cascade properties (Goto and Vassilicos, 2016; Ortiz-Tarin et al., 2021). In turn, different dissipation scalings lead to different self-similar mean flow profile evolutions as already found in various spatially developing turbulent flows (e.g. Cafiero and Vassilicos (2019); Dairay et al. (2015); Ortiz-Tarin et al. (2021); Vassilicos (2015)) and to different TNTI mean propagation speeds as demonstrated by Cafiero and Vassilicos (2020) for the spatially developing turbulent planar jet.

The temporally developing self-similar turbulent planar jet is exceptional because the scalings of its mean flow profile evolution do not depend on the scalings of the turbulence dissipation rate. Whatever the exponent m in eq. 3.18, the scalings of the centreline mean

flow velocity u_0 and jet width δ are given by eqs. 3.19 and 3.20. The reason why the temporally developing self-similar jet is fundamentally different from its spatially developing counterpart is that it conserves volume flux and has identically zero cross-stream mean flow velocity, whereas spatially developing turbulent planar jets do not conserve volume flux and have non-zero cross-stream mean flow velocity. As a result, in the case of the temporally developing self-similar turbulent planar jet, the δ, η and λ, all grow as the square root of time, and u_0, u_η and v_n all decay as the inverse square root of time irrespective of turbulence dissipation scaling. The Reynolds number based on λ remains constant in time. All these theoretical predictions and the assumptions that they are based on have been verified by our DNS of a temporally evolving turbulent planar jet. Note that the volume flux which is conserved in our flow is not conserved in many other flows with a TNTI besides spatially-developing jets such as wakes (e.g. Watanabe et al. (2016b)), boundary layers (e.g. Borrell and Jimenez (2016)) and mixing layers (e.g. Attili et al. (2014) and Balamurugan et al. (2020)). One should therefore be very careful if attempting to extend the applicability of the present results to other turbulent flows with a TNTI.

The prediction for the TNTI mean propagation speed has been made on the basis of (i) a proportionality between the turbulent jet volume and the jet width growth rates which have been verified by our DNS; (ii) an assumption that the TNTI is fractal with a well-defined fractal dimension; (iii) an assumption that the smallest geometrical scale on the TNTI scales with the Corrsin length which characterises generation of vorticity by viscous diffusion; and (iv) a particular way to blend assumptions (ii) and (iii) together, eq. 3.25. The geometrical picture of the TNTI returned by our DNS has turned out to be more involved than assumptions (ii), (iii) and (iv) which make no reference to the TNTI's inner structure. Even so, the prediction that the TNTI mean propagation speed evolves as the inverse square root of time has been validated by our DNS.

The TNTI has an inner structure over a wide range of closely spatially packed iso-enstrophy surfaces and it turns out that different iso-enstrophy surfaces have different fractal dimensions. These fractal dimensions vary from about $7/3$ at the innermost iso-enstrophy surface on the fully turbulent side of the TNTI to close to 2 at the outermost iso-enstrophy surface on the non-turbulent flow side of the TNTI. However, the $7/3$ value, which according to the theory based on assumptions (i), (ii) and (iii), corresponds to a TNTI mean propagation speed that scales with the Kolmogorov velocity u_η, is not well-defined in the sense that it is a fit through a range of scales where the fractal dimension is not scale-independent as it should be. Lower fractal dimension values between about 2.2 and under 2.1 are found for iso-enstrophy surfaces with lower enstrophy values, i.e. towards the TNTI's outer side. These lower fractal dimensions are well-defined in a range of scales bounded by λ from below and

δ from above. However, the smallest geometrical scales on these iso-enstrophy surfaces are close to η and the scales between λ and η contribute significantly to the surface areas of the iso-enstrophy surfaces even though these scales are not characterised by a well-defined fractal dimension. The formula for the TNTI mean propagation speed v_n obtained from assumptions (i), (ii) and (iii) captures its time dependence because the time dependence is the same for all iso-enstrophy surfaces. Perhaps remarkably, it also captures the iso-enstrophy dependence of v_n via the iso-enstrophy dependence of the fractal dimension. However, the DNS invalidates eq. 3.25 on which the formula for v_n is partly based and supports a form such as eq. 3.35 instead.

Having found that different iso-enstrophy surfaces within the TNTI have different sufficiently well-defined fractal dimensions over a range of scales bounded from below by λ and that length scales below λ on these surfaces also contribute significantly to their surface area, it is not possible to sweepingly argue that the Corrsin length η_I is the smallest length-scale on the fractal/fractal-like/multiscale TNTI. Aiming to keep the model's correct predictions while at the same time abandoning the wrong premise (iv), we nevertheless keep the main structure of our model by keeping assumptions (i) and (ii) and modifying (iii) and (iv).

For this, we introduce a generalised Corrsin length defined on the basis of an iso-enstrophy surface-dependent turbulent viscosity ν_T which tends to the fluid's kinematic viscosity ν as the iso-enstrophy level tends to near-vanishing values at the viscous superlayer but is independent of ν at higher iso-enstrophy levels. We demonstrate the physical viability of such a model but leave for future investigation the detailed relation between ν_T and the enstrophy production processes which vary from being viscosity dominated at the outer edge of the TNTI (viscous superlayer) to being controlled by vortex stretching further in the turbulent region. We do, however, show with our DNS that the generalised Corrsin length η_T depends on iso-enstrophy levels similarly to the length-scale η_ω defined by the local enstrophy gradients within the TNTI: in particular, η_ω is smaller than η at the outer edge of the TNTI, larger than η at the inner edge of the TNTI, and monotonically increasing in between. Even if incomplete at this stage, our revised model predicts that the mean propagation speed at the outer edge of the viscous superlayer is proportional to the Kolmogorov velocity multiplied by the $1/4$th power of the global Reynolds number. We stress that this prediction is specific to temporally developing self-similar turbulent planar jets which are very idiosyncratic flows and that it should not necessarily be extended to spatially developing free turbulent shear flows. Current computational capabilities at our disposal are insufficient for the wide range of global Reynolds numbers required to verify this prediction.

Chapter 4

Local Analysis of the TNTI

4.1 Introduction

The TNTI is characterized by sharp gradients of vorticity and enstrophy in the interface normal direction. This implies that the transition from the non-turbulent region to the turbulent region occurs over a very short distance, typically of the order of $10-15\eta$ as documented in the literature (Silva et al., 2018). Furthermore, the local position and orientation of the TNTI are highly irregular and vary significantly. Detecting, computing, or measuring the gradients associated with the TNTI is particularly challenging due to these traits of the interface.

Despite the gradients being sharp locally at the TNTI location, they quickly get smeared out when the statistics are obtained by the application of an averaging operation, without taking into account the orientation and the position of the interface. To overcome this issue, an averaging technique was introduced by Bisset et al. (2002) where they obtained statistics of flow field variables conditionally on the interface location and, up to some extent, to its local orientation. They have chosen to interpolate the local flow field variables on local 1D grids aligned with the cross-stream direction (*y-axis*), stream-wise direction (*x-axis*), or span-wise direction (*z-axis*). The grid's origin is set at the points on the interface which is identified by a certain vorticity magnitude threshold. In their study, they decided not to directly utilize the local surface normal vector for the alignment of the local 1D grid. Instead, they divided the TNTI regions into distinct groups, such as those facing downstream, upstream, spanwise, and vertical (cross-stream) directions (Bisset et al., 2002). For each facing direction, a local 1D grid was aligned according to the specific condition. For instance, in regions facing in the streamwise direction, they used a local 1D grid aligned with the global *x-axis*.

With this methodology, they are able to analyze the properties of the TNTI surfaces facing in various directions, effectively capturing the sharp gradients of flow variables associated

with the interface. This method has proven to be valuable for investigating the irregular TNTI layer and has been employed in numerous subsequent studies, including those by da Silva and Pereira (2008); Silva et al. (2018); Watanabe et al. (2015); Zhou and Vassilicos (2020). In these later studies, the local 1D grid is directly aligned with the direction of the local surface normal vector. The direct use of the surface normal vector for the alignment of the local 1D grid allows for the investigation of TNTI without any constraints on the orientation of the interface as opposed to the approach used by Bisset et al. (2002).

In chapter 3, we introduced a global approach to calculate the average propagation velocity of the interface, as shown in equation 3.33. However, starting from this chapter, we shift our focus towards examining the local characteristics of the flow field near the TNTI. In chapters 4 and 5 of this study, we employ a methodology based on the conditional averaging technique introduced by Bisset et al. (2002) to analyze the local fields in the vicinity of the TNTI. We will refer to this averaging process as TNTI-averaging in the text, as it involves the averaging of the profiles and the local fields over the detected iso-enstrophy surface (IES) while taking into account the location and local orientation of the TNTI.

There are two primary distinctions between the methodology employed in the current study and that in the previous studies in the literature (da Silva and Pereira, 2008; Silva et al., 2018; Watanabe et al., 2015; Zhou and Vassilicos, 2020). Firstly, for each local point considered on the TNTI, the velocity field $\boldsymbol{u}$ with components (u, v, w) in the global coordinate system is expressed in a local reference frame with components (u_l, v_l, w_l). The expression of the vector quantities in the TNTI local reference frame permits us to isolate the effects of the local inhomogeneity associated with the presence of the TNTI in the statistics of one of the components of the vector fields. This direction varies at each location on the interface due to the changing orientation of the TNTI. For instance, in regions where the TNTI is facing in the cross-stream direction, the ω_y component decreases more rapidly when going towards the non-turbulent direction than the other components, which are aligned with the tangential directions of the TNTI and in regions where the interface is oriented towards the spanwise direction, it will be the ω_z component that is affected due to the presence of the TNTI related to the fact that different components becoming interface normal/tangential in different regions of the interface (see Watanabe et al. (2020) for the difference between the local profiles of normal/tangential vorticity components).

Considering the irregular shape of the TNTI, even though the local flow field is averaged conditionally on the location of the interface, the effects of the presence of the TNTI are distributed between different components of vector quantities such as velocity, vorticity, etc. depending on the local orientation of the TNTI. This can be observed by examining the conditional profiles of the magnitudes of vorticity components given by da Silva and

dos Reis (2011) and Taveira and da Silva (2013). The results presented in these studies exhibit minor differences between the conditional profiles of each vorticity component such as the rate of change of $|\omega_y|$ towards the turbulent core is a bit lower compared to the other two vorticity components, due to the TNTI predominantly facing in cross-stream direction on average. However, this difference between the components of ω remains relatively small when compared to the difference given by Watanabe et al. (2020) for the normal and tangential components of vorticity with respect to the interface.

The expression of the local velocity field in the TNTI local coordinate system also enables us to examine previous analyses, such as the one conducted by Reynolds (1972), which suggests a balance of variables in the reference frame of the TNTI. Moreover, our investigation extends beyond the analysis of just the 1D TNTI normal profile; we also delve into the examination of the local 3D fields near the TNTI points. This is highly valuable for comprehending the presence of average flow field patterns and properties in the vicinity of the interface, including specific vortical structures that influence or are influenced by the TNTI, as well as flow patterns that stretch or compress the interface layer. Additionally, a deeper understanding of the TNTI-averaged 3D flow fields is crucial for interpreting the results obtained through the application of the K'arm'an-Howarth-Monin-Hill (KHMH) equation, as presented in Chapter 5.

The various sublayers of the TNTI are analyzed with the help of the enstrophy transport equation following the studies by Silva et al. (2018); Taveira and da Silva (2014a); Watanabe et al. (2015), including discussion on the thickness and the properties of these sublayers. Moreover, the local propagation velocity relative to the fluid v_n^l of the IES at various locations is investigated by employing the formula given in Holzner and Lüthi (2011). In relation to chapter 3, the variation of the local propagation velocity v_n^l is compared with the variation of the mean propagation velocity v_n at different IES (corresponds to the dependence on $\omega_{th}^2/\omega_{ref}^2$). The TNTI-averaged statistics are analyzed for different regions of the interface by conditioning them on the mean curvature and the local propagation velocity. Consequently, this chapter aims to provide a comprehensive understanding of the TNTI in a temporally developing turbulent planar jet by examining the statistics of local fields near the TNTI.

In order to examine the TNTI-averaged local fields near the interface, a specific IES must be chosen. Contrary to the physical criteria proposed for the determination of the extent of VSL and TSL in the direction of the turbulent core, establishing a clear physical criterion for the outer boundary of the TNTI is challenging. The lack of a physical criterion makes determining this location somewhat arbitrary, as emphasized in the study by van Reeuwijk and Holzner (2014). A similar point is raised by Silva et al. (2018), where it is also noted

that defining this boundary is inevitably non-physical due to the presence of experimental or numerical noise in the non-turbulent region.

To address this issue, Silva et al. (2018) employ the method introduced by Taveira et al. (2013), which relies on the direct observation that vorticity profiles when conditionally averaged based on the TNTI location, do not exhibit significant variations across a range of threshold values. It should be noted that this method for the determination of the external boundary of the TNTI, is more empirical and it does not originate from a physical definition (Silva et al., 2018).

In chapter 3 of the current study, a wide range of values for $\omega_{th}^2/\omega_{ref}^2$ are considered in order to check the dependence of the mean propagation velocity v_n on $\omega_{th}^2/\omega_{ref}^2$ through the dependence of D_f on $\omega_{th}^2/\omega_{ref}^2$ in eq. 3.26. For each ω_{th}^2 value, a slightly different surface is detected with varying D_f.

The analysis in Chapter 3 considers specific threshold values, namely $\omega_{th}^2/\omega_{ref}^2 = 10^{-6}$, 10^{-5}, 10^{-4}, and 10^{-3}. These values are chosen because they fall within the range of $\omega_{th}^2/\omega_{ref}^2$ where V_J/V_{tot} in figure 2.7 exhibits a plateau. Special care is taken to ensure the quality of the DNS dataset so that no numerical effects are present for even the lowest threshold considered in that analysis and the geometrical properties of the IES are captured accurately (see section 2.2).

In the range of $\omega_{th}^2/\omega_{ref}^2$ values considered, chapter 3 of the study investigates the variation in the geometrical characteristics of different IES. This exploration involves calculating the fractal dimension D_f of each IES using the box-counting algorithm. The relationship between D_f and v_n is established through eq. 3.25.

The findings reveal a trend where D_f decreases toward 2 as the enstrophy threshold value is decreased to very low values. The smallest threshold used in chapter 3 is $\omega_{th}^2/\omega_{ref}^2 = 10^{-6}$, which corresponds to an IES with $D_f \approx 2.09$ indicating that this threshold is still relevant for the analysis conducted in chapter 3, as the IES exhibits a fractal dimension larger than 2.

In contrast, the current chapter and chapter 5 analyze the local flow field using the local reference frame of the TNTI, which takes into account the orientation of the interface. As can be observed in figure 2.2c, the IES associated with $\omega_{th}^2/\omega_{ref}^2 = 10^{-3}$ is more contorted (see also the higher D_f value for the IES of $\omega_{th}^2/\omega_{ref}^2 = 10^{-3}$ in figure 3.7) and it can be suggested that it follows more closely the outer boundaries of turbulent structures compared to the IES associated to lower $\omega_{th}^2/\omega_{ref}^2$ values. This characteristic of the IES at $\omega_{th}^2/\omega_{ref}^2 = 10^{-3}$ renders it more suitable for the TNTI-averaging process. In other words, alignment between the local ω^2 gradient and the ω^2 gradient across the whole interface layer is higher for the IES at $\omega_{th}^2/\omega_{ref}^2 = 10^{-3}$.

Considering the extent of the plateau towards the higher values of $\omega_{th}^2/\omega_{ref}^2$ in figure 2.7, the slope $dV_J/d(\omega_{th}^2)$ starts changing after certain values. Due to this reason, the IES of $\omega_{th}^2/\omega_{ref}^2 = 10^{-3}$ which still falls in the plateau region in figure 2.7 is used in this chapter and chapter 5 for the TNTI-averaging operation and the analysis of the local fields at the vicinity of the interface.

Despite the variation of ω_{th}^2 does not lead to a significant change in the spatial location of the IES, the variations in the enstrophy normal vector $\boldsymbol{n}$ have a more pronounced effect on the TNTI-averaged profiles of the variables. Further discussion on the differences in the TNTI-average profiles resulting from the choice of different ω_{th}^2 values are given in section 4.4.

The threshold value used in the present study can be compared with the one used in the study of Taveira et al. (2013) where they have analyzed the TNTI by using a DNS of a temporally developing planar jet with identical global Reynolds number Re_G with the present simulations PJx-HR. In their work, they reported a range of ω_{th} between $\omega_{th} \approx 0.08U_J/H_J$ and $\omega_{th} \approx 0.3U_J/H_J$ (where ω_{th} is the threshold value for vorticity magnitude) for the detection of the interface in which the TNTI geometry and conditional vorticity profiles remain similar for different values of ω_{th} (Taveira et al., 2013).

Taking into account the U_J, H_J parameters in the present study and the fact that the enstrophy threshold value is defined relative to a reference value where $\omega_{ref}^2 = \omega_c^2$, the threshold value $\omega_{th}^2/\omega_{ref}^2 = 10^{-3}$ falls in the range reported by Taveira et al. (2013) at $t/T_{ref} = 50$.

The present chapter begins with the definition of the local coordinate system and its positioning. Then the definition of the TNTI-averaging operation is given. Two distinct but complementary averaging operations used in the chapter are explained, namely the $x-z$ averaging and the TNTI-averaging. The chapter proceeds with the presentation of profiles of flow quantities that are averaged over the TNTI. A discussion on TNTI normal profiles follows which includes the investigation of the contributions of $\boldsymbol{U}$ and $\boldsymbol{u}'$ on the TNTI-averaged velocity components.

Subsequently, the shape and the orientation of the interface are explored through an analysis of the face normal vector over the IES and the TNTI-averaged local 3D fields are presented. After the analysis of the primary flow quantities in the vicinity of the TNTI, the enstrophy transport equation is introduced and the various terms acting on the balance are analyzed along the normal axis of the interface.

The variation of non-linearity across the TNTI is examined through an investigation of relative helicity, a parameter related to the orientation of the $\boldsymbol{u}$ and $\boldsymbol{\omega}$ vectors with respect to

each other. The relationship between the enstrophy production close to the TNTI and the variation of non-linearity across the normal direction is discussed.

In relation to the transport equation for the enstrophy, the concept of local propagation velocity is introduced for IES elements. A comparison is made between the mean propagation velocity v_n obtained in chapter 3 and the TNTI-averaged value of the local propagation velocity at various thresholds. Local entrainment/detrainment regions are detected related to the local propagation velocity for the IES. The TNTI-averaged statistics are conditioned on the local values of mean curvature and the local propagation velocity of the IES in order to investigate the variation of the local fields for distinct regions of the interface.

Finally, bringing together the picture of the TNTI of the temporally developing turbulent planar jet by the interpretation of the results obtained and the observations made throughout the chapter.

4.2 Definition of the local coordinate system at the TNTI

Similarly to the above-mentioned studies, we introduce a local coordinate system to analyze the flow field near the TNTI and perform ensemble average operation conditioned on the interface location. The detection of the IESs constituting the TNTI has been explained in section 2.6. The local coordinate system is defined for each point $\boldsymbol{X}_0$ on the IES detected by a specific ω^2_{th}, taking into account the position $\boldsymbol{X}_0$ and the orientation of the IES at that location. The enstrophy normal vector at each point is calculated as follows:

$$\boldsymbol{n} = \nabla\omega^2/|\nabla\omega^2|. \tag{4.1}$$

A local coordinate system is placed at each point considered on the detected IES, where the unit vectors of the local coordinate system are denoted by $\boldsymbol{e}_x$, $\boldsymbol{e}_y$ and $\boldsymbol{e}_z$. The local coordinate system is defined for each point on the detected IES by a procedure starting with the positioning of the origin of the local coordinate system on a given point $\boldsymbol{X}_0$ along the IES. The condition for the local y-axis is chosen to be $\boldsymbol{e}_y = -\boldsymbol{n}$. Note that by using this definition, the positive y-direction in the local coordinate system points towards the non-turbulent region. The unit vector $\boldsymbol{e}_y$ is referred to as the face normal vector in the text since it indicates the local facing direction of the IES and is used in discussions related to the TNTI orientation. Meanwhile, the normal vector $\boldsymbol{n}$ on the other hand, is referred to as the enstrophy normal vector in the text.

Apart from the local face normal direction, there is no evident constraint for the remaining two unit vectors, which are tangential to the IES. Considering the temporal planar jet flow

having a mean velocity only in the global x-direction, we have chosen to maximize the projection of the $\boldsymbol{e}_x$ on the global x-axis. With the determination of the unit vectors $\boldsymbol{e}_y$ and $\boldsymbol{e}_x$, the local z-coordinate is defined by the cross-product of these two vectors. So the conditions defining the unit vectors of the local coordinate system $(\boldsymbol{X}_0, \boldsymbol{e}_x, \boldsymbol{e}_y, \boldsymbol{e}_z)$ at each point on the IES are:

$$\begin{aligned} \boldsymbol{e}_x \cdot \boldsymbol{k} &= 0, \\ \boldsymbol{e}_x \cdot \boldsymbol{n} &= 0, \\ |\boldsymbol{e}_x| &= 1, \end{aligned} \tag{4.2}$$

$$\boldsymbol{e}_y = -\boldsymbol{n}, \tag{4.3}$$

$$\boldsymbol{e}_z = \boldsymbol{e}_x \times \boldsymbol{e}_y. \tag{4.4}$$

Here the vectors $\boldsymbol{i}$, $\boldsymbol{j}$, $\boldsymbol{k}$ represent the unit vectors of the global coordinate system and correspond to the streamwise, cross-stream, and spanwise directions. Two examples of the local coordinate system on different locations on the IES are shown in figure 4.1 following the conditions given in eqs. 4.2, 4.3 and 4.4. In order to eliminate possible confusion, it should be remarked that for the two local coordinate systems shown in figure 4.1, the $\boldsymbol{e}_z$ vector perfectly aligns with $\boldsymbol{k}$ vector. However, this alignment is a result of the 2D representation of the local grid positioning. In practice, the face normal vector $\boldsymbol{e}_y$ can be oriented in any direction, thus the $\boldsymbol{e}_z$ vector can be oriented in other directions than $\boldsymbol{k}$ or $-\boldsymbol{k}$.

4.3 The TNTI-averaging operation

The positioning of the local coordinate system is a precursor step for the generation of a local grid centred on the detected IES. Once the local coordinate system is positioned and the local 3D grid is placed, the global flow field variables are interpolated at the local grid points by using the trilinear interpolation method. Given the very high spatial resolution of the simulations, a trilinear interpolation is observed to be enough for the post-processing of the interpolated fields including the computation of the second-order derivatives. The interpolated variables include, $\boldsymbol{u}$, $\boldsymbol{\omega}$ vectors and scalars such as p, ω^2. After the interpolation of the variables, a transformation is applied to the vector quantities by the application of a rotation operation, $\boldsymbol{R}$ in order to express the vector fields with components in the local coordinate system $(\boldsymbol{e}_x, \boldsymbol{e}_y, \boldsymbol{e}_z)$. The rotation operation $\boldsymbol{R}$ which relates the expression of an

arbitrary vector $\boldsymbol{a}$ in the global coordinate system with its expression in the local coordinate system $\boldsymbol{a}^l$ can be written as;

$$\begin{bmatrix} a^l{}_1 \\ a^l{}_2 \\ a^l{}_3 \end{bmatrix} = \begin{bmatrix} \boldsymbol{e}_x \cdot \boldsymbol{i} & \boldsymbol{e}_x \cdot \boldsymbol{j} & \boldsymbol{e}_x \cdot \boldsymbol{k} \\ \boldsymbol{e}_y \cdot \boldsymbol{i} & \boldsymbol{e}_y \cdot \boldsymbol{j} & \boldsymbol{e}_y \cdot \boldsymbol{k} \\ \boldsymbol{e}_z \cdot \boldsymbol{i} & \boldsymbol{e}_z \cdot \boldsymbol{j} & \boldsymbol{e}_z \cdot \boldsymbol{k} \end{bmatrix} \begin{bmatrix} a_1 \\ a_2 \\ a_3 \end{bmatrix} \tag{4.5}$$

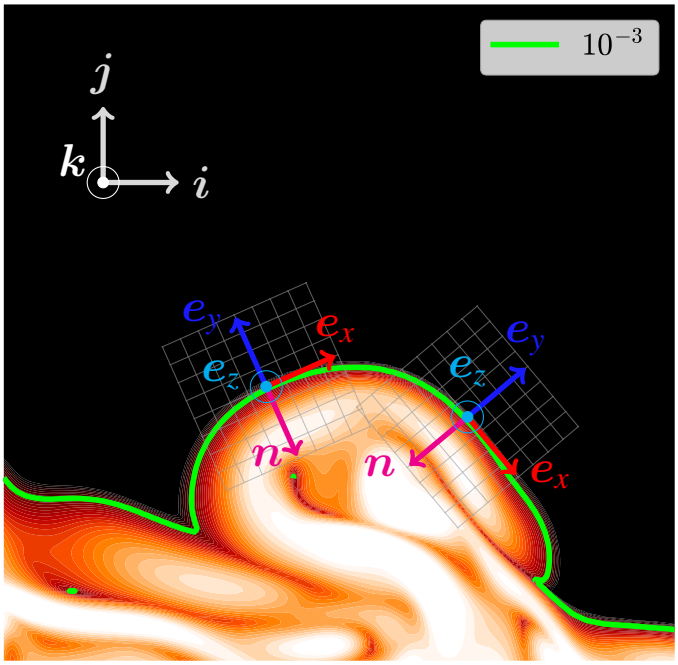

Fig. 4.1 Example of the two local coordinate systems placed on two different locations on the IES of $\omega_{th}^2/\omega_{ref}^2 = 10^{-3}$. The unit vectors of the local coordinate systems are denoted by $\boldsymbol{e}_x$, $\boldsymbol{e}_y$ and $\boldsymbol{e}_z$. $\boldsymbol{n}$ is the enstrophy normal vector defined as $\boldsymbol{n} = \boldsymbol{\nabla}\omega^2/|\boldsymbol{\nabla}\omega^2|$ and the unit vectors of the global coordinate system, $\boldsymbol{i}$, $\boldsymbol{j}$, $\boldsymbol{k}$ are shown on the top left of the figure. It must be noted that due to the constraints of the demonstration on a 2D figure, $\boldsymbol{e}_z$ looks aligned with $\boldsymbol{k}$ and $\boldsymbol{e}_y$ rests fully on the x-y plane for all the locations, which is not the general case. The orientation of $\boldsymbol{e}_y$ is not constrained in any way in 3D, thus the orientation of $\boldsymbol{e}_z$.

To ensure that the TNTI does not fold on itself and that there are no engulfed turbulent or non-turbulent regions near the interface, an additional condition called the *no multi-cross* condition is applied. This condition checks whether the TNTI normal axis, i.e., the local y-axis, crosses the TNTI multiple times within a certain distance on each side of the IES. This condition is applied as we are interested in capturing the variation of variables across the turbulent to non-turbulent sides of the interface. Normal axis crossing the interface multiple times will make the TNTI-average profiles hard to interpret and possibly affect the parts associated with the non-turbulent part of the TNTI-averaged data and is therefore omitted also

in previous studies (da Silva and Pereira, 2008; Watanabe et al., 2014b). Different methods have been used in the literature to overcome this issue, either by completely neglecting the points on the IES where the local normal axis has multiple crossings of the interface (Zhou and Vassilicos, 2020), or by defining a margin of length in order to exclude certain parts of the local profile from the conditional averaging operation (Watanabe et al., 2019, 2020) or by using an envelope surface rather than the full interface with all its contortions Westerweel et al. (2009).

In the present work, we follow the methodology applied in Zhou and Vassilicos (2020). On the non-turbulent side of the interface, a check is made to see if there is a point where $\omega^2(y_I) > c_{mc}\omega_{th}^2$ along the interface normal axis from the IES location towards the non-turbulent region until the maximum extent of the interpolated field. On the turbulent side of the interface, a check is made if there is a point having $\omega^2(y_I) < (1/c_{mc})\omega_{th}^2$ between the IES location towards the direction of the turbulent core, again until the end of the interpolated local field. In the present study, a local interpolated field with a size of $-50 < y_I/dy < 50$ in the interface normal direction is used, meaning that the check for *no multi-crossing* condition is carried out in this range, corresponding to $-23 < y_I/\eta < 23$ where dy is the uniform grid size in all the directions and η is the Kolmogorov length scale computed at the centre-plane of the jet. Along the 1D normal grid, $y_I/\eta = 0$ corresponds to the IES location. Here, the free parameter c_{mc} is $c_{mc} = 5$ taking into account that the different thresholds analyzed in chapter 3 are chosen with an interval of a decade of ω_{ref}^2 values, thus choosing $c_{mc} = 10$ corresponds to the next threshold considered. This parameter serves as a modifier for the sensitivity of the *no multi-cross* check, which is useful when the local grid used for the conditional analysis is of the same order or finer than the grid used for the TNTI detection. With the improved detection method for the TNTI position utilized in this chapter (see section 2.6), it is observed that the values $c_{mc} = 1$ and $c_{mc} = 5$ do not lead to a change in the results obtained in this chapter, as for the $\omega_{th}^2/\omega_{ref}^2$ of the order of 10^{-3}-10^{-6}, it is mainly the ω_{th}^2 term which determines the threshold value (rather than c_{mc} or $1/c_{mc}$) used for the *no multi-cross* condition i.e., $\omega^2(y_I) < (1/c_{mc})\omega_{th}^2$. However, $c_{mc} = 5$ is used to retain the locations where the enstrophy profiles are not perfectly monotonic. If a multi-crossing is detected on either side of the interface, this point on the IES is excluded from the local analysis and the TNTI averaging operation.

Before moving on to the local analysis of the interface and the application of the TNTI-averaging operation, it is beneficial to clarify the two distinct averaging operations used in this study to distinguish and comprehend their interactions. Firstly, we have the averaging over the homogeneous directions as introduced in chapter 3, where $\langle\cdot\rangle$ denotes the averaged quantity in two homogeneous directions of the global coordinate system i.e. x and z,

$$\boldsymbol{a} = \boldsymbol{A} + \boldsymbol{a}'. \tag{4.6}$$

In this chapter, a capital letter is used for the quantity averaged in the homogeneous directions, i.e. $A = \langle \boldsymbol{a} \rangle$. To prevent confusion with the TNTI-averaging operation introduced in this section, the notation in the form of $\langle \boldsymbol{a} \rangle$ is omitted. The second averaging operation is defined conditional on the interface location $\boldsymbol{X}_0$ and will be referred to as "TNTI-averaging" and the obtained profiles/local fields will be referred to as "TNTI-average" or "TNTI mean".

The local fields are averaged along the interface while keeping the local coordinates x_I, y_I, and z_I constant. This operation is denoted by $\langle \cdot \rangle_I$. When applied to a vector quantity, it leads to a result in the form,

$$\boldsymbol{a} = \langle \boldsymbol{a} \rangle_I + \boldsymbol{a}''. \tag{4.7}$$

It is important to point out the fact that these are two independent definitions of averaging processes and the TNTI-average values of the fluctuating component $\boldsymbol{a}'$ in eq. 4.6 is not zero i.e. $\langle \boldsymbol{a}' \rangle_I \neq 0$. On the other hand, due to the definition of the TNTI averaging process, $\langle \boldsymbol{a}'' \rangle_I = 0$.

As shown in chapter 3, for the case of a temporally developing jet, the mean velocity profile is solely a function of y-direction for a given time, i.e. $U(y)$. Using eq. 4.5, it can be expressed with respect to the TNTI local coordinates as $U(Y_0 + \boldsymbol{R}_2^{-1}(\boldsymbol{X}_0) \cdot \boldsymbol{x}_I)$. Both averaging operations, which are defined by eqs. 4.6 and 4.7, are applied spatially so we consider an instant of the velocity field for the demonstration of these operations on the flow field variables and the time variable will be omitted in the notation. With the application of the decomposition in eq. 4.6 to the velocity vector for a given time, at any location can be written as,

$$\boldsymbol{u}(x_I, y_I, z_I, \boldsymbol{X}_0) = U(Y_0 + \boldsymbol{R}_2^{-1}(\boldsymbol{X}_0) \cdot \boldsymbol{x}_I) + u'(x_I, y_I, z_I, \boldsymbol{X}_0). \tag{4.8}$$

Apart from that, averaging the velocity vector, conditionally on the TNTI location leads to,

$$\boldsymbol{u}(x_I, y_I, z_I, \boldsymbol{X}_0) = \langle \boldsymbol{u}(x_I, y_I, z_I, \boldsymbol{X}_0) \rangle_I + u''(x_I, y_I, z_I, \boldsymbol{X}_0). \tag{4.9}$$

The local velocity vector field can be expressed in the local coordinate system as;

$$\begin{aligned} u_l &= \boldsymbol{u} \cdot \boldsymbol{e}_x \\ v_l &= \boldsymbol{u} \cdot \boldsymbol{e}_y \\ w_l &= \boldsymbol{u} \cdot \boldsymbol{e}_z. \end{aligned} \tag{4.10}$$

Here, v_l is the TNTI normal component, and u_l and w_l are components of the velocity vector, tangential to the interface.

The TNTI averaging operation across the interface can be applied to these local vector fields. In this case, the components of TNTI-averaged local velocity can be written as;

$$\begin{aligned} \langle u_l \rangle_I &= \langle \boldsymbol{U} \cdot \boldsymbol{e}_x \rangle_I + \langle \boldsymbol{u}' \cdot \boldsymbol{e}_x \rangle_I, \\ \langle v_l \rangle_I &= \langle \boldsymbol{U} \cdot \boldsymbol{e}_y \rangle_I + \langle \boldsymbol{u}' \cdot \boldsymbol{e}_y \rangle_I, \\ \langle w_l \rangle_I &= \langle \boldsymbol{U} \cdot \boldsymbol{e}_z \rangle_I + \langle \boldsymbol{u}' \cdot \boldsymbol{e}_z \rangle_I. \end{aligned} \tag{4.11}$$

The profiles of TNTI-averaged velocities and the mean local 3D fields are mostly obtained by this operation in the current chapter and in chapter 5. Here it should be remarked that as the TNTI averaging operation is applied for fixed x_I, y_I, and z_I locations, it averages the $x-z$ averaged $\boldsymbol{U}$ at various global y-coordinate values.

On the other hand, another decomposition for the components of the TNTI-averaged local velocity can be written by using eq. 4.9 and eqs. 4.10;

$$\begin{aligned} u_l &= \langle \boldsymbol{u} \rangle_I \cdot \boldsymbol{e}_x(\boldsymbol{X}_0) + \boldsymbol{u}'' \cdot \boldsymbol{e}_x(\boldsymbol{X}_0) \\ v_l &= \langle \boldsymbol{u} \rangle_I \cdot \boldsymbol{e}_y(\boldsymbol{X}_0) + \boldsymbol{u}'' \cdot \boldsymbol{e}_y(\boldsymbol{X}_0) \\ w_l &= \langle \boldsymbol{u} \rangle_I \cdot \boldsymbol{e}_z(\boldsymbol{X}_0) + \boldsymbol{u}'' \cdot \boldsymbol{e}_z(\boldsymbol{X}_0) \end{aligned} \tag{4.12}$$

This decomposition is now further investigated in order to show the various terms constituting $\langle \boldsymbol{u} \rangle_I$. Applying the TNTI averaging operation we obtain,

$$\begin{aligned} \langle u_l \rangle_I &= \langle \boldsymbol{u} \rangle_I \cdot \langle \boldsymbol{e}_x \rangle_I + \langle \boldsymbol{u}'' \cdot \langle \boldsymbol{e}_x \rangle_I \rangle_I + \langle \boldsymbol{u}'' \cdot \boldsymbol{e}_x'' \rangle_I, \\ \langle v_l \rangle_I &= \langle \boldsymbol{u} \rangle_I \cdot \langle \boldsymbol{e}_y \rangle_I + \langle \boldsymbol{u}'' \cdot \langle \boldsymbol{e}_y \rangle_I \rangle_I + \langle \boldsymbol{u}'' \cdot \boldsymbol{e}_y'' \rangle_I, \\ \langle w_l \rangle_I &= \langle \boldsymbol{u} \rangle_I \cdot \langle \boldsymbol{e}_z \rangle_I + \langle \boldsymbol{u}'' \cdot \langle \boldsymbol{e}_z \rangle_I \rangle_I + \langle \boldsymbol{u}'' \cdot \boldsymbol{e}_z'' \rangle_I, \end{aligned} \tag{4.13}$$

where $\boldsymbol{e}(\boldsymbol{X_0}) = \langle \boldsymbol{e} \rangle_I + \boldsymbol{e}''(\boldsymbol{X}_0)$ with $\langle \boldsymbol{e}'' \rangle_I = 0$.

The second term on the right-hand side of the equation is zero due to the definition of the TNTI averaging in eq. 4.7. So the term becomes,

$$\begin{aligned}\langle u_l\rangle_I &= \langle \boldsymbol{u}\rangle_I \cdot \langle \boldsymbol{e}_x\rangle_I + \langle \boldsymbol{u}'' \cdot \boldsymbol{e}_x''\rangle_I,\\ \langle v_l\rangle_I &= \langle \boldsymbol{u}\rangle_I \cdot \langle \boldsymbol{e}_y\rangle_I + \langle \boldsymbol{u}'' \cdot \boldsymbol{e}_y''\rangle_I,\\ \langle w_l\rangle_I &= \langle \boldsymbol{u}\rangle_I \cdot \langle \boldsymbol{e}_z\rangle_I + \langle \boldsymbol{u}'' \cdot \boldsymbol{e}_z''\rangle_I,\end{aligned} \tag{4.14}$$

By applying the decomposition 4.8 to the first term on the right-hand side in eq. 4.14 we obtain,

$$\begin{aligned}\langle u_l\rangle_I &= \langle \boldsymbol{U}\rangle_I \cdot \langle \boldsymbol{e}_x\rangle_I + \langle \boldsymbol{u}'\rangle_I \cdot \langle \boldsymbol{e}_x\rangle_I + \langle \boldsymbol{u}'' \cdot \boldsymbol{e}_x''\rangle_I,\\ \langle v_l\rangle_I &= \langle \boldsymbol{U}\rangle_I \cdot \langle \boldsymbol{e}_y\rangle_I + \langle \boldsymbol{u}'\rangle_I \cdot \langle \boldsymbol{e}_y\rangle_I + \langle \boldsymbol{u}'' \cdot \boldsymbol{e}_y''\rangle_I,\\ \langle w_l\rangle_I &= \langle \boldsymbol{U}\rangle_I \cdot \langle \boldsymbol{e}_z\rangle_I + \langle \boldsymbol{u}'\rangle_I \cdot \langle \boldsymbol{e}_z\rangle_I + \langle \boldsymbol{u}'' \cdot \boldsymbol{e}_z''\rangle_I,\end{aligned} \tag{4.15}$$

Using the TNTI averaging, the fluctuations of the local velocity components can be written as,

$$\begin{aligned}u_l'' &= u_l - \langle u_l\rangle_I\\ v_l'' &= v_l - \langle v_l\rangle_I\\ w_l'' &= w_l - \langle w_l\rangle_I\end{aligned} \tag{4.16}$$

By using this definition (eq. 4.16) of fluctuating velocities, normal and cross stresses can be defined in the TNTI local coordinate system e.g. $\langle v_l''^2\rangle_I$, $\langle u_l'' v_l''\rangle_I$ similarly to the classical turbulent stress terms. Turbulent stresses defined this way in the local coordinate system are used in the interpretation of the theoretical approach put forth in the study of Reynolds (1972) (see section 4.5).

4.4 TNTI-averaged profiles of the flow field variables

It has been demonstrated in chapter 3 that the instant $t/T_{ref} = 50$ falls within the time range where the turbulent jet exhibits self-similarity and is unaffected by boundary conditions. TNTI-averaged profiles have been examined at different times with the PJ1 simulation, and it has been observed that $t/T_{ref} = 50$ is representative of a wide range of times in the aforementioned time range. All results presented in this chapter are obtained from the PJx-HR simulations at $t/T_{ref} = 50$ unless stated otherwise. In order to increase statistical

convergence, the results are obtained as the ensemble average over the five simulations whenever possible. In case a specific result is based on data from a single simulation rather than the ensemble average, this is explicitly mentioned in the caption.

In this section, the analysis is conducted using a local grid that spans from $-50dy$ to $50dy$ in each direction of the local coordinate system, which corresponds to a range -23η to 23η in the local coordinates y_I, x_I, and z_I. The points $\boldsymbol{X}_0$ considered over the interface are the numerical mesh points where the enstrophy is closest to the enstrophy threshold, although their exact locations are refined with the method described in section 2.6. It is worth noting that the *no multi-crossing* condition results in the exclusion of 40% of the total number of points for the IES of $\omega_{th}^2/\omega_{ref}^2 = 10^{-3}$.

Before delving into the discussion of the results, it is important to address the choice of using the $\omega_{th}^2/\omega_{ref}^2 = 10^{-3}$ IES for the TNTI averaging operation, as mentioned in the introduction of this chapter (see Section 4.1). Now that the TNTI-averaging operation is defined, let's attempt to quantify the differences between various ω_{th}^2 values. Figure 4.2 presents TNTI-average profiles of $\langle\omega^2\rangle_I$ for comparison of the TNTI-averaged profiles of ω^2 for the IES of $\omega_{th}^2/\omega_{ref}^2 = 10^{-3}$ and $\omega_{th}^2/\omega_{ref}^2 = 10^{-6}$.

In figure 4.2a, the $\langle\omega^2\rangle_I/\omega_c^2$ profile is shown in solid line for the IES of $\omega_{th}^2/\omega_{ref}^2 = 10^{-6}$. Along this profile, the location of $\langle\omega^2\rangle_I/\omega_{ref}^2 = 10^{-3}$ is marked by a red vertical dashed line. The TNTI-average profile of $\langle\omega^2\rangle_I/\omega_c^2$ for the IES of $\omega_{th}^2/\omega_{ref}^2 = 10^{-3}$ is plotted on top, by offsetting its origin ($y_I/\eta = 0$ location) to coincide with the $\langle\omega^2\rangle_I/\omega_{ref}^2 = 10^{-3}$ location computed from the TNTI normal profile for the IES of $\omega_{th}^2/\omega_{ref}^2 = 10^{-6}$. The offset between these two profiles is found to be 2.85η. This can be considered as a maximum limit for the mean distance between the IES of $\omega_{th}^2/\omega_{ref}^2 = 10^{-3}$ and $\omega_{th}^2/\omega_{ref}^2 = 10^{-6}$. The reason it is referred to as the maximum value is that it is computed by using the profile of $\langle\omega^2\rangle_I/\omega_c^2$ obtained for $\omega_{th}^2/\omega_{ref}^2 = 10^{-6}$ IES. As has been mentioned in section 4.1, the local orientation of $\boldsymbol{n}$ at the IES can lead to a reduction of the gradient of $\langle\omega^2\rangle_I$ along the y_I axis, thus the mean distance between the IES of $\omega_{th}^2/\omega_{ref}^2 = 10^{-6}$ and $\omega_{th}^2/\omega_{ref}^2 = 10^{-3}$ is higher when the gradient is measured by the profile $\langle\omega^2\rangle_I$ averaged over the IES of $\omega_{th}^2/\omega_{ref}^2 = 10^{-6}$.

Even though three orders of magnitude variation of $\omega_{th}^2/\omega_{ref}^2$ does lead to a slight change of the spatial location of the IES i.e. $\approx 2.85\eta$, the effect of the variation of the contortion of the IES is more dramatic on the TNTI-averaged profiles. Figure 4.2b shows the TNTI-average profiles in a linear plot, in order to see their differences more clearly. A much steeper gradient is observed for the $\langle\omega^2\rangle_I$ profile obtained by averaging over the IES of $\omega_{th}^2/\omega_{ref}^2 = 10^{-3}$. This is due to the different geometrical structure of the IES which has also been shown in figure 2.2c with the visualization of the IES for various $\omega_{th}^2/\omega_{ref}^2$ values and the variation of D_f for the corresponding surfaces (see figure 3.7). It is observed that due to the orientation

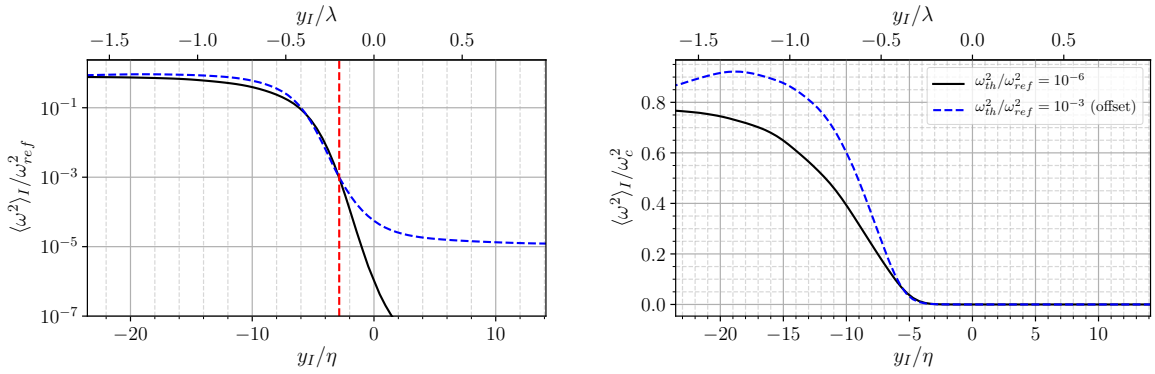

(a) $\langle\omega^2\rangle_I$ in log-lin plot

(b) $\langle\omega^2\rangle_I$ in linear plot

Fig. 4.2 TNTI-averaged profiles of $\langle\omega^2\rangle_I$ for IES of $\omega^2_{th}/\omega^2_{ref} = 10^{-6}$ and $\omega^2_{th}/\omega^2_{ref} = 10^{-3}$ at $t/T_{ref} = 50$. The red line shows the y_I location where $\langle\omega^2\rangle_I/\omega^2_{ref} = 10^{-3}$ in the TNTI-average profile obtained for the IES of $\omega^2_{th}/\omega^2_{ref} = 10^{-6}$

of IES of $\omega^2_{th}/\omega^2_{ref} = 10^{-3}$ following more closely the underlying relatively intense turbulent zones, the gradient obtained for this IES is also higher.

Following the discussion regarding the choice of using $\omega^2_{th}/\omega^2_{ref} = 10^{-3}$ to detect the IES and an attempt to quantify its implications, we can now begin our analysis by examining the profiles of flow field variables averaged over the specified IES. Enstrophy, being a marker variable for distinguishing the turbulent and non-turbulent regions, is the first variable to look at, along with the components of the local vorticity, along the axis normal to the IES.

Many previous studies have reported profiles of $|\omega_x|$, $|\omega_y|$, $|\omega_z|$, $|\omega|$, or ω^2 conditioned on the TNTI location (da Silva et al., 2011; da Silva and Pereira, 2008; da Silva and Taveira, 2010; Silva et al., 2018; Watanabe et al., 2014b). These profiles have been related to the average TNTI thickness or the vortical structures near the interface. An important distinction between these studies and the present one is that in our study, the vorticity vector $\boldsymbol{\omega} = (\omega_x, \omega_y, \omega_z)$ is expressed in the local coordinate system as $\boldsymbol{\omega} = (\omega^l_x, \omega^l_y, \omega^l_z)$, where ω^l_y corresponds to the local vorticity in the TNTI normal direction, while ω^l_x and ω^l_z correspond to the local vorticity components in the two tangential directions of the TNTI.

Figure 4.3 shows the profiles of ω^2 and of the magnitudes of the components ω^l_x, ω^l_y and ω^l_z all normalized by the mean centre-plane value of $|\omega_z|$, along with the gradient $-d\langle u_l\rangle_I/dy_I$ in the interface normal direction. The centre-plane mean value of $|\omega_z|$, is used for the normalization of all the profiles as $\langle|\omega_x|\rangle_c \approx \langle|\omega_y|\rangle_c \approx \langle|\omega_z|\rangle_c$ at the centre-plane of the jet, due to isotropy. In relation to the term $-d\langle u_l\rangle_I/dy_I$, it should be noted that the derivative operation d/dy_I commutes with the TNTI-averaging operation $\langle\cdot\rangle_I$.

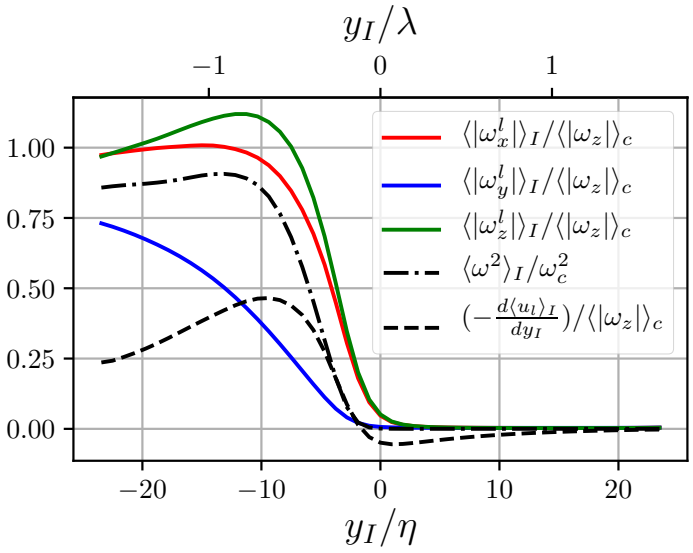

Fig. 4.3 TNTI-averaged profiles of $\langle|\omega_x^l|\rangle_I$, $\langle|\omega_y^l|\rangle_I$, $\langle|\omega_z^l|\rangle_I$, $\langle\omega^2\rangle_I$ and the gradient of local u_l velocity in the TNTI normal direction $-d\langle u_l\rangle_I/dy_I$, normalized by the mean $|\omega_z|$ at the centre-plane of the jet. The interface location ($y_I = 0$) used for the conditioning of the profile is defined with the IES of $\omega_{th}^2/\omega_{ref}^2 = 10^{-3}$. Distance from the IES y_I is normalized by the Kolmogorov length scale η computed at the centre-plane of the jet.

The profiles of vorticity components exhibit clear differences. Notably, the magnitude of ω_y^l increases at a slower rate compared to the other components. In contrast, the other two vorticity components tangential to the interface rise sharply, where the profile of spanwise component $\langle|\omega_z^l|\rangle_I$ exhibits a distinct peak.

A similar analysis for the interface normal component of vorticity is indirectly presented in Watanabe et al. (2020). In their study, the conditional profile of the tangential component is computed by subtracting the contribution of $(\boldsymbol{\omega}\cdot\boldsymbol{e}_y)^2$ from the conditional profile of ω^2. The profiles of $\langle|\omega_x^l|\rangle_I$, $\langle|\omega_y^l|\rangle_I$ and $\langle|\omega_z^l|\rangle_I$ given in figure 4.3 are in parallel with the results given by Watanabe et al. (2020).

The expression of the vectors in the local coordinate system enables us to observe the variation of the interface normal/tangential components of the vorticity vector more directly along the interface normal axis. It can be useful to recall at this point that, due to the orientation of the local x-direction $\boldsymbol{e}_x$ given by eq. 4.2, the local spanwise component is primarily aligned with the global spanwise direction (further details on this particular orientation can be found in section 4.6). By taking this fact into account, a comparison of the current TNTI-averaged profiles can be made with the profiles given in the literature (Bisset et al., 2002; Westerweel et al., 2009).

In the study by Bisset et al. (2002), TNTI-averaged profiles of vorticity components are obtained specifically for the regions of TNTI surface facing the cross-stream direction. For these specific regions, the components of the vorticity vector in the global reference frame align with those in the local reference frame. However, it is essential to note that the TNTI-averaged profiles in the present study include not only the cross-stream facing regions but all the regions of the interface with any conditions applied in terms of orientation. Nevertheless, considering that the TNTI introduces an inhomogeneity in the interface normal direction, the effects due to the presence of the TNTI on the TNTI-averaged profiles are qualitatively similar, in figure 4.3 and the conditional profiles presented in Bisset et al. (2002) e.g., the peak observed in the profile of the tangential vorticity component and the slower rise of the component normal to the interface.

A similar analysis is conducted by Westerweel et al. (2009) in an experimental setup of an axisymmetric jet. They employ the interface envelope to obtain the conditional profiles of ω_z, where a local normal axis aligned with the direction $\boldsymbol{j}$ is used for the TNTI-averaging process. This approach results in slightly less sharp profiles of $\langle\omega_z\rangle_I$ as the gradient of ω_z is most significant in the interface normal direction, whereas the axis being used by Westerweel et al. (2009) makes an angle with the interface normal axis depending on the local orientation of the interface envelope. However, on average, the interface predominantly faces in the $\pm\boldsymbol{j}$ direction and thus the conditional profile of $\langle\omega_z^l\rangle_I$ has again a bump associated with the presence of the TNTI, which relates to the bump observed in the profile of $\langle\omega_z^l\rangle_I$ in figure 4.3.

In the study by da Silva and Taveira (2010), the conditional profiles of ω_z are obtained using a methodology similar to that employed by Westerweel et al. (2009). This approach is applied to DNS datasets of temporally developing planar jets with varying Re_λ values. The study documents the presence of a bump in the mean profile of ω_z conditioned on the interface location.

Furthermore, Taveira and da Silva (2013) present conditional profiles of $|\omega_x|$, $|\omega_y|$, and $|\omega_z|$. In this case, the local grid used for the conditional profiles is positioned directly aligned with the surface normal vector of the interface envelope. It is important to note that while the local axis used for conditional averaging takes into account the local orientation of the TNTI envelope, the effects of the interface-induced inhomogeneity are distributed in conditional profiles of $|\omega_x|$, $|\omega_y|$, and $|\omega_z|$ rather than affecting only the conditional profile of $|\omega_z|$ as the TNTI normal direction does not always align perfectly with $\boldsymbol{k}$.

However, taking into account that, on average, the TNTI is oriented towards $\pm\boldsymbol{k}$ (which is valid also for the TNTI envelope defined in da Silva and Taveira (2010); Taveira and da Silva (2013); Westerweel et al. (2009)), the bump presented in the conditional profile of $|\omega_z|$ in the

above-mentioned studies can be related qualitatively with the bump observed in the profile of $\langle|\omega_z^l|\rangle_I/\langle|\omega_z|\rangle_c$ in figure 4.3. Hence, it can be asserted that the TNTI-averaged profiles of $\langle\omega^2\rangle_I$ and $\langle|\omega_x^l|\rangle_I$, $\langle|\omega_y^l|\rangle_I$, and $\langle|\omega_z^l|\rangle_I$ are in alignment with the findings in the existing literature.

In the analysis conducted by Westerweel et al. (2009) two possible reasons are proposed in order to explain this bump, which are the formation of a vortex sheet at the outer edge of the jet, or the presence of small individual vortices. A jump in the mean stream-wise velocity is also reported in this study, across the detected interface, and it is suggested that this velocity jump can be related to the peak of spanwise vorticity close to the interface (Westerweel et al., 2009). Supporting this point, Bisset et al. (2002) reports the contribution of the $d\langle U\rangle_I/\partial y_I$ on $\langle|\omega_z|\rangle_I$ is indeed significant for the regions of the interface facing towards global y-direction (cross-stream).

On a related note, da Silva and Taveira (2010) and da Silva et al. (2011) present results showing the influence of the interface on the spatial alignment of the vortical structures. The vortical structures are studied in two different classes large-scale vortical structures (LVS), which are associated with low-pressure iso-surfaces and are suggested to be remnants of Kelvin-Helmholtz instability and secondary instabilities (da Silva and dos Reis, 2011; da Silva and Taveira, 2010; Taveira and da Silva, 2013) and the intense vortical structures (IVS) associated with very high values of enstrophy (da Silva and dos Reis, 2011; da Silva et al., 2011). This particular alignment of the vortical structures will also account for a part of the observed bump in the profile of $\langle|\omega_z|\rangle_I$ as mentioned by Silva et al. (2018).

The rapid increase of $\langle\omega_z^l\rangle_I$, along with its peak inside the interface, prompts an investigation into the relationship between the profile of $\langle|\omega_z^l|\rangle_I$ and the local velocity gradient in the interface normal direction. In the present case, it is observed that the contribution of $-d\langle u_l\rangle_I/dy_I$ at the peak location accounts for less than half of the total $|\omega_z^l|$.

This observation slightly differs from the results presented in Bisset et al. (2002), in terms of the magnitude of the contribution from the gradient of the mean streamwise velocity, where a more substantial contribution is reported. The difference between the current study and Bisset et al. (2002) primarily arises from the fact that Bisset et al. (2002) considers only the interface locations facing in the cross-stream direction. In contrast, the profiles in figure 4.3 are obtained for the entire interface, without imposing any conditions on the orientation, with the exception of excluding points detected by the *no multi-cross* condition.

Even though it is not the main contributor to $\langle|\omega_z^l|\rangle_I$, the peak of $-d\langle u_l\rangle_I/dy_I$ indicates a change of local streamwise velocity along the interface normal direction in agreement with the predictions made by Reynolds (1972) and the results shown by Bisset et al. (2002) and Westerweel et al. (2009).

Figure 4.4a illustrates the TNTI-averaged profiles of the local velocity components, namely $\langle u_l \rangle_I$, $\langle v_l \rangle_I$, and $\langle w_l \rangle_I$, in the interface normal direction. These profiles are normalized by the centre-plane u_η. A rapid change is observed in both the $\langle u_l \rangle_I$ and $\langle v_l \rangle_I$ components across the TNTI.

On the other hand, $\langle w_l \rangle_I$ remains zero throughout the interfacial layer which is mainly due to the definition of the local coordinate system. Specifically, the orientation of the $\boldsymbol{e}_x$ vector is chosen to align maximally with the global streamwise direction, which leads to $\boldsymbol{e}_x$ being in the x-y plane. Furthermore, the vector $\boldsymbol{e}_z$ is defined by the cross-product of $\boldsymbol{e}_x$ and $\boldsymbol{e}_y$ (as per eq. 4.4). Given these definitions, the average $\langle \boldsymbol{e}_z \rangle_I$ vector aligns with the global +z-direction at the upper TNTI and with -z-direction at the lower TNTI, except at locations where the interface folds onto itself.

Considering this orientation of the $\boldsymbol{e}_z$ vector eq. 4.11 for $\langle w_l \rangle_I$ reveals that both terms on the right-hand side vanish. This is due to the fact that the global mean flow velocity $\boldsymbol{U}$ does not have a component in the z-direction, and both the spanwise component of the fluctuations $\boldsymbol{u}'$ and the TNTI orientation $\boldsymbol{e}_z$ do not have a preferential direction along the spanwise axis. Consequently, $\langle w_l \rangle_I$ remains zero along the interface normal y_I axis.

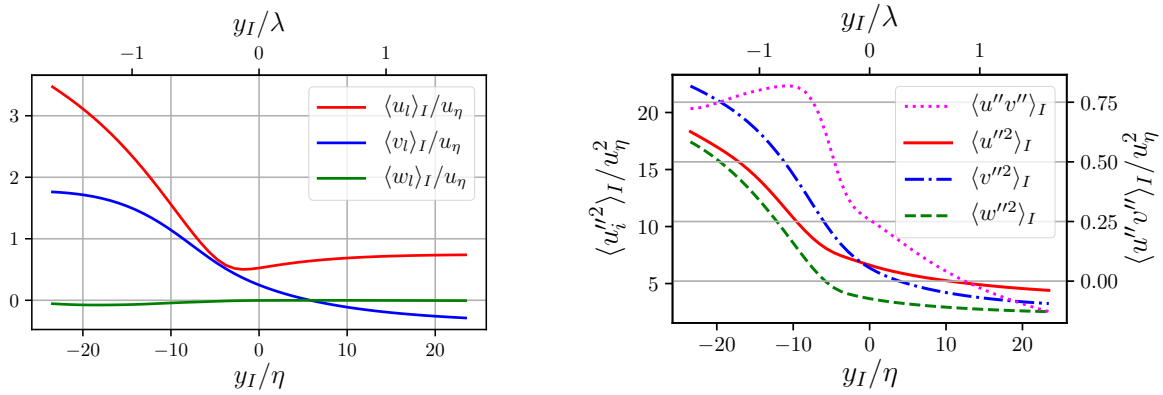

(a) Local mean velocity components

(b) Local turbulent stresses

Fig. 4.4 TNTI-averaged profiles of local velocity components and the local normal and shear turbulent stresses for the IES of $\omega_{th}^2/\omega_{ref}^2 = 10^{-3}$ at $t/T_{ref} = 50$.

In relation to the way that the orientation of $\boldsymbol{e}_x$ is chosen, $\langle u_l \rangle_I$ remains positive along the TNTI-average profile due to the jet having mean velocity in the global streamwise direction (see eq. 4.11 for $\langle u_l \rangle_I$). In contrast, the TNTI-averaged local normal velocity $\langle v_l \rangle_I$ crosses zero at a certain point.

For the region $y_I/\eta < 0$, the $\langle v_l \rangle_I$ component remains positive. This indicates that the interface perceives a local normal velocity pointing from the turbulent core towards the non-turbulent region. Furthermore, the negative gradient $d\langle v_l \rangle_I/dy_I < 0$ along the normal

TNTI axis suggests that the velocity field tends to compress in the normal direction near the interface.

The general properties of the profile of $\langle v_l \rangle_I$ show that the interface perceives a velocity field that moves towards the interface in both turbulent and non-turbulent directions. Also, the fact that the TNTI-average velocity component $\langle v_l \rangle_I$ is non-zero along the y_I axis is interesting as the mean velocity obtained by the $x-z$ averaging does not have a component in the cross-stream direction i.e. $V(y) = 0$.

In the case of spatially developing jets, the streamwise mean velocity $\boldsymbol{U}$ decreases along the streamwise direction i.e. $\partial U/\partial x < 0$. This leads to a mean cross-stream velocity in the outward direction from the centre-plane, which is consistent with the decay of $\boldsymbol{U}$ and the expansion of the jet in the streamwise direction. On the other hand, the external fluid is entrained inside the jet and a mean cross-stream velocity is induced outside the jet towards the centre-plane. These two opposing flows associated with positive/negative V velocity meet at a point along the y-axis, where the gradient of the U velocity is maximum and TNTI is most probable to exist. As previously demonstrated in the theoretical analysis presented in chapter 3, the mean flow behaviour in spatially developing jets differs significantly from its temporally developing counterpart.

A crucial distinction between both flows is that the mean cross-stream velocity $V = 0$ for each $x-z$ plane along the y-axis, meaning that there is no global cross-stream velocity V due to entrainment in the case of the temporally developing jet, unlike its spatially developing counterpart. In this context, the existence of a non-zero average velocity $\langle v_l \rangle_I$ in the reference frame of the IES is very interesting. Moreover, the profile of $\langle v_l \rangle_I$ in figure 4.4a exhibits a change of sign, even without the argumentation related to the conservation of mass for the spatially developing jet. The reason for this is discussed in more detail with the presentation of the contributions of each term in eqs. 4.15 to the TNTI-average profiles of $\langle u_l \rangle_I$, $\langle v_l \rangle_I$ and $\langle w_l \rangle_I$ at the end of this subsection.

Figure 4.4b presents the profiles of local stresses, defined by the fluctuating velocities with respect to the TNTI-average velocity values, obtained by the eqs. 4.16.

Firstly, the normal stresses i.e., $\langle u''^2 \rangle_I$, $\langle v''^2 \rangle_I$, and $\langle w''^2 \rangle_I$, exhibit significantly higher magnitudes compared to the cross-stress term $\langle u''v'' \rangle_I$. These normal stresses maintain non-zero values even on the non-turbulent side of the interface, extending as far as $y_I/\eta = 24$. However, their magnitudes decrease rapidly on the turbulent side of the IES, when going towards the non-turbulent region, particularly in the region between $y_I/\eta \approx -13.7$ and $y_I/\eta \approx -1.5$.

Secondly, the profile of $\langle u''v'' \rangle_I$ displays an even steeper gradient, primarily occurring between $y_I/\eta \approx -7.2$ and $y_I/\eta \approx -2.1$. This suggests that the TNTI is characterized

by a pronounced jump in $\langle u''v''\rangle_I$ along the normal direction. It can be noted that the very high gradient of the profile of $\langle u''v''\rangle_I$ is observed on the turbulent side of the IES of $\omega_{th}^2/\omega_{ref}^2 = 10^{-3}$ between $y_I/\eta \approx -2$ and $y_I/\eta \approx -10.5$.

The variation of the pressure across the TNTI is shown in figure 4.5a. It is observed that the pressure drops swiftly going from the non-turbulent side inside the turbulent region. This observation aligns with the idea proposed by Reynolds (1972) which suggests a balance between the high pressure in the non-turbulent region and the increased normal turbulent stresses at the turbulent side of the interface. Also, the gradient of the mean pressure in the interface normal direction is shown in figure 4.5b and exhibits a negative peak at $y_I/\eta = 8$.

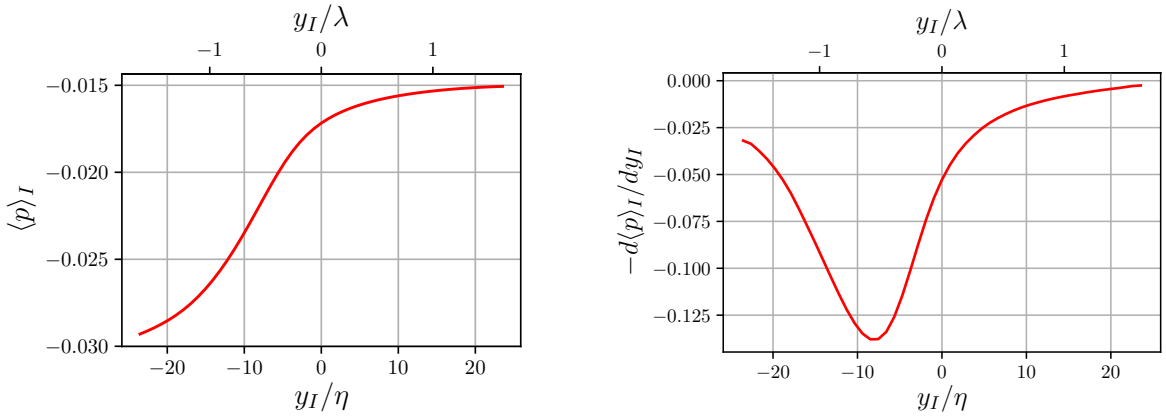

(a) Mean pressure

(b) Gradient of the mean pressure

Fig. 4.5 TNTI-averaged profiles of mean pressure $\langle p\rangle_I$ and gradient of mean pressure $d\langle p\rangle_I/dy_I$, for the IES of $\omega_{th}^2/\omega_{ref}^2 = 10^{-3}$.

Before continuing with further discussion regarding the TNTI-averaged profiles of components of $\boldsymbol{u}$ as functions of y_I, it is useful to analyze the decomposition presented in eq. 4.15 in order to investigate the contributions of $\boldsymbol{U}$, $\boldsymbol{u}'$ and the orientation of the local coordinate system $\boldsymbol{e}$ (associated with the local TNTI orientation) to the components of the TNTI-averaged velocity $\langle \boldsymbol{u}\rangle_I$.

Figure 4.6 shows the mean profiles $\langle u_l\rangle_I$, $\langle v_l\rangle_I$ and $\langle w_l\rangle_I$ obtained by applying the TNTI-averaging operation. The comparison of the profiles $\langle u_l\rangle_I$, $\langle v_l\rangle_I$ and $\langle w_l\rangle_I$ is carried out with the sum of the terms on the right-hand side of eqs. 4.15. This figure is a verification of the numerical methodology employed for the computation of the TNTI-averages of quantities by the demonstration of the equalities given in eqs. 4.15.

In figure 4.7, we present the profiles $\langle u_l\rangle_I$ and $\langle v_l\rangle_I$ alongside the three components on the right-hand side of eq. 4.15. The first term, $\langle \boldsymbol{U}\rangle_I\langle \boldsymbol{e}\rangle_I$ is the contribution of the mean flow field with respect to the $x-z$ averaging operation and the mean orientation of the TNTI. The second term $\langle \boldsymbol{u}'\rangle_I\langle \boldsymbol{e}\rangle_I$ includes the effects of the velocity fluctuation field with respect to

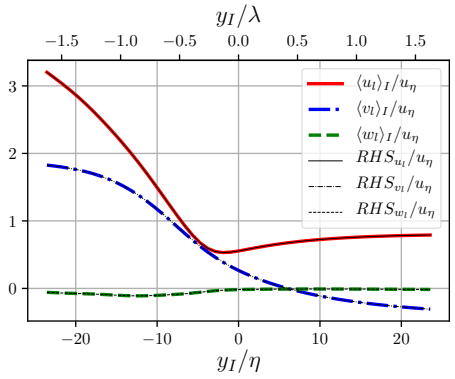

Fig. 4.6 TNTI-averaged profiles of $\langle u_l\rangle_I$, $\langle v_l\rangle_I$ and $\langle w_l\rangle_I$ and sum of the terms in the eqs. 4.15 for the IES of $\omega_{th}^2/\omega_{ref}^2 = 10^{-3}$ at $t/T_{ref} = 50$ in PJ4-LV simulation.

$x-z$ mean. And finally, the third term $\langle \boldsymbol{u}'' \cdot \boldsymbol{e}''\rangle_I$ where the $\boldsymbol{u}''$ is the fluctuating velocity with respect to TNTI-averaging and similarly $\boldsymbol{e}''$ is the fluctuation of the interface orientation with respect to the TNTI mean. Thus the last term corresponds to the correlation between the fluctuations of the velocity and of the interface orientation around the TNTI mean.

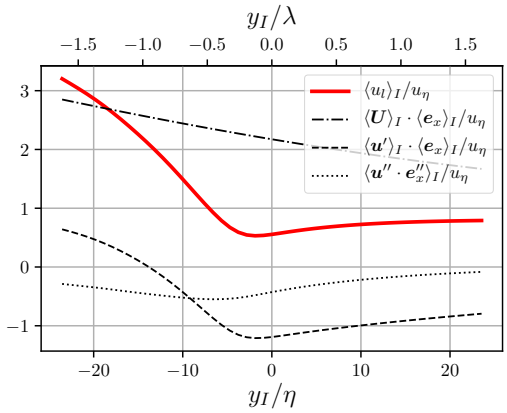

(a) $\langle u_l\rangle_I$ and constituting terms; $\langle \boldsymbol{U}\rangle_I \cdot \langle \boldsymbol{e}_x\rangle_I$, $\langle \boldsymbol{u}'\rangle_I \cdot \langle \boldsymbol{e}_x\rangle_I$ and $\langle \boldsymbol{u}'' \cdot \boldsymbol{e}_x''\rangle_I$

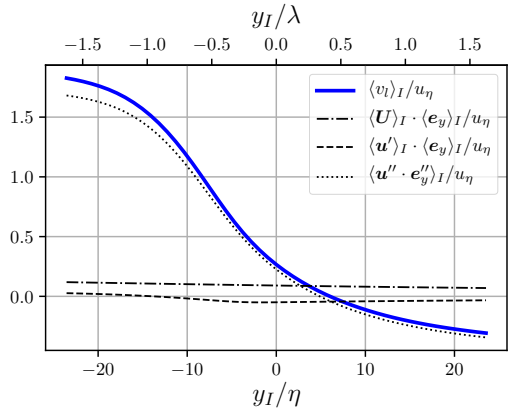

(b) $\langle v_l\rangle_I$ and constituting terms; $\langle \boldsymbol{U}\rangle_I \cdot \langle \boldsymbol{e}_y\rangle_I$, $\langle \boldsymbol{u}'\rangle_I \cdot \langle \boldsymbol{e}_y\rangle_I$ and $\langle \boldsymbol{u}'' \cdot \boldsymbol{e}_y''\rangle_I$

Fig. 4.7 TNTI-averaged profiles of $\langle u_l\rangle_I$ and $\langle v_l\rangle_I$ given with the profiles of the terms on the RHS of the eq. 4.15, for the IES of $\omega_{th}^2/\omega_{ref}^2 = 10^{-3}$ at $t/T_{ref} = 50$ in PJ4-LV simulation.

Starting with the term $\langle \boldsymbol{U}\rangle_I \cdot \langle \boldsymbol{e}\rangle_I$, the contribution of the mean velocity profile $\boldsymbol{U}$ varies linearly over the y_I/η axis for each component of the local TNTI-averaged velocity. Naturally, the highest contribution is in the component of $\langle u_l\rangle_I$, due to the positioning of the local coordinate system ensuring that the alignment of $\boldsymbol{e}_x$ is maximal with the global streamwise vector $\boldsymbol{i}$. Due to the fact that the axis goes towards the centre-plane of the jet for smaller values of y_I/η, the contribution of $\boldsymbol{U}$ increases in that direction. But there is no specific

location in the profile of $\langle \boldsymbol{U} \rangle_I \cdot \langle \boldsymbol{e} \rangle_I$ where it undergoes a dramatic change at the TNTI location.

On the other hand, figure 4.7a reveals a significant variation in $\langle u_l \rangle_I$ in the y_I direction when crossing the interface. It is evident that this jump is caused by TNTI averaging of the fluctuating velocity $\boldsymbol{u}'$ around the $x-z$ mean. The term $\langle \boldsymbol{u}' \rangle_I \cdot \langle \boldsymbol{e} \rangle_I$ crosses zero at $y_I/\eta = -13.8$ and beyond this point, it contributes negatively to the profile of $\langle u_l \rangle_I$. Although the third term also contributes to the profile of $\langle u_l \rangle_I$, the primary factor driving the jump of $\langle u_l \rangle_I$ across the TNTI is the second term, which includes the effects of $\boldsymbol{u}'$ field.

The impact of $\boldsymbol{U}$ is not particularly significant for the interface normal velocity component, $\langle v_l \rangle_I$. The profile $\langle v_l \rangle_I$ is primarily influenced by the correlation between velocity fluctuations $\boldsymbol{u}''$ and fluctuations in the orientation of the interface with respect to TNTI-average $\boldsymbol{e}_y''$ i.e., $\langle \boldsymbol{u}'' \cdot \boldsymbol{e}_y'' \rangle_I$. Thus the average interface normal velocity, perceived by the TNTI in the local reference frame is determined by the correlation between $\boldsymbol{u}''$ and $\boldsymbol{e}_y''$.

4.5 Jump condition for the tangential velocity and the vorticity at the interface

The TNTI-averaged profiles presented in section 4.4 allow us to investigate the analysis conducted by Reynolds (1972) on the interface. In the study of Reynolds (1972), the interface between the turbulent and non-turbulent regions was analyzed by placing a small control volume (CV) which covers a segment of the interface (interface referred to as *superlayer* in the original paper). Figure 4.8 shows a schematic of the CV described by Reynolds (1972).

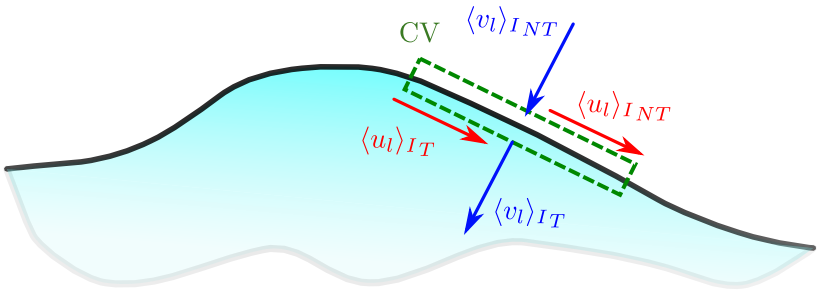

Fig. 4.8 Schematic of the local control volume defined similar to (Reynolds, 1972) (*shown in dashed green line*). The subscripts T and NT are used for the quantities in the turbulent and non-turbulent sides of the control volume.

In the analysis presented in Reynolds (1972), the mean velocity at the interface is expressed by two components: one aligned with the normal direction and the other in the tangential direction of the interface. The positioning of the local coordinate system in the

current study is important in this context by using the conditions given in eqs. 4.2, 4.3, and 4.4. As shown in figure 4.4a, the TNTI-average velocity vector $\langle \boldsymbol{u} \rangle_I$ has components in the interface normal direction $\langle v_l \rangle_I$ and another component in the tangential direction $\langle u_l \rangle_I$, whereas the second tangential average velocity component $\langle w_l \rangle_I$ is zero, compatible with the mean velocity components defined in Reynolds (1972) (see figure 4.4a).

The interface is considered to be a sheet-like surface, with an infinitesimal thickness by Reynolds (1972), thus the CV covering a section of the interface is also considered to have a negligible thickness, thus neglecting the fluxes at the side surfaces of the CV and only considering the fluxes in the interface normal direction. Furthermore, the viscous stresses on either side of the interface are neglected in the analysis by Reynolds (1972). Given these assumptions, the conservation equations for mass and momentum equations in TNTI normal and tangential directions are written for the CV, with certain terms omitted. Starting with the mass balance for the control volume, the relation is written as;

$$[\langle v_l \rangle_I]_{NT} = [\langle v_l \rangle_I]_T. \tag{4.17}$$

Here, $\langle v_l \rangle_I$ is the mean TNTI normal velocity and the subscripts NT and T stand the values of the variables at the location of the boundary surfaces of the CV on the non-turbulent and turbulent sides of the interface (see figure 4.8). Balance is written in the TNTI local coordinate system where the mean/fluctuating velocities with respect to the TNTI-averaging operation are also expressed with components normal and tangential to the interface. As the CV is taken to be infinitesimally thin in TNTI normal direction, the faces of CV facing TNTI tangential directions are neglected and we end up with a mass balance with the fluxes in the normal direction of the interface (Reynolds, 1972). This directly implies that the interface normal velocity should remain constant across the interface.

To assess the validity of this conclusion, figure 4.4a can be re-visited. It becomes apparent from this figure that the TNTI normal component $\langle v_l \rangle_I$ varies across the interface, and its derivative along the y_I direction exhibits high values, particularly in the proximity of the detected IES. Considering the CV positioned in the work of Reynolds (1972), which fully contains the jump of the vorticity at the interface, there is a significant difference between the value of $\langle v_l \rangle_I$ at the turbulent and non-turbulent sides of the interface. This result contradicts eq. 4.17 and leads to a fundamental problem due to the assumptions made in Reynolds (1972) for the balance of quantities inside the CV.

The primary problem arises because the variation in the TNTI-averaged normal velocity $\langle v_l \rangle_I$ directly implies the presence of a significant gradient of $\langle u_l \rangle_I$ in the tangential direction of the IES. Furthermore, considering that the jump in vorticity $\boldsymbol{\omega}$ occurs over a certain

distance and is not as sharp as depicted in Reynolds (1972), this gradient of $\langle u_l \rangle_I$ suggests significant outflow of mass from the neglected side surfaces of the CV.

Secondly, the momentum balance in the normal and tangential directions are written as follows by (Reynolds, 1972),

$$[\langle p \rangle_I]_{NT} = [\langle p \rangle_I + \langle \rho v_l''^2 \rangle_I]_T, \tag{4.18}$$

$$\rho \langle v_l \rangle_I ([\langle u_l \rangle_I]_{NT} - [\langle u_l \rangle_I]_T) - [\rho \langle v_l'' u_l'' \rangle_I]_T = 0. \tag{4.19}$$

Here, $\langle p \rangle_I$ denotes the TNTI-averaged pressure and $\langle v_l''^2 \rangle_I$ is the turbulent normal stress, which is considered only for the turbulent side in the model proposed by Reynolds (1972). In eq. 4.19, $-(\rho \langle v_l'' u_l'' \rangle_I)$ is the turbulent shear stress at the boundary and similarly to eq. 4.18, it has been considered only for the turbulent side of the CV.

Another important point related to this equation is that the mean velocity $\langle v_l \rangle_I$ has to be defined for the first term of eq. 4.19. In the analysis made by Reynolds (1972), the conservation of mass yields the equality given in eq. 4.17 with the assumptions being made. With this relation, there is no ambiguity in the choice of $\langle v_l \rangle_I$ appearing in the eq. 4.19 as it does not vary across the TNTI. On the other hand, a significant jump in the value of $\langle v_l \rangle_I$ across the TNTI is observed in the present study (see figure 4.4a). Without introducing any modification to the original equation, the $\langle v_l \rangle_I$ in eq. 4.19 can be determined by taking the average value of $\langle v_l \rangle_I$ along the extent of the CV on the y_I axis. So this term is not specified by a subscript T or NT and the mean value of $\langle v_l \rangle_I$ along y_I for the extent of CV is denoted as $[\langle v_l \rangle_I]_m$. Looking at eq. 4.19, a jump in the TNTI mean tangential velocity is expected in case the turbulent shear stress is non-zero on the turbulent side of the interface. There is indeed a jump in the $\langle u'' v'' \rangle_I$ across the interface which is shown in the figure 4.4b and the values of the TNTI-averaged tangential velocity $\langle u_l \rangle_I$ rise sharply in the turbulent side of the detected IES across the TNTI layer (see figure 4.4a). The local profiles obtained in the present study support the presence of a jump in the values of TNTI-averaged tangential velocity between the turbulent and non-turbulent sides of the interface.

As the TNTI-averaged profiles of velocity, pressure, turbulent stresses, and vorticity have now been computed, the relations of mass/momentum balance proposed in (Reynolds, 1972) can be checked to see if they hold near the detected IES. In order to make this check, we make use of the 1D TNTI-averaged profiles presented in section 4.4 in the interface normal direction.

An important difference between the early theoretical approaches (Corrsin and Kistler, 1955; Phillips, 1972; Reynolds, 1972) and more recent studies (da Silva et al., 2014; Taveira

and da Silva, 2014a; van Reeuwijk and Holzner, 2014; Watanabe et al., 2020) exists for the concept of TNTI. In the former, the TNTI is regarded as a surface with an infinitesimal thickness, featuring nearly singular jumps in flow variables such as tangential velocity and span-wise vorticity. In contrast, in recent studies, the TNTI has been resolved well enough, which permits us to observe the continuous variation of quantities across the interface thickness, even though the local gradients of variables are indeed very high. Due to this continuous variation, the choice of the location and the thickness of the CV to check the relations proposed by Reynolds (Reynolds, 1972) also becomes important.

Thus, it is appropriate to start by defining how the CV is placed, before presenting the results related to the balance equations 4.17, 4.18 and 4.19. For the NT side (upper face) of the CV, the point satisfying the condition $|\omega_z^l| < 10^{-3/2}$ is searched, starting from the IES location and going towards the non-turbulent region. The position of the side denoted with T, the lower surface of the CV (turbulent side) is chosen at the maximum of the profile $\langle|\omega_z^l|\rangle_I$. As a result of the procedure above, the upper surface of the CV is chosen to be at $y_I/\eta = 1$ and the location of the lower surface has been chosen as $y_I/\eta = -10.3$. The resulting CV surfaces are marked on the normal profiles given in figure 4.9.

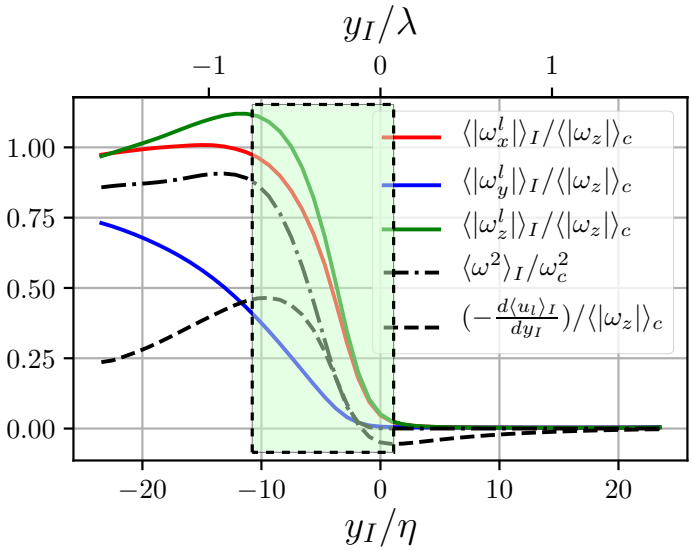

Fig. 4.9 Extent of the chosen CV by the conditions mentioned above, shown on top of the TNTI-averaged profiles on ω^2 and local components of $|\omega|$.

Using the local mean/fluctuating variables with respect to the TNTI averaging operation at the location of the interface, the balance of mass and the normal/tangential momentum can be written as;

$$B_c^R = \frac{[\langle v_l \rangle_I]_{NT}}{[\langle v_l \rangle_I]_T} = 0.17, \tag{4.20}$$

$$B_{nm}^R = \frac{[\langle p \rangle_I]_{NT}}{[\langle p \rangle_I + \langle \rho v_l''^2 \rangle_I]_T} = 1.40, \tag{4.21}$$

$$B_{tm}^R = \frac{[\langle v_l \rangle_I]_m([\langle u_l \rangle_I]_{NT} - [\langle u_l \rangle_I]_T)}{[\langle u_l'' v_l'' \rangle_I]_T} = -0.83. \tag{4.22}$$

The errors in the balance relations can be observed from the ratio of the balancing terms on both sides of eqs. 4.20, 4.21 and 4.22. The superscript R stands for relations given by Reynolds (1972). A very large error is present for the continuity equation, eq. 4.17. It can be noted that in 4.17, it is assumed that the interface normal velocity is equal on both sides of the CV. However, as has been shown in figure 4.4a, the value of $\langle v_l \rangle_I$ is not equal at the upper and lower sides of the CV. It varies across the thickness of the TNTI and even a change in the sign of $\langle v_l \rangle_I$ occurs along the y_I/η axis. This indicates that there is a considerable mass flux from the faces perpendicular to the interface, which is not accounted for in the analysis conducted by Reynolds (1972). This outwards mass flux in tangential direction at the interface is mentioned again in section 4.7 where the TNTI-averaged 3D local velocity fields are presented. For the sake of consistency, the variation of the velocity in the tangential direction is not further elaborated here and we continue the current discussion with the TNTI-average normal 1D profiles, in relation to the model proposed by Reynolds (1972).

Considering the normal momentum balance, the error B_{nm}^R remains smaller compared to B_c^R given in eq. 4.20. In eq. 4.21, the error in the balance of normal momentum is mainly due to the neglected term $\langle v_l''^2 \rangle_I$ in the non-turbulent side of the interface. It can be seen from the figure 4.4b that even though the normal stress reduces significantly across the interface, it does not go to zero in the non-turbulent region. Thus neglecting this term contributes to the imbalance in the eq. 4.18.

The balance of the tangential momentum B_{tm}^R even becomes negative as the $\langle u'' v'' \rangle_I$ takes positive values with the velocity fluctuations with respect to the TNTI-averaged local velocity.

To summarize, an imbalance exists in continuity and normal/tangential momentum balance relations of Reynolds (1972). The reason for these balance deficits is the neglected terms in the eqs. 4.17, 4.18 and 4.19. As has been shown in figure 4.4b, the normal stresses in the non-turbulent side cannot be neglected, and more importantly the prediction in eq. 4.17 by Reynolds (1972) is shown not to hold by considering the TNTI-average profile $\langle v_l \rangle_I$ in the interface normal direction given in figure 4.4a. The relations obtained in Reynolds (1972) can be improved by taking these observations into account and writing the balance equations

without applying the assumptions that are observed not to hold near the interface. With the introduction of the neglected terms, the equations for the normal and tangential momentum balance are:

$$[\langle p\rangle_I + \rho\langle v''^2_l\rangle_I + \rho\langle v_l\rangle_I^2]_{NT} = [\langle p\rangle_I + \rho\langle v''^2_l\rangle_I + \rho\langle v_l\rangle_I^2]_T, \tag{4.23}$$

$$[\rho\langle v_l\rangle_I\langle u_l\rangle_I + \rho\langle u''v''\rangle_I]_{NT} = \rho[\langle v_l\rangle_I\langle u_l\rangle_I + \rho\langle u''v''\rangle_I]_T. \tag{4.24}$$

The error for the balance of normal and tangential momentum equations (now denoted by the superscript F for "full terms") then follows;

$$B^F_{nm} = \frac{[\langle p\rangle_I + \rho\langle v''^2_l\rangle_I + \rho\langle v_l\rangle_I^2]_{NT}}{[\langle p\rangle_I + \rho\langle v''^2_l\rangle_I + \rho\langle v_l\rangle_I^2]_T} = 1.11, \tag{4.25}$$

$$B^F_{tm} = \frac{\rho[\langle v_l\rangle_I\langle u_l\rangle_I]_{NT} - \rho[\langle v_l\rangle_I\langle u_l\rangle_I]_T}{\rho[\langle u''v''\rangle_I]_T - \rho[\langle u''v''\rangle_I]_{NT}} = -3.08. \tag{4.26}$$

The error related to the tangential momentum balance B^F_{tm} is written in a form that shows the difference of the tangential momentum flux due to $\langle v_l\rangle_I$ velocity at the T and NT boundaries and the jump of the $\langle u''v''\rangle_I$ term between these two boundaries.

Equations 4.25 and 4.26 include the neglected terms in Reynolds (1972) which are observed to be significant from the current investigation. The value of $B^F_{nm} = 1.11$ (eq. 4.25) is an improvement over the value $B^R_{nm} = 1.40$ in eq. 4.21. On the contrary, the imbalance for the tangential momentum is increased when the omitted terms are included.

Another measure for the balance of the tangential momentum (eq. 4.24) would be to write the ratio of the fluxes on the top and bottom boundaries;

$$B^F_{tm,2} = \frac{[\rho\langle v_l\rangle_I\langle u_l\rangle_I + \rho\langle u''v''\rangle_I]_{NT}}{[\rho\langle v_l\rangle_I\langle u_l\rangle_I + \rho\langle u''v''\rangle_I]_T} = 0.127. \tag{4.27}$$

Written in this form, the error for the tangential momentum balance shows that in both forms i.e., 4.26 and 4.27, there exists an important imbalance in the tangential momentum balance for the CV defined.

In conclusion, the approach in the study of Reynolds (1972), placing a very thin CV on the interface has a few important shortcomings;

- The most important one is that the jump of ω^2 occurs with a certain thickness and there is significant tangential velocity at the interface location which leads to considerable outflow of mass/momentum from the side boundaries of the CV, which are neglected in

the analysis of Reynolds (1972) as the interface is considered to be much sharper and the CV containing the interface thus has negligible thickness in the interface normal direction.

- Secondly, the $\langle v_l \rangle_I$ is shown to vary significantly across the interface looking at the profiles shown in figure 4.4a. The significant change of $\langle v_l \rangle_I$ across the TNTI also relates to the previous point made, highlighting the importance of the outflux from the side boundaries of the CV.

The stretching motion in the tangential direction of the interface which is responsible for the significant outflux in the side boundaries is shown in detail with the TNTI-average 3D local fields in section 4.7.

As the main imbalance is due to this feature of the TNTI local velocity field, the inclusion of the omitted terms for the top and bottom boundaries of the CV is not enough to account for the imbalance even though it improves the situation for the momentum balance in the normal direction (see B^R_{nm} and B^F_{nm} given by the eqs. 4.21 and 4.25).

We close this subsection with a relation given by Reynolds (1972) for the jump of vorticity at the interface location, which he obtained by integration of the vorticity equation across the interface. With the use of eq. 4.17 and with the assumption of homogeneity in the plane of the interface, the vorticity jump condition at the interface is written as (Reynolds, 1972),

$$\left[\langle v_l \rangle_I \langle \omega^l_z \rangle_I + \frac{\partial}{\partial y_I} \langle u'' v'' \rangle_I \right]_T = 0, \tag{4.28}$$

which suggests a relationship between the vorticity jump across the interface and the jump of the cross-stress term. Looking at figure 4.4b, it has been observed already that the TNTI is associated with high gradients of $\langle u'' v'' \rangle_I$. This observation indeed supports the point made by Reynolds (1972).

Similar to the previous checks for the balances of mass and momentum i.e. 4.20, 4.21 and 4.22, the relation 4.28 can be checked by looking at

$$B^R_\omega = \frac{\langle v_l \rangle_I \langle \omega^l_z \rangle_I}{-\frac{\partial}{\partial y_I} \langle u'' v'' \rangle_I}. \tag{4.29}$$

Eq. 4.29 includes a derivative along the y_I direction and should be evaluated at a given value of y_I including $\langle v_l \rangle_I$. On the other hand, the value of this derivative is very low at the exact location of the peak of $|\omega^l_z|$ (see figure 4.9), and thus the relation does not hold. In order to see where the relation 4.28 for the jump of vorticity holds, B^R_ω is evaluated at different y_I locations. Figure 4.10 shows B^R_ω at various y_I locations given together with the profile

of $\langle u''v''\rangle_I$. The vertical blue dashed line marks the y_I location where the $d\langle u''v''\rangle_I/dy_I$ is maximum.

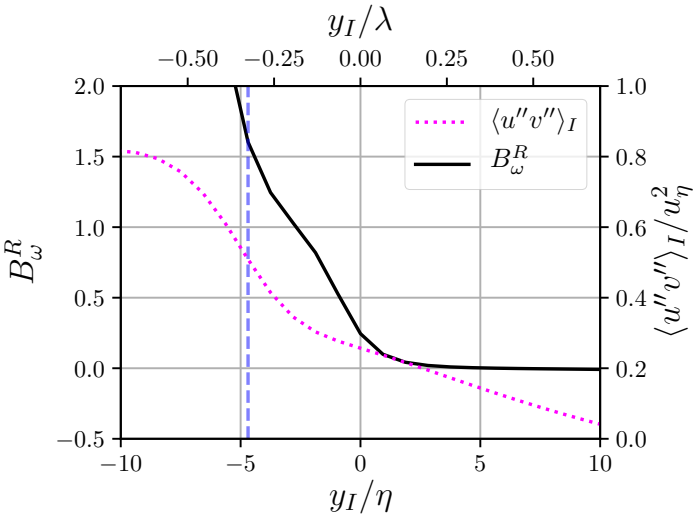

Fig. 4.10 B^R_ω (eq. 4.29) evaluated at various y_I locations along the direction normal to the interface. Dashed blue line marks where the $d\langle u''v''\rangle_I/dy_I$ is maximum.

At the point of maximum $d\langle u''v''\rangle_I/dy_I$, $B^R_\omega = 1.6$. B^R_ω is found to be unity, exactly at $y_I/\eta = -2.5$. Actually, the jump in the profile of $\langle u''v''\rangle_I$ appears to be occurring over a much shorter distance compared to the jump of $\langle \omega_z\rangle_I$.

4.6 Orientation of the TNTI

The analysis of the local flow field near the interface yields important insights into the properties of the TNTI, its persistence, and the propagation of the turbulent boundary into the non-turbulent region. In section 4.3, the properties of the TNTI-averaging operation of the local fields in the reference frame of the TNTI have been presented. Figure 4.7 demonstrated that the correlation between $\boldsymbol{u}''$ and $\boldsymbol{e}''$ over the TNTI-average significantly influences the local mean field of $\langle \boldsymbol{u}\rangle_I$. It is thus useful to analyze the properties of the interface in terms of its facing directions, symmetries, or asymmetries in certain directions for the interpretation of the TNTI-averaged fields/profiles of the flow field quantities. Analyzing the TNTI geometry also aids in gaining a better understanding of the overall structure of the interface in a temporally developing planar jet.

One informative result concerning the orientation and general shape of the TNTI is the orientation of the face normal vector $\boldsymbol{e}_y$ with respect to the unit vectors of the global coordinate system. The PDFs of $\boldsymbol{e}_y \cdot \boldsymbol{i}$, $\boldsymbol{e}_y \cdot \boldsymbol{j}$ and $\boldsymbol{e}_y \cdot \boldsymbol{k}$ are given in figure 4.11. This figure

presents the distribution of the orientation of the face normal vector along the entire IES of $\omega_{th}^2/\omega_{ref}^2 = 10^{-3}$, without applying the *no multi-cross* condition.

The projections of $\langle e_y \rangle_I$ on the cross-stream axis for the upper/lower interfaces are symmetric with respect to the centre-plane of the jet, as can be seen in figure 4.11 from the two, nearly identical peaks, at $\boldsymbol{e}_y \cdot \boldsymbol{j} \approx \pm 0.75$. The value at which the peaks are located shows that the most probable angle between the vector $\boldsymbol{e}_y$ and the global cross-stream direction, $\boldsymbol{j}$ is 40 degrees.

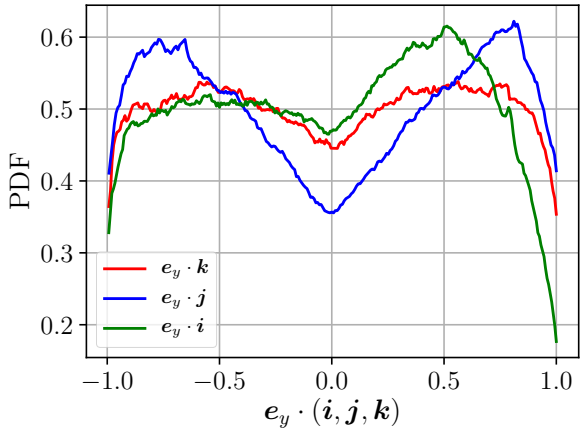

Fig. 4.11 PDF of the scalar product of the local y-axis unit vector $\boldsymbol{e}_y$ with the global unit vectors $\boldsymbol{i}$, $\boldsymbol{j}$ and $\boldsymbol{k}$ for the IES of $\omega_{th}^2/\omega_{ref}^2 = 10^{-3}$ at $t/T_{ref} = 50$. Results for the full IES, i.e. *no multi-cross* condition is not applied.

The distribution of $\boldsymbol{e}_y \cdot \boldsymbol{i}$ is observed to be asymmetric with respect to zero, which is not surprising due to the existence of a mean streamwise velocity profile. The peak at $\boldsymbol{e}_y \cdot \boldsymbol{i} = 0.5$ implies that the TNTI surface regions, facing towards the downstream direction, are mostly oriented at an angle of approximately 60° with respect to the streamwise direction. Conversely, TNTI surfaces facing upstream do not exhibit a dominant angle; the angle between $\boldsymbol{e}_y$ and $\boldsymbol{i}$ is more evenly distributed. This implies that the upstream-facing surfaces resemble a half-sphere or dome shape, with the top facing upstream direction, whereas the downstream-facing surfaces exhibit a more pronounced inclination. This observation is supported by the fact that the probability of finding surfaces with $\boldsymbol{e}_y \cdot \boldsymbol{i} = -1$ is significantly higher than surfaces where $\boldsymbol{e}_y \cdot \boldsymbol{i} = 1$. The dome-like surfaces in the upstream-facing parts of the interface are facing directly towards the $-\boldsymbol{i}$ direction, while the downstream-facing faces exhibit an inclination that results in a lower proportion of the surface pointing directly downstream.

It should also be noted that the orientation of the face-normal vector $\boldsymbol{e}_y$ does not show any preference in the global spanwise direction, which is attested by the PDF of the $\boldsymbol{e}_y \cdot \boldsymbol{k}$ being symmetric with respect to $\boldsymbol{e}_y \cdot \boldsymbol{k} = 0$ line.

For the sake of completeness, the PDFs related to the orientation of the unit vectors of the local coordinate system, which lie in the tangential plane of the IES are given in figure 4.12. As described in section 4.2, $\boldsymbol{e}_x$ is positioned to maximize its projection onto the global streamwise direction, resulting in $\boldsymbol{e}_x \cdot \boldsymbol{i}$ always being positive. Consequently, the local spanwise direction mostly aligns with the global spanwise direction i.e. the peaks at $\boldsymbol{e}_z \cdot \boldsymbol{k} \pm 1$. The reason for two peaks appearing in the PDF of $\boldsymbol{e}_z \cdot \boldsymbol{k}$ is due to the $\boldsymbol{e}_y$ being in inverse directions for the surfaces of upper and lower TNTI.

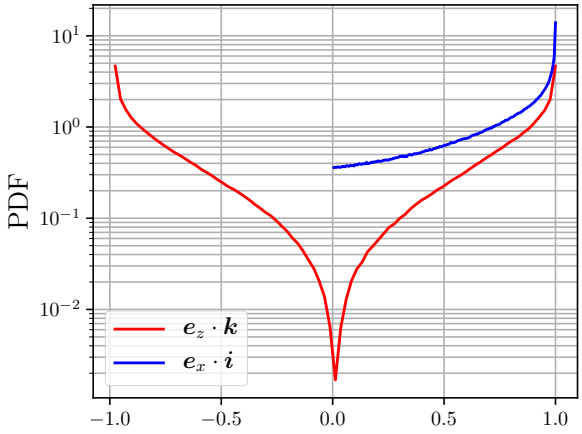

Fig. 4.12 PDF of the scalar product of the local y-axis unit vector $\boldsymbol{e}_y$ with the global unit vectors $\boldsymbol{i}$, $\boldsymbol{j}$ and $\boldsymbol{k}$ for the case where the *no multi-cross* condition is applied.

In figure 4.13 the orientation of the local face-normal vector $\boldsymbol{e}_y$ is shown when the *no multi-cross* condition is applied. The expected effect of applying the *no multi-cross* condition is that the probability of having $\boldsymbol{e}_y$ aligned with $\boldsymbol{j}$ is increased (comparison of the PDF of $\boldsymbol{e}_y \cdot \boldsymbol{j}$ in figures 4.11 and 4.13). This can be explained by the fact that the TNTI normal axis has less chance of crossing the turbulent region several times when it is oriented in the cross-stream direction. Conversely, the TNTI locations where $\boldsymbol{e}_y$ makes a high angle with the cross-stream direction $|\boldsymbol{e}_y \cdot \boldsymbol{j}| < 0.5$ reduces with the application of *no multi-cross* condition. At these locations, the TNTI normal axis is closer to the tangential plane, thus multi-crossing occurs more frequently.

Another significant difference between figures 4.11 and 4.13 is due to the asymmetry of the TNTI shape in the streamwise direction. The upstream-facing regions have more instances facing towards the centre-plane or the upstream direction i.e., $\boldsymbol{e}_y \cdot \boldsymbol{i} \approx -1$ compared to the faces oriented towards the downstream direction. Due to the change in the total number of points, the magnitude of the positive peak of the curve $\boldsymbol{e}_y \cdot \boldsymbol{i}$ increases but it can be said that the shape of the PDF does not vary significantly as the location of the peak remains at $\boldsymbol{e}_y \cdot \boldsymbol{i} \approx 0.5$.

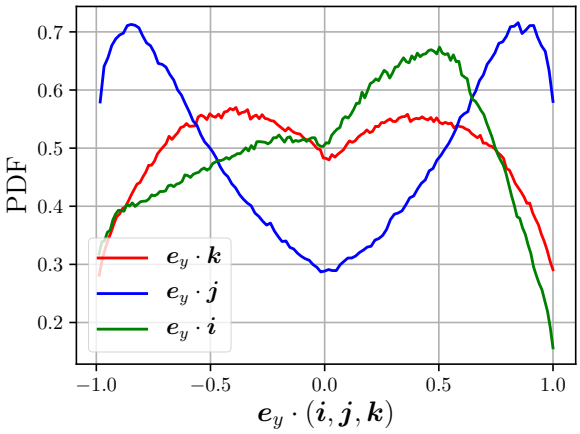

Fig. 4.13 PDF of the scalar product of the local y-axis unit vector e_y with the global unit vectors i, j and k for the case where the *no multi-cross* condition is applied.

The change in the PDF of $e_y \cdot k$ is not as dramatic as the other ones when the figures 4.11 and 4.13 are considered. The faces contributing the extremities of the PDF, i.e. $|e_y \cdot k| > 0.5$, are those facing close to the tangential plane of the TNTI in the spanwise direction, making them likely to cross the TNTI multiple times.

As a result, the PDFs of the scalar product of the unit vectors of the local and global coordinate systems and their variation with and without the application of the *no multi-cross* condition, provide valuable information about the geometry of the TNTI surface. Documentation of the PDFs reported in figure 4.13 is important as they show the orientation of e_y for the regions of the IES used to compute the TNTI-averaged local flow statistics.

4.7 TNTI-averaged 3D fields of velocity, vorticity, pressure and enstrophy

In this section, the 3D TNTI-averaged local fields of flow variables are presented. As a reminder, the local coordinate system is placed on a specified IES where the exact location of the surface corresponds to the point $(x_I, y_I, z_I) = (0,0,0)$ in the local 3D grid. Again, the *no multi-cross* condition is checked along the normal axis y_I on both sides of the interface. Considering an individual TNTI location X_0, the checks related to the *no multi-cross* condition are made only along the axis normal to the IES. Thus, on the tangential plane, as one moves further away from the point $(x_I, y_I, z_I) = (0,0,0)$, it cannot be strictly determined if a particular point (x_I, y_I, z_I) is in the turbulent or non-turbulent region. The turbulent/non-turbulent state of any point (x_I, y_I, z_I) depends on the local shape of the IES e.g. if the surface is concave in each tangential direction, the tangential plane will entirely be in the

non-turbulent region. This reminder is provided mainly to point out the possible difference between the tangential plane $x_I - z_I$ and the exact IES. Keeping this in mind, the TNTI-averaged 3D local fields of flow variables are investigated in order to gain insight into the local fields that influence the interface.

4.7.1 TNTI-averaged velocity field and the contributions from the planar mean U and fluctuation u'

Figure 4.14a shows the cut-sections of the TNTI-averaged 3D velocity field in the local reference frame $\langle \boldsymbol{u} \rangle_I(x_I, y_I, z_I)$, near the interface. Figure 4.14a is obtained by applying the TNTI-averaging process on the full velocity field $\boldsymbol{u}$, while figure 4.14b and 4.14c are obtained by the application of the same operation on the fluctuating and mean velocity fields obtained by the $x-z$ averaging i.e., $\boldsymbol{u'}$ and $\boldsymbol{U}$ respectively.

Looking at Figure 4.14a, the first observation is the symmetry of the field with respect to the $z_I = 0$ plane, which is evident in the $x_I - z_I$ and $z_I - y_I$ cut-sections. In both planes, the local mean spanwise velocity $\langle w_l \rangle_I$ changes sign at $z_I = 0$, indicating a stretching motion at the TNTI point $\boldsymbol{X_0}$ along the z_I axis. Additionally, when considering the $x_I - z_I$ cut-section, it becomes evident that the stretching motion is not confined solely to the z_I axis but is also present along the local streamwise axis x_I. Along the x_I axis, the velocity component $\langle u_l \rangle_I$ increases in the positive x_I direction, despite not changing sign as the $\langle w_l \rangle_I$ along the z_I axis does. Consequently, the velocity field experiences stretching in the local streamwise direction due to $d\langle u_l \rangle_I / dx_I > 0$.

As has been discussed in section 4.5, the primary reason for the imbalance in the continuity relation proposed by Reynolds (1972), in eq. 4.17, is observed to be a substantial outflow of mass from the neglected sides of the CV. This outflow is associated with the TNTI-average stretching motion observed along the tangential plane of the TNTI in figure 4.14. Consequently, improving the mass/momentum balance for the CV defined in section 4.5 becomes problematic without taking into account these neglected boundaries. Improving the precision of the fluxes on the T and NT faces by the consideration of the neglected terms in the equations i.e., eqs. 4.23 and 4.24 only increases the imbalance, as the boundary normal velocities $\langle v_l \rangle_I$ on both faces are directed inward into the CV.

When examining the $\langle v_l \rangle_I$ component of the local velocity in the $x_I - y_I$ and $z_I - y_I$ cut-sections (figures 4.14a, 4.14b, and 4.14c), the same observation that can be made for the normal profile of $\langle v_l \rangle_I$ in figure 4.4a holds true for the local 3D velocity field: along the y_I axis, there is a consistent $d\langle v_l \rangle_I / dy_I < 0$ for the entire tangential plane. This compressive

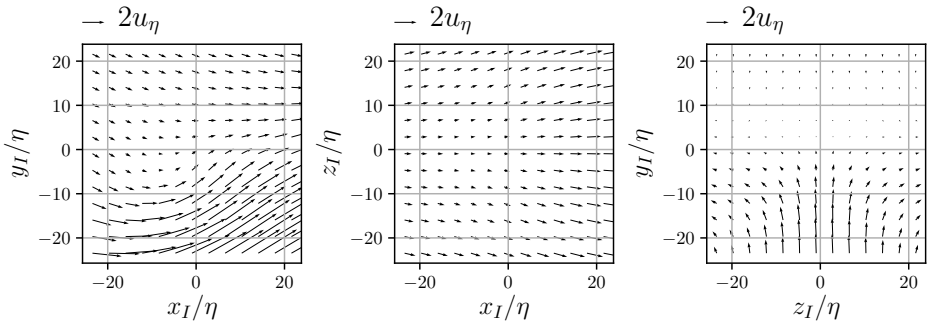

(a) TNTI-averaged local velocity field; $\langle \boldsymbol{u} \rangle_I$ (Term on the LHS of the eqs. 4.11)

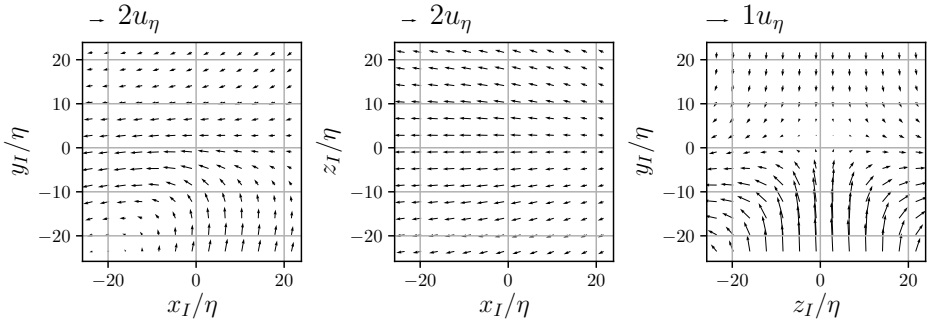

(b) TNTI-averaged local fluctuating velocity field with respect to $x-z$ average; $\langle \boldsymbol{u}' \rangle_I$ (Second term on the RHS of the eqs. 4.11)

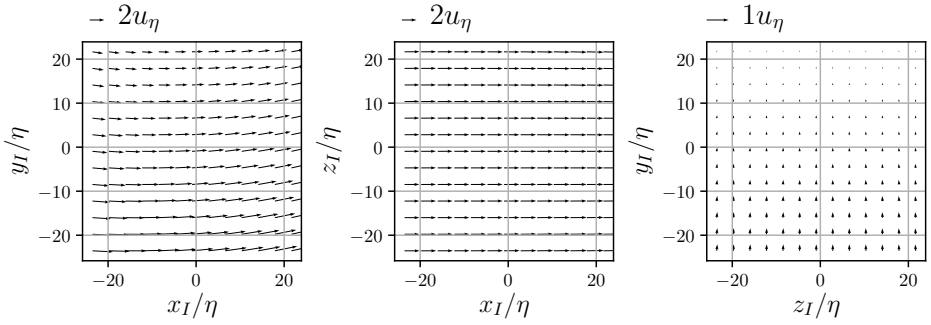

(c) TNTI-averaged mean velocity field with respect to $x-z$ averaging; $\langle \boldsymbol{U} \rangle_I$ (First term on the RHS of the eqs. 4.11)

Fig. 4.14 TNTI-averaged fields $\langle \boldsymbol{u} \rangle_I$, $\langle \boldsymbol{U} \rangle_I$ and the $\langle \boldsymbol{u}' \rangle_I$. The velocity scale is given in the top left corner of each figure. The position of the IES is at $\boldsymbol{X}_0 = (0,0,0)$. Results are obtained from PJ4-HR data and for the IES of $\omega_{th}^2/\omega_{ref}^2 = 10^{-3}$ at $t/T_{ref} = 50$.

motion in the interface normal direction has a direct connection with the stretching motion in the tangential plane, mentioned in the previous paragraph.

Looking at the middle cut-sections ($x_I - z_I$ plane) of figures 4.14a, 4.14b, and 4.14c, it can be seen that even though the direction of $\langle u_l \rangle_I$ is determined by $\langle \boldsymbol{U} \rangle_I$, its gradient along

x_I is influenced by the contribution of the $\langle \boldsymbol{u}' \rangle_I$ field, where $d\langle u_l \rangle_I / dx_I > 0$ is present along the local streamwise axis. This suggests that the TNTI-average rotating motion observed in the $x_I - y_I$ cut-section in figure 4.14b on the turbulent side of the interface induces a positive gradient of $\langle u_l \rangle_I$ along x_I. Consequently, this leads to $d\langle v_l \rangle_I / dy_I < 0$ on the plane $y_I = 0$ due to the conservation of mass in the local frame of the TNTI. This observation is important as it sheds light on the existence of a TNTI-averaged interface normal velocity $\langle v_l \rangle_I$, even though it is known that the $x-z$ averaged V velocity is zero for the temporally developing turbulent jet at each y-location.

In figure 4.14c, a negative gradient $d\langle U_l \rangle_I / dy_I$ is observed in the local mean stream-wise velocity, particularly in the leftmost cut-section of figure 4.14c. The $\langle U_l \rangle_I$ values are slightly higher on the turbulent side of the interface. However, it is notable that the gradient $d\langle u_l \rangle_I / dy_I$ observed in the cut-section of $x_I - y_I$ in figure 4.14a is primarily influenced by the contribution of the $\langle \boldsymbol{u}' \rangle_I$ field presented in figure 4.14b.

Figure 4.15 provides a clearer view of the contributions of $\langle \boldsymbol{u}' \rangle_I$ and $\langle \boldsymbol{U} \rangle_I$ to $\langle \boldsymbol{u} \rangle_I$ through TNTI-averaged 1D profiles normal to the IES (see eq. 4.11). As previously mentioned, the contribution of the $\langle u_l' \rangle_I$ term to $\langle u_l \rangle_I$ is significant, resulting in a jump in $\langle u_l \rangle_I$ in the y_I direction. Additionally, $\langle U_l \rangle_I$ contributes to this jump due to its negative gradient across y_I. A similar pattern is observed for the interface normal component, where the most substantial contribution comes from $\langle v_l' \rangle_I$, while the contribution of $\langle V_l \rangle_I$ remains marginal.

The local mean stream-wise velocity fluctuation $\langle u_l' \rangle_I$ predominantly exhibits negative values in the $x_I - y_I$ plane in figure 4.14b. Its most significant negative contribution to $\langle u_l \rangle_I$ occurs near the location of the IES, which is easier to see in figure 4.15b as a negative peak of the $\langle u_l' \rangle_I$ along the normal axis y_I. Furthermore, in figure 4.14b, it can be observed that this negative contribution to the $\langle u_l \rangle_I$ near the IES location is due to a rotating motion present in the turbulent side of the cut-section ($y_I < 0$) of the $\langle \boldsymbol{u}' \rangle_I$ field. This motion appears to have a rotation axis in the z_l direction and rotates in the counter-clockwise direction.

It is possible that this mean behaviour is related to the vortical structures reported near the interface by various studies in the literature (da Silva and dos Reis, 2011; da Silva et al., 2011; da Silva and Taveira, 2010). The presence of a spanwise roller in the vicinity of the TNTI is also compatible with the picture given in Cimarelli et al. (2022) describing the structure of turbulence in temporally developing planar jets. The centre of the mean rotating motion is observed to be at $y_I/\eta \approx -20$, $x_I/\eta \approx -20$ (see figure 4.14b) while the total size of this motion is not covered by the employed local averaging window. Thus it is analyzed further down in this section by using results from the TNTI-averaging operation conducted with a wider local grid.

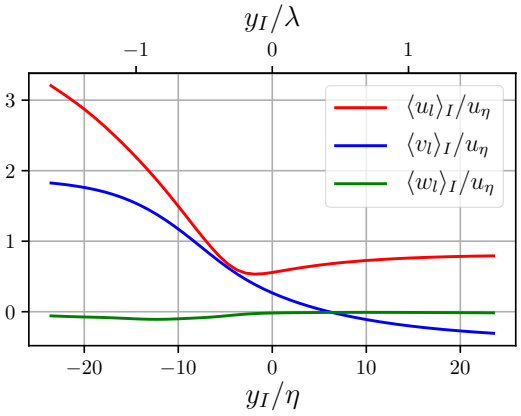

(a) TNTI-averaged profile of $\langle \boldsymbol{u} \rangle_I$

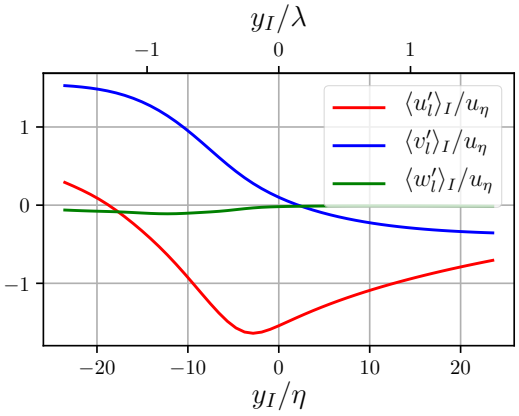

(b) TNTI-averaged profile of $\langle \boldsymbol{u}' \rangle_I$.

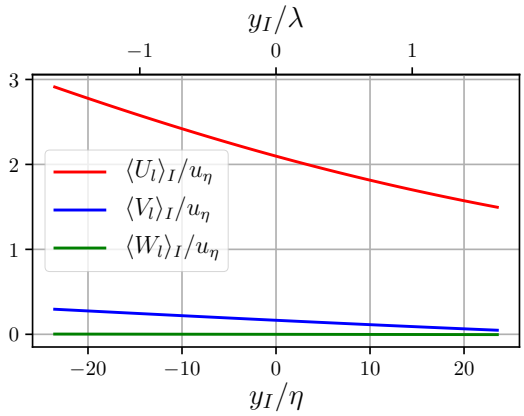

(c) TNTI-averaged profile of $\langle \boldsymbol{U} \rangle_I$.

Fig. 4.15 TNTI-averaged profiles of $\boldsymbol{u}$, $\boldsymbol{u}'$ and $\boldsymbol{U}$ obtained normal to the IES for PJ4-HR data and for the IES of $\omega_{th}^2/\omega_{ref}^2 = 10^{-3}$ at $t/T_{ref} = 50$.

The average stretching motion observed in the $x_I - z_I$ plane for $\langle \boldsymbol{u} \rangle_I$ in figure 4.14a can also be spotted in the field of $\langle \boldsymbol{u}' \rangle_I$. This observation highlights that the stretching in the z_I direction primarily arises from the contribution of the fluctuating field $\langle \boldsymbol{u}' \rangle_I$, with no significant contribution from $\langle U \rangle_I$ to the $\langle w_l \rangle_I$ component of $\langle \boldsymbol{u} \rangle_I$ (see figure 4.14c). Likewise, the compression event in the interface normal direction is predominantly a result of the fluctuating component of the velocity, although it can be qualitatively noted that there is a slight compression in the TNTI normal direction due to the influence of the $\langle \boldsymbol{U} \rangle_I$ field (see figure 4.14c, $z_I - y_I$ plane). However, the magnitudes are very small compared to the other components of $\langle \boldsymbol{U} \rangle_I$.

It is noteworthy that, although quite small in magnitude, there exists a positive $\langle v_l \rangle_I$ field in the $z_I - y_I$ plane as shown in figure 4.14c. This phenomenon can be attributed to the asymmetry in the PDF of the projection of interface-facing direction on the streamwise

direction (see figure 4.11). Specifically, there are more regions of the interface facing downstream than facing upstream. This preferred downstream orientation results in the relatively small positive values of $\langle v_l \rangle_I$ in the $z_I - y_I$ plane shown in figure 4.14c. This behaviour can be understood by examining the distribution of the most probable orientation angle for the downstream-facing regions, which is approximately $\pm 60^\circ$ between the face-normal vector $\boldsymbol{e}_y$ and the streamwise direction vector $\boldsymbol{i}$ for the upper and lower TNTI, respectively.

Consider a location on the interface where the face normal vector $\boldsymbol{e}_y$ makes a 60° angle with $\boldsymbol{i}$. In this case, the mean streamwise velocity U contributes primarily to the local component u_l and less to the v_l component, resulting in values of $U\cos(\pi/6)$ and $U\sin(\pi/6)$, respectively. The contribution of u_l becomes even more significant for cases where $\boldsymbol{e}_y$ is more perpendicular to the streamwise direction $\boldsymbol{i}$. Consequently, the effect of $\boldsymbol{U}$ is more pronounced in the $x_I - y_I$ plane in figure 4.14c compared to the $z_I - y_I$ plane. The gradient of the TNTI-average velocities in the y_I direction is influenced by the global streamwise velocity gradient dU/dy because the y_I axis aligns with the $\pm y$-directions in the upper and lower TNTI, respectively.

To confirm that the feature observed in the $x_I - y_I$ cut-section of figure 4.14b is indeed a rotating motion aligned in the local spanwise direction, the TNTI-average velocity field is obtained for a wider field of view, shown in figure 4.16. By calculating the local spanwise vorticity in this TNTI-averaged velocity field, it was observed that the radius of this vortical motion is approximately 1.5λ (21η). This radius is similar to the radius of the large-scale vortical structures (LVS) reported in the study conducted by da Silva and Taveira (2010) which is of the order of λ.

The diameter of the rotating motion is comparable to the jet half-width δ for the present simulations (0.46δ). It can be noted that the Reynolds number of the present dataset is limited due to the constraints on the resolution mentioned in chapter 2. Simulations with higher Reynolds numbers can give a more definitive conclusion for the size of the mean rotating motion observed in the TNTI-averaged velocity fields with a larger separation between the length scales λ and δ.

4.7.2 TNTI-averaged fields of enstrophy and pressure

The TNTI-averaged local enstrophy field is shown in figure 4.17. A detail linking this figure with figure 4.14a is that the location of the enstrophy peak in the $x_I - y_I$ plane is not directly aligned with the interface normal axis. Instead, it is positioned more towards the upstream direction in the local streamwise axis x_I. As a result, the field exhibits asymmetry with respect to $x_I = 0$ along the x_I axis. This observation underscores the presence of strong

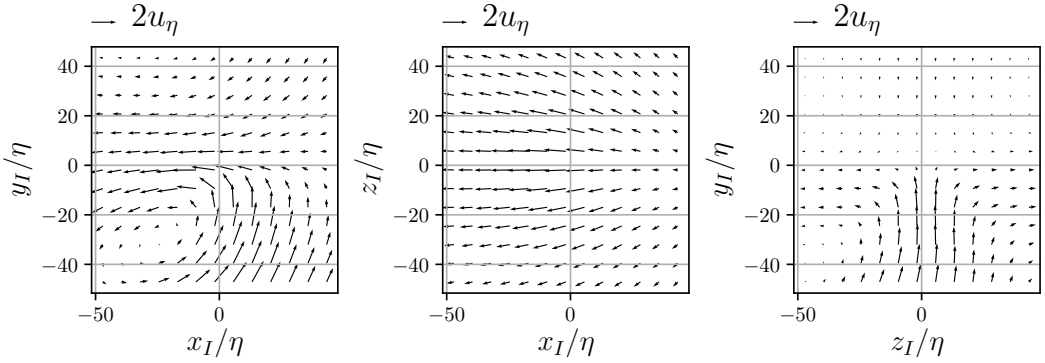

Fig. 4.16 TNTI-averaged field $\langle \boldsymbol{u}' \rangle_I$ near the IES with a wider local field of view. The velocity scale for each figure is given in the top left corner. The location of the IES is at $\boldsymbol{X}_0 = (0,0,0)$. Results obtained from PJ4-HR data and for the IES of $\omega^2_{th}/\omega^2_{ref} = 10^{-3}$ at $t/T_{ref} = 50$.

turbulent structures near the interface, primarily associated with spanwise vorticity, which significantly influences the characteristics of the TNTI. In figure 4.17, the outline of these structures in the $z_I - y_I$ plane can be seen, although the cut section does not pass through the centre of the vortex. It can be seen that the high enstrophy region extends more in the z_I direction compared to the local peak observed in the $x_I - y_I$ plane.

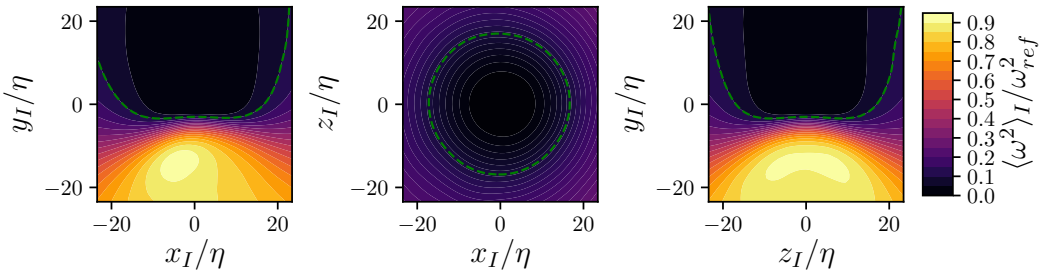

Fig. 4.17 TNTI-averaged local enstrophy field.

The corresponding locally averaged pressure field is given in figure 4.18a. Here the pressure field is given after subtracting the pressure at the TNTI location i.e. $\langle p \rangle_I - \langle p \rangle_I(\boldsymbol{X}_0)$. Notably, negative values of local pressure are noticeable in the turbulent side of the interface. This observation aligns with the predictions put forth by Reynolds (1972), with the simplified balance equations and by considering the significant disparity in local normal stresses between the turbulent and non-turbulent sides of the interface. As can be seen from eq. 4.18, the pressure difference is balanced by the difference in normal stresses across the interface (see figures 4.5a and 4.4b).

A slight asymmetry of TNTI-averaged pressure field is present in the $x_I - y_I$ plane. This asymmetry might be attributed to the presence of large vortical structures described by da Silva and Taveira (2010) which are associated with low-pressure iso-surfaces. It is possible that due to the asymmetric shape of the interface in the streamwise direction, these rollers might have been sampled in a way that the TNTI-average effect related to these vortical structures appears slightly towards the local upstream direction.

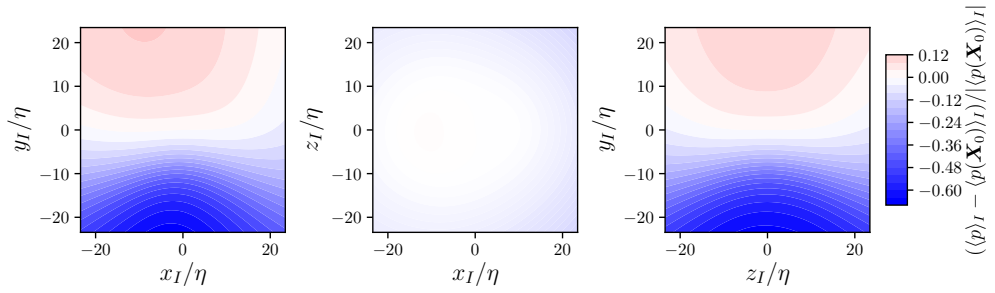

(a) TNTI-averaged local pressure field.

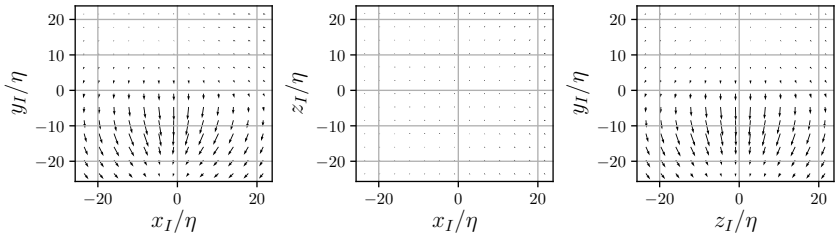

(b) Local field of $-\boldsymbol{\nabla}\langle p\rangle_I$ in the vicinity of the TNTI.

Fig. 4.18 (a) Local mean pressure field near the TNTI. The mean pressure at the interface $\langle p\rangle_I(\boldsymbol{X}_0)$ has been subtracted from the full field. (b) Local vector field of the negative mean pressure gradient near the interface $-\boldsymbol{\nabla}\langle p\rangle_I$.

Looking at the gradient of the TNTI-averaged pressure field, shown in figure 4.18b, it is observed that the pressure gradient tends to act in a manner that directs the flow towards the centre-plane of the jet in the vicinity of the interface. The vectors associated with $-\nabla\langle p\rangle_I$ also align with the IES normal vector i.e., $x_I/\eta = 0$, going inside the turbulent region. This alignment can be attributed to the predominant concave shape of the IES, and the average pressure gradient acting normal to the interface.

However, despite the pressure gradient tends to push the flow towards the centre-plane, the mean local velocity field in figure 4.14a reveals that the flow is moving towards the IES within the turbulent region. On the other hand, it has been observed from figure 4.4a that the interface normal component $\langle v_I\rangle_I$ decreases rapidly when going towards the non-turbulent side of the IES in the positive y_I direction.

4.8 Enstrophy transport equation and the sublayers of the TNTI

Another important analysis is the balance of enstrophy at the location of the TNTI as it has been used as the criterion for the detection of the turbulent jet and the TNTI in the present study, following numerous studies in the literature (Holzner and Lüthi, 2011; Krug et al., 2017; van Reeuwijk and Holzner, 2014).

The variation of the local geometrical features of the interface across its thickness has been investigated by the analysis of various IES inside the TNTI layer in chapter 3. Being the marker of the TNTI, the terms of the enstrophy balance equation at the TNTI bring insights into the local characteristics of the sublayers of the interface and also the expansion of the turbulent volume into the non-turbulent external flow. The balance equation for the enstrophy can be written as follows,

$$\frac{D\omega^2/2}{Dt} = \omega_i \omega_j S_{ij} + \nu \nabla^2 \left(\omega^2/2\right) - \nu \nabla \omega_i \cdot \nabla \omega_i. \tag{4.30}$$

The left-hand side is the material derivative of the enstrophy and the terms on the right-hand side of the equation are the production P_{ω^2}, viscous diffusion D_{ω^2} and the dissipation ε_{ω^2} of enstrophy respectively. Thus eq. 4.30 can also be written in the symbolic form:

$$\frac{D\omega^2/2}{Dt} = P_{\omega^2} + D_{\omega^2} - \varepsilon_{\omega^2}. \tag{4.31}$$

It has been documented in the literature that different terms in eq. 4.31 are dominant in the balance of ω^2 across the thickness of the TNTI. A separation of the TNTI into distinct sublayers has been proposed taking into account the varying picture of the balance of ω^2 along the interface normal axis (da Silva et al., 2014; Silva et al., 2018; Taveira and da Silva, 2014a). A fundamental point, as highlighted in the seminal work of Corrsin and Kistler (1955), is that an irrotational fluid packet can acquire vorticity solely through the action of viscosity. The outer region of TNTI is thus characterized by viscous diffusion being the principal term driving the transport of enstrophy towards the non-turbulent region and named as viscous superlayer (VSL) (Taveira and da Silva, 2014a). Characteristics of this layer are thus similar to the laminar superlayer described by (Corrsin and Kistler, 1955).

Going deeper into the turbulent side, the production term P_{ω^2} gradually increases, eventually reaching a point where it is as significant as the viscous diffusion term D_{ω^2}. The location where $P_{\omega^2} = D_{\omega^2}$ is being considered as the border of the VSL towards the turbulent side of the TNTI (Silva et al., 2018; Taveira and da Silva, 2014a; Watanabe et al., 2015). In this

region, while enstrophy levels remain notably lower than those within the turbulent core, the dominant mechanism in the balance of enstrophy changes from viscous diffusion to the production of enstrophy. This intermediate layer is referred to as the turbulent sublayer (TSL) and is suggested to extend up to the first peak of the TNTI-averaged profile $\langle\omega^2\rangle_I$ (Silva et al., 2018; Taveira and da Silva, 2014a; Watanabe et al., 2015).

A reminder can be made at this point about the $y_I = 0$ location used in this chapter. As has been explained in the introduction of this chapter, the TNTI-averaging operation is conducted over the IES of $\omega^2_{th}/\omega^2_{ref} = 10^{-3}$ due to the reasons discussed in section 4.1. Thus the location for the arbitrary outer boundary of the TNTI (the VSL is within that boundary) is taken to be $\omega^2_{th}/\omega^2_{ref} = 10^{-3}$ for the measurements given in this section. It is important to keep this in mind because, in this section, we determine the thickness of various sublayers within the TNTI, by using the TNTI-average profiles of the terms in eq. 4.30 for a specific IES. The average distance between IES $\omega^2_{th}/\omega^2_{ref} = 10^{-3}$ and $\omega^2_{th}/\omega^2_{ref} = 10^{-6}$ is approximately 2.85η if measured from the IES of $\omega^2_{th}/\omega^2_{ref} = 10^{-6}$. It should also be noted that, as has been shown in section 4.4, different choices of IES do not lead only to an offset of the same profile, but also the TNTI-average profiles of enstrophy and all the terms in eq. 4.30 changes slightly (see figure 4.2).

Figure 4.19 shows the TNTI-average profiles of the terms P_{ω^2}, D_{ω^2}, ε_{ω^2} and $\omega^2/2$ as functions of y_I. The $|\langle D(\omega^2/2)/Dt\rangle_I$ is computed by the sum of the terms on the right-hand side of the eq. 4.31 and plotted in figure 4.19 along with the other terms. The enstrophy threshold used for the detection of the IES, $\omega^2_{th}/\omega^2_{ref} = 10^{-3}$, corresponds to $y_I/\eta = 0$.

Going towards the turbulent side from the location of the IES, the viscous diffusion term D_{ω^2} is indeed the main source of increase of ω^2 in the external part of the TNTI layer. The dissipation term ε_{ω^2} is also active along with the D_{ω^2} which is responsible for the viscous destruction of enstrophy. Moving towards negative y_I values, the production of enstrophy P_{ω^2} starts to rise after $y_I/\eta \approx -2$ and cross D_{ω^2} near $y_I/\eta \approx -3.3$, where $P_{\omega^2} = D_{\omega^2}$ (marked by the dashed line in figure 4.19 which denotes the extent of the VSL in the direction of the turbulent core). Considering the arbitrary external boundary to be our choice of IES, the thickness of the VSL can be estimated as $\delta_\nu \approx 3.3\eta$.

Furthermore, in various studies in the literature, the total thickness of the TNTI is often measured by locating the first peak in the TNTI-averaged enstrophy profile (Silva et al., 2018; Taveira and da Silva, 2014a; Watanabe et al., 2015). This peak's position is denoted by the dash-dot vertical line in figure 4.19. According to this definition, the total TNTI thickness is measured to be $\delta_I \approx 16\eta$, with the thickness of the TSL being $\delta_{\omega^2} \approx 16\eta - 3.3\eta = 12.7\eta$. The production of enstrophy reaches its peak around $y_I/\eta \approx -10$. Simultaneously, the viscous diffusion term D_{ω^2} attains negative values, indicating that the enstrophy generated at

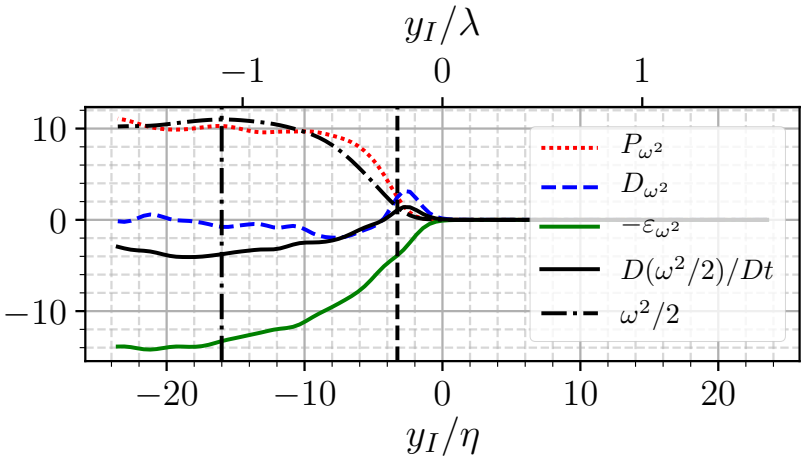

Fig. 4.19 TNTI-averaged profiles of the terms of the enstrophy transport equation, eq. 4.30, P^2_ω, D^2_ω, ε^2_ω and $\omega^2/2$ at the TNTI location. $D(\omega^2/2)/Dt$ profile is computed as the balance of the terms on the RHS of the eq. 4.30. The extent of VSL in the turbulent side is marked by (- - -) i.e. the location of $P_{\omega^2} = D_{\omega^2}$ and (-·-·) shows the extent of δ_I determined by the first peak of $\langle\omega^2\rangle_I$. Figure obtained for the IES of $\omega^2_{th}/\omega^2_{ref} = 10^{-3}$, obtained for PJ4-HR at $t/T_{ref} = 50$.

this location is being transported towards the non-turbulent region, where the contribution of D_{ω^2} is positive on average.

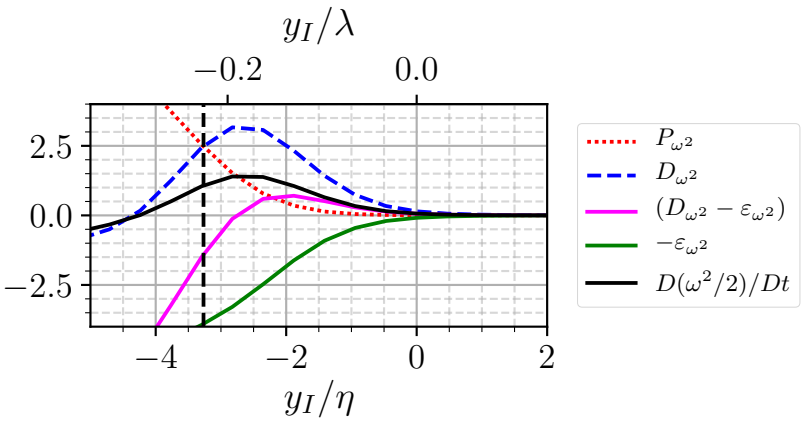

Fig. 4.20 TNTI-averaged profiles of P^2_ω, D^2_ω and ε^2_ω given along with the balance of $(D^2_\omega + \varepsilon^2_\omega)$ and the term $D(\omega^2/2)/Dt$ computed from the balance of the RHS of the eq.4.30. (- - -) marks the extent of VSL. Figure obtained for the IES of $\omega^2_{th}/\omega^2_{ref} = 10^{-3}$, obtained for PJ4-HR at $t/T_{ref} = 50$.

Figure 4.20 provides a closer look at the terms in eq. 4.31 in the vicinity of the VSL. It also illustrates the approximate balance between viscous diffusion D_{ω^2} and viscous dissipation ε_{ω^2} i.e., $(D_{\omega^2} - \varepsilon_{\omega^2})$ in the VSL. The significance of D_{ω^2} at the outer regions of the TNTI

is acknowledged in the literature due to its crucial role in the spread of enstrophy into the non-turbulent region (Bisset et al., 2002; Taveira and da Silva, 2014a; Watanabe et al., 2015). This term contains the effects of the viscous mechanism mentioned by Corrsin and Kistler (1955) for an irrotational fluid acquiring vorticity. Consequently, it is the primary contributor to the positive $D(\omega^2)/Dt$ observed at the outer edge of the TNTI.

An interesting observation from figure 4.20 is that $D(\omega^2)/Dt$ remains positive until $y_I/\eta \approx -4.2$ even though $(D_{\omega^2} - \varepsilon_{\omega^2})$ becomes negative at $y_I/\eta \approx -2.75$. For this range, the contribution of P_{ω^2} is crucial because $D(\omega^2/2)/Dt$ remains positive even after viscous dissipation of enstrophy ε_{ω^2} exceeds viscous diffusion D_{ω^2}. This highlights the significance of the rate with which P_{ω^2} diminishes along the y_I axis for the expansion of the turbulent volume and its extension into the non-turbulent external region.

4.9 Relative helicity at the TNTI

The crucial role of the viscous diffusion mechanism for the net increase of the enstrophy at the outer edge of the TNTI i.e., $D(\omega^2/2)/Dt > 0$ is observed in figure 4.19. In addition to that, a closer look into the balance of ω^2 at the VSL region in figure 4.20 highlights the important role of the production of enstrophy P_{ω^2} for the increase of ω^2 in a range of y_I location spanning over the boundary between TSL and VSL. As has been remarked at the end of the previous section, the variation of P_{ω^2} with y_I is observed to be important, where $D(\omega^2/2)/Dt$ is positive and the partial balance of $(D_{\omega^2} - \varepsilon_{\omega^2})$ is negative i.e., within the range $-4.2 < y_I/\eta < -2.75$.

The production term P_{ω^2}, is directly related to the non-linear term of the Navier-Stokes equation. Writing the non-linear term $\boldsymbol{u} \cdot \nabla \boldsymbol{u}$ in the momentum equation with the help of vorticity as $(\boldsymbol{\omega} \times \boldsymbol{u}) + \frac{1}{2}\nabla|\boldsymbol{u}|^2$, the first term, namely the Lamb vector, is responsible for the non-linearity of the equation. In the regions without non-linearity, i.e. $\boldsymbol{\omega} \times \boldsymbol{u} = 0$, the production of enstrophy P_{ω^2} is zero. Rather than looking at the Lamb vector, it is more practical to analyze the scalar field of relative helicity (Alves Portela et al., 2018),

$$\hat{h} = \frac{(\boldsymbol{u} \cdot \boldsymbol{\omega})}{|\boldsymbol{u}||\boldsymbol{\omega}|} \tag{4.32}$$

to characterize the alignment of the velocity and vorticity vectors, for the investigation of the non-linearity. Another reason for looking at $\hat{h}$ is that it separates the effect of the change of the magnitudes of the constituting vectors with the effect of their respective orientations. The Lamb vector will, of course, decrease together with P_{ω^2} due to the decay of $|\omega|$ with

increasing y_I towards the non-turbulent region, but a variation of the alignment of the vectors $\boldsymbol{u}$ and $\boldsymbol{\omega}$, might also have an effect on the rate of change of the non-linearity.

Considering the value of $\hat{h}$ for any given location in the flow field, it can be observed that when $\hat{h} = \pm 1$, the Lamb vector becomes zero, and on the contrary when $\hat{h} = 0$, non-linearity is maximal for a given vorticity magnitude ($\boldsymbol{u}$ and $\boldsymbol{\omega}$ are perpendicular to each other).

Figure 4.21 shows the TNTI-averaged profile of $\langle|\hat{h}|\rangle_I$ as a function of y_I/η for the IES of $\omega_{th}^2/\omega_{ref}^2 = 10^{-3}$.

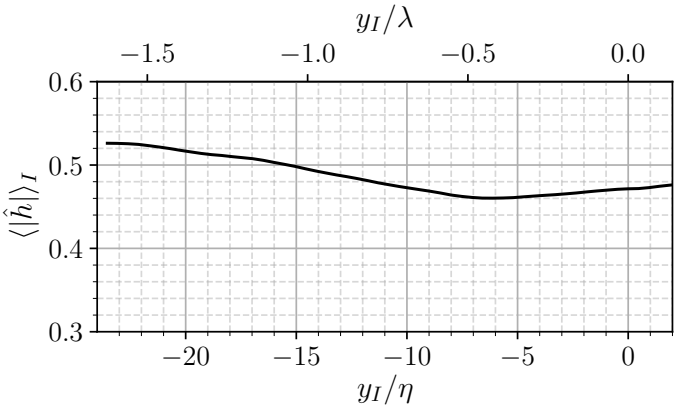

Fig. 4.21 Profile of $\langle|\hat{h}|\rangle_I$ averaged over the IES of $\omega_{th}^2/\omega_{ref}^2 = 10^{-3}$.

A slight drop of $\langle|\hat{h}|\rangle_I$ over the interface can be observed. The variation is maximum as we enter the TSL region and there is a negative peak at $y_I/\eta = -6.5$, indicating the $\boldsymbol{u}$ and $\boldsymbol{\omega}$ vectors become more orthogonal to each other.

Apart from the average profile of $\langle|\hat{h}|\rangle_I$, the PDF of $\hat{h}$ can also be investigated at each distance y_I from the detected IES as shown in figure 4.22. For the purpose of comparison, the PDF of $\hat{h}$ inside the entire volume of the turbulent jet is also given. The PDF of $\hat{h}$ for the whole turbulent region is obtained by considering all the points satisfying the condition of $\omega^2 > 10^{-3}\omega_{ref}^2$ and it is labelled $V(\omega^2 > 10^{-3}\omega_{ref}^2)$ in figure 4.22.

The shape of the PDF of $\hat{h}$ is fundamentally different in the TSL compared to the PDF obtained for the bulk of the turbulent volume. More specifically, this transition corresponds to the difference between the PDF curves of $y_I/\eta < -14.1$ and the rest of the PDF curves which are obtained at locations $y_I/\eta \geq -4.7$.

Within the bulk turbulent region i.e. $V(\omega^2 > 10^{-3}\omega_{ref}^2)$, the PDF of $\hat{h}$ displays two peaks at -1 and 1. The PDF obtained at the location of $y_I/\eta = -23.5$, which is situated inside the turbulent core region as indicated in figure 4.19, exhibits similar behaviour to the PDF obtained for the entire turbulent volume (the green line in figure 4.22).

As we move to the location $y_I/\eta = -14.1$ the peaks at ± 1 are reduced and the distribution of $\hat{h}$ looks flatter across a wider range. Additionally, the probability distribution shows an increase for values close to $\hat{h} = 0$, indicating a transient region. Moving further towards the non-turbulent region, a peak appears centred at $\hat{h} = 0$ and it is observed that the PDF remains similar afterwards.

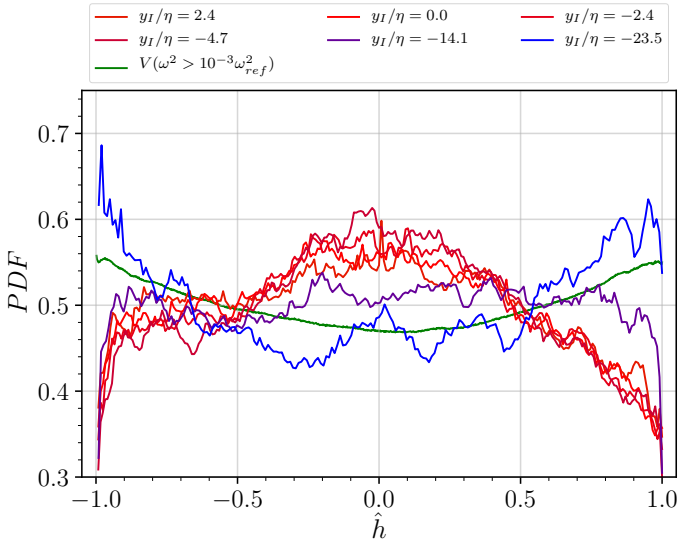

Fig. 4.22 PDF of $\hat{h}$, at various y_I locations with respect to the IES of $\omega^2_{th}/\omega^2_{ref} = 10^{-3}$.

In conclusion, this transition of the shape of the PDF suggests that going across the TNTI, the relative orientation of the vectors $\boldsymbol{u}$ and $\boldsymbol{\omega}$ is affected in a way that the non-linearity is maximized for a given $\boldsymbol{\omega}$ and $\boldsymbol{u}$ magnitudes (probability of $\hat{h}$ values close to zero gets higher) as we go across the interface. We know that ω^2 and P_{ω^2} values drop swiftly with increasing y_I (see figure 4.19), but the transition of the shape of the PDF in figure 4.22 suggests that the change of the alignment of $\boldsymbol{u}$ and $\boldsymbol{\omega}$ vectors has an effect which slows down the decay of P_{ω^2} along the y_I direction, even though the magnitudes of $\boldsymbol{u}$ and $\boldsymbol{\omega}$ are decreasing drastically across the TNTI.

Without this specific orientation of the vectors, and if the PDF remained the same as that obtained for the turbulent bulk, the decay of P_{ω^2} would be much steeper. The more orthogonal alignment of $\boldsymbol{u}$ and $\boldsymbol{\omega}$ contribute to keeping P_{ω^2} high enough for a net increase of ω^2 in spite of D_{ω^2} not being high enough to compensate ε_{ω^2} in the region $y_I/\eta = -4.2$ to $y_I/\eta = -2.7$ (see end of section 4.8 and figure 4.20).

4.10 Definition of local propagation velocity v_n^l

In chapter 3, a relationship for the mean propagation velocity v_n is derived, based on the equilibrium between the increase of the turbulent volume, dV_J/dt, and the product of the interface area, S, and mean propagation velocity v_n, which is given in equation 3.21. The variation of v_n, across the thickness of the TNTI layer has been examined. In this section, the local definition of the propagation velocity is introduced, which is denoted as v_n^l, which is related to the mean propagation velocity v_n (Jahanbakhshi and Madnia, 2018; van Reeuwijk and Holzner, 2014).

By defining the turbulent volume V_J using the condition $\omega^2 > \omega_{th}^2$, and taking the bounding surfaces as the IES of ω_{th}^2, a relation was obtained by Holzner and Lüthi (2011), for the local propagation velocity of IES elements in the interface normal direction. This relation was later used in other studies for the analysis of the propagation of the interface (van Reeuwijk and Holzner, 2014; Wolf et al., 2013a) into the non-turbulent region.

For the sake of completeness, the derivation of the local propagation velocity is given here following the studies Holzner and Lüthi (2011) and van Reeuwijk and Holzner (2014). We start by writing the total rate of change of the enstrophy, in the reference frame of the moving enstrophy iso-surface. D^s/Dt^s being the total derivative operation following the iso-enstrophy surface element, the total rate of change of enstrophy can be written as

$$\frac{D^s\omega^2}{D^st} = \frac{\partial\omega^2}{\partial t} + \boldsymbol{u}^{tot}\cdot\boldsymbol{\nabla}\omega^2 = 0, \tag{4.33}$$

where the velocity of the iso-surface element, $\boldsymbol{u}^{tot}$ can be written as the sum of fluid velocity $\boldsymbol{u}$ and the velocity of the IES element relative to the fluid $\boldsymbol{v}_{\omega^2}$ as $\boldsymbol{u}^{tot} = \boldsymbol{u} + \boldsymbol{v}_{\omega^2}$. The total derivative is equal to zero as it is the total rate of change of enstrophy written in the reference frame moving with the IES element. Substituting the decomposition given for the $\boldsymbol{u}^{tot}$, eq. 4.33 can be re-written as;

$$\frac{D^s\omega^2}{D^st} = \frac{D\omega^2}{Dt} + \boldsymbol{v}_{\omega^2}\cdot\boldsymbol{\nabla}\omega^2 = 0. \tag{4.34}$$

Here, D/Dt denotes the material derivative following the fluid element. The local normal propagation velocity of the IES element is,

$$v_n^l = \boldsymbol{v}_{\omega^2}\cdot\boldsymbol{n} \tag{4.35}$$

where $\boldsymbol{n} = \boldsymbol{\nabla}\omega^2/|\boldsymbol{\nabla}\omega^2|$. Using eqs. 4.34 and 4.35 we obtain

$$v_n^l = -\frac{1}{|\nabla\omega^2|}\frac{D\omega^2}{Dt}. \tag{4.36}$$

The $D\omega^2/Dt$ term can be expanded by using the enstrophy transport equation, i.e. eq. 4.30, such that a relation for the local normal propagation velocity can be obtained (Holzner and Lüthi, 2011; van Reeuwijk and Holzner, 2014);

$$v_n^l = -\frac{2\omega_i\omega_j s_{ij}}{|\boldsymbol{\nabla}\omega^2|} + \frac{2\nu\nabla\omega_i\cdot\nabla\omega_i}{|\boldsymbol{\nabla}\omega^2|} - \frac{\nu\nabla^2\omega^2}{|\boldsymbol{\nabla}\omega^2|}. \tag{4.37}$$

In the study of Holzner and Lüthi (2011), the first term in the RHS of eq. 4.37 is referred to as the inviscid part of the local TNTI propagation velocity, denoted with a superscript (inv) as ${v_n^l}^{(inv)}$ and the last two terms containing the kinematic viscosity of the fluid are referred to as the viscous part of the local TNTI propagation velocity ${v_n^l}^{(vis)}$,

$${v_n^l}^{(inv)} = \frac{2\omega_i\omega_j s_{ij}}{|\boldsymbol{\nabla}\omega^2|} \tag{4.38}$$

$${v_n^l}^{(vis)} = \frac{2\nu\nabla\omega_i\cdot\nabla\omega_i}{|\boldsymbol{\nabla}\omega^2|} - \frac{\nu\nabla^2\omega^2}{|\boldsymbol{\nabla}\omega^2|} \tag{4.39}$$

The second term in the RHS of eq. 4.39 is further decomposed, which yields a relation in the form of,

$${v_n^l}^{(vis)} = \frac{2\nu\nabla\omega_i\cdot\nabla\omega_i}{|\boldsymbol{\nabla}\omega^2|} - \nu(\boldsymbol{\nabla}\cdot\boldsymbol{n}) - \frac{\nu(\boldsymbol{n}\cdot\nabla|\boldsymbol{\nabla}\omega^2|)}{|\boldsymbol{\nabla}\omega^2|}, \tag{4.40}$$

where the divergence of $\boldsymbol{n}$ appears which is related to the mean curvature of the IES given by eq. 2.2, meaning that the shape of the IES also has an effect on its local propagation velocity.

Due to the definition of the normal vector $\boldsymbol{n}$, pointing towards the turbulent core, when v_n^l is negative, it means that the element of the IES is expanding towards the non-turbulent side relative to the fluid velocity at that specific point in the flow field. Conversely, positive values of v_n^l indicate that the IES is propagating towards the turbulent core. In this context, the terms "entrainment" and "detrainment" are used to describe the sign of the local propagation velocity v_n^l in relation to the fluid. Depending on the sign of v_n^l the local contribution to the rate of change of turbulent volume at a given location can be either positive or negative for each iso-surface element.

When there is a positive contribution, the IES expands into the non-turbulent volume. This expansion can occur due to the diffusion of vorticity/enstrophy at the outer edge of the

TNTI, driven by fluid viscosity. Conversely, the enstrophy region can shrink when there is a negative contribution, which can happen as a result of the viscous dissipation of enstrophy.

Figure 4.23 displays the PDFs of the local TNTI propagation velocity v_n^l and its viscous and inviscid components, $v_n^{l\,(vis)}$ and $v_n^{l\,(inv)}$. These velocities are normalized by the Kolmogorov velocity computed at the centre-plane of the planar jet. The results are consistent with findings in the literature (Holzner and Lüthi, 2011; Watanabe et al., 2015; Wolf et al., 2012).

The total propagation velocity v_n^l is primarily dominated by the viscous term $v_n^{l\,(vis)}$. The peak of the PDF occurs on the negative side at approximately $v_n^l/u_\eta \approx 0.5$. This indicates that, on average, the turbulent jet is expanding, even though locally, in some regions of the interface, the IES may retract towards the turbulent core. Both the extreme values and the mean of v_n^l are mostly influenced by the $v_n^{l\,(vis)}$ term. Also, it is noteworthy to mention that, even in extreme cases, the magnitude of the local propagation velocity remains comparable to the Kolmogorov velocity.

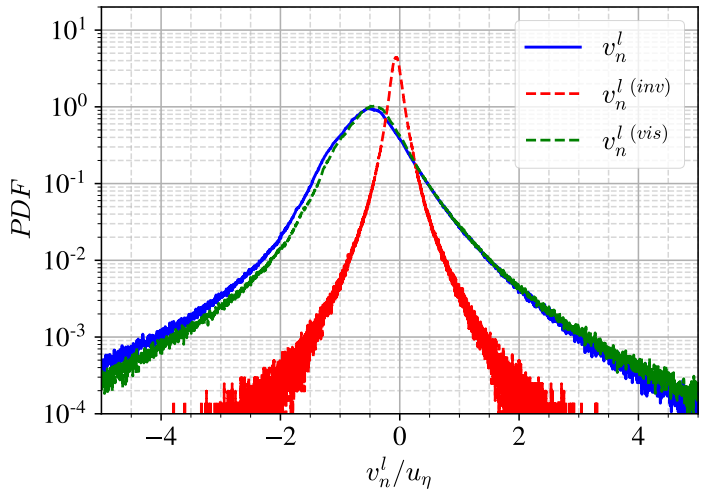

Fig. 4.23 PDF of v_n^l, $v_n^{l\,(inv)}$ and $v_n^{l\,(vis)}$ defined by the eqs. 4.37, 4.38 and 4.39 respectively. PDFs are obtained for the IES of $\omega_{th}^2/\omega_{ref}^2 = 10^{-3}$ at $t/T_{ref} = 50$ for the PJ4-HR simulation.

It is essential to clarify that the local propagation velocity, denoted as v_n^l, is calculated for each IES element. As demonstrated in chapter 3, the TNTI layer is composed of a collection of different IESs associated with a wide range of $\omega_{th}^2/\omega_{ref}^2$. Therefore, it is crucial to emphasize that v_n^l is a function of both the position on an IES and the threshold $\omega_{th}^2/\omega_{ref}^2$. Throughout the present study, v_n^l might be referred to as the local propagation velocity of the interface. However, in this context, the term "interface" does not refer to the entire TNTI layer with its various IES but to the specific IES being investigated in that particular analysis.

4.10.1 Effect of resolution on the local propagation velocity

As discussed in section 2.5, the increased resolution of the simulation has led to improved quality in calculating various quantities, including high-order derivatives of flow field variables, such as the mean curvature of the IES, given by eq. 2.2. In this study, we explore the variation of the mean propagation velocity across the TNTI, specifically its dependence on the enstrophy threshold, as presented in chapter 3. To understand the scaling of v_n with $\omega_{th}^2/\omega_{ref}^2$, it is desirable to have a wide range of enstrophy thresholds.

In chapter 3, the mean propagation velocity is computed with the global quantities, and only the geometrical resolution of the IES is used to get information about the fractal dimension of each IES. However, it is important to note that obtaining similar information with the local propagation velocity v_n^l places even stricter resolution constraints. This is because higher-order derivatives of enstrophy/vorticity need to be computed, and the terms in eq. 4.37 are normalized by the magnitude of the gradient of enstrophy, which can become quite small (at least on average) as one moves towards the non-turbulent region through the VSL.

The PDF of the local propagation velocity can be seen in figure 4.24 for the IES of $\omega_{th}^2/\omega_{ref}^2 = 10^{-3}$ and the IES of $\omega_{th}^2/\omega_{ref}^2 = 10^{-6}$. It can be observed from figure 4.24a that the tails of the PDF vary with spatial resolution. For the positive values of the v_n^l/u_η the tail of the PDF varies significantly between the resolutions $dy/\eta = 1.4$ and $dy/\eta = 0.7$ and this part of the PDF converges for the resolution $dy/\eta \leq 0.7$.

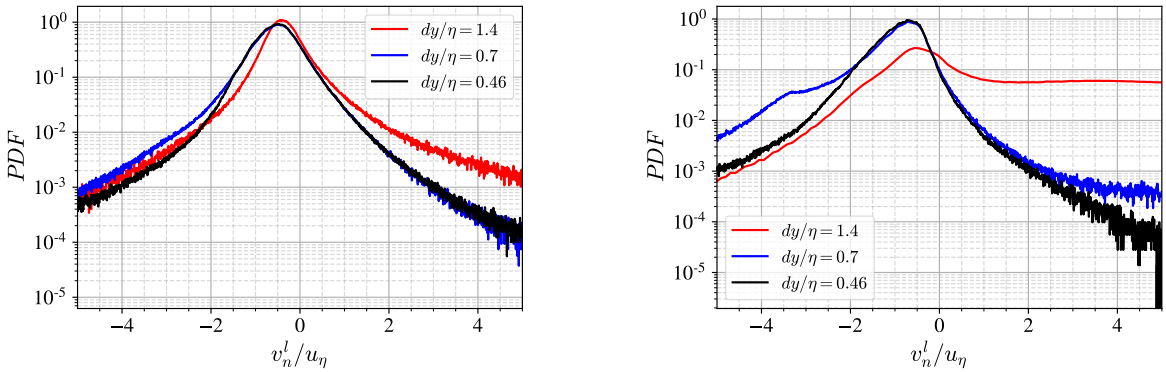

(a) IES of $\omega_{th}^2/\omega_{ref}^2 = 10^{-3}$ (b) IES of $\omega_{th}^2/\omega_{ref}^2 = 10^{-6}$

Fig. 4.24 PDF of v_n given for simulations with varying resolutions of $dy/\eta = 1.4$, $dy/\eta = 0.7$ (PJ4), and $dy/\eta = 0.46$ (PJ4-HR), for the IES of $\omega_{th}^2/\omega_{ref}^2 = 10^{-3}$.

On the other hand, for the regions of entrainment i.e. negative values of the v_n^l/u_η, the tail of the PDF changes even from the medium resolution, $dy/\eta = 0.7$ to the high-resolution case, $dy/\eta = 0.46$. The average value of the local propagation velocity v_n^l over the IES

detected by the condition $\omega_{th}^2/\omega_{ref}^2 = 10^{-3}$ is computed and found to be $\langle v_n^l \rangle_I / u_\eta = -0.268$, $\langle v_n^l \rangle_I / u_\eta = -0.544$ and $\langle v_n^l \rangle_I / u_\eta = -0.517$ for the cases with grid resolutions $dy/\eta = 1.4$, $dy/\eta = 0.7$ and $dy/\eta = 0.46$ respectively and the corresponding standard deviations are $\sigma_{v_n^l} = 1.267$, $\sigma_{v_n^l} = 0.697$ and $\sigma_{v_n^l} = 0.631$.

The effect of resolution becomes more drastic for the IES of $\omega_{th}^2/\omega_{ref}^2 = 10^{-6}$ (see figure 4.24b), where the mean value over the IES is $\langle v_n^l \rangle_I / u_\eta = 4.484$, $\langle v_n^l \rangle_I / u_\eta = -1.014$ and $\langle v_n^l \rangle_I / u_\eta = -0.906$ and the standard deviations are $\sigma_{v_n^l} = 8.466$, $\sigma_{v_n^l} = 1.230$ and $\sigma_{v_n^l} = 0.665$ for the cases with grid resolutions $dy/\eta = 1.4$, $dy/\eta = 0.7$ and $dy/\eta = 0.46$ respectively.

In conclusion, it has been observed that the mean and standard deviation of v_n^l over the IES of $\omega_{th}^2/\omega_{ref}^2 = 10^{-3}$ is starting to be captured by grid resolutions higher than η. On the other hand, the distribution over the IES of $\omega_{th}^2/\omega_{ref}^2 = 10^{-6}$ is more problematic. The comparison of the v_n and $\langle v_n^l \rangle_I$ over the IESs was not carried out in chapter 3 due to the variation observed in the PDF of the quantities containing the higher order derivatives of vorticity/enstrophy such as v_n^l seen in figure 4.24 and H_m seen in figure 2.11.

4.10.2 Comparison of the global and local propagation velocity across the TNTI

In chapter 3, a global approach is employed following the study of Zhou and Vassilicos (2017) to compute the mean propagation velocity for a specific IES. This was done using eq. 3.21, which establishes a relation between the rate of change of the turbulent volume and the volume swept by the IES surface due to its mean propagation velocity in the normal direction, denoted as v_n. By taking into account the fractal properties of the interface, a relation for the mean propagation velocity for the IES was derived, as shown in eq. 3.26.

Considering the variation of the fractal properties of the IESs at the outer regions of the TNTI, a relation for the variation of v_n as a function of $\omega_{th}^2/\omega_{ref}^2$ is obtained in eq. 3.26 and the dependence of v_n on $\omega_{th}^2/\omega_{ref}^2$ is demonstrated in figure 3.12a. Values of v_n for different $\omega_{th}^2/\omega_{ref}^2$ corresponds to the mean propagation velocity of IES associated with different threshold values $\omega_{th}^2/\omega_{ref}^2$.

The main reason for employing the global approach is to evade the computation of the high order derivatives of ω and ω^2 for the computation of the v_n^l given by eq. 4.37. The variation of v_n is demonstrated for a very wide range of $\omega_{th}^2/\omega_{ref}^2$ values in chapter 3, which spans three decades (see figure 3.12). The accurate computation of eq. 4.37 is not straightforward for this wide range of threshold values as has been demonstrated in sections 4.10.1 and 2.5.

On the other hand, for the local analysis of the TNTI, the dataset has been improved as explained in section 2.5. The effects of the increased resolution on the local quantities such as H_m and v_n^l have been documented in sections 2.5 and 4.10.1. With the improved dataset, the v_n^l values are calculated for various IES which allows us to obtain the TNTI-averaged values $\langle v_n^l \rangle_I$ for iso-surfaces of different $\omega_{th}^2/\omega_{ref}^2$.

A direct relationship between the global and the local approaches exists with a consistent definition of the turbulent volume and the bounding surface (see (Jahanbakhshi and Madnia, 2018; van Reeuwijk and Holzner, 2014)). Thus a comparison can be made between v_n and the TNTI-averaged value of v_n^l for each individual IES.

Figure 4.25 shows the $\langle v_n^l \rangle_I / u_\eta$ computed by averaging v_n^l over various IESs associated with different $\omega_{th}^2/\omega_{ref}^2$ values and normalization is made by the u_η computed at the centre-plane. In parallel and in agreement with the observation made for v_n in section 3.4.4, it can be seen in figure 4.25 that $\langle v_n^l \rangle_I$ increases as the threshold value decreases and more external iso-surfaces are considered.

The external surfaces being less contorted (lower fractal dimension D_f of the IES) with low surface area have higher propagation velocity compared to the highly contorted IES (higher fractal dimension D_f) with high surface area (see figures 3.10a and 3.7).

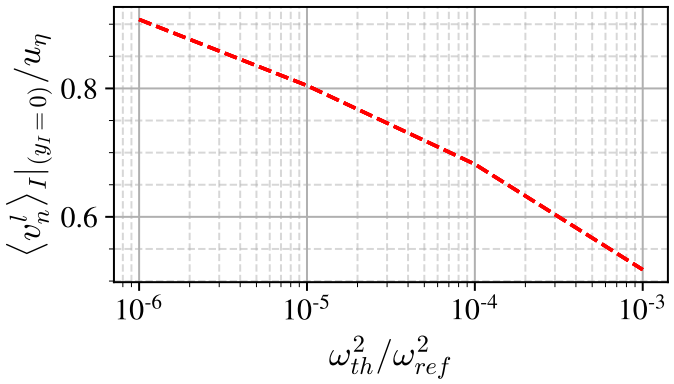

Fig. 4.25 Variation of the $\langle v_n^l \rangle_I (y_I = 0)$ over various IESs $\langle v_n^l \rangle_I$.

In figure 4.26, the ratio of $\langle v_n^l \rangle_I / v_n$ is plotted as a function of $\omega_{th}^2/\omega_{ref}^2$. It can be seen from this figure that the ratio does not vary significantly considering three decades of variation of the $\omega_{th}^2/\omega_{ref}^2$. On the other hand, the ratio is observed to be of the order of 2.5 rather than unity.

This ratio might be caused by the method used for the calculation of the surface area of the IES. The box-counting method is employed for the calculation of the fractal dimension of each IES. As described in section 3.4.4, the surface area S_R is also computed with the help of the box-counting algorithm, and is then used for the computation of v_n using eq. 3.21. It

is thus possible that this ratio between the two evaluations of the mean propagation velocity is introduced by this rather basic approximation of the areas of the various IES considered.

Another detail must also be noted for the computation of the $\langle v_n^l \rangle_I$. In the present study, v_n^l is computed locally in order to detect the various regions of the interface such as entrainment/detrainment regions. The v_n^l is obtained for each point detected on the IES, where the detection of the points on the IES is described in section 2.4. This methodology does not guarantee each point is associated with exact same surface area element. Thus there will be a certain error when $\langle v_n^l \rangle_I$ and the surface weighted average of the v_n^l are compared, at any IES location.

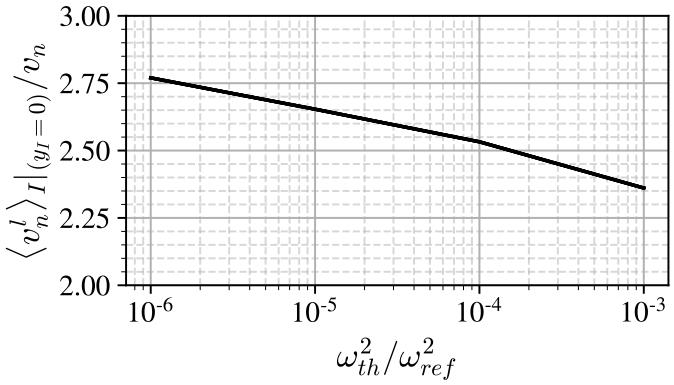

Fig. 4.26 Variation of the ratio of global mean TNTI propagation velocity v_n and the local propagation velocity v_n^l averaged over various IES $\langle v_n^l \rangle / v_n$.

4.11 Conditioning TNTI-average statistics on H_m and v_n^l

The local characteristics of the flow field at the TNTI location are being examined using the tools developed to compute TNTI-averages of flow field properties, including velocity, vorticity, pressure, enstrophy, and the components of the enstrophy transport equation, all expressed in the local coordinate system. The use of a local coordinate system, as mentioned by Bisset et al. (2002) is crucial.

It is reasonable to expect that the characteristics of the TNTI exhibit variations across the interface. These variations may result in distinct local topological features of the interface, different enstrophy balance profiles, and varying entrainment and detrainment properties.

To explore these variations across the TNTI, the TNTI-averaged statistics are conditioned on parameters such as the local mean curvature H_m (see definition in eq. 2.2) and the local propagation velocity v_n^l of the IES. In addition to these conditions, the *no multi-cross*

condition is also applied to ensure that the TNTI does not fold on itself and that no turbulent or non-turbulent pockets are present near the interface.

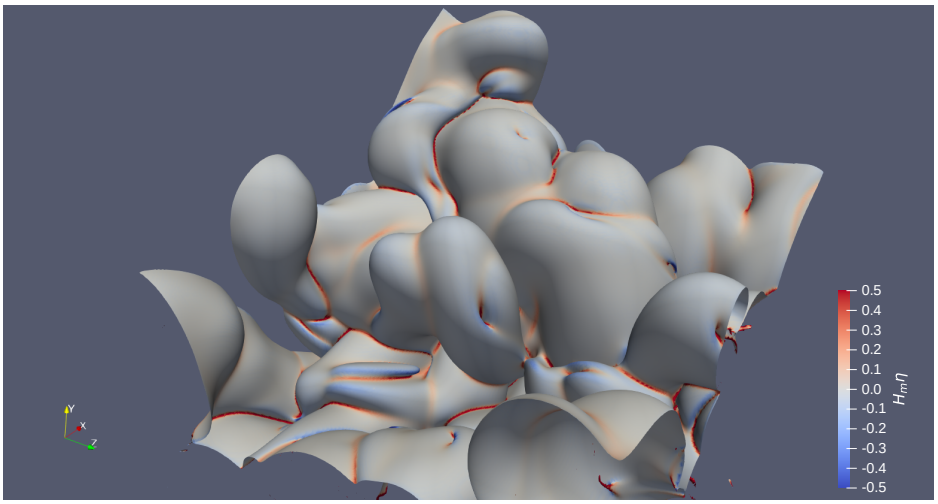

Fig. 4.27 The IES of $\omega_{th}^2/\omega_{ref}^2 = 10^{-3}$ drawn for a part ($256 \times 384 \times 256$) of PJ1 simulation, colored by the $H_m\eta$ showing concave/convex regions.

The 2D histogram of $H_m\eta$ and v_n^l/u_η is presented in figure 4.28a, while the PDFs of $H_m\eta$ and v_n^l/u_η are shown in figures 4.28b and 4.28c for the IES of $\omega_{th}^2/\omega_{ref}^2 = 10^{-3}$ from the PJ4-HR simulation. These plots are based on the analysis of a total of 22×10^6 points, which corresponds to the number of nearest mesh points to the specified IES. The locations of these points have been improved as described in section 2.6.

In the histogram and PDF shown in figures 4.28a and 4.28b respectively, it can be observed that the peak of the curvature PDF is close to zero but slightly on the negative side, indicating that the most probable shape of the interface is concave. This concave shape is also visible in figure 4.27, which displays a part of the IES of $\omega_{th}^2/\omega_{ref}^2 = 10^{-3}$ within a portion of the full domain extracted from the PJ1 simulation.

Analyzing the PDF of v_n^l in figure 4.28c, it can be observed that the peak is located on the negative side, consistent with the expansion of the jet on average. The highest probability corresponds to the situation where the IES element propagates into the non-turbulent region with a velocity of approximately $0.5u_\eta$. Even for extreme values of $|v_n^l|$, the magnitudes remain in the order of the Kolmogorov velocity u_η.

No strong correlation between v_n^l and H_m is observed considering the 2D histogram given in figure 4.28a. A possible weak correlation can nevertheless be noted due to the high probability region (in yellow) deviating towards lower $H_m\eta$ values for increasing positive v_n^l.

The mean curvature can also be expressed as $H_m = 1/R_{curv}$, where R_{curv} represents the radius of curvature. In order to ensure the physical accuracy and account for any potential

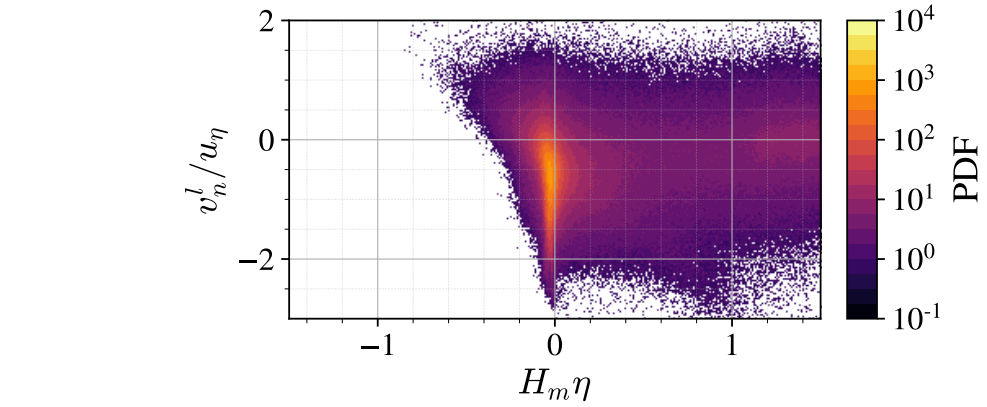

(a) 2D histogram of H_m and v_n^l

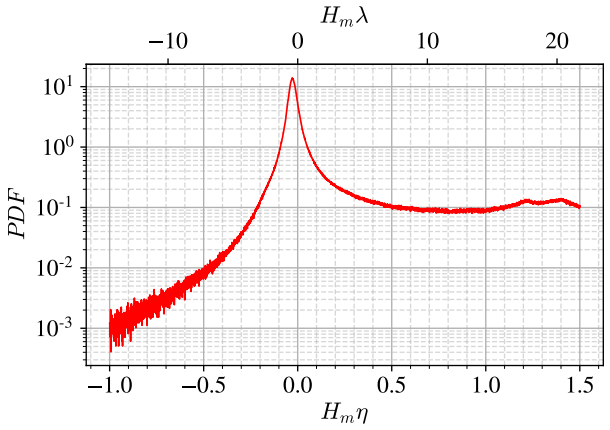

(b) PDF of $H_m\eta$

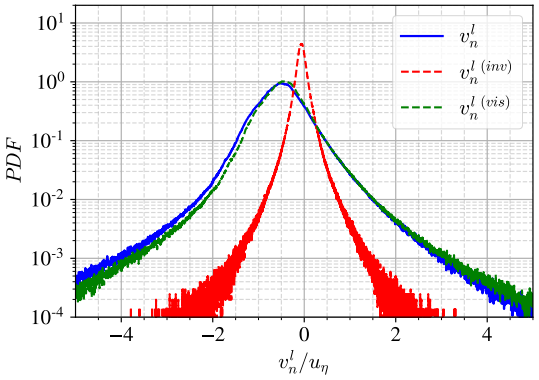

(c) PDF of v_n^l/u_η

Fig. 4.28 (a) 2D histogram of H_m/η and v_n^l/u_η (b) PDF of H_m/η and (c) PDFs of v_n^l (eq. 4.37), $v_n^{l\ inv}$ (eq. 4.38) and $v_n^{l\ vis}$ (eq. 4.39). The results are for the IES of $\omega_{th}^2/\omega_{ref}^2 = 10^{-3}$ for PJ4-HR simulation. The total number of TNTI points used for the PDF is 22×10^6.

numerical artefacts despite the special attention paid to the spatial resolution, the TNTI points with $|H_m|$ values exceeding $1/\eta$ are excluded from the TNTI-averaging process, wherever a condition on H_m is applied. It can be noted that the fraction of the TNTI points where the $|H_m|$ value exceeds $1/\eta$ is 8.7% of the total TNTI points (without applying *no multi-cross* condition).

Considering the distribution of v_n^l and H_m, the $v_n^l - H_m$ parameter space is divided into regions, and these additional conditions are referred to as "ED conditions" where "ED" stands for entrainment and detrainment. In the present study, the entrainment and detrainment terms refer to the sign of the local propagation velocity of the IES i.e., negative and positive values of v_n^l.

The conditions on H_m are set with respect to the length scales η and λ at the centre-plane, i.e. $H_m = \pm 1/\lambda$, $H_m = \pm 1/\eta$. For v_n^l, the distinction has been made between detrainment cases, ($v_n^l/u_\eta > 0$), moderate entrainment cases ($-1 < v_n^l/u_\eta < 0$) and fast entrainment cases ($v_n^l/u_\eta < -1$). For the sake of clarity, the conditions applied on the variables H_m and v_n^l for the conditional TNTI-averages are given for each case in table 4.1.

D1	**D2**	**D3**	**D4**
$-1/\eta < H_m < -1/\lambda$	$-1/\lambda < H_m < 0$	$0 < H_m < 1/\lambda$	$1/\lambda < H_m < 1/\eta$
$v_n^l > 0$	$v_n^l > 0$	$v_n^l > 0$	$v_n^l > 0$
(3.4 %) (1.54 %)	(2.6 %) (1.46 %)	(1.0 %) (0.37 %)	(3.0 %) (0.57 %)
E1	**E2**	**E3**	**E4**
$-1/\eta < H_m < -1/\lambda$	$-1/\lambda < H_m < 0$	$0 < H_m < 1/\lambda$	$1/\lambda < H_m < 1/\eta$
$-u_\eta < v_n^l < 0$	$-u_\eta < v_n^l < 0$	$-u_\eta < v_n^l < 0$	$-u_\eta < v_n^l < 0$
(4.0 %) (2.22 %)	(45.3 %) (33.94 %)	(9.9 %) (6.17 %)	(7.6 %) (3.11 %)
E5	**E6**	**E7**	**E8**
$-1/\eta < H_m < -1/\lambda$	$-1/\lambda < H_m < 0$	$0 < H_m < 1/\lambda$	$1/\lambda < H_m < 1/\eta$
$-2u_\eta < v_n^l < -u_\eta$	$-2u_\eta < v_n^l < -u_\eta$	$-2u_\eta < v_n^l < -u_\eta$	$-2u_\eta < v_n^l < -u_\eta$
(0.3 %) (0.11 %)	(9.7 %) (7.68 %)	(1.6 %) (0.97 %)	(2.9 %) (1.14 %)

Table 4.1 The conditions applied on H_m and v_n^l, for each of the ED conditions during the TNTI averaging operation. D stands for the detrainment ($v_n^l > 0$) and E stands for the entrainment cases ($v_n^l < 0$). The probabilities of each condition over total TNTI locations without and with *no multi-cross* condition are given in black and in red respectively. The probabilities of the conditions are obtained for the IES of $\omega_{th}^2/\omega_{ref}^2 = 10^{-3}$ at $t/T_{ref} = 50$ for PJ1-HR simulation.

The joint conditional cases are shown in figure 4.29 on the 2D histogram of $H_m\eta$-v_n^l/u_η over the IES of $\omega_{th}^2/\omega_{ref}^2 = 10^{-3}$. The green lines showing the borders defined by the above-mentioned conditions on the variables correspond to $H_m = -1/\eta$, $H_m = -1/\lambda$, $H_m = 1/\lambda$ and $H_m = 1/\eta$ from left to right. Each blue-shaded region corresponds to a specific condition on H_m and v_n^l. Table 4.1 shows all conditions with their respective percentage of occurrences amongst all the points considered on the IES. The green grid seen in figure 4.29 limits the various conditions of table 4.1.
If we consider the E2 condition as an example, it is obtained by the following conditions;

1. $-1/\lambda < H_m < 0$
2. $-1 < v_n^l/u_\eta < 0$
3. No multi-crossing of TNTI in the range $[-23\eta, +23\eta]$, on each side of the TNTI along the normal axis.

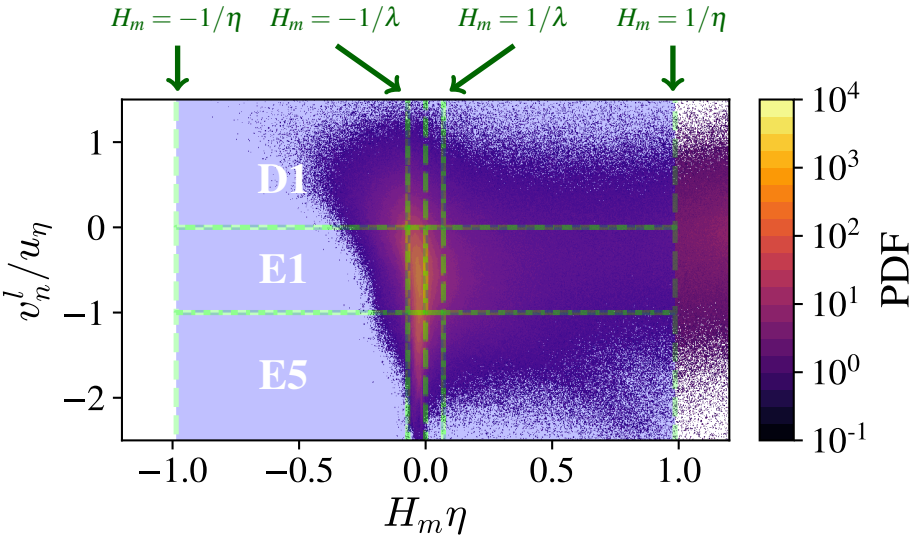

Fig. 4.29 2D histogram of H_m and v_n^l given for the IES of $\omega_{th}^2/\omega_{ref}^2 = 10^{-3}$. The regions of ED conditions for H_m and v_n^l in the blue-shaded region are divided by the green dashed lines. Horizontal lines stand for $v_n^l/u_\eta = -1$ and $v_n^l/u_\eta = 0$. Vertical lines stand for $H_m = -1/\eta$, $H_m = -1/\lambda$, $H_m = 1/\lambda$ and $H_m = 1/\eta$. The regions of the histogram corresponding to D1, E1 and E5 are marked on the plot as examples.

Among all the points considered on the TNTI, 33.94% satisfy all the three conditions above. 11.36% of the points are eliminated due to the *no multi-crossing* condition, meaning that 45.3% of the total TNTI points satisfy the first two criteria.

To facilitate the comparison of TNTI-averaged statistics, we have selected a subset of conditions, specifically D2, E2, E3, and E6. This choice helps us avoid an overwhelming amount of results, given the number of possible joint conditions defined on both H_m and v_n^l. These selected ED cases offer an opportunity to explore the local TNTI structure across different regions of the interface, each exhibiting distinct characteristics in terms of H_m and v_n^l. By focusing on these cases, we aim to isolate the impact of either H_m or v_n^l on the conditional TNTI-averages.

The cases D2, E2, and E6, effectively span the range of v_n^l, while E2 and E3 allow us to investigate the influence of the IES shape, whether it is concave or convex. In addition to that, the probabilities of occurrence of each condition over the interface are also considered when these conditions are chosen. After applying the *no multi-cross* condition, the chosen joint conditions (D2, E2, E3, and E6) emerge as the predominant representations of certain local TNTI characteristics, such as regions of detrainment, and convex curvature, etc.

To summarize the selected subset of the ED cases; the D2 condition corresponds to the regions of detrainment i.e. where the v_n^l is positive and the IES element retracts towards the

turbulent core. These are also the regions of the IES where the surface is concave (see figure 2.9a). The E2 condition also contains the regions at which the mean curvature is concave. Conversely to the D2 condition, the E2 condition is associated with negative values of v_n^l i.e., locations where the IES element is moving towards the non-turbulent region relative to the fluid velocity at that location. The E3 condition includes the regions which are convex in shape and they are expanding into the non-turbulent region similar to the E2 condition. Lastly, the E6 condition includes the regions where the mean curvature is concave similar to D2 and E2 conditions, and the IES propagates towards the non-turbulent direction with a higher velocity compared to the regions included in E2 and E3 i.e., $|v_n^l| > u_\eta$.

4.11.1 Conditional TNTI-average profiles and local fields

The variations in H_m and v_n^l across the IES indicate potential differences in the local surface geometry and the influence of the local flow field, including distortion, transport, and folding of the interface. Figure 4.30 presents the conditional profiles of $\langle\omega^2\rangle_I/\omega_c^2$ and the components of local vorticity $\langle\omega_{x,y,z}^l\rangle_I/|\omega_{x,y,z}|_c$ for the conditions D2, E2, E3, and E6.

The first observation concerns the sharpness of the $\langle\omega^2\rangle_I$ profiles at the interface. In the D2 condition, enstrophy continues to rise even at $y_I = -23\eta$ inside the turbulent region. In the other cases, a peak in enstrophy can be observed as one moves towards the turbulent core from the IES location. This peak is particularly pronounced in the E6 condition, characterized by high negative values of v_n^l. In this case, the $\langle\omega^2\rangle_I$ peak inside the TNTI reaches much higher values, nearly double the mean centre-plane value, and occurs at a distance less than 10η from the detected IES. This suggests that the regions of the IES satisfying the E6 condition are situated adjacent to high vorticity/enstrophy regions.

Conversely, in the E2 condition, the peak of $\langle\omega^2\rangle_I$ occurs at approximately 12η from the IES, and the value remains lower than the centre-plane value ω_c^2. It can be observed that the profile of $\langle|\omega^2|\rangle_I$ is influenced by the local spanwise vorticity, perhaps indicating the presence of vortical structures oriented in the local spanwise direction. This observation aligns with findings in the literature (da Silva et al., 2011) and in section 4.7. The effect is most pronounced in the E6 condition, which focuses on the regions of the TNTI where the IES propagation velocity is high in the direction of the non-turbulent region. This suggests a potential connection between the local entrainment process and the intensity of vortical structures near the IES on the turbulent side of the interface.

The effect of the vortical structures located just next to the interface has been discussed in the literature including the relation between the thickness of the TNTI and the radius of LVS (da Silva and Taveira, 2010) and these vortical structures affecting the TNTI-average profile of the tangential component of the vorticity, due to their predominant alignment when

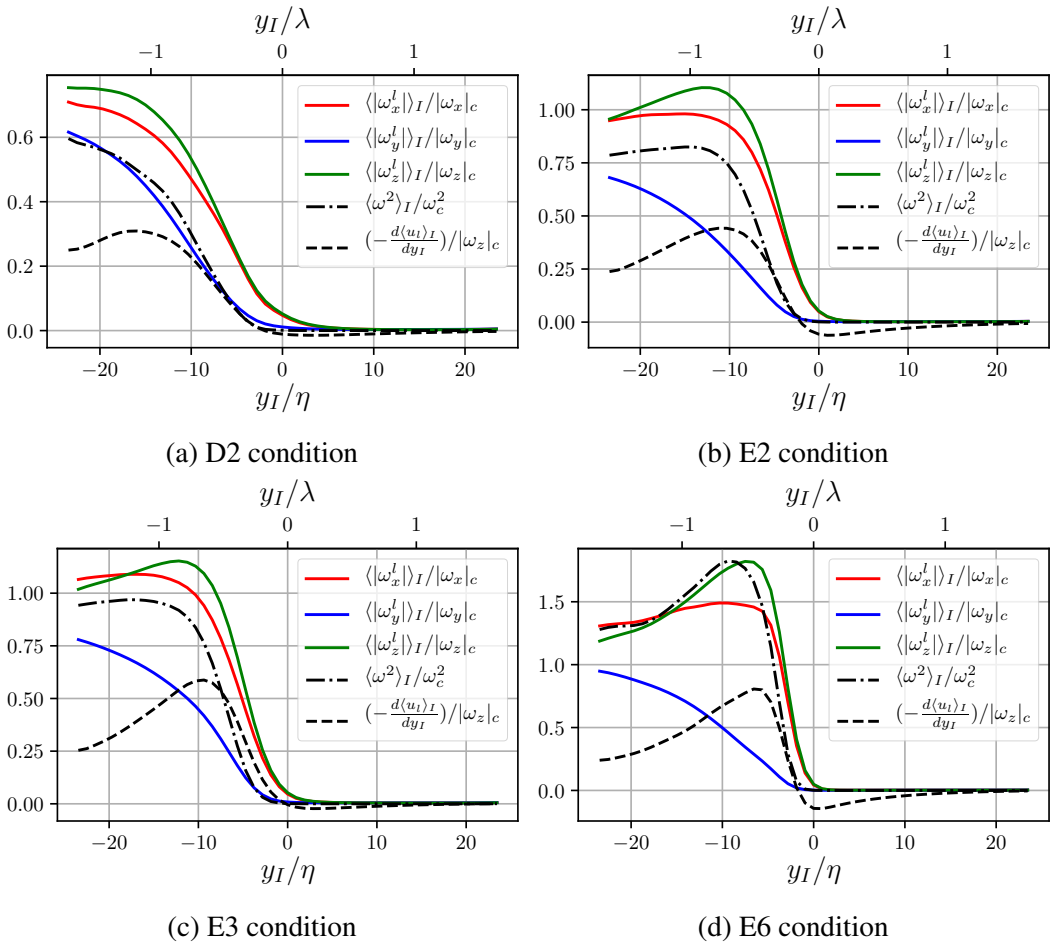

(a) D2 condition

(b) E2 condition

(c) E3 condition

(d) E6 condition

Fig. 4.30 Conditionally averaged profiles of the terms of enstrophy transport equation near the TNTI. PJ4-HR simulation, $\omega_{th}^2/\omega_{ref}^2 = 10^{-3}$.

approaching the interface (da Silva and dos Reis, 2011; da Silva et al., 2011; Westerweel et al., 2009).

The vortical structures located adjacent to the interface and their effects on TNTI have been discussed in the literature, including the relation between the thickness of TNTI and the radius of LVS (da Silva and Taveira, 2010), or the contribution of the vortical structures to the TNTI-average profile of the vorticity component tangential to the interface, due to the predominant alignment of vortical structures close to the interface (da Silva and dos Reis, 2011; da Silva et al., 2011; Westerweel et al., 2009).

The properties of the IVS near the interface have been documented by (da Silva et al., 2011). These structures are reported to exhibit a predominant alignment in the tangential direction of the interface, even though they do not exhibit any preferential alignment direction inside the turbulent core. The radius of these IVS was analyzed in conjunction with the

stretching experienced by these vortical structures and it was found that their radius reaches its maximum value of 5η at $y_I = -\lambda$ (da Silva et al., 2011). Given the findings in the literature, it may be possible to attribute the bump in the profile of $\langle|\omega_z^l|\rangle_I/|\omega_z|_c$ to these IVS structures residing near the IES, considering the extent of this bump is approximately 10η along the y_I axis.

Moreover, it has been reported (da Silva et al., 2011) that the stretching experienced by IVS near the interface is small compared to the IVS located within the turbulent core. This reduced stretching is attributed to a local minimum of strain at the locations of these structures, which arises due to the presence of the TNTI. In essence, the TNTI inhibits the stretching of the IVS by the large-scale motions as the fraction of LVS near the interface decreases getting closer to the non-turbulent region (da Silva et al., 2011).

On the other hand, the bump observed in the profile of $\langle|\omega_z^l|\rangle_I/|\omega_z|_c$ is notably more pronounced in the case of E6 compared to other conditions, such as the E2 condition (see figures 4.30d and 4.30b). This suggests that the regions associated with the E6 condition may be where the IVSs are swept closer to the TNTI by the larger motions (see very high positive values of $\langle v_l\rangle_I$ in figure 4.32e), confining them in a narrow region between the LVS and TNTI. In these regions, the stretching of the IVSs is possibly stronger, due to the more pronounced expansion in the tangential direction of the TNTI for the case of E6 given in figure 4.32e, when compared with other conditions, e.g. the E2 condition (see figure 4.32c).

To evaluate the influence of H_m on the TNTI-averaged profiles of ω^2 and ω, a comparison between conditions E2 and E3 can be conducted (see figures 4.30b and 4.30c). It is evident that the effects of H_m on the profiles are relatively minor compared to the conditioning on v_n^l. In general, the values of ω^2 and ω are slightly higher for the E3 condition in the inner-most side of the TNTI-averaged profiles (see $y_I/\eta \lessapprox -20$ in figures 4.30b and 4.30b).

This difference may be attributed to the fact that the convex surfaces, which are represented by the E3 condition, are located between the concave bulges that extend towards the non-turbulent region. Consequently, these convex regions are positioned closer to the centre-plane compared to the concave regions of the interface (i.e., D2, E2, and E6 conditions) and they correspond to the valley-like sections of the interface, which are depicted in red in figure 4.27 when viewed from the non-turbulent side of the interface.

Figure 4.31 displays the TNTI-average normal profiles of local velocity components $\langle u_l\rangle_I$, $\langle v_l\rangle_I$, and $\langle w_l\rangle_I$ normalized by u_η for conditions D2, E2, E3 and E6. Similar to the observation for the TNTI-averaged profiles of ω^2 and ω, the most significant variation is observed when comparing conditions with different v_n^l ranges. Especially, the profile of the interface-normal component of the local velocity, $\langle v_l\rangle_I$, exhibits notable variations for regions with different values of v_n^l/u_η i.e., D2, E2, and E6.

In the D2 condition, $\langle v_l \rangle_I$ remains negative along the entire y_I axis. However, for the moderate entrainment conditions E2 and E3, $\langle v_l \rangle_I$ experiences a change in sign. Finally, in the E6 condition, $\langle v_l \rangle_I$ is positive throughout the entire TNTI normal axis.

It is useful to recall that the negative values of $\langle v_l \rangle_I$ do not directly translate into entrainment/detrainment as the local propagation velocity for the IES element, v_n^l, is computed relative to the fluid velocity at the IES location. It can even be noted that $\langle v_l \rangle_I < 0$ is observed in both D2 and E3 conditions (see figures 4.32b and 4.32d) which are associated with local detrainment and entrainment respectively. The fact that $\langle v_l \rangle_I$ is negative at $y_I/\eta = 0$ does not lead to an entrainment in the D2 condition. This picture suggests that the local entrainment/detrainment is associated more with the compression/stretching of the interface than the direction of the flow velocity at the interface.

In the D2 case, it can be suggested that the negative TNTI-averaged velocity in the normal direction ($\langle v_l \rangle_I < 0$) pushes the vortical structures away from the IES location. This may have an impact on how sharp the TNTI is and affect the non-linear production of enstrophy, P_{ω^2}. It should also be noted that the positive gradient of $\langle v_l \rangle_I$ along the y_I axis leads to the stretching of the interface layer in the normal direction (see figure 4.31a).

Conversely, for the E6 condition, the gradient of $\langle v_l \rangle_I$ along the y_I axis is negative, suggesting that the TNTI-average velocity field induces a transport from the turbulent core towards the interface. This will lead to a sweep of IVS closer to the interface, perhaps contributing to the prominent bump observed in the profile of $\langle |\omega_z^l| \rangle_I$ in figure 4.30d, on the turbulent side of the IES. This interpretation is further supported by the jump of $\langle u_l \rangle_I$ across the interface, for D2, E2, and E6 conditions. In the D2 case, the observed jump in $\langle u_l \rangle_I$ across the TNTI is smaller and occurs over a wider range of y_I, whereas it is much higher in magnitude and occurs much sharply in the case of the E6 condition given in figure 4.31d.

The jump of $\langle u_l \rangle_I$ is shown to be due to the $\boldsymbol{u}'$ field near the interface (see figures 4.14b and 4.15b), where the relationship between $\langle u_l \rangle_I$ and $\boldsymbol{u}'$ is given by eq. 4.15. In cases where vortical structures may be transported closer to the IES, the tangential velocity induced by these structures will be higher, resulting in the differences between figures 4.31d, 4.31b and 4.31a.

One less prominent feature in the profiles given in figure 4.31 is the region in the profile of $\langle u_l \rangle_I$ where $d\langle u_l \rangle_I / dy_I$ changes its sign. This feature is most noticeable in figure 4.31d for the E6 condition, occurring at $y_I/\eta = -2$. Upon examining the TNTI-averaged profiles for the D2 and E3 conditions, it becomes evident that this inverse bump is not present for these conditions, contrary to E2 and E6 conditions. This discrepancy suggests a difference in the local flow field topology near the IES for the E3 and D2 conditions.

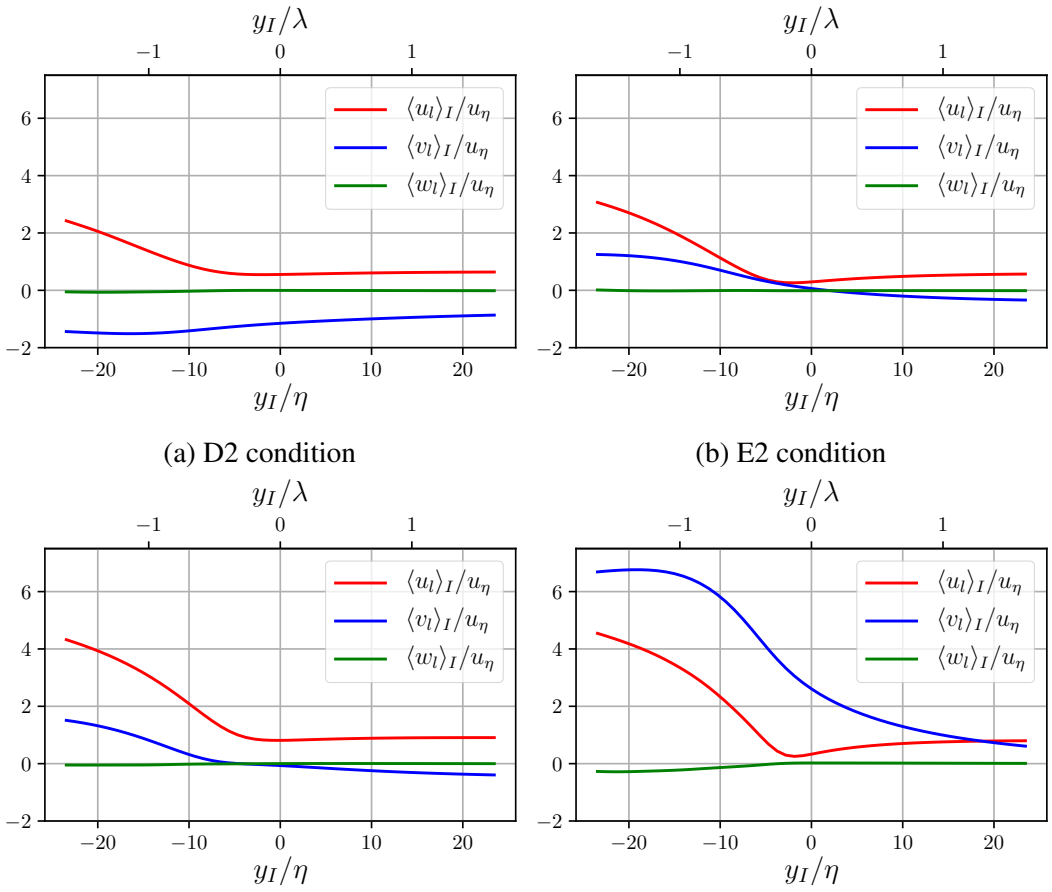

(a) D2 condition

(b) E2 condition

(c) E3 condition

(d) E6 condition

Fig. 4.31 Conditionally averaged profiles of local velocity $\langle \boldsymbol{u} \rangle_I$ near the TNTI. IES of $\omega_{th}^2/\omega_{ref}^2 = 10^{-3}$.

The vortical motion depicted in figure 4.16 contributes to a local negative peak in the $\langle u_l \rangle_I$ component very close to the $y_I/\eta = 0$ location. For the D2 and E3 conditions, the impact of this vortical motion appears less significant, as the local minimum of $\langle u_l \rangle_I$ is absent in these conditions. This observation may indicate a lack of tangentially aligned vortical structures or a lower intensity of such structures in these specific regions. The reason for this difference might vary between the D2 and E3 conditions.

In the case of the D2 condition, we mentioned that the TNTI-averaged velocity field acts in a way that transports the vortical structures away from the interface. In contrast, the convex regions of the IES associated with the E3 condition are situated between the bulges, resembling valley-like regions (see figure 4.27). Unlike the concave regions of IES, which follow the underlying vortical motions, there is no reason to expect the same picture for the convex regions of the IES.

Therefore, even though the $\langle u_l \rangle_I$ values are higher for the E3 condition compared to the E2 condition, the inverse bump does not exist for the E3 condition as prominently as in conditions E2 and E6. Meanwhile, the higher values of $\langle u_l \rangle_I$ in the E3 condition can be attributed to the fact that concave surfaces reach further into the non-turbulent region, hence farther from the center-plane, compared to the convex regions. In support of this last point, the average distance of regions satisfying the E2 condition with respect to the jet centre-plane is computed to be $1.68H_J$, whereas the same average distance is $1.55H_J$ for the regions associated with the E3 condition.

The TNTI-averaged local velocity fields are presented in figure 4.32 for conditions D2, E2, E3, E6, and for the case without any conditioning on H_m and v_n^l. As mentioned earlier, the local velocity field exhibits notable differences for the D2 and E3 cases, where the rotational motion observed in the $x_I - y_I$ cut section in figure 4.16 is not present.

In the D2 condition, the velocity field exhibits a rotational pattern around a point in the local upstream region of the $x_I - y_I$ cross-section i.e. at a location where $x_I/\eta > 0$. The interface normal velocity $\langle v_l \rangle_I$ is directed towards the turbulent core, not only along the normal axis but across the entire TNTI-averaged field.

In the E3 condition, the influence of the convex IES can be seen in the $z_I - y_I$ cross-section. The $\langle v_l \rangle_I$ component is directed towards the non-turbulent region, and its magnitude remains significant at $z_I = \pm 23\eta$, which is different from the mean picture obtained for the E2 condition in figure 4.32*c*. This observation further supports the notion that the regions identified by the E3 condition are not directly positioned on top of significant vortical motions but rather between them.

For the E6 condition, the velocity vectors of the TNTI-averaged velocity field given in figure 4.32e, are nearly perpendicular to the IES at the location of $\boldsymbol{x}_I = (0,0,0) \equiv \boldsymbol{X}_0$. The magnitudes of $\langle v_l \rangle_I$ are significantly higher compared to the other cases. The stretching motion centred at the $\boldsymbol{X}_0$ location is much more pronounced in the tangential plane defined by the $x_I - z_I$ cut section, especially compared to the E2 condition. Conversely, in the $x_I - z_I$ cut section for the D2 condition, shown in figure 4.32b, compression of the flow field can be observed in the tangential direction of the interface, where, $d\langle w_l \rangle_I / dz_I < 0$ along the z_I axis, and $d\langle u_l \rangle_I / dx_I$ is close to zero near the $z_I/\eta = 0$ line, indicating that the gradient of $\langle v_l \rangle_I$ in the interface normal direction is maximized along the y_I axis.

Figure 4.33 displays the TNTI-averaged local fields of ω^2 for various conditions across the IES of $\omega_{th}^2/\omega_{ref}^2 = 10^{-3}$. A notable observation is the exceptionally high enstrophy values in close proximity to the IES for the E6 condition. This is consistent with the findings in figure 4.32e, where the TNTI-averaged local velocity field transports ω^2 towards the interface. Additionally, the analysis of $\hat{h}$ across the interface reveals that the alignment

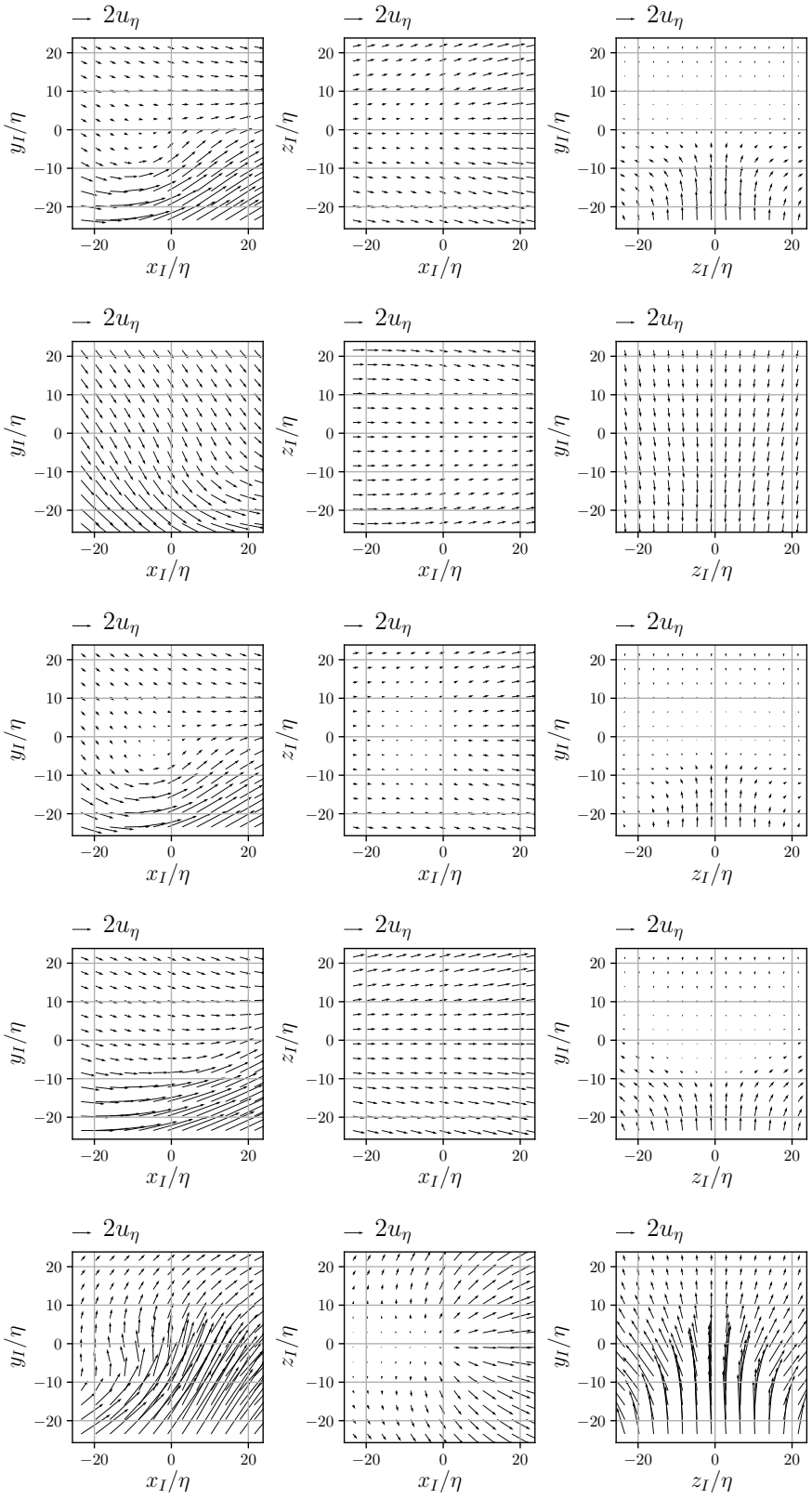

(a) Without any condition on H_m and v_n

(b) D2 condition

(c) E2 condition

(d) E3 condition

(e) E6 condition

Fig. 4.32 TNTI-averaged local velocity field near the detected IES for the conditions D2, E2, E3, and E6. The scales for vectors are given on the top left of the figures. The location of the IES is $\boldsymbol{X}_0 = (0,0,0)$. Results for the IES of $\omega_{th}^2/\omega_{ref}^2 = 10^{-3}$ at $t/T_{ref} = 50$.

of ω is influenced by the presence of the interface, with a higher likelihood of alignment perpendicular to $\boldsymbol{u}$.

Given these observations, a plausible scenario for the regions corresponding to the E6 condition is as follows: The vortical structures are advected towards the interface by a significant $\langle v_l \rangle_I$, after which they are stretched in the tangential direction of the interface due to the mean velocity field shown in figure 4.32e for the $x_I - z_I$ cut section. This stretching process can be associated with the increased non-linear production of enstrophy P_{ω^2}, in close proximity to the IES. This increase in P_{ω^2} is particularly important for the net increase of ω^2 in the outer regions of the TNTI, where the viscous destruction of ω^2 already exceeds the viscous diffusion, i.e., $(D_{\omega^2} - \varepsilon_{\omega^2}) < 0$.

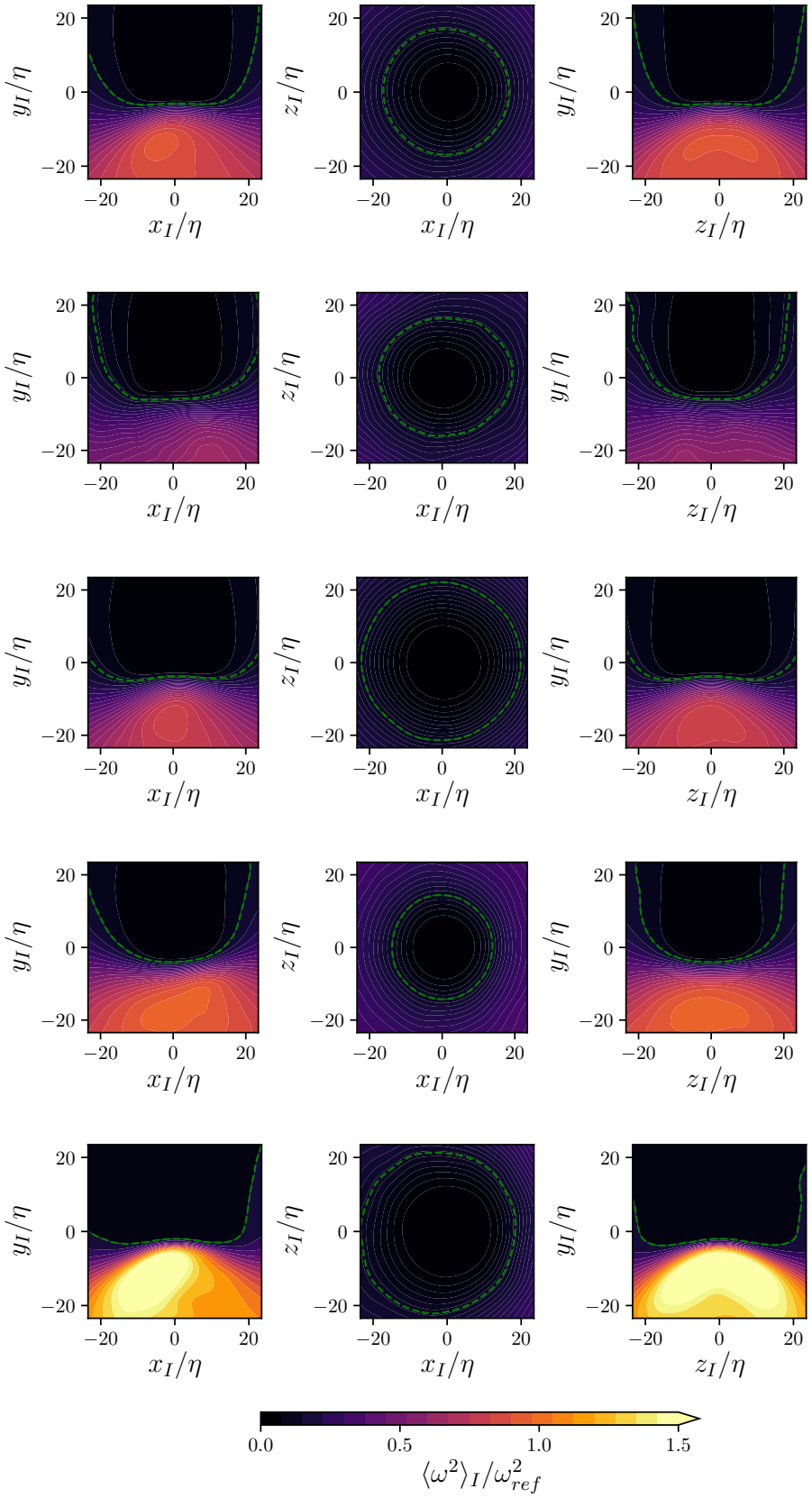

(a) Without any condition on H_m and v_n^l

(b) D2 condition

(c) E2 condition

(d) E3 condition

(e) E6 condition

Fig. 4.33 TNTI-averaged local enstrophy fields for various ED conditions (IES of $\omega^2_{th}/\omega^2_{ref} = 10^{-3}$). The green dashed line shows the iso-contour of $\omega^2_{th}/\omega^2_{ref} = 10^{-1}$. The same colour scale is used for all the contour plots for the comparison, which is over-saturated for the E6 condition due to very intense ω^2 values for this case compared to the other conditions.

4.11.2 Conditional enstrophy balance

The TNTI-averaged profiles of the terms of the enstrophy transport equation (eq. 4.30) have been computed conditionally on the H_m and v_n^I of the detected IES. Figure 4.34 shows the profiles normal to the interface for the cases D2, E2, E3, and E6 where the $D(\omega^2/2)/Dt$ term is calculated from the balance of the terms in the right-hand side of the eq. 4.30.

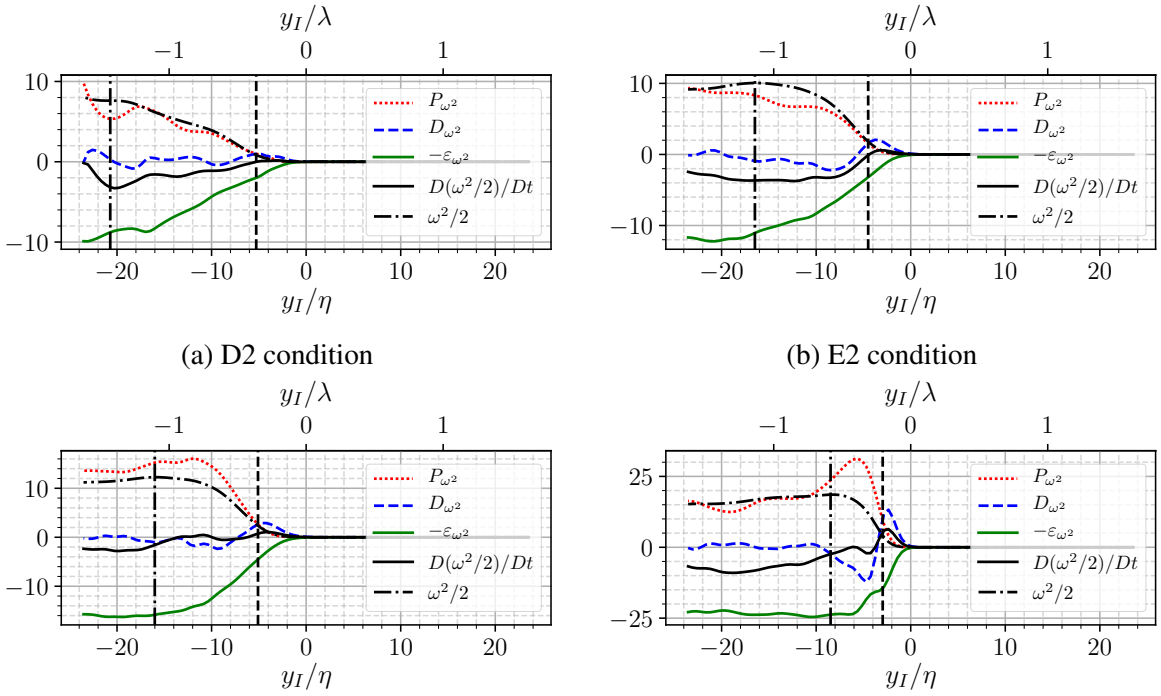

(a) D2 condition

(b) E2 condition

(c) E3 condition

(d) E6 condition

Fig. 4.34 Conditionally averaged profiles of the terms of enstrophy transport equation near the TNTI. PJ4-HR simulation, $\omega_{th}^2/\omega_{ref}^2 = 10^{-3}$.

A notable distinction can be observed between the conditional enstrophy profiles for the D2 case and the E2, E3, and E6 cases, which corresponds to a comparison between regions of detrainment and entrainment. In figure 4.34a for the D2 condition, it is observed that as we move towards the turbulent core from $y_I/\eta = 0$, the ε_{ω^2} increases more rapidly compared to the D_{ω^2} and P_{ω^2} terms. This results in the destruction of ω^2 as the diffusion and production terms are not able to balance ε_{ω^2}, causing the IES to retreat towards the turbulent core. Another difference between the D2 condition and the entrainment cases is that the P_{ω^2} and ε_{ω^2} terms continue to rise along with the $\omega^2/2$ profile, even at $y_I = -23\eta$. It should also be noted that the magnitudes of all the terms in the D2 condition are lower compared to the other conditions.

The impact of the conditioning on H_m appears to have a less significant effect on the variation of TNTI-averaged terms in the enstrophy transport equation. To assess how the enstrophy balance changes between convex and concave regions of the IES, figure 4.34c can be compared with figures 4.34b and 4.34d. As a reminder, it can be noted that the E3 condition corresponds to convex regions ($0 < H_m < 1/\lambda$), while the E2 and E6 conditions correspond to concave regions ($-1/\lambda < H_m < 0$) of the IES. Even though it can be said that, qualitatively the profiles of the terms appear similar for concave and convex regions, a difference can be noted for the profile of the $D(\omega^2/2)/Dt$ term as we move towards the turbulent core.

In figures 4.34b and 4.34d, it can be observed that $D(\omega^2/2)/Dt$ crosses zero relatively close to the IES location and remain negative until $y_I/\eta = -23$. On the other hand, for the E3 condition, $D(\omega^2/2)/Dt$ remains close to zero until $y_I/\eta = -14$, which is nearly the extent of the full TNTI layer located at $y_I/\eta = -16$.

When considering the thickness of the VSL and TSL for each condition, similar behaviour is also observed for the E6 condition. The $D(\omega^2/2)/Dt$ remains near zero over the full extent of the TNTI, even though the TNTI thickness δ_I for the E6 condition is half that computed for the E2 and E3 conditions.

Furthermore, it is noteworthy that P_{ω^2} appears to be more dominant for the E3 and E6 conditions than for the E2 condition. This suggests a similarity between the E3 and E6 conditions in the sense that there is significant production of enstrophy inside the TNTI.

For the E6 condition, the mean profile of P_{ω^2} supports the discussion made in relation to figure 4.33e regarding the intense ω^2 near the IES. It has been discussed that the vortical structures transported by the TNTI-averaged interface normal velocity, are subjected to vortex stretching in the tangential direction close to the IES location, particularly in the regions associated with the E6 condition. The P_{ω^2} peak appears at $y_I/\eta \approx -5.5$, which is the same location where the negative peak of D_{ω^2} is observed. This demonstrates the significant amount of ω^2 that is produced at this location is on average, transported by the action of viscosity towards the non-turbulent region.

On the contrary, the TNTI-averaged velocity field significantly differs between the E3 and E6 conditions (see figures 4.32d and 4.32e). Consequently, the same reasoning does not seem very plausible for the profiles obtained for the E3 case. However, previously demonstrated, the regions associated with the E3 condition are predominantly situated within the turbulent region, nested between the bulges. In these convex regions, vortical structures near the IES might experience more stretching due to straining by the LVS, akin to the stretching of vortex filaments in isotropic turbulence subjected to background strain, as documented by Jiménez and Wray (1998). The higher stretching effect is likely because these convex regions

are enveloped by the turbulent region, in contrast to the concave sections of the interface. In concave regions, the LVSs are confined more by the interface, leading to fewer LVSs near the location of the IES. This interpretation aligns with the findings of da Silva et al. (2011), where they illustrated TNTI and vortical motions at various scales, discussing the relationship between strain acting on the IVS near the TNTI in detail, while the statistics were not specifically conditioned on the shape of the interface i.e., concave/convex shaped regions.

The separation of the TNTI thickness into various sublayers by considering the terms of the ω^2 balance equation is described in section 4.8 and the computations of the total TNTI thickness δ_I, VSL thickness δ_ν, and TSL thickness, δ_{ω^2} are carried out from the profiles obtained for the entire TNTI i.e., without applying any conditions on H_m and v_n^l. Now, by employing the same methodology, the thicknesses of the TNTI and its sublayers are investigated in various regions of the interface associated with each ED condition. It must be noted that the number of points satisfying each condition varies significantly (see table 4.1) which may affect the convergence of the profiles in certain cases.

Table 4.2 provides the thicknesses of the TNTI and its sublayers for all the ED cases. Some values in the table are left empty because the conditional profile of ω^2 does not exhibit a visible peak value within the investigated range. As a reminder, the thicknesses obtained without imposing any conditions on v_n and H_m are $\delta_I = 16\eta$, $\delta_\nu = 3.27\eta$ and $\delta_{\omega^2} = 12.74\eta$.

D1	D2	D3	D4
$\delta_I =$ *not defined*	$\delta_I = 20.7\eta$	$\delta_I = 16\eta$	$\delta_I = 17.4\eta$
$\delta_\nu = 4.1\eta$	$\delta_\nu = 5.3\eta$	$\delta_\nu = 6\eta$	$\delta_\nu = 4.4\eta$
$\delta_{\omega^2} =$ *not defined*	$\delta_{\omega^2} = 15.4\eta$	$\delta_{\omega^2} = 10\eta$	$\delta_{\omega^2} = 13\eta$
E1	E2	E3	E4
$\delta_I =$ *not defined*	$\delta_I = 16.5\eta$	$\delta_I = 16\eta$	$\delta_I = 18.4\eta$
$\delta_\nu = 4\eta$	$\delta_\nu = 4.5\eta$	$\delta_\nu = 5.1\eta$	$\delta_\nu = 4.7\eta$
$\delta_{\omega^2} =$ *not defined*	$\delta_{\omega^2} = 12\eta$	$\delta_{\omega^2} = 11\eta$	$\delta_{\omega^2} = 13.6\eta$
E5	E6	E7	E8
$\delta_I = 9.9\eta$	$\delta_I = 8.5\eta$	$\delta_I = 8\eta$	$\delta_I = 10.4\eta$
$\delta_\nu = 2.7\eta$	$\delta_\nu = 3\eta$	$\delta_\nu = 3.3\eta$	$\delta_\nu = 2.8\eta$
$\delta_{\omega^2} = 7.2\eta$	$\delta_{\omega^2} = 5.5\eta$	$\delta_{\omega^2} = 4.7\eta$	$\delta_{\omega^2} = 7.5\eta$

Table 4.2 Thickness of the TNTI, VSL and TSL layers, δ_I, δ_ν, δ_{ω^2}, for different ED conditions. PJ4-HR simulation for the IES defined by $\omega_{th}^2/\omega_{ref}^2 = 10^{-3}$ at $t/T_{ref} = 50$.

In the table 4.2, the thicknesses of all the layers tend to decrease for increasing local entrainment i.e. from top to bottom in each column. For the conditions with moderate entrainment velocity ($-1 < v_n^l/u_\eta < 0$), the thickness of layers are; $\delta_I/\eta = 16.5$, $\delta_\nu/\eta = 4.6$ and $\delta_{\omega^2}/\eta = 12$ (average of E2, E3 and E4 conditions). For the fast entrainment regions

($v_n^l/u_\eta < -1$), the interface and the sublayer thicknesses are as follows: $\delta_I/\eta = 8.6$, $\delta_\nu/\eta = 3$ and $\delta_{\omega^2}/\eta = 5.7$. Notably, the total TNTI thickness is halved at the high entrainment regions, indicating a much sharper TNTI at these locations. Conversely, the VSL thickness δ_ν does not decrease to the same extent as δ_I and is reduced by a factor of $2/3$ when comparing the mild entrainment regions (E1, E2, E3, E4) with the fast entrainment regions (E5, E6, E7, E8).

Overall, the total thickness of the TNTI and the thickness of its sublayers exhibit more significant variations when comparing the fast entrainment regions to other cases. In contrast, the differences in thicknesses are less pronounced when comparing the regions of detrainment with the mild entrainment regions.

The terms of the enstrophy balance equation, alongside the balance between $\langle D_{\omega^2}\rangle_I$ and $\langle \varepsilon_{\omega^2}\rangle_I$, are shown in figure 4.35 for the conditions D2, E2, E3, and E6, near the detected IES with $\omega_{th}^2/\omega_{ref}^2 = 10^{-3}$. It must be noted that the magnitudes of the terms are significantly higher for the E6 case compared to the other cases, even an order of magnitude difference is present between the D2 and E6 conditions.

The D_{ω^2} term shows a significant amount of enstrophy diffusion towards the non-turbulent region, but the region where the balance $(D_{\omega^2} - \varepsilon_{\omega^2})$ changes its sign is much closer to the IES for the E6 case compared to the other entrainment cases, E2 and E3. This behaviour is consistent with the observation that the vortical activity is tightly packed near the IES in the E6 condition, possibly due to the significant positive values of $\langle v_l\rangle_I$ which may also lead to the P_{ω^2} term remaining much higher until very close to the IES location along the axis of y_I/η for the E6 condition.

The variation of $\hat{h}$ across the TNTI for the conditional cases is shown in figure 4.36. It is evident that the TNTI-averaged behaviour of $\hat{h}$ is very different for the D2 and E6 conditions on the one hand and for the E2 and E3 conditions on the other. The unconditioned TNTI-average profile $\langle|\hat{h}|\rangle_I$ presented in figure 4.21 is similar to the TNTI-average behaviour of $\langle|\hat{h}|\rangle_I$ conditioned by E2 and E3.

In the cases of D2 and E6, the values of $\langle|\hat{h}|\rangle_I$ drop significantly as one approaches the IES. This behaviour is particularly pronounced for the E6 condition. It can be noted also that the TNTI-averaged profile of $\langle P_{\omega^2}\rangle_I$ in figure 4.34d shows a peak in mean production of enstrophy close to the IES, at $y_I/\eta \approx -5.75$.

Regarding the D2 condition, there is also a significant drop in $\langle|\hat{h}|\rangle_I$ across the TNTI. It should be reminded that $\hat{h}$ gives information about the orientation of the velocity and vorticity vectors with respect to each other but not about their magnitudes. Taking this into account, the ω^2 values are significantly low as we approach the IES for the D2 condition. Thus it is possible that the vorticity aligns in such a way that it is perpendicular to the local velocity

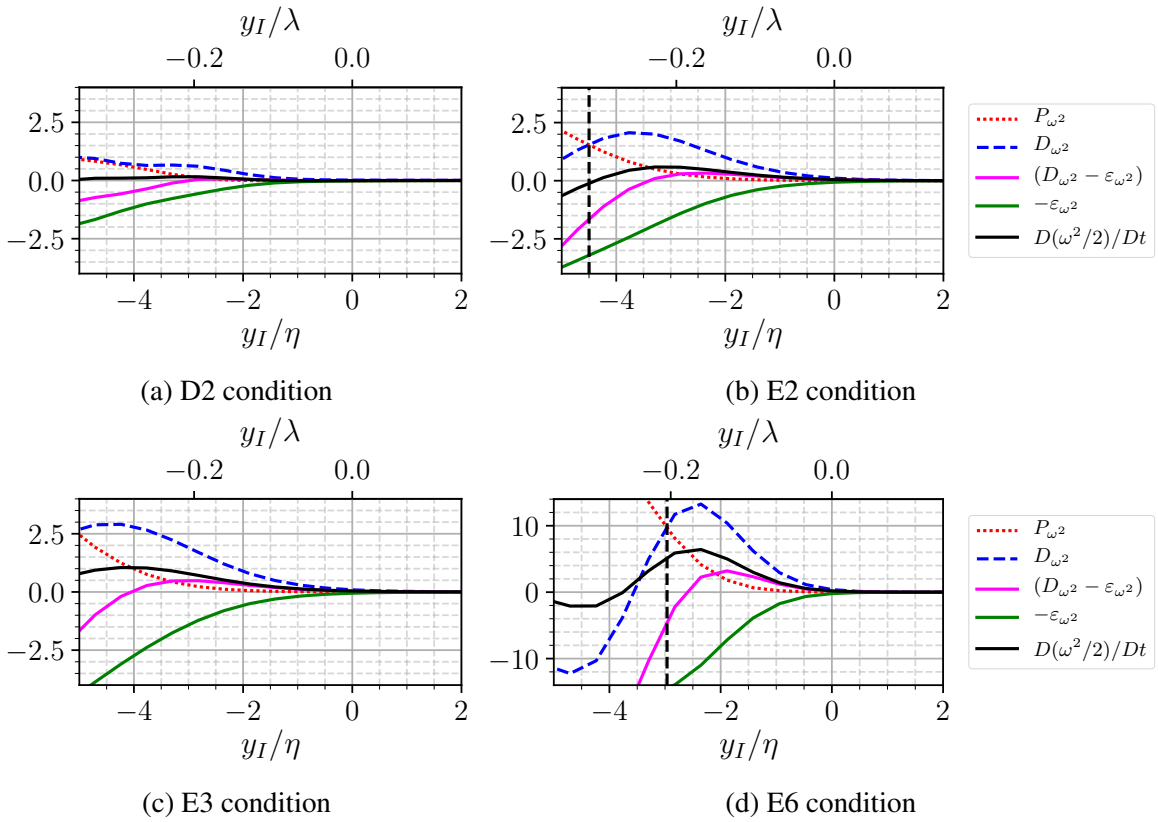

(a) D2 condition

(b) E2 condition

(c) E3 condition

(d) E6 condition

Fig. 4.35 TNTI-averaged profiles of P^2_ω, D^2_ω and ε^2_ω given along with the balance of $(D_{\omega^2} - \varepsilon_{\omega^2})$ and the term $D(\omega^2/2)/Dt$ computed from the balance of the RHS of the eq. 4.30 for the conditions of D2, E2, E3 and E6. The vertical dashed line marks the extent of VSL. Profiles are obtained for the IES of $\omega^2_{th}/\omega^2_{ref} = 10^{-3}$, for PJ4-HR at $t/T_{ref} = 50$.

near the IES, but looking at the figure 4.34a, it can be observed that this does not lead to a significant P_{ω^2} across the interface.

Another interesting observation is that the $\langle \hat{h} \rangle_I$ values are higher towards the turbulent core for the D2 condition compared to the E2, E3 and especially E6 conditions (at $y_I/\eta = -23$ in figures 4.36a, 4.36b, 4.36c and 4.36d). This suggests that non-linearity is less on the turbulent side of the regions associated with D2 compared to the E2, E3 and E6 conditions. Due to the local fields at regions associated with the D2 condition, P_{ω^2} does not contribute to $D(\omega^2/2)/Dt$ as much as in the regions associated with regions where local entrainment is present.

The profiles of $\langle |\hat{h}| \rangle_I$ for the regions satisfying the E2 and E3 conditions indeed appear to be more similar to the unconditioned TNTI mean profile along the y_I/η axis. However, a slight change can be observed for the location y_I/η where the $\langle |\hat{h}| \rangle_I$ has a minimum. It is not surprising to see that the local flow topology is different for the concave/convex shapes as a

significant difference is already observed for the $\langle P_{\omega^2} \rangle_I$ profiles between figures 4.34c and 4.34b.

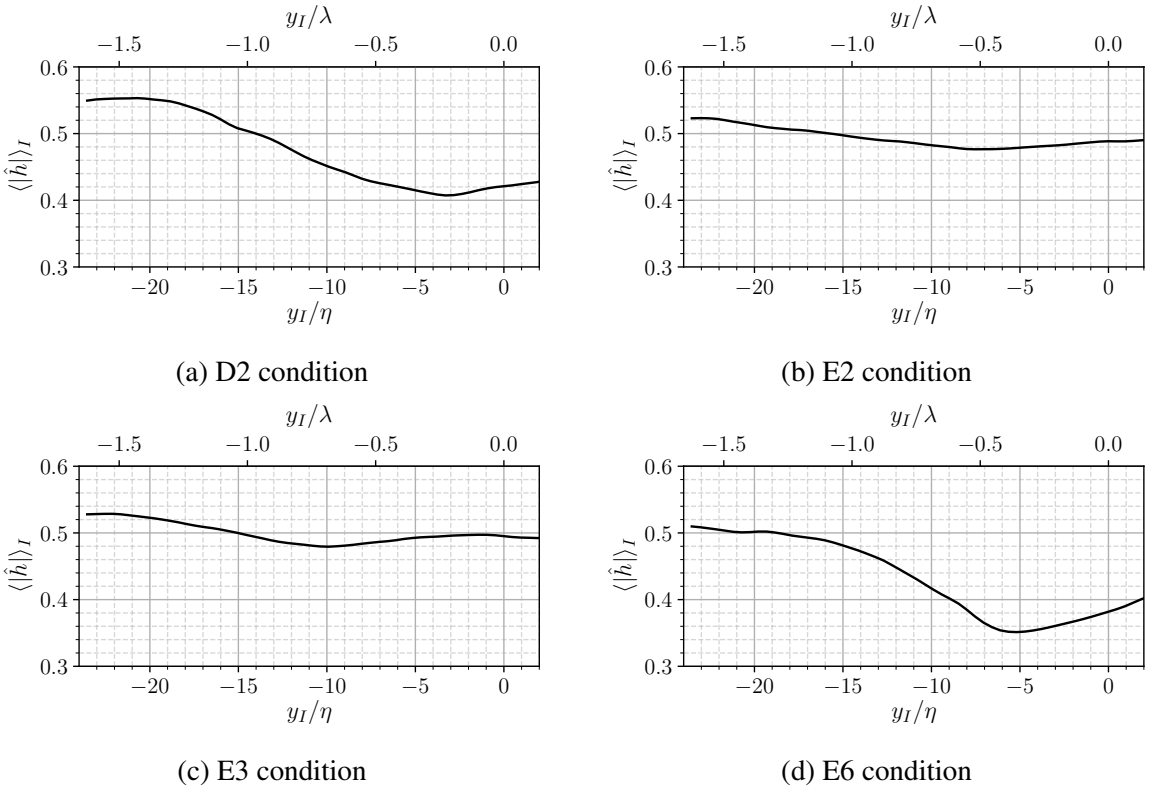

(a) D2 condition

(b) E2 condition

(c) E3 condition

(d) E6 condition

Fig. 4.36 TNTI-averaged profiles of the absolute value of the relative helicity $\langle |\hat{h}| \rangle_I$ (eq. 4.32) computed for the conditions of D2, E2, E3 and E6. Profiles obtained for the IES of $\omega_{th}^2/\omega_{ref}^2 = 10^{-3}$. At $t/T_{ref} = 50$ for PJ4-HR simulation.

The variation of the PDF of $\hat{h}$ at various locations from the IES is given in figure 4.37 for the various conditions. Again a similarity between the D2 and E6 cases is visible, while there is of course a difference in terms of the convergence of the PDFs considering the number of locations on IES satisfying the D2 and E6 conditions. Otherwise, an abrupt change in the shape of the PDF is present for these two conditions, which occurs between $y_I/\eta = -14.1$ and $y_I/\eta = -4.7$ as in the unconditioned situation (see figure 4.22).

For the conditions of E2 and E3, the shape of the PDFs remains the same across the interface. The PDFs are checked also at locations further towards the non-turbulent side ($y_I/\eta > 2.4$) and no transition of the shape of the PDFs is observed as has been shown to be the case for D2 and E6 conditions. The PDFs remain similar until y_I/η locations where the values of $|\boldsymbol{u}|$ and $|\boldsymbol{\omega}|$ are getting so small that $\hat{h}$ becomes irrelevant.

Finally, to investigate if the ED conditions correlate with specific interface orientations, we examine the PDFs of $\boldsymbol{e}_y \cdot \boldsymbol{i}$ for D2, E2, E3, and E6 conditions, as illustrated in figure

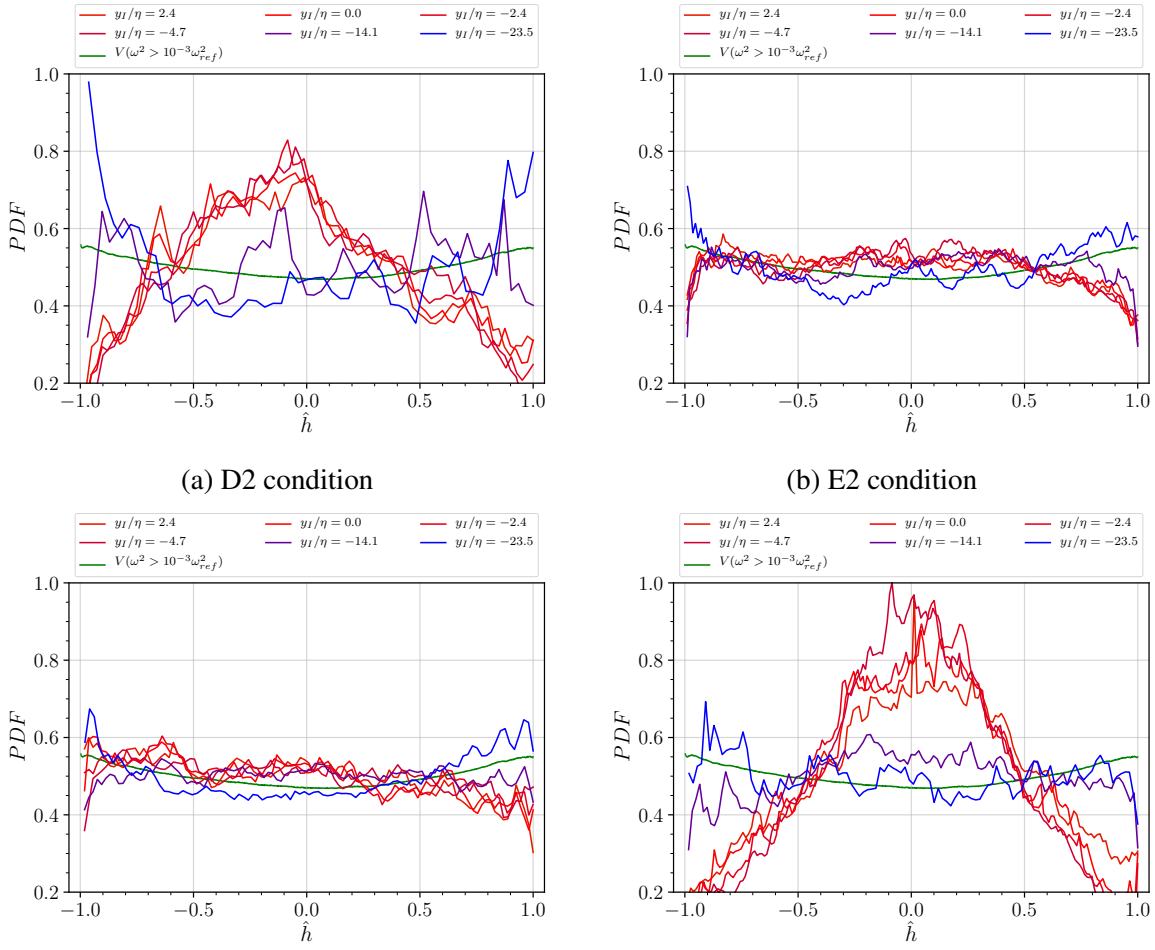

(a) D2 condition

(b) E2 condition

(c) E3 condition

(d) E6 condition

Fig. 4.37 PDF of $\hat{h}$, at various y_I locations for the conditions D2, E2, E3 and E6, with respect to the IES of $\omega^2_{th}/\omega^2_{ref} = 10^{-3}$ at $t/T_{ref} = 50$ for PJ4-HR simulation.

4.38. The PDFs reveal a notable trend that the local entrainment predominantly occurs in the downstream-facing regions of the interface, which aligns with the findings by Watanabe et al. (2014a) for the spatially developing turbulent jets. This preference becomes particularly pronounced in cases with high entrainment velocities, such as the E6 condition. Although there are still instances of other orientations, the PDF for the E6 condition exhibits a prominent peak around $\boldsymbol{e}_y \cdot \boldsymbol{i} \approx 0.52$, corresponding to an angle of approximately 60° between the face normal vector $\boldsymbol{e}_y$ and $\boldsymbol{i}$. Implying that the IES extends into the non-turbulent region primarily in the downstream-facing regions of the TNTI.

Even though the asymmetry observed in the orientation of the $\boldsymbol{e}_y$ vector for regions meeting the D2 condition is not as pronounced as the E6 condition, there exists a clear and strong trend showing that the regions of the interface where local detrainment occurs are

more often at the upstream-facing regions of the interface. Watanabe et al. (2014a) present similar results showing the propagation of the interface regions towards the turbulent core in the regions facing in the upstream direction.

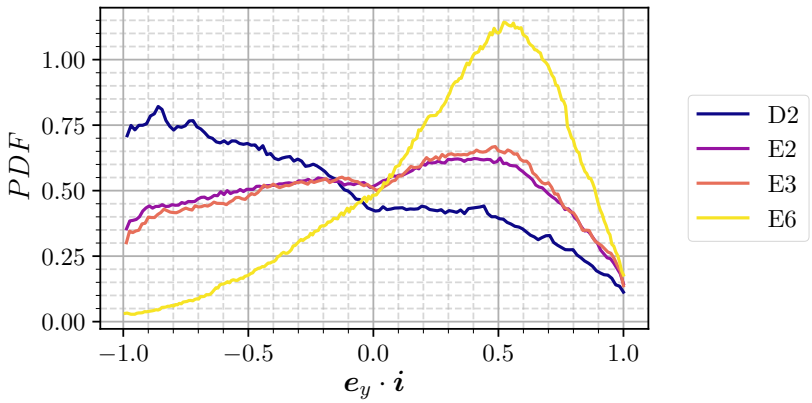

Fig. 4.38 PDF of the orientation of the face normal e_y with respect to the global streamwise direction i, for the conditions of D2, E2, E3 and E6.

4.12 Conclusions on the TNTI-average statistics of the flow field

In contrast to chapter 3, a spatially local methodology is used to analyze the flow field in the proximity of the TNTI and its various sublayers. The chapter begins by providing a definition of the TNTI-averaging operation, which is also utilized in chapter 5.

The TNTI-averaged local statistics are analyzed in the vicinity of the interface. Also, the orientation of the interface surface has been discussed with respect to the streamwise, cross-stream, and spanwise directions. Following the literature, the ω^2 balance equation has been used in order to distinguish the various sublayers of the TNTI by the TNTI-average profiles of the terms of the enstrophy balance equation.

Subsequently, the local propagation velocity v_n^l of the IES has been presented following the studies by Holzner and Lüthi (2011) and van Reeuwijk and Holzner (2014). The TNTI-average statistics for the local entrainment/detrainment regions are distinguished by conditioning the local fields on v_n^l. Similarly, the TNTI-average statistics for the concave/convex regions are distinguished by applying a condition on the mean curvature H_m. The variation of the local TNTI properties such as the TNTI local fields of velocity, vorticity, pressure, enstrophy, the thicknesses of the interface and its sublayers have been investigated

conditionally, for regions of the interface, which have different entrainment/detrainment - concave/convex characteristics.

Figure 4.39 gives an overview of the TNTI of the temporally developing turbulent planar jet, which summarizes the observations made throughout the present chapter as a result of all the analysis being conducted.

A sketch of the geometrical property of the interface is given in figure 4.39a. The shape of the TNTI has been mainly discussed in section 4.6 in terms of the PDFs of the orientation of the face normal vector $\boldsymbol{e}_y$ with respect to the global streamwise, cross-stream, and spanwise directions (see figure 4.11) and in sections 2.5 and 4.11 in terms of the PDF of the local mean curvature H_m.

It has been concluded that the TNTI mostly consists of concave surfaces and the average value of H_m across the IES shows that the most probable radius of curvature for the IES of $\omega_{th}^2/\omega_{ref}^2 = 10^{-3}$ is $R_c \approx 0.5\lambda = 7\eta$ (see figure 4.28b). By analyzing the PDFs presented in figure 4.11, it has been shown that in the regions facing towards the downstream direction, $\boldsymbol{e}_y$ makes predominantly a 60° angle with the unit vector pointing in the streamwise direction, $\boldsymbol{i}$. Conversely, the distribution for the upstream-facing regions (corresponding to $\boldsymbol{e}_y \cdot \boldsymbol{j} < 0$ in the PDF shown in figure 4.11) is observed to be flatter without exhibiting any particular angle, which suggests that these regions have features closer to a half-sphere.

Furthermore, the analysis of the TNTI-averaged local fields of $\boldsymbol{u}'$, p and ω^2 (see figures 4.14b, 4.18a and 4.17) show that there exists a rotating motion near the interface, which is oriented in the spanwise direction and rotates in the counter-clockwise direction in the TNTI-average local frame, which is an average over many local frames along the interface. This observation is also depicted in figure 4.39a with the mention of the radius of these rotating motions observed to be approximately $1.5\lambda = 0.23\delta$. A possible reason for the mean rotating motion is located asymmetrically along x_I instead of $x_I/\eta = 0$, in figure 4.16, is the asymmetric shape of the TNTI in the streamwise direction (the difference between upstream/downstream facing regions). The peculiar shape of the interface, which exhibits an extension in the downstream direction (see figure 4.39a) leads to more frequent sampling of the rotating motion at the local upstream part of the TNTI-average field which corresponds to $x_I < 0$ regions in TNTI-average local fields such as in figure 4.14b.

On the other hand, figure 4.39b illustrates the various regions associated with D2, E2, E3, and E6 conditions, which are distinguished by the application of different conditions on the local values of H_m and v_n^l (see table 4.1). The regions of $D\omega^2/Dt > 0$ and $D\omega^2/Dt < 0$ are also marked with red and green shading respectively, which are observed as a result of the investigation of the terms for the ω^2 balance equation conditional on H_m and v_n^l in section 4.11.2.

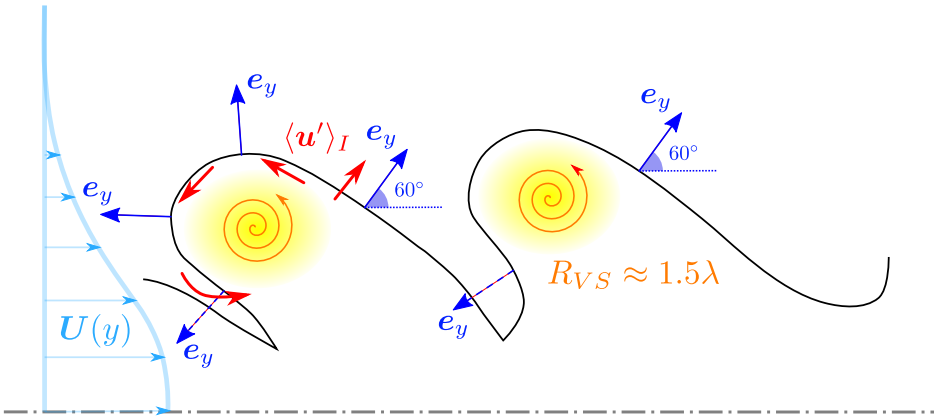

(a) A sketch of the TNTI (black line represents the IES of $\omega_{th}^2/\omega_{ref}^2 = 10^{-3}$), where the face normal vector $\boldsymbol{e}_y$ and its predominant orientation of 60° is illustrated with respect to $\boldsymbol{i}$. The fluctuating velocity field relative to the TNTI is denoted by red arrows $\langle \boldsymbol{u}' \rangle_I$. The arrows are placed by taking into account the TNTI-average velocity fields obtained for ED conditions and the predominant orientations for each condition. The rotating motions observed in the TNTI-averaged local field $\langle \boldsymbol{u}' \rangle_I$ are also shown by orange arrows in the TNTI local reference frame. where $R_{VS} \approx 1.5\lambda$ stands for the radius of these vortical structures.

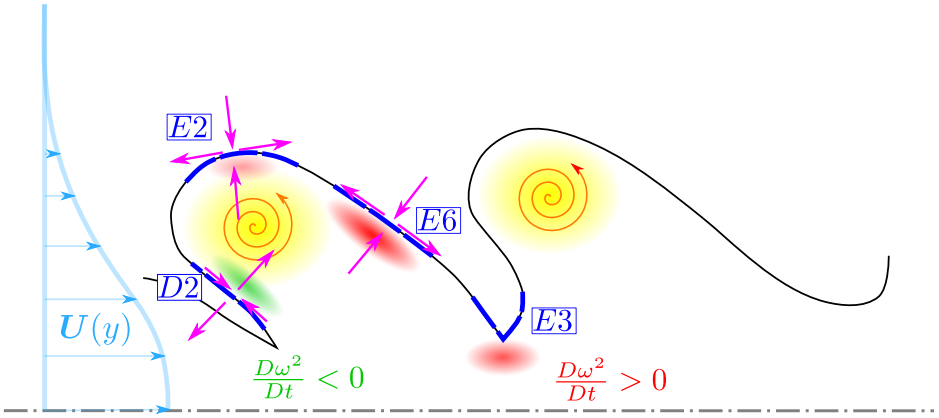

(b) Showing the regions associated with D2, E2, E3 and E6 conditions on the same sketch of the interface. The regions where $D\omega^2/Dt > 0$ and $D\omega^2/Dt < 0$, are denoted by the red and green shadings, and the magenta arrows indicate the directions of TNTI-average compression/stretching motions at certain locations.

Fig. 4.39 General picture of the TNTI of temporally developing turbulent planar jet.

An important result from the analysis of the ω^2 balance across the interface is that the P_{ω^2} is observed to be crucial in the regions of local entrainment regions. The investigation of the PDF of relative helicity $\hat{h}$ at various distances from the interface, in figure 4.22, shows the vectors of $\boldsymbol{\omega}$ and $\boldsymbol{u}$ being oriented more orthogonally with respect to each other, as the outer edge of the interface is approached, which limits the rate of decay of P_{ω^2} towards the non-turbulent region.

The main observations made in the chapter can be summarized as:

- The magnitudes of the tangential components of the vorticity vector rise sharply, and even exhibit a peak on the turbulent side of the TNTI for the local spanwise component. On the contrary, the vorticity component normal to the interface shows much smaller gradients as the TNTI acts as a boundary for the turbulent region.

- The TNTI is associated with very high gradients of TNTI-average turbulent stress $\langle u''v'' \rangle_I$ along the interface normal direction, where $''$ stands for the fluctuations with respect to the TNTI-averaging.

- A non-zero TNTI normal velocity $\langle v_l \rangle_I$ is observed along the y_I axis, even though the cross-stream velocity, averaged over the homogeneous $(x-z)$ directions, is zero for all the locations along y. Moreover, the profile of $\langle v_l \rangle_I$ is determined by the correlation between $\boldsymbol{u}''$ and $\boldsymbol{e}''$ vectors i.e., the term $\langle \boldsymbol{u}'' \cdot \boldsymbol{e}'' \rangle_I$.

- In qualitative agreement with the prediction of Reynolds (1972), a jump in the tangential component of the TNTI-average velocity i.e., $\langle u_l \rangle_I$, across the thickness of the TNTI is observed. On the other hand, the prediction that $\langle v_l \rangle_I$ is equal on both sides of the TNTI by Reynolds (1972) is shown not to hold.

  The principal reason why the relations obtained by Reynolds (1972) do not hold is the stretching motion on average, in the tangential direction of the interface. This mean velocity in the outwards direction on the tangential plane causes a significant outward flux of mass/momentum from the side faces of the CV, which have been omitted in the study of Reynolds (1972).

- The orientation of the TNTI has shown that the regions of the interface facing in the downstream direction predominantly make a 60° angle with the unit vector pointing in the downstream direction in the global coordinate system $\boldsymbol{i}$ (see section 4.6).

- A rotating, vortex-like motion is observed in the TNTI-averaged local velocity field $\langle \boldsymbol{u}' \rangle_I$ which is aligned in the local spanwise direction. It should be noted that this motion is observed in the TNTI local reference frame, which is an average of many local frames. The contribution of $\langle \boldsymbol{u}' \rangle_I$ is found to be crucial for the local features observed in the TNTI local velocity field both for the rotational motion and also for the jump of the tangential velocity across the TNTI.

- The terms of the enstrophy budget equation are analyzed in the vicinity of the TNTI. Both the qualitative balance of the terms and the measured thicknesses of the TNTI

and its sublayers are in agreement with the results in the literature (see section 4.8). It has been known that the propagation of the ω^2 into the non-turbulent region occurs due to the D_{ω^2} in the outer regions of the TNTI. In addition to that, the importance of the production term P_{ω^2} has been pointed out in the present analysis, especially in the y_I locations where $D\omega^2/Dt > 0$ while $(D_{\omega^2} - \varepsilon_{\omega^2}) < 0$.

- In relation to P_{ω^2}, the $\boldsymbol{\omega}$ and $\boldsymbol{u}$ vectors are oriented more orthogonally near the TNTI, compared to the centre-plane of the jet. This maximizes the non-linearity (for given the magnitudes of $\boldsymbol{\omega}$ and $\boldsymbol{u}$) across the TNTI, which in turn contributes locally to P_{ω^2}.

- The local detrainment/entrainment can be associated with the interface normal component of $\langle \boldsymbol{u} \rangle_I$ pointing towards the turbulent core/non-turbulent region respectively.

- Considering the detrainment, entrainment, and fast entrainment conditions (associated with different values of v_n^I), the mean thicknesses of the TNTI, VSL and TSL are observed to vary for each condition. More radical differences in the thicknesses have been observed between moderate entrainment ($-1 < v_n^I/u_\eta < 0$) and fast entrainment ($-2 < v_n^I/u_\eta < -1$) regions, while the mean thicknesses at the detrainment regions ($-1 < v_n^I/u_\eta < 0$) remain similar to moderate entrainment condition. For moderate entrainment regions, the thicknesses for the whole TNTI layer, VSL and TSL are observed to be $\delta_I = 16.5\eta$, $\delta_v = 4.6\eta$ and $\delta_{\omega^2} = 12\eta$, while at the fast entrainment regions, these thicknesses are measured to be $\delta_I = 8.6\eta$, $\delta_v = 3\eta$ and $\delta_{\omega^2} = 5.7\eta$.

- The fast entrainment regions can be associated with very high values of local P_{ω^2}. A significant peak is present in the TNTI-average profile of P_{ω^2} for the E6 condition.

- The face normal vector $\boldsymbol{e}_y$ has different predominant facing directions for each condition at the regions of the TNTI associated with detrainment, entrainment, and fast entrainment, which are upstream, slightly downstream and more significantly downstream (see figure 4.38).

Chapter 5

Interscale/Interspace Energy Transfer at the TNTI

5.1 Kármán-Howarth-Monin-Hill equation

As demonstrated in previous chapters and numerous prior studies, the TNTI is a highly localized phenomenon. Consequently, investigating the energy cascade in proximity to this interface presents its own set of challenges. In this chapter, we undertake an analysis of the energy balance on a scale-by-scale basis near the TNTI using the Kármán-Howarth-Monin-Hill (KHMH) equation. The KHMH equation, in its most general form, was derived by Hill (2002) (equations for the structure functions of all orders are obtained in Hill (2001)) without making any assumptions regarding flow field characteristics such as isotropy or homogeneity. Moreover, it does not involve any averaging or decomposition of velocity. Essentially, this equation is an evolution equation that describes the instantaneous, local turbulent kinetic energy associated with scales determined by the separation vector $\boldsymbol{r}$. It offers valuable insights into how kinetic energy varies at different scales due to various mechanisms of energy transfer in both physical and scale space.

The derivation of the KHMH equation starts by writing the Navier-Stokes equations

$$\frac{\partial u_i}{\partial t} + u_j \frac{\partial u_i}{\partial x_j} = -\frac{1}{\rho}\frac{\partial p}{\partial x_i} + \nu \frac{\partial^2 u_i}{\partial x_j^2}, \tag{5.1}$$

at two points $\boldsymbol{\xi}_1$ and $\boldsymbol{\xi}_2$, separated by a vector $\boldsymbol{r}$ ($\boldsymbol{r} = (\boldsymbol{\xi}_2 - \boldsymbol{\xi}_1)$), where the mid-point between these two points (centroid) is denoted $\boldsymbol{X} \equiv \frac{1}{2}(\boldsymbol{\xi}_1 + \boldsymbol{\xi}_2)$ (see figure 5.1).

By subtracting the Navier-Stokes equation at $\boldsymbol{\xi}_1$ from the Navier-Stokes equation at $\boldsymbol{\xi}_2$, equations for components of $\delta\boldsymbol{u}$ are obtained, where each component δu_i is defined by the

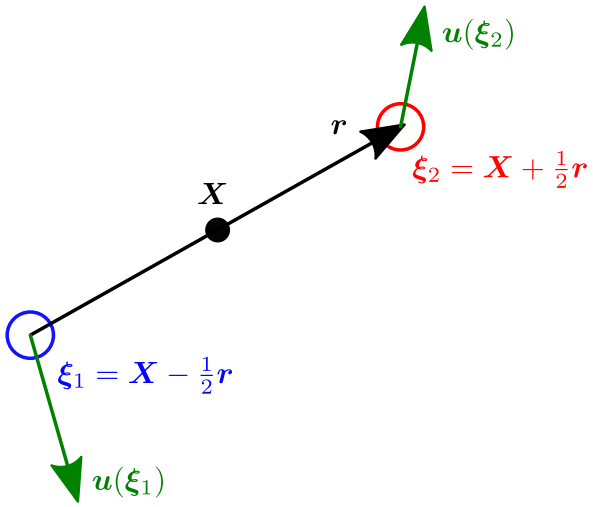

Fig. 5.1 Schematic of the two-point separation.

difference between the one-point velocity components at the two points;

$$\delta u_i = u_i(\boldsymbol{\xi}_2) - u_i(\boldsymbol{\xi}_1). \tag{5.2}$$

Changing variables from $\boldsymbol{\xi}_1$ and $\boldsymbol{\xi}_2$ to $\boldsymbol{X}$ and the separation vector $\boldsymbol{r}$ and multiplying by δu_k leads to an equation for $\delta u_k \frac{\partial}{\partial t}\delta u_i$. The same procedure can be applied to obtain an equation for $\delta u_i \frac{\partial}{\partial t}\delta u_k$. The two equations can be summed in order to have the symmetry under the interchange of the pair of indices, and the equation for $|\delta \boldsymbol{u}|^2$ can be obtained by taking the trace of the result (Hill, 2002):

$$\begin{aligned}
&\frac{\partial}{\partial t}|\delta \boldsymbol{u}|^2 + \delta u_j \frac{\partial}{\partial r_j}(|\delta \boldsymbol{u}|^2) + u_j^* \frac{\partial}{\partial X_j}|\delta \boldsymbol{u}|^2 = \\
&-\frac{2}{\rho}\delta u_i \frac{\partial}{\partial X_i}(\delta p) + 2\nu \frac{\partial^2}{\partial r_j^2}|\delta \boldsymbol{u}|^2 + \frac{\nu}{2}\frac{\partial^2}{\partial X_j^2}|\delta \boldsymbol{u}|^2 - 2\nu\left[\left(\frac{\partial u_i}{\partial x_j}\right)^2\Big|_1 + \left(\frac{\partial u_i}{\partial x_j}\right)^2\Big|_2\right].
\end{aligned} \tag{5.3}$$

Here, the terms with $\partial/\partial X_i$ are associated with variations in physical space, while the terms with $\partial/\partial r_i$ are associated with variations in scale space. The $\boldsymbol{u}^*$ stands for the sum of velocities at two points $\boldsymbol{u}^* = (\boldsymbol{u}_2 + \boldsymbol{u}_1)$. The notation for each term in the presentation of the results in this chapter is as follows;

$$D_t + T_y + T_r = -T_p + D_r + D_c - \varepsilon \tag{5.4}$$

Each term in the KHMH eq. 5.3 (equivalently eq. 5.4) corresponds to a different mechanism contributing to the balance of the local, instantaneous scale-by-scale kinetic energy, $|\delta \boldsymbol{u}|^2$;

- $D_t = \frac{\partial}{\partial t}|\delta \boldsymbol{u}|^2$ is the rate of change of $|\delta \boldsymbol{u}|^2$ in time, at a location $\boldsymbol{X}$, for the separation vector $\boldsymbol{r}$. Due to the nature of the flow that we consider in this study, the average of D_t is non-zero (both TNTI-averaging and $(x-z)$ averaging), which differs from some other studies where this term vanishes as a result of the averaging procedure employed (Apostolidis et al., 2023; Yuvaraj, 2021).

- $T_r = \delta u_j \frac{\partial}{\partial r_j}|\delta \boldsymbol{u}|^2$ represents the interscale transfer of $|\delta \boldsymbol{u}|^2$ and the redistribution of the energy in scale space.

- $T_y = u_j^* \frac{\partial}{\partial X_j}|\delta \boldsymbol{u}|^2$ is the advection term, responsible for the interspace energy transfer, and redistribution of the energy in physical space.

- $T_p = -\frac{2}{\rho}\delta u_i \frac{\partial}{\partial X_i}(\delta p)$ is the pressure-velocity term, accounting for the effects of pressure.

- $D_r = 2\nu \frac{\partial^2}{\partial r_j^2}|\delta \boldsymbol{u}|^2$ is the term responsible for the viscous diffusion of $|\delta \boldsymbol{u}|^2$ in scale-space. This term reduces to ε when the separation between the two points is zero ($\boldsymbol{r} = 0$). With ε, it is the only non-zero term in eq. 5.3 at $\boldsymbol{r} = 0$. In addition to that, it has been shown by Valente and Vassilicos (2015) that the contribution of this term becomes negligible compared to the dissipation term, for separations larger than the Taylor length scale λ.

- $D_c = \frac{\nu}{2}\frac{\partial^2}{\partial X_j^2}|\delta \boldsymbol{u}|^2$ is the viscous diffusion of $|\delta \boldsymbol{u}|^2$ in physical space. This term is analogous to the diffusion term in the one-point turbulent kinetic energy equation and is expected to have a small contribution when averaged over homogeneous directions, at all scales.

- $\varepsilon = 2\nu\left[\left(\frac{\partial u_i}{\partial x_j}\right)^2\Big|_1 + \left(\frac{\partial u_i}{\partial x_j}\right)^2\Big|_2\right]$ is referred to as the dissipation term. It is the sum of pseudo-dissipation at the two points $\boldsymbol{\xi}_1$ and $\boldsymbol{\xi}_2$.

In the present chapter, all the individual terms of the KHMH equation are expressed in TNTI local reference frame variables introduced in section 4.2 in order to investigate the contributions of the various mechanisms on the evolution of $|\delta \boldsymbol{u}|^2$ in the vicinity of the TNTI. Similarly to chapter 4, we focus on the flow field at time $t/T_{ref} = 50$ which is in the range of times where the temporally developing turbulent planar jet is self-similar. Computation

results at times $t/T_{ref} = 38$, $t/T_{ref} = 62$ and $t/T_{ref} = 74$ showed that the TNTI-averaged KHMH terms remain qualitatively the same at these instants, showing a similar balance between the different terms.

The details for the post-processing of the individual terms are described by Yuvaraj (2021), where the terms in eq. 5.3 are computed on the basis of spatial derivatives with respect to $\boldsymbol{\xi}_1$ and $\boldsymbol{\xi}_2$. The derivatives of the flow quantities for the TNTI local fields are computed by using 4^{th} order finite differences applied to the local coordinate system e.g. to the fields of u_l, v_l, w_l defined in section 4.3. Due to the high resolution of the dataset being used, our 4^{th} order scheme has sufficient accuracy for the calculation of the derivatives, which is verified by checking the balance of NS and KHMH equations in the local fields.

Following the analysis conducted in the work of Zhou and Vassilicos (2020), we place the centroid $\boldsymbol{X}$ on the detected IES for the investigation of the budget at the border of the turbulent jet. By fixing the location $\boldsymbol{X}$ at a given time, the remaining dependencies of the terms are reduced to (r_x, r_y, r_z) which correspond to two-point separations in x_I, y_I and z_I directions. The TNTI-averaging process is applied at this stage to each KHMH term. Following the methodology used in Zhou and Vassilicos (2020), the obtained TNTI-average fields (3D in scale space) are further averaged over the angle tangential to the IES (rotation around the IES normal axis) resulting in the TNTI local mean KHMH terms becoming only function of r_n and r_t where r_n is the separation of the two points in the IES normal direction and r_t is the separation of the two points in the direction tangential to the IES. A schematic is given in figure 5.2, where the tangential plane at the location $\boldsymbol{X}_0$, on the IES is denoted by a green shade, given along with the location of the two-points $\boldsymbol{\xi}_1$ and $\boldsymbol{\xi}_2$ with respect to the centroid $\boldsymbol{X}$ and the angles θ and ϕ (in the figure, the centroid $\boldsymbol{X}$ is placed on the IES location $\boldsymbol{X}_0$ thus $\boldsymbol{X} = \boldsymbol{X}_0$).

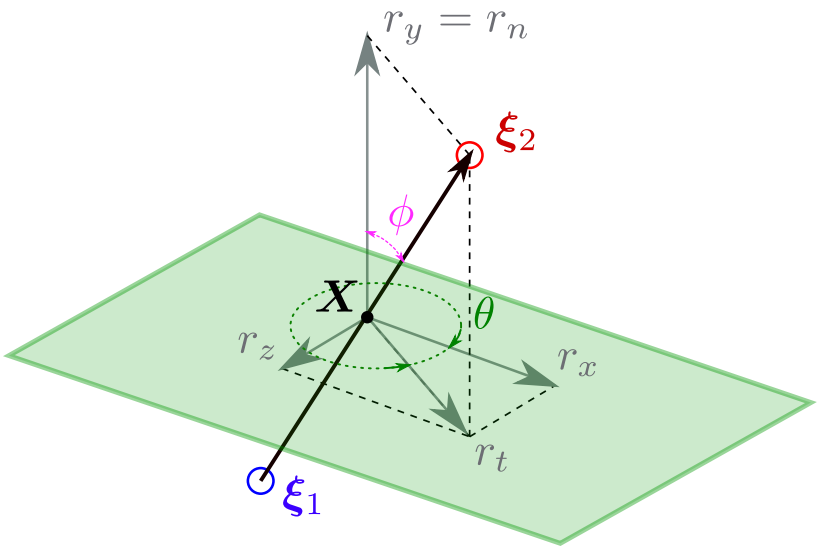

Fig. 5.2 Schematic showing the local separation vector $\boldsymbol{r}$ and its components $r_y = r_n$, r_x, r_z and r_t, and the θ angle along which the averaging operation is applied.

5.2 KHMH balance at the TNTI location

Figure 5.3 shows 1D profiles of TNTI-averaged KHMH terms, as functions of the separation vector r_n/η in the interface normal direction and r_t held at zero. For the analysis of the profiles, we have employed two different normalizations.

Firstly, we have normalized the profiles by the average dissipation at the centre-plane ε_c as shown in figure 5.3a, and secondly by the $\varepsilon(r_n)$ profile in figure 5.3b. The latter normalization allows us to assess the magnitude of the terms relative to the ε for each separation r_n/η, where η is calculated based on the centre-plane one point dissipation ε_c.

As anticipated, all the terms, except for $\langle D_r \rangle_I$ and $\langle \varepsilon \rangle_I$, become zero when $r_n/\eta = 0$. At this point, these two terms are in equilibrium, which can be seen in figure 5.3b. As separation values r_n increase slightly, we observe a rapid increase in the magnitudes of the time derivative term $\langle D_t \rangle_I$ and the transport in physical space $\langle T_y \rangle_I$. Following closely behind are the pressure-velocity $\langle T_p \rangle_I$ and the interscale transfer $\langle T_r \rangle_I$ terms, even though their rates of increase are comparatively slower compared to the former two.

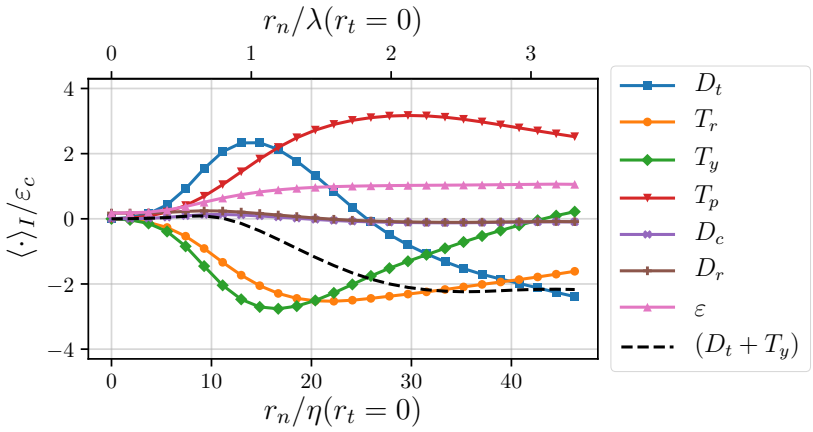

(a) TNTI-averaged KHMH terms normalized by the mean centre-plane dissipation ε_c.

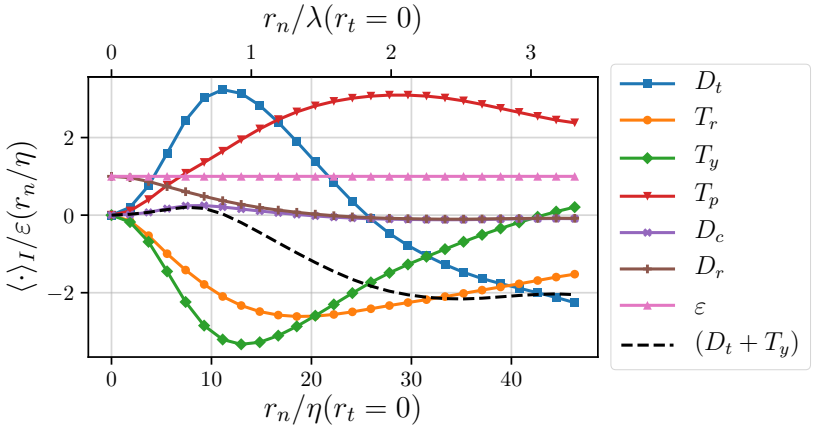

(b) TNTI-averaged KHMH terms normalized by the profile of $\varepsilon(r_n/\eta)$.

Fig. 5.3 KHMH terms computed centred at the IES location, as functions of separation vector in TNTI normal direction r_n/η for iso-surface of $\omega_{th}^2/\omega_{ref}^2 = 10^{-3}$.

5.2.1 The role of advection at the TNTI location

The $\langle D_t\rangle_I$ and $\langle T_y\rangle_I$ terms exhibit an inverse correlation over the entire range of r_n. Their magnitudes are approximately equal, establishing the approximate relationship $\langle D_t\rangle_I \approx -\langle T_y\rangle_I$ until $r_n/\eta = 11.4$. At $r_n/\eta = 4.3$, the magnitudes of $\langle D_t\rangle_I$ and $\langle T_y\rangle_I$ reach the same magnitude as $\langle\varepsilon\rangle_I$ ($|\langle D_t\rangle_I| = |\langle T_y\rangle_I| = |\langle\varepsilon\rangle_I|$) while $\langle D_r\rangle_I$ remains significant in the local balance of $|\delta\boldsymbol{u}|^2$ for these scales.

Around $r_n/\eta = 11.1$, $\langle D_t\rangle_I/\langle\varepsilon\rangle_I$ reaches its highest contribution, aligning with the negative peak location of $\langle T_y\rangle_I/\langle\varepsilon\rangle_I$. Beyond this point, $|\langle D_t\rangle_I/\langle\varepsilon\rangle_I|$ and $|\langle T_y\rangle_I/\langle\varepsilon\rangle_I|$ begin to diminish, and the difference between their magnitudes increases with increasing r_n/η. Consequently, the sum $(\langle D_t\rangle_I + \langle T_y\rangle_I)/\langle\varepsilon\rangle_I$ starts to decrease. This inverse correlation

between $\langle D_t \rangle_I$ and $\langle T_y \rangle_I$ suggests that the advection of $|\delta \boldsymbol{u}|^2$ is effective across various scales.

Figure 5.3 presents the sum $(\langle D_t \rangle_I + \langle T_y \rangle_I)$ alongside the individual terms of the KHMH equation. According to eq. 5.3, $(\langle D_t \rangle_I + \langle T_y \rangle_I)$ can be interpreted as a material derivative for the rate of change of $|\delta \boldsymbol{u}|^2$ while moving with the flow.

An interesting observation for scales $r_n/\eta < 11.4$ is that a slight imbalance exists between $\langle D_t \rangle_I$ and $\langle T_y \rangle_I$, which results in positive values of $(\langle D_t \rangle_I + \langle T_y \rangle_I)$. Notably, in figure 5.3, $(\langle D_t \rangle_I + \langle T_y \rangle_I)$ closely follows the small $\langle D_c \rangle_I$ term. Even though it may be tempting to conclude that the net increase in $|\delta \boldsymbol{u}|^2$ is due to spatial diffusion by $\langle D_c \rangle_I$, this local balance requires careful consideration since other terms are also significant for these scales.

Additionally, due to the centroid being on the IES of $\omega_{th}^2/\omega_{ref}^2 = 10^{-3}$, a question arises about whether this particular balance $(\langle D_t \rangle_I + \langle T_y \rangle_I) \approx \langle D_c \rangle_I$ for $r_n/\eta < 11.4$ is a result of the external regions of the TNTI being dominated by viscous processes (Corrsin and Kistler, 1955). The investigation of this balance is given also on the IES of $\omega_{th}^2/\omega_{ref}^2 = 10^{-6}$ in section 5.4 to address this question. It should be noted that the viscous mechanism addressed by Corrsin and Kistler (1955) is primarily in relation to the irrotational flow acquiring vorticity when crossing the TNTI. In this analysis, we focus on the rate of change of $|\delta \boldsymbol{u}|^2$, mainly associated with turbulent kinetic energy at specific scales. Therefore, while the positive contribution of $\langle D_c \rangle_I$ to the $|\delta \boldsymbol{u}|^2$ balance is essential for some scales, the balance among $\langle T_r \rangle_I$, $\langle T_p \rangle_I$, $\langle D_r \rangle_I$, and $\langle \varepsilon \rangle_I$ should also be investigated before drawing general conclusions.

5.2.2 Pressure and interscale transfer

The observed partial balance $(\langle D_t \rangle_I + \langle T_y \rangle_I) \approx \langle D_c \rangle_I$ in figure 5.3 also implies another partial balance for scales $r_n < 11.4\eta$, where the interscale transfer $\langle T_r \rangle_I$, over-compensates the pressure-velocity term $\langle T_p \rangle_I$ and also balances $\langle \varepsilon \rangle_I$ along with the viscous diffusion in scale-space $\langle D_r \rangle_I$.

Regarding viscous diffusion in scale space in figure 5.3b, it balances $\langle \varepsilon \rangle_I$ for $r_n = 0$ i.e., $\langle D_r \rangle_I = \langle \varepsilon \rangle_I$. Going to larger scales r_n, it starts diminishing after $r_n/\eta \approx 4$, eventually becoming negligible at $r_n \approx 1.42\lambda$ together with $\langle D_c \rangle_I$, and remains very small but negative for larger values of r_n/η.

The pressure-velocity term $\langle T_p \rangle_I$ increases until $r_n/\eta = 29$ ($r_n/\lambda \approx 2$). Its maximum contribution occurs when points $\boldsymbol{\xi}_1$ and $\boldsymbol{\xi}_2$ on the turbulent and non-turbulent sides are at a distance of the order of λ from the IES. On the other hand, the maximum contribution of the interscale transfer term $\langle T_r \rangle_I$ occurs at $r_n/\eta = 18.4$ ($r_n/\lambda = 1.27$), which corresponds to a situation where the two points are at a distance 9.2η (0.63λ) from the IES. Consequently, the scales which are primarily affected by pressure are larger than those where interscale

transfer is maximal. Nevertheless, the balance $(\langle D_t \rangle_I + \langle T_y \rangle_I) \approx \langle D_c \rangle_I$ (which holds at small $r_n \lessapprox 9\eta$ for the IES $\omega^2_{th}/\omega^2_{ref} = 10^{-3}$) implies the balance $\langle T_r \rangle_I + \langle T_p \rangle_I = \langle D_r \rangle_I - \langle \varepsilon \rangle_I$.

5.2.3 TNTI sublayers and the KHMH balance at various scales

Having observed a local balance between certain terms of the KHMH equation in the previous subsection for $r_n \leq 11.4\eta$ on the IES of $\omega^2_{th}/\omega^2_{ref} = 10^{-3}$, we now aim to explore if there is a connection between these scales and the TNTI sublayers discussed in section 4.8. To do so, we can begin with a brief review of the various TNTI sublayers and their measured sizes, as presented in the previous chapter, chapter 4.

In section 4.8, the various sublayers of the TNTI are identified by examining the terms in the ω^2 evolution equation at different y_I locations along the direction normal to the interface, following previous studies in the literature (Holzner et al., 2008; Silva et al., 2018; Taveira and da Silva, 2014a; Watanabe et al., 2015). These layers have distinct characteristics such as the viscous effects being dominant in the external region of the TNTI, i.e. the VSL and the non-linear production of the enstrophy getting more prominent in the TSL.

Furthermore, as demonstrated in section 4.9, the non-linearity is enhanced by the preferentially orthogonal alignment of the $\boldsymbol{u}$ and the $\boldsymbol{\omega}$ vectors, independent of the decay of their magnitudes. The implications of this observation on ω^2 production have been discussed in sections 4.9 and 4.11.2. It can be anticipated that these distinct sublayers, each possessing unique characteristics, may have consequences on the local scale-by-scale kinetic energy balance.

Of course, it should be kept in mind that these layers are defined by the terms of the enstrophy balance equation (eq. 4.30), while the KHMH equation is formulated for $|\delta \boldsymbol{u}|^2$, which is associated with the kinetic energy at various scales. Consequently, the relationship between these layers and KHMH terms is not straightforward. However, we can compare specific scales with notable contributions from individual terms of the KHMH equation or the size of scales where we observe the scale-local balance between specific terms with the thickness of the layers detected in section 4.8. As a reminder, the average thicknesses of the TNTI, VSL and TSL have been found to be $\delta_I = 16\eta$, $\delta_\nu = 3.3\eta$ and $\delta_{\omega^2} = 12.7\eta$ respectively, based on the TNTI-averaged profiles of the terms acting on the local enstrophy balance (see section 4.8).

Taking these thicknesses into account, it is observed that the $\langle T_p \rangle_I / \langle \varepsilon \rangle_I$ term reaches its peak contribution when the point on the turbulent side reaches the limit of the TNTI layer on the turbulent side, demarcated by the first peak of the TNTI-average profile $\langle \omega^2 \rangle_I$ (see figure 5.3b). Furthermore, when we examine the peak of $|\langle T_r \rangle_I / \langle \varepsilon \rangle_I|$ along the r_n/η axis in relation to the thickness of the TNTI sublayers, we find that the maximum contribution

occurs at approximately $r_n \approx 20\eta$. This location aligns roughly with the middle of the TSL ($\delta_\nu + \delta_\omega/2 = 9.65\eta$) relative to the IES of $\omega_{th}^2/\omega_{ref}^2 = 10^{-3}$.

In the previous section, we observed the relationship $(\langle D_t\rangle_I + \langle T_y\rangle_I) \approx \langle D_c\rangle_I$, for scales $r_n < 11.4\eta$ at the IES of $\omega_{th}^2/\omega_{ref}^2 = 10^{-3}$ (see figure 5.3b). Since $\langle T_y\rangle_I$ represents the transport of $|\delta\boldsymbol{u}|^2$ in physical space, the sum $(\langle D_t\rangle_I + \langle T_y\rangle_I)$ can be interpreted as a material derivative of $|\delta\boldsymbol{u}|^2$. Keeping this in mind, the relation $(\langle D_t\rangle_I + \langle T_y\rangle_I) \approx \langle D_c\rangle_I$, along with the observation that $\langle D_c\rangle_I > 0$, suggests a positive contribution to $|\delta\boldsymbol{u}|^2$ for scales $r_n < 11.4\eta$ by the viscous diffusion in physical space when moving with the flow. Therefore, the observation of $(\langle D_t\rangle_I + \langle T_y\rangle_I) > 0$ for these scales may be associated with the dominant viscous mechanisms expected to operate in the VSL.

Meanwhile, it can be noted that the scales where $(\langle D_t\rangle_I + \langle T_y\rangle_I) > 0$, are larger than the extent of the VSL in the direction of the turbulent core at the IES of $\omega_{th}^2/\omega_{ref}^2 = 10^{-3}$. Taking into account the VSL thickness δ_ν being 3.3η, the scales at which the point on the turbulent side reaches the limit of VSL, corresponds to $r_n/\eta \leq 6.6$ in figure 5.3.

Between $r_n/\eta = 11.4$ and $r_n/\eta = 20$, no specific balance is observed based on the TNTI-average profiles presented in figure 5.3. Within this range of scales, all mechanisms contribute significantly to the scale-by-scale kinetic energy balance, including advection $\langle T_y\rangle_I$, interscale transfer $\langle T_r\rangle_I$, pressure-velocity term $\langle T_p\rangle_I$ and diffusion terms like $\langle D_r\rangle_I$ and $\langle D_c\rangle_I$ even though the latter two are much smaller than the former ones. It is worth noting that this range corresponds to scales associated with length scales close to λ, where λ is the Taylor length scale computed at the centre-plane of the planar jet.

For scales $r_n > 20\eta$, both diffusion terms, $\langle D_c\rangle_I$ and $\langle D_r\rangle_I$, become very small, and the balance of $|\delta\boldsymbol{u}|^2$ is primarily driven by the rest of the terms. For these scales, the balance cannot be reduced to $\langle D_t\rangle_I + \langle T_y\rangle_I \approx 0$ (which could have been a consequence of advection) or to a Kolmogorov-like balance such as $\langle T_r\rangle_I = \langle\varepsilon\rangle_I$.

5.2.4 KHMH balance for the IES of $\omega_{th}^2/\omega_{ref}^2 = 10^{-6}$

Looking at various terms of the KHMH equation presented in figure 5.3, it is apparent that the small scales are predominantly influenced by flow advection i.e., $|\langle D_t\rangle_I + \langle T_y\rangle_I| << min(|D_t|, |T_y|)$. Moreover, there is a net increase in turbulent kinetic energy at these scales when moving with the flow, following a trend similar to viscous diffusion in physical space i.e., $(\langle D_t\rangle_I + \langle T_y\rangle_I) \approx \langle D_c\rangle_I$. The range where $\langle D_c\rangle_I$ is positive is observed to be the scales $r_n/\eta < 18$ and the relation $(\langle D_t\rangle_I + \langle T_y\rangle_I) \approx \langle D_c\rangle_I$ is observed to hold very precisely for scales $r_n/\eta \lessapprox 9$ on the IES of $\omega_{th}^2/\omega_{ref}^2 = 10^{-3}$. It must be noted that the balance $(\langle D_t\rangle_I + \langle T_y\rangle_I) \approx \langle D_c\rangle_I$ does not appear due to the absence of other mechanisms, but it is observed even though the contribution of the other terms are significant (they are even much

higher than the magnitude of $\langle D_c \rangle_I$ for all r_n). Consequently, the question arises about the generality of this balance at different layers of the TNTI i.e., at locations of IES defined by different $\omega_{th}^2/\omega_{ref}^2$.

In order to investigate whether and to what extent local balances such as $(\langle D_t \rangle_I + \langle T_y \rangle_I) \approx \langle D_c \rangle_I$ hold at the locations of different IES, and to document the robustness of the TNTI-averaged KHMH profiles, the TNTI-average profiles of KHMH terms as functions of r_n are given in figure 5.4 for the IES of $\omega_{th}^2/\omega_{ref}^2 = 10^{-6}$. Analysis of the TNTI-averaged profiles at the IES of $\omega_{th}^2/\omega_{ref}^2 = 10^{-6}$ allows us to investigate the generality of the trends observed for the IES of $\omega_{th}^2/\omega_{ref}^2 = 10^{-3}$ in figure 5.3.

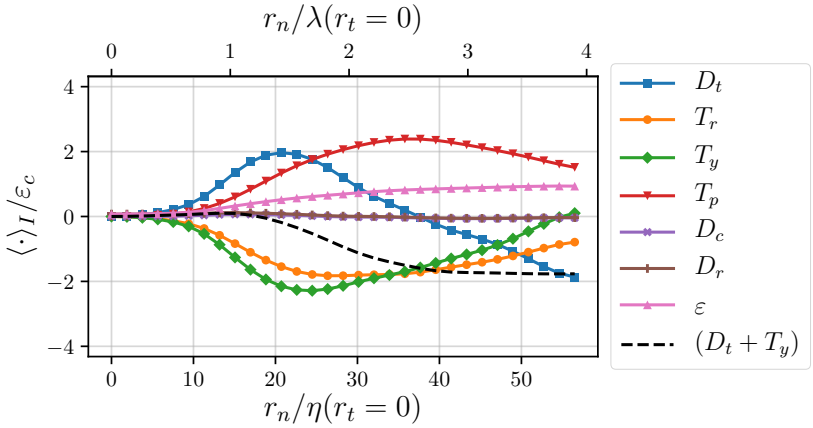

(a) KHMH terms normalized by the mean centre-plane dissipation ε_c (IES of $\omega_{th}^2/\omega_{ref}^2 = 10^{-6}$).

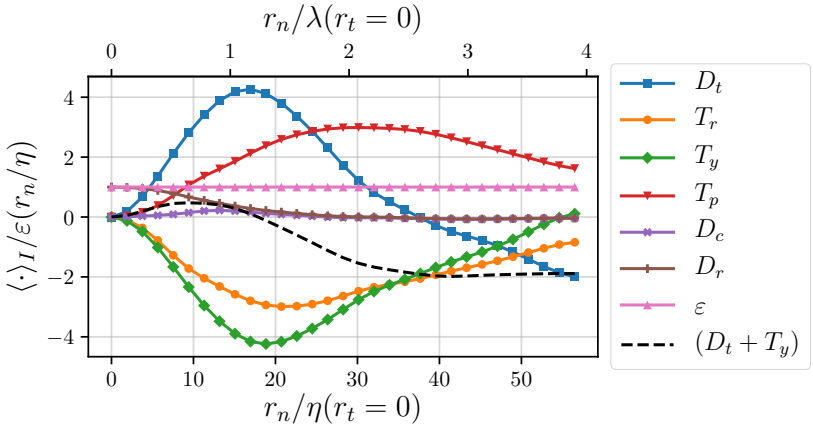

(b) KHMH terms normalized by the profile of $\varepsilon(r_n/\eta)$ (IES of $\omega_{th}^2/\omega_{ref}^2 = 10^{-6}$).

Fig. 5.4 KHMH terms computed centered at the IES of $\omega_{th}^2/\omega_{ref}^2 = 10^{-6}$, as functions of separation vector in TNTI normal direction r_n/η. Computed for the PJ4-HR simulation at $t/T_{ref} = 50$.

In figure 5.4b, it is noticeable that at the location of the IES of $\omega_{th}^2/\omega_{ref}^2 = 10^{-6}$, the sum $(\langle D_t\rangle_I + \langle T_y\rangle_I)$ exceeds the value of $\langle D_c\rangle_I$ for scales $r_n/\eta < 16$. This indicates that there are mechanisms other than $\langle D_c\rangle_I$ contributing to the net kinetic energy increase at these scales. This difference between the profiles of $(\langle D_t\rangle_I + \langle T_y\rangle_I)$ for the IES of $\omega_{th}^2/\omega_{ref}^2 = 10^{-3}$ and $\omega_{th}^2/\omega_{ref}^2 = 10^{-6}$ can be mainly attributed to the variation of $\langle T_p\rangle_I$ profile and to the observation that $\langle D_r\rangle_I$ appears to be non-negligible over a wider range of scales at the IES of $\omega_{th}^2/\omega_{ref}^2 = 10^{-6}$ compared to the IES of $\omega_{th}^2/\omega_{ref}^2 = 10^{-3}$.

Meanwhile, figure 5.4 is important for the demonstration of the robustness of the TNTI-averaged KHMH terms computed at various IES locations. The qualitative similarity between the results presented in figures 5.3 and 5.4 indicates that the main qualitative conclusions drawn for the IES of $\omega_{th}^2/\omega_{ref}^2 = 10^{-3}$ are not highly sensitive to the exact location within the TNTI layer between $\omega_{th}^2/\omega_{ref}^2 = 10^{-3}$ and 10^{-6}. Even though some variations exist in the actual values of the KHMH terms and the specific r_n scales where certain terms peak or diminish (see figures 5.3 and 5.4), these variations remain relatively small, considering the three decades of variation in ω_{th}^2.

However, it is important to note that the reduced KHMH balance identified as $(\langle D_t\rangle_I + \langle T_y\rangle_I) \approx \langle D_c\rangle_I$, in figure 5.3 for $r_n \lessapprox 9\eta$ is observed to be specific to the IES of $\omega_{th}^2/\omega_{ref}^2 = 10^{-3}$ and does not hold for $\omega_{th}^2/\omega_{ref}^2 = 10^{-6}$. On the other hand, the observation that all terms are significant for the large scales, except for $\langle D_c\rangle_I$ and $\langle D_r\rangle_I$, holds true for $\omega_{th}^2/\omega_{ref}^2 = 10^{-6}$.

5.2.5 Decomposition of the KHMH into solenoidal/irrotational parts

At this point, it is beneficial to examine the terms responsible for physical space transport and interscale transfer by employing the decomposition of the KHMH equation into two components: solenoidal and irrotational, as introduced by Larssen and Vassilicos (2023). The decomposition of the KHMH equation (eq. 5.3) can be given in the symbolic form (Larssen and Vassilicos, 2023),

$$D_t + T_y^S + T_r^S = D_r + D_c - \varepsilon, \tag{5.5}$$

$$T_r^I = T_y^I = -\frac{1}{2}T_p. \tag{5.6}$$

Here the superscripts S and I denote the solenoidal and irrotational parts of the respective terms. It must be emphasized that these two equations, and eq. 5.6 in particular, are exact everywhere and at any time in the flow field for fully periodic boundary conditions, while different boundary conditions can introduce additional terms (Larssen and Vassilicos, 2023).

Given the fully periodic boundary conditions utilized in PJx-HR simulations, eq. 5.6 can be employed to compute the irrotational parts of $\langle T_y \rangle_I$ and $\langle T_r \rangle_I$. The relations involving the irrotational and solenoidal parts of the interscale and interspace transfer terms are as follows;

$$T_r = T_r^I + T_r^S = -\frac{1}{2} T_p + T_r^S, \tag{5.7}$$

$$T_y = T_y^I + T_y^S = -\frac{1}{2} T_p + T_y^S. \tag{5.8}$$

Therefore, we can compute T_r^I and T_y^I by using equations 5.7, 5.8 and the $\langle T_p \rangle_I$. Then, the solenoidal contributions can be obtained by subtracting the irrotational parts from $\langle T_r \rangle_I$ and $\langle T_y \rangle_I$.

It has been shown by Larssen and Vassilicos (2023) that in fully developed periodic/homogeneous turbulence, only the solenoidal component of the interscale transfer plays an active role in the mean behaviour of the cascade towards smaller scales. The PDF of the irrotational part T_r^I is symmetrical around zero and T_r^I thus becomes zero when averaged.

Meanwhile, it can also be seen from eqs. 5.5 and 5.6 that the direct contribution to the D_t term from T_y comes from its solenoidal part T_y^S. On the other hand, the irrotational part, T_y^I, is counterbalanced by the pressure-velocity term as shown by eq. 5.6.

Starting with the interscale transfer term T_r and applying the decomposition provided in eq. 5.7, the solenoidal and irrotational parts are shown in figure 5.5, alongside $\langle T_p \rangle_I$, and are compared to $\langle \varepsilon \rangle_I$ to assess their local magnitudes across the scales. When normalized by $\langle \varepsilon \rangle_I$, it is observed that the solenoidal part $\langle T_r^S \rangle_I$ reaches its peak at a scale close to $r_n \approx \lambda$, as shown in figure 5.5b. Furthermore, the contribution of $\langle T_r^S \rangle_I$ to $\langle T_r \rangle_I$ is more significant for scales $r_n < 17.2\eta$ compared to the contribution of $\langle T_r^I \rangle_I$. However, for scales r_n larger than 17.2η, the irrotational part $\langle T_r^I \rangle_I$ becomes more prominent, even though both terms have considerable effects on the total $\langle T_r \rangle_I$ term.

Similarly, $\langle T_y \rangle_I$ is also decomposed into irrotational and solenoidal parts using eqs. 5.8 and 5.6. The terms $\langle T_y^S \rangle_I$ and $\langle T_y^I \rangle_I$ are shown in figure 5.6 along with the $\langle D_t \rangle_I$ term and the $(\langle D_t \rangle_I + \langle T_y^S \rangle_I)$ sum as functions of r_n/η. Comparing figure 5.6 to figure 5.3, it becomes apparent that $(\langle D_t \rangle_I + \langle T_y^S \rangle_I)$ is smaller in magnitude than $(\langle D_t \rangle_I + \langle T_y \rangle_I)$ for r_n larger than 20η. Conversely, it exhibits a larger magnitude at smaller scales, reaching as high as $\langle \varepsilon \rangle_I$ for scales close to $r_n/\eta = 10$.

As indicated by eq. 5.5, the solenoidal part T_y^S directly contributes to the time derivative term D_t. In contrast, the irrotational part T_y^I is balanced by T_r^I, which represents the irrotational part of the interscale transfer rate, related to pressure effects. Therefore, it is intriguing to examine $(\langle D_t \rangle_I + \langle T_y^S \rangle_I)$ due to the relationship between these terms given by eq. 5.5. The

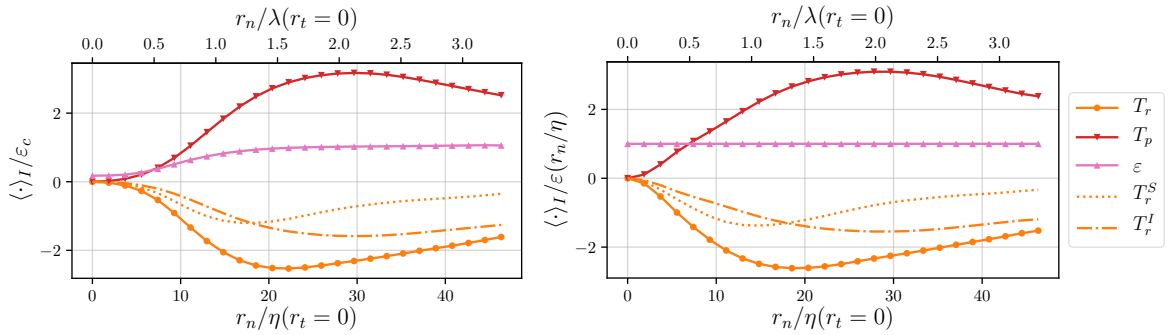

(a) Normalized by ε_c.

(b) Normalized by the profile of $\varepsilon(r_n/\eta)$.

Fig. 5.5 Pressure-velocity term $\langle T_p\rangle_I$, dissipation term $\langle\varepsilon\rangle_I$, interscale transfer term $\langle T_r\rangle_I$ and its solenoidal/irrotational parts $\langle T_r^S\rangle_I$, $\langle T_r^I\rangle_I$ as functions of separation vector in TNTI normal direction r_n/η, at $\omega_{th}^2/\omega_{ref}^2 = 10^{-3}$.

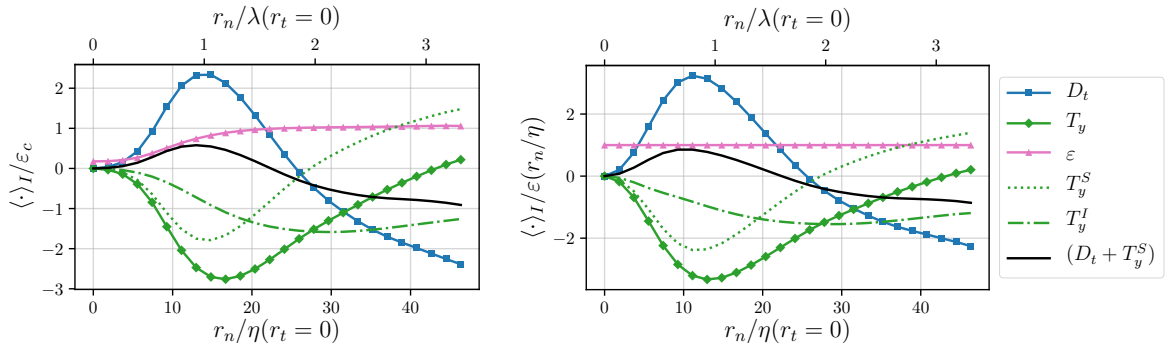

(a) Terms normalized by the mean centre-plane dissipation ε_c.

(b) Terms normalized by the profile of $\varepsilon(r_n/\eta)$.

Fig. 5.6 Pressure-velocity term $\langle T_p\rangle_I$, dissipation term $\langle\varepsilon\rangle_I$, interscale transfer term $\langle T_r\rangle_I$ and its solenoidal/irrotational parts $\langle T_r^S\rangle_I$, $\langle T_r^I\rangle_I$ as functions of separation vector in TNTI normal direction r_n/η, at $\omega_{th}^2/\omega_{ref}^2 = 10^{-3}$.

sum $(\langle D_t\rangle_I + \langle T_y^S\rangle_I)$ remains positive for scales larger than those where $(\langle D_t\rangle_I + \langle T_y\rangle_I)$ is positive, extending up to $r_n = 22.7\eta(1.62\lambda)$.

5.2.6 The KHMH balance as a function of r_t and r_n

Up to this point, our discussion of the KHMH balance has primarily focused on scales associated with the separation vector in the interface normal direction i.e. r_n (for $r_t = 0$). However, in this subsection, we expand our examination of the KHMH terms to include all directions, which is not only the separations in the normal direction but also in the tangential direction of the interface.

As described in Section 5.1, the local TNTI-averaged KHMH terms are initially obtained near the interface as functions of separation vectors r_x, r_y and r_z. Following Zhou and Vassilicos (2020) we apply an averaging operation over the angular direction θ, as illustrated in figure 5.2. This allows us to express the KHMH terms as functions of r_n and r_t, which reduces the complexity of the analysis significantly when compared to each term being a 3D field in scale space (r_x, r_y, r_z).

Figure 5.7 shows the terms $\langle D_t \rangle_I$, $\langle T_y \rangle_I$, $\langle T_r \rangle_I$ and $\langle T_p \rangle_I$, normalized by the centre-plane average dissipation ε_c. These terms dominate the local balance of $|\delta \boldsymbol{u}|^2$ when compared to the terms related to diffusion.

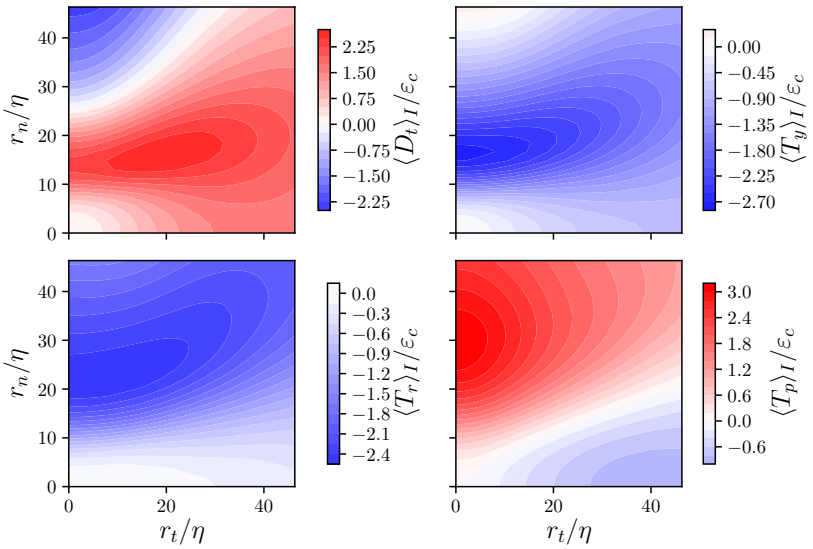

Fig. 5.7 $\langle D_t \rangle_I$, $\langle T_y \rangle_I$, $\langle T_r \rangle_I$ and $\langle T_p \rangle_I$ terms of the KHMH equation, eq. 5.3, computed at the TNTI location.

The $\langle D_t \rangle_I$ term maintains a positive value when considering $|\boldsymbol{r}|/\eta < 25$ but becomes negative for larger separation values in the normal direction ($r_n/\eta > 25$). In contrast, $\langle T_y \rangle_I$ consistently remains negative for most of the local field analyzed, with only an exception in a small region at large r_n and very small r_t.

Concerning the interscale energy transfer rate $\langle T_r \rangle_I$, a comparison can be made between the $\langle T_r \rangle_I$ in figure 5.7 and the findings by Zhou and Vassilicos (2020), where they report the TNTI-average statistics $\langle T_r \rangle_I$ along the TNTI of a spatially developing turbulent wake. The $\langle T_r \rangle_I$ contours as a function of $(r_t - r_n)$ exhibits similar qualitative behaviour near the TNTI of temporally developing planar jet and spatially developing turbulent wake flows.

In addition to the $\langle T_r \rangle_I$, Zhou and Vassilicos (2020) also shows results for the spatial transfer of $|\delta \boldsymbol{u}|^2$, but their calculations were made for the fluctuating velocities and excluded the mean velocity component. In contrast, our approach employs the KHMH equation for the

full velocity field without any decomposition. Interestingly, we observe a similar correlation between $\langle T_r \rangle_I$ and $\langle T_y \rangle_I$ in figure 5.7 and thus the results concerning the relationship between interscale and spatial transfer aligns with the findings reported by Zhou and Vassilicos (2020). A closer look at the PDF of the TNTI location given in figure 5.8 can give a clue about why the $\langle T_y \rangle_I$ obtained using the full-velocity in the present study and the spatial nonlinear energy transfer rate obtained using the fluctuating velocity in Zhou and Vassilicos (2020) are comparable. The PDF in figure 5.8 reveals that the TNTI is predominantly located around $y/\delta \approx 3/2$, where the influence of the mean flow is limited. This suggests that mean advection may not be a dominant contributor in our $\langle T_y \rangle_I$ contours, explaining partially the similarity between the $\langle T_y \rangle_I$ in the present study and the spatial energy transport given by (Zhou and Vassilicos, 2020).

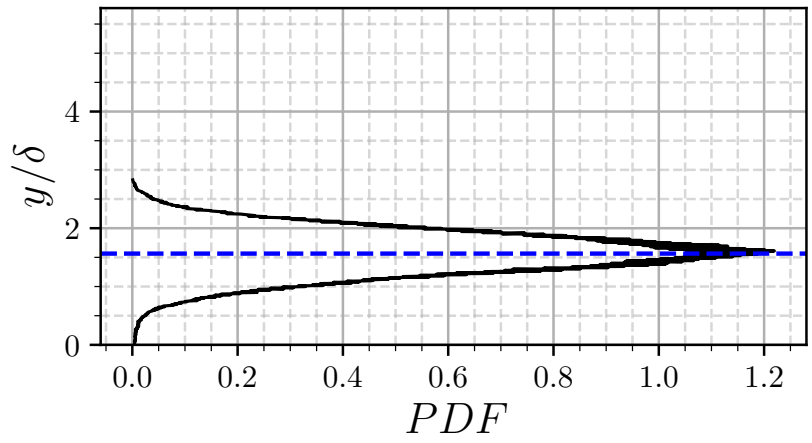

Fig. 5.8 PDF of the location of IES defined by the condition $\omega_{th}^2/\omega_{ref}^2 = 10^{-3}$ for $t/T_{ref} = 50$ normalized by the jet half-width δ.

Finally, it is important to note that the $\langle T_p \rangle_I$ term takes positive values for the separation vectors in the TNTI normal direction, thus contributing negatively to $|\delta \boldsymbol{u}|^2$ (see eq. 5.4). In figure 5.7, we can observe that the value of the $\langle T_p \rangle_I$ term becomes negative when the angle ϕ between $\boldsymbol{r}$ and the r_n axis exceeds 66°.

In figure 5.3b, we observed a balance between the terms $\langle D_t \rangle_I$ and $\langle T_y \rangle_I$, suggesting an effect of flow advection for scales associated with separations comparable to the TNTI thickness. In this figure, the balance of $(\langle D_t \rangle_I + \langle T_y \rangle_I)$ is shown for separation along the interface normal direction ($r_n > 0$ and $r_t = 0$). However, the balance can be analyzed for all the separation directions including both r_n/η and r_t/η as presented in figure 5.9. The scale range where $(\langle D_t \rangle_I + \langle T_y \rangle_I)$ is positive along the r_n axis, indicating an increase in kinetic energy in a material derivative sense following advection, is illustrated in figure 5.3b. In figure 5.9, a more significant rate of increase in $|\delta \boldsymbol{u}|^2$ can be observed in the tangential

direction. The absolute value of $(\langle D_t\rangle_I + \langle T_y\rangle_I)$ increases in both the normal and tangential directions. However, in the normal direction, it consistently remains negative except for scales $r_n/\eta < 11.4$, whereas it always remains positive along the tangential direction.

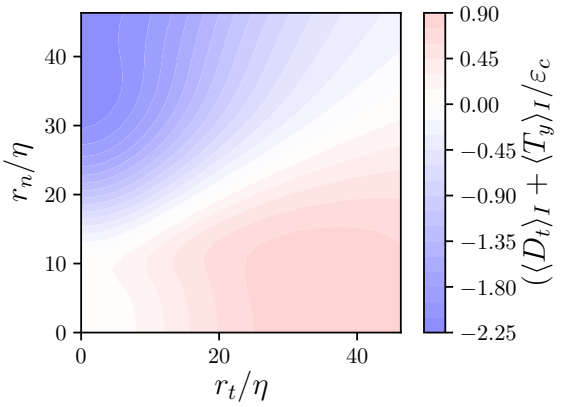

Fig. 5.9 $(\langle D_t\rangle_I + \langle T_y\rangle_I)$ as a function of r_t and r_n, computed at the TNTI location and normalized by average centre-plane dissipation ε_c.

5.2.7 Summary of main results for the analysis of the KHMH balance across scales at the TNTI location

In this section, we carried out the analysis of the terms of the KHMH equation (eq. 5.3) in the vicinity of the TNTI. The terms have also been analyzed by carrying out the decomposition of the KHMH equation into solenoidal/irrotational parts. The main points that are observed from the local balance of these terms for various scales are:

- The advection mechanism plays an important role in the evolution of $|\delta\boldsymbol{u}|^2$ at the interface location.
- When moving with the flow i.e. $(\langle D_t\rangle_I + \langle T_y\rangle_I)$, a specific balance exists among the terms $\langle T_r\rangle_I$, $\langle T_p\rangle_I$, $\langle D_r\rangle_I$ and $\langle\varepsilon\rangle_I$ for scales $r_n/\eta < 11.4$ $(r_t/\eta = 0)$ and can be simplified to $(\langle D_t\rangle_I + \langle T_y\rangle_I) \approx \langle D_c\rangle_I$ at the IES of $\omega^2_{th}/\omega^2_{ref} = 10^{-3}$. Notably, at these scales, $\langle D_c\rangle_I$ is greater than zero and the sum $(\langle D_t\rangle_I + \langle T_y\rangle_I)$ is positive. The analysis of the KHMH terms for the IES of $\omega^2_{th}/\omega^2_{ref} = 10^{-6}$ reveals that $(\langle D_t\rangle_I + \langle T_y\rangle_I)$ is indeed positive over an even broader range of scales in this case. However, the balance is not strictly $(\langle D_t\rangle_I + \langle T_y\rangle_I) \approx \langle D_c\rangle_I$ at the location of IES of $\omega^2_{th}/\omega^2_{ref} = 10^{-6}$.
- The highest contribution to $\langle T_r\rangle_I$ from the solenoidal part of the interscale transfer $\langle T_r^S\rangle_I$ is observed at scales that are of the order of λ.

- $\langle T_r^I \rangle_I$ plays a substantial role across all scales in the interface normal direction r_n. Its contribution to $\langle T_r \rangle_I$ becomes more pronounced compared to $\langle T_r^S \rangle_I$ as the separation length r_n increases.

- The local fields of $\langle T_r \rangle_I$ and $\langle T_y \rangle_I$ in the $(r_t - r_n)$ plane at the interface of the temporally developing turbulent jet exhibit similarities to the findings reported by Zhou and Vassilicos (2020) for the TNTI of a spatially developing turbulent wake. In both flows, a correlation between $\langle T_r \rangle_I$ and $\langle T_y \rangle_I$ is observed at the TNTI location.

- It is observed that, except for the diffusion terms which become less significant for scales larger than approximately λ, all the terms in the KHMH equation play significant roles in the local scale-by-scale balance of $|\delta \boldsymbol{u}|^2$ at the interface location. Specifically, for r_n values greater than λ, the equation 5.5 holds in a simplified form, indicating a balance between D_t, T_y^S, and T_r^S, approximately equal to $-\varepsilon$ i.e. $D_t + T_y^S + T_r^S \approx -\varepsilon$.

5.3 TNTI-averaged KHMH statistics conditioned on H_m and v_n^l

In sections 4.11.2 and 4.11.1, it has been demonstrated that the local characteristics of the interface vary across different parts of the IES. These variations include differences in the total thickness of the TNTI, the sublayer thicknesses, the details of the local ω^2 balance, and the TNTI-averaged normal profiles of various quantities.

In these sections, the various regions of the IES are distinguished by conditioning the TNTI-averaged statistics on the local mean curvature H_m and local propagation velocity v_n^l values. We now apply the same conditions introduced in section 4.11 to explore the variation of the KHMH balance at these distinct regions along the IES.

Figure 5.10 presents the TNTI-averaged KHMH terms as functions of r_n, for D2, E2, E3 and E6 conditions (see table 4.1), for the IES of $\omega_{th}^2/\omega_{ref}^2 = 10^{-3}$. These terms are normalized by ε_c. Notably, the magnitudes of these terms exhibit significant variations among the different conditions. Especially, in the range $10 < r_n/\eta < 20$, where the peaks of $\langle D_t \rangle_I$ and $\langle T_y \rangle_I$ are located for all conditions, the magnitude of terms $\langle D_t \rangle_I$, $\langle T_r \rangle_I$, $\langle T_y \rangle_I$, and $\langle T_p \rangle_I$ in the $r_n \neq 0$, $r_t = 0$ axis is approximately an order of magnitude higher for condition E6 compared to conditions E2 and E3.

The differences between the profiles of $(\langle D_t \rangle_I + \langle T_y \rangle_I)$ along r_n, for various conditions are also noteworthy. In the case of D2, $(\langle D_t \rangle_I + \langle T_y \rangle_I)$ remains positive over a substantial range of r_n, extending up to $r_n/\eta = 37$. However, for the E2 condition, the extent of this

range is only up to $r_n/\eta = 14$. On the other hand for the E3 condition, which represents convex-shaped regions, the balance between $\langle D_t \rangle_I$ and $\langle T_y \rangle_I$ remains positive over a wide range of r_n, reaching up to $r_n/\eta = 24.3$. It is worth noting that in the E3 case, this imbalance is not solely due to the viscous diffusion terms $\langle D_c \rangle_I$ and $\langle D_r \rangle_I$, but also involves other terms, particularly at scales $r_n/\eta = 24.3$ and smaller.

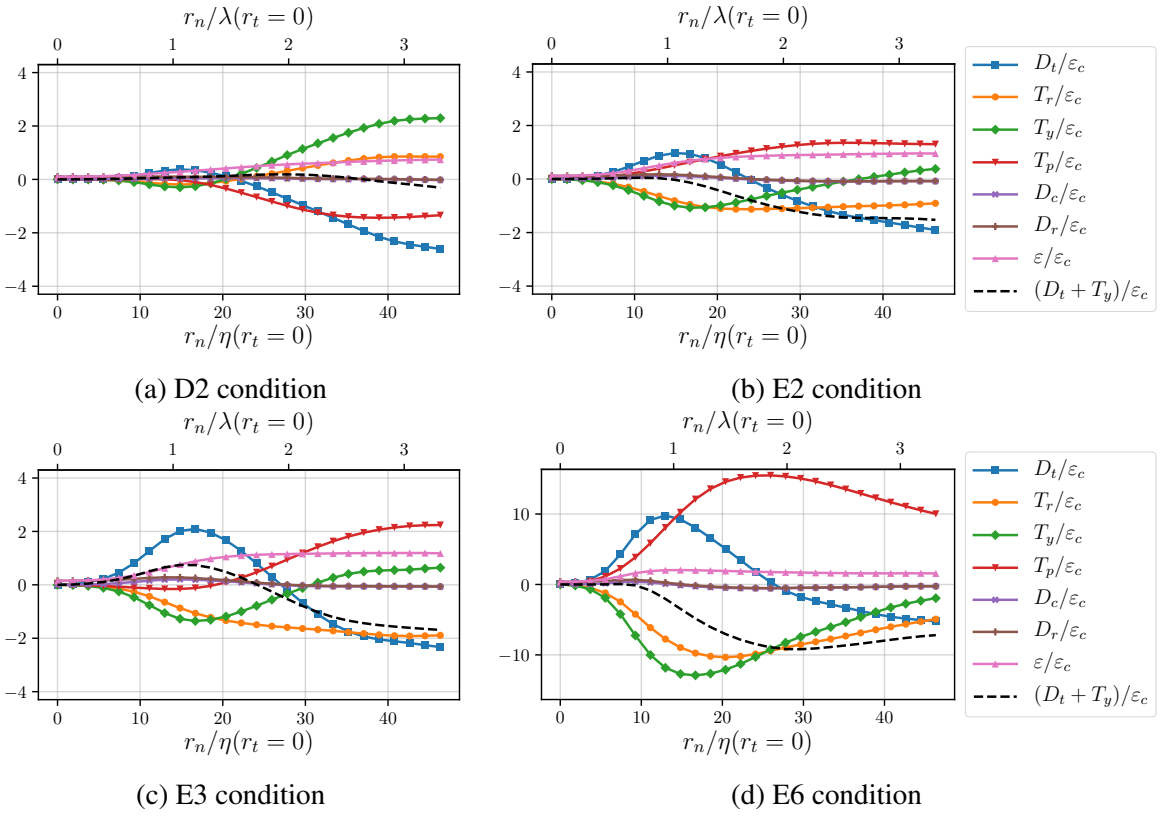

(a) D2 condition

(b) E2 condition

(c) E3 condition

(d) E6 condition

Fig. 5.10 TNTI-averaged profiles of KHMH terms as functions of r_n. Computed for the conditions D2, E2, E3, E6, normalized by ε_c at $\omega_{th}^2/\omega_{ref}^2 = 10^{-3}$.

Figure 5.11 shows the same profiles given in figure 5.10, this time normalized by the TNTI-averaged profile of $\langle \varepsilon \rangle_I(r_n)$ in order to see the balance of the various terms for each individual condition. Again, the sum $(\langle D_t \rangle_I + \langle T_y \rangle_I)$ is given along with the KHMH terms in order to see the rate of change of $|\delta \boldsymbol{u}|^2$ when moving with the flow for various scales r_n.

In figure 5.11, we can observe an interesting feature related to the variation of $(\langle D_t \rangle_I + \langle T_y \rangle_I)$. Specifically, the E3 condition stands out because $(\langle D_t \rangle_I + \langle T_y \rangle_I)$ is close to $\langle \varepsilon \rangle_I$ for scales $r_n/\eta \simeq 12$, where $(\langle D_t \rangle_I + \langle T_y \rangle_I)$ is at its maximum. This behaviour is mainly due to the unique characteristics of $\langle T_p \rangle_I$ at the convex regions associated with the E3 condition.

5.3.1 Interscale transfer and pressure effects for various ED conditions

In figure 5.11a, we can see that for the D2 condition, the terms $\langle T_y \rangle_I$, $\langle T_r \rangle_I$, and $\langle D_t \rangle_I$ remain comparable to $\langle \varepsilon \rangle_I$ for most scales r_n/η. However, $\langle T_p \rangle_I$ is approximately zero until $r_n/\eta = 13.3$, which corresponds to the turbulent point being slightly further than the extent of the VSL, given that $\delta_v = 5.3\eta$ for the D2 condition (see table 4.2). Therefore, we can infer that an approximate balance exists between the terms $\langle D_r \rangle_I$, $\langle T_r \rangle_I$, and $\langle \varepsilon \rangle_I$ until the TSL is reached. Additionally, an approximate balance is evident between $\langle D_t \rangle_I$ and $\langle T_y \rangle_I$. Within the TSL, the $\langle T_p \rangle_I / \langle \varepsilon \rangle_I$ term becomes more influential, reaching its maximum value at $r_n/\eta \approx 35$, which corresponds to the scale separation where the turbulent point on the turbulent side reaches the inner limit of the full TNTI for the D2 condition.

Furthermore, $\langle T_r \rangle_I$ exhibits an interesting behaviour in the detrainment regions of the IES. It has negative values for scales $r_n/\eta < 22.3$ but beyond this point, it changes sign and becomes positive for scales $r_n/\eta > 22.3$, suggesting the presence of an inverse cascade in the interface normal direction for scales $r_n/\eta > 22.3$. This is interesting because the investigation of the TNTI-averaged local velocity field in chapter 4 in the vicinity of the TNTI showed that only the regions of the IES conditioned on D2 exhibited stretching in the interface normal direction (and compression in the tangential direction), while the other regions associated with local entrainment exhibited compression in the normal direction of the interface (and stretching in the tangential direction).

For the TNTI points satisfying the E2 condition, the magnitudes of the $\langle T_y \rangle_I$, $\langle T_r \rangle_I$, and $\langle D_t \rangle_I$ terms remain similar to those in the D2 condition, roughly of the order of $\langle \varepsilon \rangle_I$ for most r_n/η scales (see figure 5.11b). The most notable difference between the E2 and D2 conditions is due to the $\langle T_r \rangle_I$ and $\langle T_p \rangle_I$ terms. What is particularly intriguing is the presence of a very approximate balance between the terms $\langle T_r \rangle_I$ and $\langle \varepsilon \rangle_I$ starting from $r_n/\eta = 9.4$ (see figure 5.11b). This scale separation corresponds to a situation where one of the two points is located just at the limit of the VSL region in the turbulent direction because $\delta_v/\eta = 4.5$ for the E2 condition (see table 4.2). It is an unexpected result to see even a very approximate and imperfect balance between the dissipation rate and the interscale energy transfer rate at the TNTI where none of the conditions for Kolmogorov equilibrium hold.

It is worth noting that the E2 condition concerns concave regions with mild local entrainment, which are the most probable regions across the IES (see table 4.1). Therefore, it may be reasonable to expect that the E2 condition will be representative of the unconditioned KHMH balance in the vicinity of the interface. However, when comparing figure 5.11b with figure 5.3b (TNTI-average without any conditioning) it becomes evident that even though $\langle T_r \rangle_I$ remains close to $\langle \varepsilon \rangle_I$ in magnitude for scales $r_n/\eta \geq 9.4$ for the E2 condition, it reaches values close to $|\langle T_r \rangle_I| \approx 2|\langle \varepsilon \rangle_I|$ in the absence of any conditioning on H_m and v_n^l. This shows

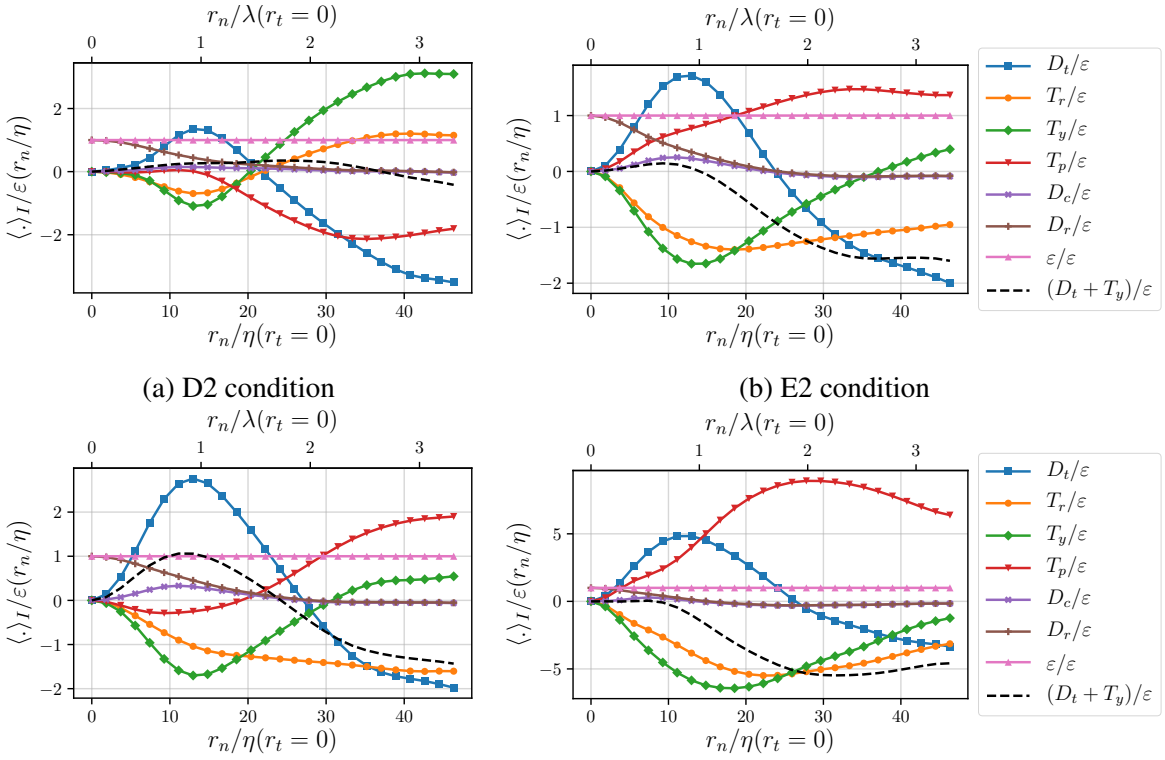

(a) D2 condition

(b) E2 condition

(c) E3 condition

(d) E6 condition

Fig. 5.11 TNTI-averaged profiles of KHMH terms as a function of r_n/η, computed with the conditions D2, E2, E3, E6 and normalized by the $\langle\varepsilon(r_n)\rangle_I$ at $\omega_{th}^2/\omega_{ref}^2 = 10^{-3}$.

that the extreme values of $\langle T_r\rangle_I$, such as in the case for the E6 condition (see figure 5.11d), has a significant effect on the TNTI-average profile of $\langle T_r\rangle_I$ for the entire TNTI without conditioning applied.

The comparison of figures 5.11c, 5.11b, 5.11d and 5.11a reveals some interesting insights into the KHMH balance across scales in the interface normal direction for regions of entrainment and detrainment.

Firstly, there is a noticeable similarity in the behaviour of the $\langle T_r\rangle_I$ term for the E2, E3, and E6 conditions, which is distinct from the behaviour observed in the D2 condition. This suggests a particular variation of the $\langle T_r\rangle_I$ term in the vicinity of the interface at the local entrainment and detrainment regions of the IES.

Secondly, when examining figures 5.11c and 5.11b, it becomes apparent that the $\langle D_t\rangle_I$ term and the sum $(\langle D_t\rangle_I + \langle T_y\rangle_I)$ are higher for the E3 condition compared to the E2 condition. This difference can be attributed to the influence of the pressure-velocity term $\langle T_p\rangle_I$, which acts differently in the concave and convex regions of the interface.

The magnitudes of the TNTI-averaged KHMH terms exhibit significant differences in the E6 condition compared to the other conditions, with an order of magnitude disparity between $\langle T_p \rangle_I$ and $\langle \varepsilon \rangle_I$. However, a qualitative resemblance can be observed between the general patterns in the E6 and E2 cases, except for the extreme contribution of the $\langle T_p \rangle_I$ term and the locations of peaks in $\langle T_r \rangle_I$ and $\langle T_y \rangle_I$, which affect larger scales r_n for the E6 condition.

As presented in section 4.11.2, the thicknesses of the TNTI and TSL are observed to be halved for the E6 condition compared to the E2 condition. This reduction in thicknesses may be related to the TNTI-averaged local fields discussed in section 4.11.1, where there is a transport of vorticity/enstrophy towards the TNTI by the TNTI-average velocity field. Possibly, the transport of IVS (da Silva et al., 2011) towards the interface may lead to an increase in interscale energy transfer rates due to the mean stretching in the tangential direction.

However, a clear demarcation of the transition between the layers of VSL and TSL in terms of dramatic changes in the KHMH balance is not evident, except for the rapid rise of the $\langle T_p \rangle_I$ term for r_n/η values beyond the extent of the TNTI in the E6 condition.

5.3.2 Solenoidal/irrotational decomposition of $\langle T_r \rangle_I$ and $\langle T_y \rangle_I$ for various ED conditions

The interscale transfer term $\langle T_r \rangle_I$ exhibits an exceptional behaviour in the D2 case, as seen in figure 5.11a, where it becomes positive after $r_n/\eta = 22.3$ contrary to the other cases. Likewise, the $\langle T_p \rangle_I$ term behaves differently in the convex entrainment regions (E3) compared to the concave entrainment regions (E2, E6) of the interface. Therefore, it is intriguing to investigate how the irrotational and solenoidal parts of $\langle T_r \rangle_I$ contribute to these particular behaviours for various ED conditions.

In figure 5.12, the terms $\langle T_r^S \rangle_I$ and $\langle T_r^I \rangle_I$ are presented alongside $\langle T_p \rangle_I$ and $\langle \varepsilon \rangle_I$, all normalized by the profile of $\langle \varepsilon \rangle_I$. The comparison of $\langle T_r^S \rangle_I$ profiles across various conditions reveals a consistent qualitative similarity when normalized by the respective $\langle \varepsilon \rangle_I$ profiles, except for a slight deviation in the case of D2, where $\langle T_r^S \rangle_I$ exhibits an unusually positive trend at $r_n/\eta \geq 35$. Notably, the TNTI-average profile of $\langle T_r^S \rangle_I$ exhibits a negative peak at scales close to λ. This peak occurs at $r_n = 1.1\lambda$ for both the D2 and E6 conditions, while it occurs at $r_n = 1.2\lambda$ for the E2 and E3 conditions.

It has been demonstrated by Apostolidis et al. (2023) that the negative contribution of the T_r term, indicative of a forward cascade towards smaller scales, reaches its maximum value at scales approximately $|\boldsymbol{r}| \approx \lambda$ within the inertial layer of channel flows (in the study of Apostolidis et al. (2023) T_r is investigated over all the $\boldsymbol{r}$ directions). Similarly, studies on

homogeneous, isotropic turbulence (HIT) by Yasuda and Vassilicos (2018), Obligado and Vassilicos (2019), and Meldi and Vassilicos (2021) also observed that the average interscale transfer towards smaller scales attains its maximum around scales of $|\boldsymbol{r}| \approx \lambda$ in homogeneous turbulence.

Considering the findings in the literature, it is intriguing to observe that $\langle T_r^S \rangle_I$ exhibits a peak close to $r_n \approx \lambda$ at the TNTI for all conditions considered. This pattern persists regardless of whether the conditions involve detrainment or entrainment regions, or if the mean curvature of the IES is concave or convex.

It is important to emphasize that here, we present the profiles of $\langle T_r^S \rangle_I$ in figure 5.12. The studies which are referred to above, report the complete averaged T_r term rather than just the solenoidal part (Apostolidis et al., 2023; Meldi and Vassilicos, 2021; Obligado and Vassilicos, 2019; Yasuda and Vassilicos, 2018). Additionally, Yasuda and Vassilicos (2018) provide data on the average T_p term as a function of separation vector $\boldsymbol{r}$. Notably, this term was found to be consistently zero for all scales in homogeneous turbulence, which is significantly different from the turbulent region near the TNTI, which is characterized by a local inhomogeneity. It is also important to remember that the difference between T_r and T_r^S is precisely $\frac{1}{2}T_p$ (see equation 5.6) for fully periodic boundary conditions, which is the case for the simulations conducted by Yasuda and Vassilicos (2018). Consequently, in their case, $\langle T_r \rangle$ presented is entirely composed of $\langle T_r^S \rangle$, rendering the profiles of $\langle T_r^S \rangle_I$ in the present study comparable with $\langle T_r^S \rangle$ term reported for homogeneous turbulence in these studies (Obligado and Vassilicos, 2019; Yasuda and Vassilicos, 2018), even though in their flow the term is averaged over the whole flow, while we apply the TNTI-averaging.

On the other hand, care should be taken while comparing with the results of Apostolidis et al. (2023) as eq. 5.6 is exact for fully periodic boundary conditions, and additional terms prevail in eqs. 5.5 and 5.6 for channel flow due to the different boundary conditions (Larssen and Vassilicos, 2023).

An examination of figure 5.12a reveals that, for scales larger than $r_n = \lambda$, $\langle T_r^I \rangle_I$ becomes positive. This positive trend in $\langle T_r^I \rangle_I$ is primarily responsible for $\langle T_r \rangle_I$ changing its sign at scales corresponding to $r_n = 1.57\lambda$ and remains positive afterwards. Notably, $\langle T_r^S \rangle_I$ also exhibits a positive trend, but this occurs only at scales greater than $r_n = 2.5\lambda$. It can thus be concluded that for the D2 condition, the inverse cascade observed at the location of the IES is largely due to pressure effects and the irrotational component $\langle T_r^I \rangle_I$ plays a significant role in this process.

For conditions E2 and E6, the behaviour of $\langle T_r^I \rangle_I$ is quite different compared to the D2 case. For these conditions, $\langle T_r^I \rangle_I$ acts in a manner that enhances the forward cascade for all scales r_n. Remarkably, its magnitude becomes comparable to $\langle T_r^S \rangle_I$, or even sometimes

much higher e.g., the E6 condition at large separations r_n/η. This observation highlights the significant role of $\langle T_r^I \rangle_I$ in promoting the forward cascade of turbulent kinetic energy for the regions of local entrainment where the IES has a concave shape. On the other hand, the role of $\langle T_r^I \rangle_I$ is reversed for the regions of local detrainment at the concave-shaped regions of the IES.

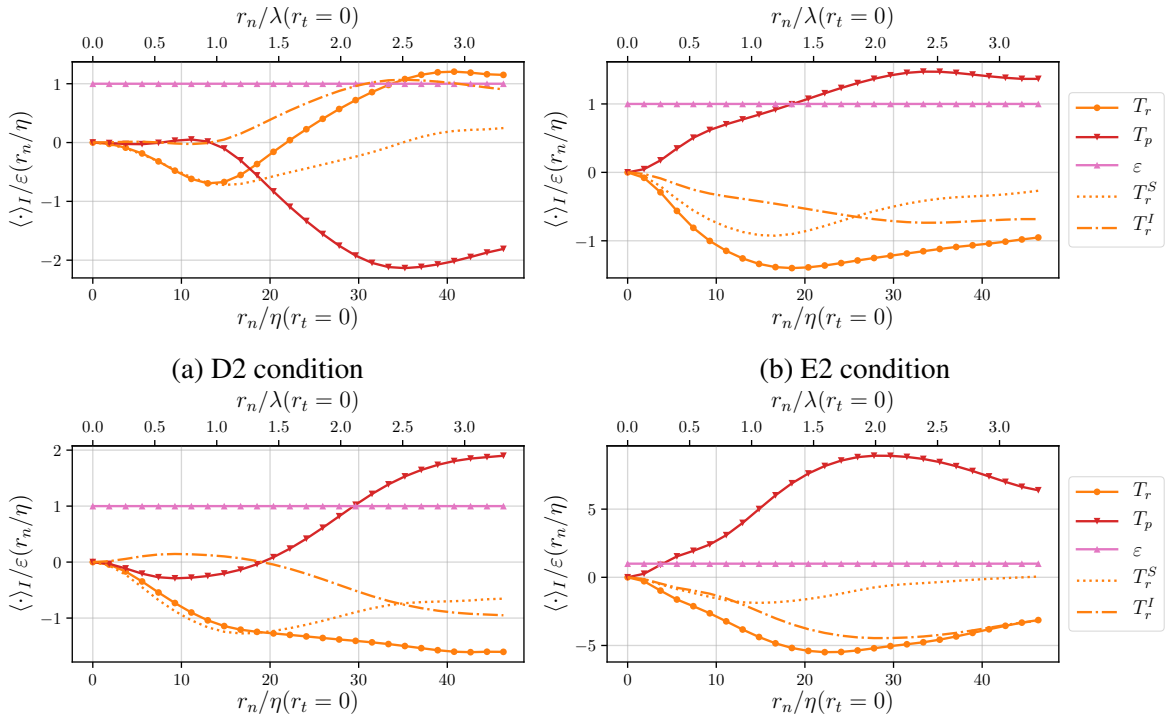

(a) D2 condition

(b) E2 condition

(c) E3 condition

(d) E6 condition

Fig. 5.12 Decomposition of the $\langle T_r \rangle_I$ with the eq. 5.7 into solenoidal and irrotational parts, $\langle T_r^S \rangle_I$ and $\langle T_r^I \rangle_I$.

For completeness, we also present the solenoidal and irrotational components that constitute $\langle T_y \rangle_I$ in figure 5.13. For all three conditions D2, E2, and E6 where the IES has a concave shape, the $(\langle D_t \rangle_I + \langle T_y^S \rangle_I)$ changes its sign from positive to negative at scales $r_n = 20\eta$ (see figures 5.13a, 5.13b, 5.13d), while for the convex regions of the IES i.e. E3 condition, $(\langle D_t \rangle_I + \langle T_y^S \rangle_I) > 0$ extends as far as $r_n = 26.2\eta$. Meanwhile, for the E3 and E6 conditions, $(\langle D_t \rangle_I + \langle T_y^S \rangle_I)$ reaches as high as $\langle \varepsilon \rangle_I$ for certain scales.

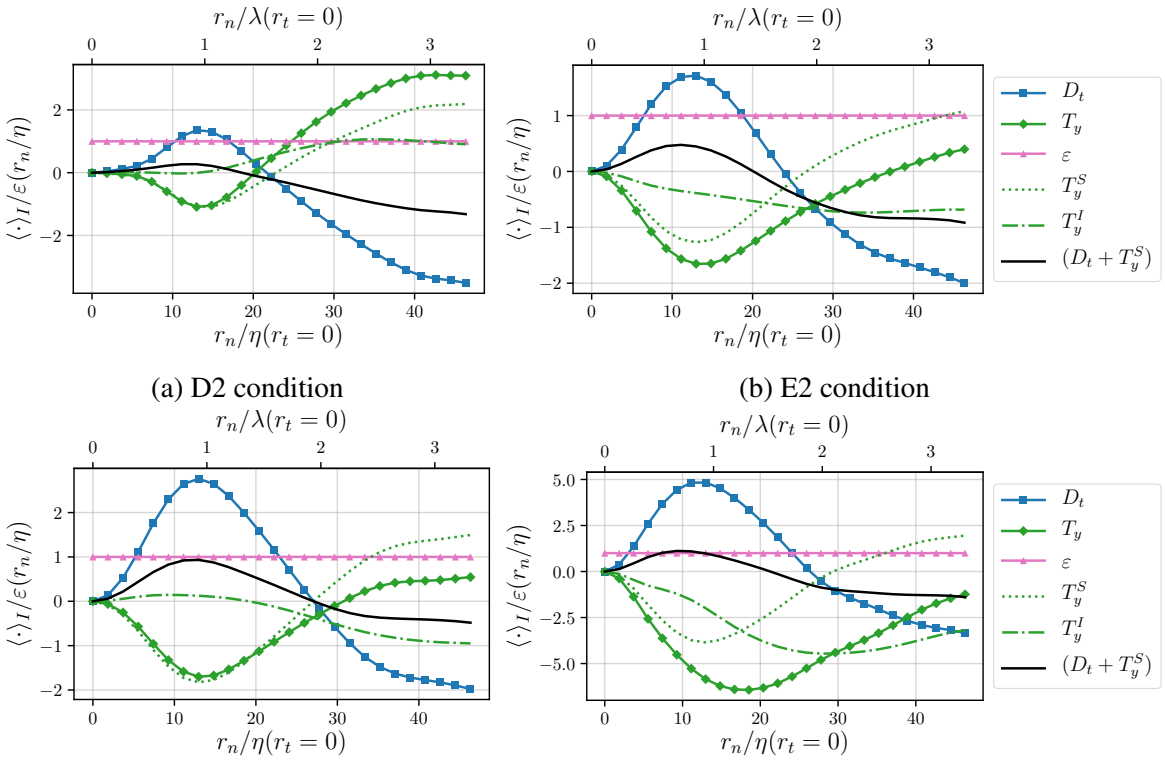

(a) D2 condition

(b) E2 condition

(c) E3 condition

(d) E6 condition

Fig. 5.13 Decomposition of the $\langle T_y \rangle_I$ with the eq. 5.8 into solenoidal and irrotational parts, $\langle T_y^S \rangle_I$ and $\langle T_y^I \rangle_I$.

5.3.3 KHMH terms near TNTI as functions of r_t and r_n for ED conditions

Figure 5.14 provides an overview of the dominant KHMH terms in the vicinity of the IES, as functions of both r_n/η and r_t/η for the D2, E2, E3, and E6 conditions. When comparing the contour fields of $\langle D_t \rangle_I$ for the D2, E2, E3, and E6 conditions, several qualitative similarities stand out.

Primarily, $\langle D_t \rangle_I$ exhibits a consistent behaviour across all the conditions, showing negative values in the local fields for two-point separations along the interface normal direction where $r_n/\eta \gtrapprox 25$. This indicates a decreasing $|\delta \boldsymbol{u}|^2$ in time for scales $r_n/\eta \gtrapprox 25$ along the TNTI normal direction. This reduction in $|\delta \boldsymbol{u}|^2$ is a result of the combination of various mechanisms, including advection, interscale transfer, interspace transfer, pressure-velocity terms, and dissipation. Notably, diffusion terms have negligible effects at these scales, as shown in figure 5.3b. Conversely, the rate of change of $|\delta \boldsymbol{u}|^2$ in time is consistently positive for all scales in the direction tangential to the interface, regardless of the condition applied on the local values of H_m and v_n^I along the interface.

A closer examination of the contour field of $\langle D_t \rangle_I$ for the D2 condition (figure 5.14a) reveals that the $\langle D_t \rangle_I$ field in the scale space is primarily influenced by the contributions of $\langle T_r \rangle_I$ and $\langle T_y \rangle_I$ in this case. However, for the E3 condition (figure 5.14c), the qualitative behavior of $\langle D_t \rangle_I$ is mainly driven by the contributions of $\langle T_y \rangle_I$ and $\langle T_p \rangle_I$. Furthermore, it can be observed that the pressure-velocity term $\langle T_p \rangle_I$ exhibits a significant difference between regions of local detrainment (figure 5.14a) and regions of local entrainment (figures 5.14b, 5.14c, 5.14d).

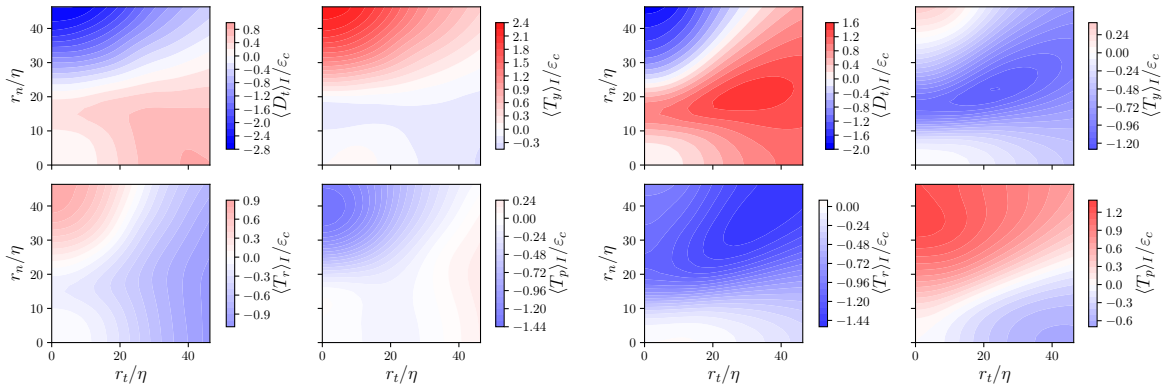

(a) D2 condition

(b) E2 condition

(c) E3 condition

(d) E6 condition

Fig. 5.14 $\langle D_t \rangle_I$, $\langle T_y \rangle_I$, $\langle T_r \rangle_I$ and $\langle T_p \rangle_I$ terms of the KHMH equation computed at the TNTI location for D2, E2, E3 and E6 conditions, normalized by ε_c. The colour scale ranges are the same for all the terms given for each condition, but the range varies between different conditions.

A crucial qualitative difference arises in the behaviour of the interscale transfer term $\langle T_r \rangle_I$ between the detrainment case D2 and the entrainment cases E2, E3, and E6. Notably, positive values of $\langle T_r \rangle_I$ are evident in figure 5.14a (in the detrainment regions) for separation vectors oriented in the interface normal direction, specifically for scales $r_n > 20\eta$. It shows an energy loss at scales smaller than $r_n = 22\eta$ due to the inverse cascade and the energy

is transferred to larger scales. A more comprehensive exploration of this phenomenon is provided in section 5.5, which delves deeper into the interscale transfer term.

Contrary to the D2 condition, at the regions characterized by mild entrainment conditions, such as E2 and E3, $\langle T_r \rangle_I$ consistently maintains negative values across all scales, regardless of the local mean curvature of the IES (as seen in figures 5.14b and 5.14c).

Figure 5.14d reveals a unique behaviour for the E6 condition, where $\langle T_r \rangle_I > 0$ is observed primarily for separations oriented tangentially to the IES (i.e., $r_t \neq 0$ and $r_n \approx 0$). This behaviour may be linked to the more pronounced stretching observed in the extreme entrainment condition, in the tangential direction of the interface, as shown in figure 4.32e for the $x_I - z_I$ cross-section of the TNTI-average velocity field.

The term which is responsible for pressure effects on the local scale-by-scale kinetic energy balance $\langle T_p \rangle_I$, also exhibits qualitative differences in detrainment regions. In the context of the balance outlined in eq. 5.4, the negative values of the $\langle T_p \rangle_I$ result in a net increase in the kinetic energy at a given scale over time. Specifically, the $\langle T_p \rangle_I$ term contributes in a manner that increases the kinetic energy of scales $r_t < 36.7\eta$ only for the D2 condition (see figure 5.14a). Despite the significant contribution of $\langle T_p \rangle_I$, which becomes prominent at $r_n = 40\eta$ mainly along the interface normal direction, the $\langle D_t \rangle_I$ term attains high negative values for the same r_n separations, due to the influences of $\langle T_y \rangle_I$ and $\langle T_r \rangle_I$ (see figure 5.14a).

Finally, for separations $r_n/\eta \gtrapprox 27$, the $\langle D_t \rangle_I$ term is consistently negative for all conditions. Although it displays the same qualitative behaviour, the magnitude of this term is notably higher for the D2 and E6 conditions compared to the E2 and E3 conditions, indicating a more significant reduction in kinetic energy associated with scales larger than $r_n = 27\eta$ for the two former conditions.

In regions characterized by local detrainment, the variation in scale-by-scale kinetic energy is primarily influenced by the term associated with transport in physical space, $\langle T_y \rangle_I$, which contributes to $\langle D_t \rangle_I$, both qualitatively and quantitatively (see figure 5.14a). Notably, for the D2 condition, $\langle T_y \rangle_I$ primarily gets positive values for separation vectors $r_n \gtrapprox 20\eta$. Conversely, for the E2, E3, and E6 conditions, this term displays a negative peak near $r_n/\eta \approx 17$, and $\langle T_y \rangle_I$ generally remains negative for all $\boldsymbol{r}$.

Considering the separation values of r_n in figure 5.12, the decomposition of $\langle T_r \rangle_I$ into the irrotational and solenoidal parts leads to interesting observations such as $\langle T_r^S \rangle_I$ remaining relatively similar across r_n for all the conditions, while the contribution of $\langle T_r^I \rangle_I$ varies significantly between each condition, exhibiting much different pressure effects at various regions.

The solenoidal/irrotational decomposition is applied in figure 5.15 to the local fields of $\langle T_r \rangle_I$ for various conditions in order to see the complete picture, for the separation vector $\boldsymbol{r}$ in all directions. For the sake of comparison, figure 5.15a shows the contour fields of $\langle T_r \rangle_I$, $\langle T_r^I \rangle_I$ and $\langle T_r^S \rangle_I$ for the general case, without any conditioning applied on H_m or v_n^l when computing the statistics.

It should be noted that the colour scale used in figures 5.15a, 5.15b, 5.15c, 5.15d, 5.15e for each condition is unique, meaning that the same colour scale is used for the three terms $\langle T_r \rangle_I$, $\langle T_r^I \rangle_I$ and $\langle T_r^S \rangle_I$, but this scale varies between different conditions.

Apart from the variation of the magnitudes of terms between various conditions, a significant change is observed concerning the contribution of $\langle T_r^I \rangle_I$, especially between the detrainment and entrainment regions. It can be seen in figure 5.15b that the $\langle T_r^I \rangle_I > 0$ for nearly all the separation vectors $\boldsymbol{r}$ irrespective of the direction and the length of $\boldsymbol{r}$ in scale-space, except for a limited region where $r_t \gtrapprox 35$.

On the contrary, $\langle T_r^I \rangle_I$ contributes with negative values for separations in the interface normal direction and with positive values in the tangential direction i.e., r_n and r_t respectively, in the case of E2, E3, and E6 conditions (also in the unconditioned statistics). Taking into account the direct relation between T_r and T_p (see eq. 5.6), it can be said that the compressive/stretching motions in the normal/tangential directions are mostly caused by the effects of pressure at the interface.

It is observed that generally, the qualitative behaviour of $\langle T_r \rangle_I$ in scale-space is determined by $\langle T_r^S \rangle_I$ part, which is the case in figures 5.15c, 5.15d and 5.15a. On the other hand, in the cases of D2 and E6 conditions, the $\langle T_r^I \rangle_I$ has important contributions, notably for the scales and directions where the inverse cascade is present.

When $\langle T_r^S \rangle_I$ is compared for the conditions D2, E2, E3, and E6, it can be observed that the general picture remains similar for all the cases including the D2 condition. This suggests that the terms other than the pressure act qualitatively similar, irrespective of the v_n^l and H_m values along the IES. For all the conditions, $\langle T_r^S \rangle_I$ has a minima at a certain location along the interface normal axis, and then starts rising, and only in the D2 condition, it becomes positive for scales $r_n \gtrapprox 34\eta$.

5.3.4 Summary of the main observations on KHMH balance for various ED conditions

We have analyzed the KHMH balance in the vicinity of the TNTI in section 5.2 for the entire TNTI without applying any conditions on the mean curvature H_m and the local propagation velocity v_n^l of the IES. In the present section 5.3, we have looked closer at how this balance

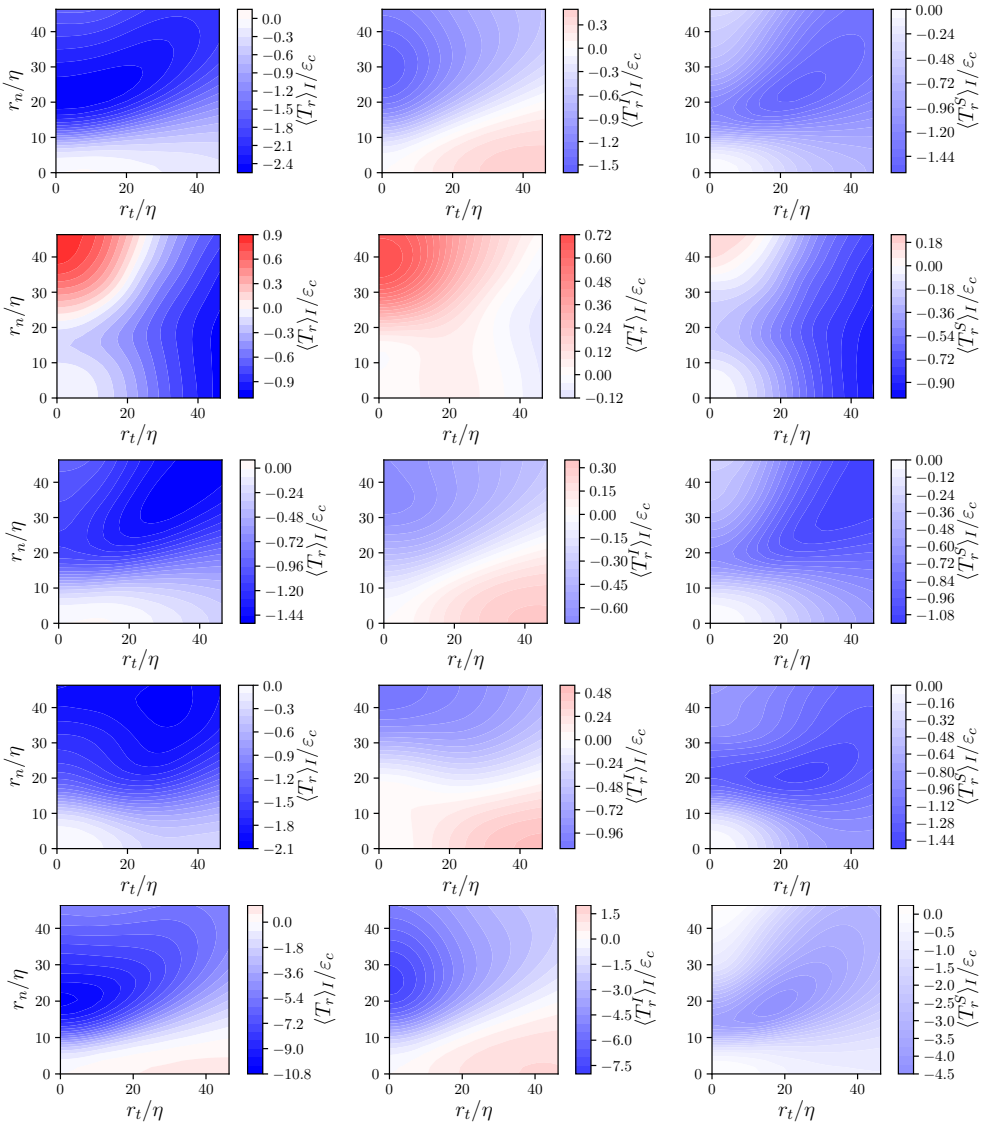

(a) Without any condition on H_m and v_n

(b) D2 condition

(c) E2 condition

(d) E3 condition

(e) E6 condition

Fig. 5.15 TNTI-averaged fields of $\langle T_r \rangle_I$, $\langle T_r^S \rangle_I$ and $\langle T_r^I \rangle_I$ near the detected IES of $\omega_{th}^2/\omega_{ref}^2 = 10^{-3}$, (a) without any conditioning of the statistics on H_m or v_n^l and (b, c, d, e) for the conditions D2, E2, E3, and E6 as functions of r_t/η and r_n/η.

varies in different regions of the IES with distinct characteristics in terms of H_m and v_n^l, namely the ED conditions. The main observations made for the local balance in the cases of ED conditions can be given as follows;

- An approximate balance, more or less close to $\langle T_r \rangle_I \approx -\langle \varepsilon \rangle_I$, is observed for the E2 and E3 cases over a wide range of scales in the interface normal direction. On the contrary, $\langle T_r \rangle_I \approx -2\langle \varepsilon \rangle_I$ is observed when the TNTI-averaged results are not conditioned on H_m and v_n^l. This discrepancy between the unconditioned observation and the case of mild entrainment conditions suggests the significance of regions like E6, where the TNTI-average values of the KHMH terms exhibit more extreme behaviour, even though E2 and E3 regions represent a substantial portion of the total IES.

- The pressure term $\langle T_p \rangle_I$ makes significant contributions to the scale-by-scale energy balance which varies drastically for concave/convex regions at scales up to $r_n \approx 1.5\lambda$, even leading to positive values of $\langle T_r^I \rangle_I$ at convex regions. Similarly, a significant qualitative difference is observed in terms of the effects of pressure between the regions of entrainment and detrainment.

- The solenoidal part of the interscale transfer $\langle T_r^S \rangle_I$ is observed to make its maximal contribution enhancing the forward cascade at scales $r_n \approx \lambda$ in the interface normal direction. This behaviour is observed for all conditions D2, E2, E3, and E6, irrespective of the local entrainment/detrainment or convex/concave properties of the IES region.

- The irrotational part of the interscale transfer, $\langle T_r^I \rangle_I$, plays a crucial role in the overall energy transfer across scales at the interface. It contains the influence of pressure on the velocity field and is responsible for a substantial portion of the inverse cascade of energy especially for the scales in the interface normal direction.

- The local (r_t, r_n) field of $\langle T_r \rangle_I$ shows an average energy transfer towards the larger scales in the TNTI normal direction for scales $r_n > 20\eta$ at the regions of detrainment while the interscale energy transfer is towards the smaller scales in the tangential direction i.e. $\langle T_r \rangle_I < 0$. On the contrary, for the E6 condition (the regions of extreme entrainment), an inverse cascade is observed in the tangential direction while very high values of interscale transfer are observed in the interface normal direction at scales $r_n \approx 20\eta$.

5.4 KHMH balance at different centroid locations along the TNTI normal axis y_I

The KHMH balance provides insight into the scale-by-scale energy budget at the specific location where the centroid $\boldsymbol{X}$ is placed. In the previous sections, we investigated the scale-by-scale budget for $|\delta\boldsymbol{u}|^2$ precisely at the location of the IES, i.e., $\boldsymbol{X} = \boldsymbol{X}_0$. However, it is also possible to analyze the budget for $|\delta\boldsymbol{u}|^2$ at various distances from the IES by moving the centroid $\boldsymbol{X}$ along the interface normal axis y_I. In this section, we carry out the analysis of the KHMH balance at the locations $y_I/\eta = -6$ and $y_I/\eta = -10$, both located in the turbulent side of the IES of $\omega_{th}^2/\omega_{ref}^2 = 10^{-3}$. These locations have been chosen, due to the fact that they correspond to the normal distances from the IES, where the P_{ω^2} term reaches its first peak towards the turbulent core on the y_I axis in figures 4.34b and 4.34d, showing significant production of ω^2 and thus non-linear interactions between scales.

The analysis presented in this section shares some similarities with the work of Watanabe et al. (2020), as it involves applying the KHMH not only at the exact IES location but also on its turbulent side. In the study by Watanabe et al. (2020), a filter of size r is used to separate the kinetic energy associated with filtered scales (scales smaller than r) from non-filtered scales (scales larger than r). Energy transfer between these resolved and unresolved scales is examined, though not through the KHMH equation, but by using an equation for sub-grid scale (SGS) kinetic energy, following studies using the same equation in the context of large eddy simulation.

Even though some similarity between the current analysis and the methodology in Watanabe et al. (2020) is mentioned, there are crucial differences between the two approaches that make the direct comparison difficult. For example, it has been shown by Vela-Martín (2022) that SGS stresses include conservative spatial fluxes, which highlights the difference between the SGS backscatter and the inverse cascade observed for the interscale transfer term of the KHMH equation.

In addition, in the present study, we keep separations in TNTI normal and tangential directions, namely r_n and r_t, to account for the anisotropy caused by the presence of the interface.

Figure 5.16 presents the KHMH terms as functions of r_n/η at three different locations for the centroid $\boldsymbol{X}$: $y_I/\eta = 0$, $y_I/\eta = -6$, and $y_I/\eta = -10$. These terms are normalized again by ε_c and by the TNTI-average profile of $\langle\varepsilon\rangle_I(r_n/\eta)$. For the cases of $y_I/\eta = -6$ and $y_I/\eta = -10$, the point on the non-turbulent side of the centroid $\boldsymbol{X}$ reaches the location of IES at $r_n/\eta = 12$ and $r_n/\eta = 20$ respectively. For the scales r_n/η which exceed these

values, one point is located on the non-turbulent side of the IES while to other point is in the turbulent region.

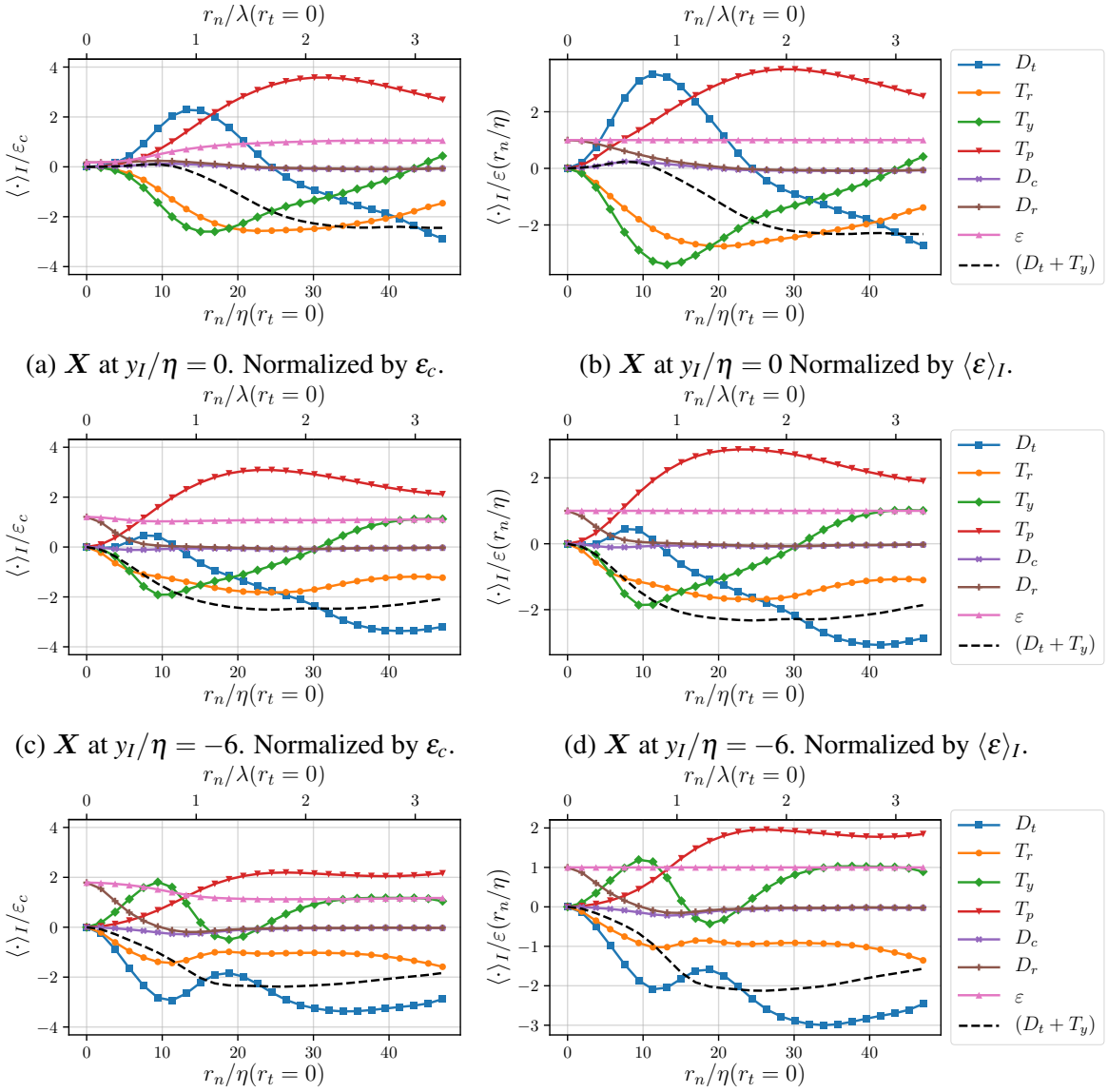

(a) $\boldsymbol{X}$ at $y_I/\eta=0$. Normalized by ε_c.

(b) $\boldsymbol{X}$ at $y_I/\eta=0$ Normalized by $\langle\varepsilon\rangle_I$.

(c) $\boldsymbol{X}$ at $y_I/\eta=-6$. Normalized by ε_c.

(d) $\boldsymbol{X}$ at $y_I/\eta=-6$. Normalized by $\langle\varepsilon\rangle_I$.

(e) $\boldsymbol{X}$ at $y_I/\eta=-10$. Normalized by ε_c.

(f) $\boldsymbol{X}$ at $y_I/\eta=-10$ Normalized by $\langle\varepsilon\rangle_I$.

Fig. 5.16 TNTI-average profiles of KHMH terms, as a function of r_n/η, computed for the center-point location at $y_I/\eta=0$, $y_I/\eta=-6$ and $y_I/\eta=-10$ for the IES $\omega_{th}^2/\omega_{ref}^2=10^{-3}$. At $t/T_{ref}=50$ for the PJ4-HR simulation.

5.4.1 Advection and diffusion at different y_I locations

The inverse relationship between $\langle D_t \rangle_I$ and $\langle T_y \rangle_I$ has already been noted since figure 5.3b. Additionally, it has been observed that these two terms have significant magnitudes at the location of the IES.

By comparing figures 5.16b, 5.16d, and 5.16f, we can conclude that the observations made regarding the profiles of $\langle D_t \rangle_I$ and $\langle T_y \rangle_I$ for $y_I/\eta = 0$ are also applicable at other locations along the normal axis. However, it is worth noting that the r_n profile of $(\langle D_t \rangle_I + \langle T_y \rangle_I)$ changes as the centroid $\boldsymbol{X}$ moves along the normal axis.

Going from $y_I/\eta = 0$ to $y_I/\eta = -6$, the negative peak of $\langle T_y \rangle_I$ is reduced in magnitude and moves from $r_n/\eta = 14.5$ to $r_n/\eta = 10$. At $y_I/\eta = 0$, an approximate balance between $\langle D_t \rangle_I$ and $\langle T_y \rangle_I$ has already been mentioned; their sum is small but roughly equal to $\langle D_c \rangle_I$ for scales $r_n \lessapprox 10\eta$ (for the IES of $\omega_{th}^2/\omega_{ref}^2 = 10^{-3}$). However, this balance changes at $y_I/\eta = -6$, where there is an apparent imbalance between $\langle D_t \rangle_I$ and $\langle T_y \rangle_I$. The contributions of $\langle T_p \rangle_I$ and $\langle T_r \rangle_I$ lead to a steep negative trend in $(\langle D_t \rangle_I + \langle T_y \rangle_I)$ starting from very small scales r_n. For larger scales, i.e. $r_n/\eta \gtrapprox 25$ at $y_I/\eta = 0$, $r_n/\eta \gtrapprox 14$ at $y_I/\eta = -6$ and $r_n/\eta \gtrapprox 18$ at $y_I/\eta = -10$, $(\langle D_t \rangle_I + \langle T_y \rangle_I)$ attains a value close to $-2\langle \varepsilon \rangle_I$ for all centroid locations. On the contrary, the range of scales where $(\langle D_t \rangle_I + \langle T_y \rangle_I) > 0$ observed at $y_I/\eta = 0$ exists only at $y_I/\eta = 0$ location.

It has been pointed out in figure 5.3 that the viscous diffusion in space $\langle D_c \rangle_I$ is positive and thus contributes to the increase of $|\delta \boldsymbol{u}|^2$ for the scales $r_n/\eta < 11.4$ at $y_I/\eta = 0$. Comparing figures 5.16b, 5.16d and 5.16f shows that $\langle D_c \rangle_I$ becomes negative for scales comparable to $r_n = 11.4\eta$ at locations in the turbulent side of the IES. At location $y_I/\eta = -6$, the peak negative contribution of $\langle D_c \rangle_I$ is at scale $r_n = 6.3\eta$ and $\langle D_c \rangle_I$ remains negative until $r_n \approx 11\eta$. When we move the centroid to $y_I/\eta = -10$, the location of this peak negative contribution moves to $r_n = 14\eta$ ($r_n \approx \lambda$) and $\langle D_c \rangle_I$ is negative until $r_n = 20.2\eta$ meaning that the kinetic energy for scales smaller than 20.2η is reduced by viscous diffusion mechanism in space. Therefore, it can be suggested that viscosity plays a role in transferring kinetic energy from a certain range of scales, and from the turbulent side of the IES towards the non-turbulent region.

5.4.2 Dissipation and interscale transfer at different y_I locations

To begin with, we can note the $\langle \varepsilon \rangle_I$ values at $r_n/\eta = 0$ in figures 5.16a, 5.16c and 5.16e, which takes a small value at $y_I/\eta = 0$, slightly higher than ε_c at $y_I/\eta = -6$ and nearly $2\varepsilon_c$ at $y_I/\eta = -10$.

As one can observe from eq. 5.3, the dissipation term consists of the sum of dissipation at the two points $\boldsymbol{\xi}_1$ and $\boldsymbol{\xi}_2$. At the location $y_I/\eta = 0$, the centroid is located directly on the IES defined by $\omega_{th}^2/\omega_{ref}^2 = 10^{-3}$, thus the $\langle\varepsilon\rangle_I$ at $r_n/\eta = 0$ is very small as dissipation is much lower than ε_c at the location of the IES. On the other hand, when the KHMH centroid is moved towards the turbulent core, the $\langle\varepsilon\rangle_I$ at $r_n/\eta = 0$ increases due to higher dissipation values at the location of centroid $\boldsymbol{X}$. At the location $y_I/\eta = -10$ the $\langle\varepsilon\rangle_I$ starts from $\langle\varepsilon\rangle_I \approx 2\varepsilon_c$ for scales $r_n/\eta = 0$ showing that the value of dissipation at this location is close to ε_c already.

A very striking observation in figure 5.16 is that at location of $y_I/\eta = -10$, given in figure 5.16f, the interscale transfer term $\langle T_r\rangle_I$ increases in magnitude as r_n approaches to $r_n = 10\eta$ where it reaches $\langle\varepsilon\rangle_I$ and remains that way for a wide range of scales (until $r_n/\eta = 40$). This balance between $\langle T_r\rangle_I$ and $\langle\varepsilon\rangle_I$ is unexpected at this location, where the centroid is located only at a distance 10η from the IES location.

Another detail that makes this observation even more interesting is that the balance $\langle T_r\rangle_I \approx \langle\varepsilon\rangle_I$ continues to hold even for large separations r_n for which one point is on the non-turbulent side and the other point is on the turbulent side of the IES. For scales that fully fit into the turbulent side of the interface ($r_n < 10\eta$), the interscale transfer term $\langle T_r\rangle_I$ increases in magnitude with increasing r_n until it reaches $\langle\varepsilon\rangle_I$. Going closer to the IES, at $y_I/\eta = -6$ and at the IES location $y_I/\eta = 0$, it is observed that the interscale transfer $\langle T_r\rangle_I$ exceeds $\langle\varepsilon\rangle_I$ over a large range of scales, showing a considerable forward cascade of the energy in the interface normal direction. It should also be noted in figure 5.16d that at $y_I/\eta = -6$, $|\langle T_r\rangle_I| = |\langle\varepsilon\rangle_I|$ is attained at scales $r_n > 40\eta$.

At $y_I/\eta = 0$, for scales $r_n < 11.4\eta$, where $(\langle D_t\rangle_I + \langle T_y\rangle_I)$ is positive, it is observed that $\langle T_r\rangle_I$ balances $\langle T_p\rangle_I$ and the net viscous loss of kinetic energy due to $(\langle D_r\rangle_I - \langle\varepsilon\rangle_I)$. If we look at figure 5.16d, this balance does not exist at location $y_I/\eta = -6$ where $\langle T_r\rangle_I$ is significantly smaller than $\langle T_p\rangle_I$ in magnitude for all the range of scales r_n. When the KHMH centroid is moved further inside the turbulent region, at $y_I/\eta = -10$ (figure 5.16f), $\langle T_r\rangle_I$ becomes larger than $\langle T_p\rangle_I$ for scales $r_n \lessapprox 13.6$ even though at larger scales r_n, the magnitude of $\langle T_p\rangle_I$ exceeds the magnitude of $\langle T_r\rangle_I$.

5.4.3 Contributions of the solenoidal and irrotational parts of the interscale transfer at different y_I locations

The observation that $\langle T_r\rangle_I = \langle\varepsilon\rangle_I$ is found for scales extending across the TNTI layer and into the non-turbulent region at $y_I/\eta = -10$ is indeed intriguing. This balance between $\langle T_r\rangle_I$ and $\langle\varepsilon\rangle_I$ near the interface is unexpected and raises questions about the underlying

mechanisms. To further investigate the mechanisms leading to this balance, we can examine the contributions of the solenoidal ($\langle T_r^S \rangle_I$) and irrotational ($\langle T_r^I \rangle_I$) parts of $\langle T_r \rangle_I$ for various scales at different locations along the interface normal axis. Figure 5.16 shows the solenoidal/irrotational parts of the $\langle T_r \rangle_I$ at IES location, at $y_I/\eta = 0$, $y_I/\eta = -6$ and $y_I/\eta = -10$, as functions of r_n.

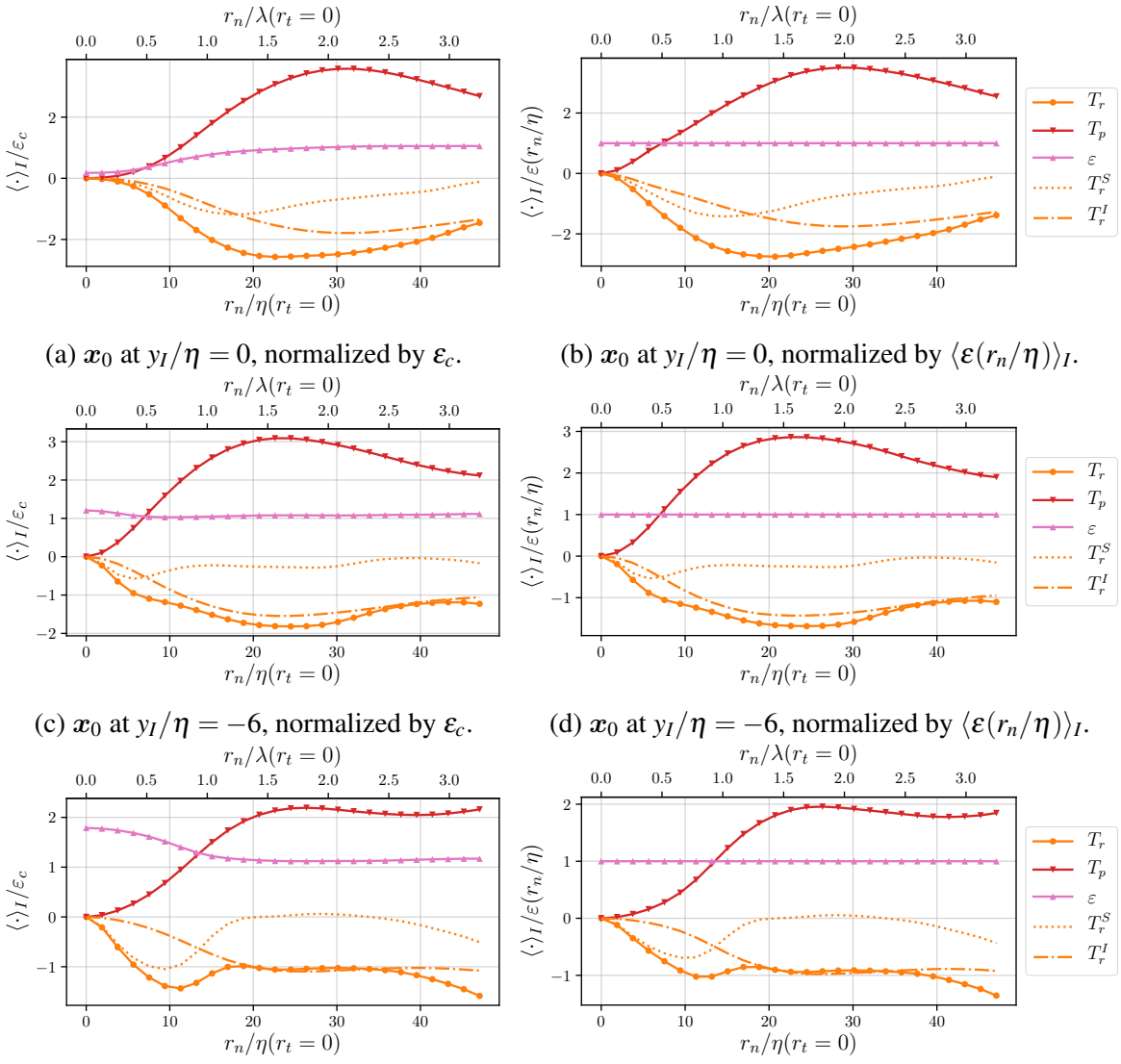

(a) $\boldsymbol{x}_0$ at $y_I/\eta = 0$, normalized by ε_c.

(b) $\boldsymbol{x}_0$ at $y_I/\eta = 0$, normalized by $\langle \varepsilon(r_n/\eta) \rangle_I$.

(c) $\boldsymbol{x}_0$ at $y_I/\eta = -6$, normalized by ε_c.

(d) $\boldsymbol{x}_0$ at $y_I/\eta = -6$, normalized by $\langle \varepsilon(r_n/\eta) \rangle_I$.

(e) $\boldsymbol{x}_0$ at $y_I/\eta = -10$, normalized by ε_c.

(f) $\boldsymbol{x}_0$ at $y_I/\eta = -10$, normalized by $\langle \varepsilon(r_n/\eta) \rangle_I$.

Fig. 5.17 Decomposition of $\langle T_r \rangle_I$ into irrotational and solenoidal parts $\langle T_r^I \rangle_I$ and $\langle T_r^S \rangle_I$, plotted as a function of r_n/η, computed at centroid placed at $y_I/\eta = 0$, $y_I/\eta = -6$ and $y_I/\eta = -10$ and normalized by ε_c and $\langle \varepsilon(r_n/\eta) \rangle_I$. At $t/T_{ref} = 50$ for the PJ4-HR simulation over the IES of $\omega_{th}^2/\omega_{ref}^2 = 10^{-3}$.

At $y_I/\eta = -10$, (figure 5.16f), it is interesting to see that the contribution from the solenoidal part $\langle T_r^S \rangle_I$ into the total interscale transfer $\langle T_r \rangle_I$ is zero for the scales associated with $r_n > 20\eta$ where $\langle T_r \rangle_I \approx \langle \varepsilon \rangle_I$. Hence $\langle T_r \rangle_I$ is fully constituted by the irrotational part $\langle T_r^I \rangle_I$ at these scales for $y_I/\eta = -10$. A particular detail about scale $r_n = 20\eta$ is that this is the largest scale that can fit into the layer between the KHMH centroid $\boldsymbol{X}$ and the IES location. At the separation length $r_n = 20\eta$, the point on the non-turbulent side reaches the IES location, thus scales of $r_n > 20$ extend over the IES into the non-turbulent region. Given this extension into the irrotational region, it is plausible that the interscale energy transfer at these scales is primarily driven by pressure variations.

As we approach closer to the IES location at $y_I/\eta = -6$, we observe in figure 5.17d that $\langle T_r^S \rangle_I$ starts taking moderate, non-zero, negative values and remains non-zero over a broad range of scales, although $\langle T_r^I \rangle_I$ still dominates $\langle T_r \rangle_I$ for scales with $r_n/\eta \gtrapprox 10$. Between the scales of $r_n/\eta = 6$ and $r_n/\eta = 10$, $\langle T_r^S \rangle_I$ diminishes rapidly in magnitude as the outer point approaches the IES location. However, its magnitude does not drop to zero for larger scales and remains relatively constant until $r_n \approx 2\lambda$. It does however reach zero between $r_n = 2.5\lambda$ and $r_n = 3\lambda$.

At the IES location ($y_I/\eta = 0$), the magnitude of $\langle T_r^S \rangle_I$ becomes comparable to that of $\langle T_r^I \rangle_I$ (see figure 5.17b). The maximum contribution of $\langle T_r^S \rangle_I$ occurs at scales around $r_n = 14.8\eta$, which corresponds to scales of the order of λ. In contrast, the contribution of $\langle T_r^I \rangle_I$ peaks for scales at $r_n = 2\lambda$, which are significantly larger.

There appears to be a continuous transition between the profiles of $\langle T_r^I \rangle_I$ and $\langle T_r^S \rangle_I$ as we move from $y_I/\eta = -10$ to $y_I/\eta = 0$. Looking at the profiles in figure 5.17, it is interesting to observe that $\langle T_r^S \rangle_I$ is strictly zero at scales extended to the non-turbulent region of the TNTI at $y_I/\eta = -10$, whereas at $y_I/\eta = -6$, a weak contribution of $\langle T_r^S \rangle_I$ exists at scales extending to the non-turbulent side of the IES. Finally, at the IES location, the contribution from the solenoidal part of the interscale transfer is significant for a wide range of scales in the interface normal direction.

5.4.4 KHMH terms at different y_I locations as functions of r_t and r_n

In figures 5.16 and 5.17, we have observed specific characteristics of the KHMH terms for various scales associated with the interface normal separation r_n. To gain a more comprehensive understanding, contour plots of the KHMH terms as functions of r_t/η and r_n/η are presented in figure 5.18.

At $y_I/\eta = 0$, the rate of change in time of $|\delta \boldsymbol{u}|^2$ for the scales $|\boldsymbol{r}| < 24.7\eta$ is positive, which is shown in figure 5.18a with the plot of $\langle D_t \rangle_I / \varepsilon_c$. In the tangential direction, the kinetic energy increases in all scales. Referring to the eq. 5.4 if we keep the D_t term on

the left-hand side and put all the other terms to the right-hand side of the equation we end up with $\langle D_t \rangle_I = -\langle T_y \rangle_I - \langle T_r \rangle_I - \langle T_p \rangle_I + ...$ The negative values of the terms $\langle T_y \rangle_I$, $\langle T_r \rangle_I$ and $\langle T_p \rangle_I$ in figure 5.18a result in positive values of $\langle D_t \rangle_I$. Among these terms, the most substantial contribution in the tangential direction comes from the $\langle T_p \rangle_I$ term, highlighting the impact of pressure. However, both $\langle T_y \rangle_I$ and $\langle T_r \rangle_I$ also contribute to $\langle D_t \rangle_I > 0$, especially for scales associated with r_t (with r_n being small).

In the interface normal direction, $\langle T_y \rangle_I$ makes a significant contribution at scales around $r_n/\eta \approx 15$ (close to λ), where $\langle D_t \rangle_I > 0$, particularly for small values of r_t. This contribution may be attributed to the transport of turbulent kinetic energy toward the IES location by the TNTI-averaged velocity field (see figure 4.14a).

On the other hand, $\langle T_r \rangle_I$ makes its most significant contribution at scales around $r_n \approx 23\eta$, leading to an increase in $\langle D_t \rangle_I$. However, it is important to note that $\langle D_t \rangle_I = 0$ can still be observed in figure 5.18a at the exact same location. At this scale, the contributions from $\langle T_y \rangle_I$ and $\langle T_r \rangle_I$ are completely counteracted by the $\langle T_p \rangle_I$ term.

In summary, in figure 5.18a, for scales in the interface normal direction, $\langle T_y \rangle_I$ has its maximum impact on scales around $r_n \approx 15\eta$, $\langle T_r \rangle_I$ is most influential at scales around $r_n \approx 23\eta$, and $\langle T_p \rangle_I$ dominates at scales around $r_n \approx 32\eta$. This indicates that the scales most affected by the spatial transfer in physical space are on the order of λ and are the smallest among the three. $\langle T_r \rangle_I$ attains its maximum point at slightly larger scales, while the effects of pressure are most pronounced for even larger scales, approximately $r_n \approx 2\lambda$.

At $y_I/\eta = -10$ (figure 5.18c), the interscale transfer term appears to exhibit a somewhat more isotropic behaviour compared to the other two locations closer to the IES. The negative values of $\langle T_r \rangle_I$ related to the forward cascade are also present for separations in the tangential direction, in contrast to the $\langle T_r \rangle_I$ results for the $y_I/\eta = 0$ given in figure 5.18a. In addition to that, there is still a more prominent interscale transfer rate at scales $r_n \approx 11\eta$ at $y_I/\eta = -10$. It can be reminded that the $y_I/\eta = -10$ location is picked for the placement of the centroid due to the peak observed in the profile of P_{ω^2} in figure 4.34d, thus the non-linear production of ω^2 is high at this particular distance from the interface for the regions of the IES with high local entrainment velocity.

For the completeness of the picture, $\langle T_y \rangle_I$ at $y_I/\eta = -10$ (figure 5.18c) can also be compared with the results at $y_I/\eta = 0$ and $y_I/\eta = -6$ (figures 5.18a and 5.18b). At $y_I/\eta = 0$ and $y_I/\eta = -6$, $\langle T_y \rangle_I$ becomes positive for large scales of r_n. At $y_I/\eta = -10$, a second region of $\langle T_y \rangle_I > 0$ appears for scales between $r_n/\eta = 0$ and $r_n/\eta = 15$. Recalling that $\langle T_y \rangle_I > 0$, is associated with a decay of $|\delta \boldsymbol{u}|^2$ due to advection, this positive region might be related to the advection of these small scales towards the IES by the local velocity field.

In figure 5.19, the decomposition of the $\langle T_r \rangle_I$ into $\langle T_r^S \rangle_I$ and $\langle T_r^I \rangle_I$ has been given. In relation with the similarity of $\langle T_p \rangle_I$ in scale-space at $y_I/\eta = 0$, $y_I/\eta = -6$ and $y_I/\eta = -10$ locations, the irrotational part $\langle T_r^I \rangle_I$ remains qualitatively the same for these locations across the y_I/η axis.

On the other hand, at $y_I/\eta = -10$, the location where the balance of $\langle T_r^I \rangle_I = \langle \varepsilon \rangle_I$ is observed for scales $r_n \gtrapprox 10$ (see figure 5.16f), $\langle T_r^S \rangle_I$ is observed to be zero only for separations in the normal direction. In the tangential direction, significant negative $\langle T_r^S \rangle_I$ values show an intense forward cascade in this direction. Moreover, the peak of $\langle T_r \rangle_I$ along the r_n axis at $r_n \approx 10\eta$ in figure 5.16f is observed to be due to the $\langle T_r^S \rangle_I$. The contour field presented in figure 5.19c for $\langle T_r^S \rangle_I$ can be said to be more or less isotropic for scales $\boldsymbol{r} < 10\eta$ as the value of $\langle T_r^S \rangle_I$ seems to be independent from the orientation of $\boldsymbol{r}$.

5.4.5 Main observations for the KHMH balance at different y_I locations

After examining the KHMH balance at the precise location of the IES defined by $\omega_{th}^2/\omega_{ref}^2 = 10^{-3}$, we have proceeded to analyze this balance at various locations along the normal axis for the same IES. To achieve this, KHMH terms have been computed by placing the centroid $\boldsymbol{X}$ at $y_I/\eta = -6$ and $y_I/\eta = -10$. The objective of this analysis has been to investigate how the scale-by-scale energy balance is established in different regions near the interface. The primary observations from this analysis are as follows;

- At $y_I/\eta = 0$, we observe that $(\langle D_t \rangle_I + \langle T_y \rangle_I) > 0$ for relatively small r_n scales, suggesting an increase of kinetic energy for scales up to some extent in the normal direction. In contrast, $(\langle D_t \rangle_I + \langle T_y \rangle_I)$ remains negative for all scales of r_n at both locations $y_I/\eta = -6$ and $y_I/\eta = -10$ (figure 5.16).

- The viscous diffusion of kinetic energy in physical space $\langle D_c \rangle_I$, has different effects at different locations. At $y_I/\eta = 0$, it increases the kinetic energy associated with scales $r_n \approx \lambda$. Conversely, at $y_I/\eta = -10$, it contributes to a reduction of the kinetic energy associated with scales $r_n \approx \lambda$. This suggests a possible diffusion of kinetic energy in physical space, from the turbulent core towards the non-turbulent region, due to the action of viscosity (figure 5.16).

- At $y_I/\eta = -10$, a Kolmogorov-like balance is observed in the form $\langle T_r \rangle_I = \langle \varepsilon \rangle_I$. This is an interesting observation given how close this location is to the IES of $\omega_{th}^2/\omega_{ref}^2 = 10^{-3}$. Further decomposition of $\langle T_r \rangle_I$ into its solenoidal and irrotational parts, $\langle T_r^S \rangle_I$ and $\langle T_r^I \rangle_I$, reveals that $\langle T_r^S \rangle_I$ is non-zero for scales fully contained on the turbulent side of the TNTI, while for scales extending beyond $y_I/\eta = 0$, the irrotational part,

directly associated with pressure effects, becomes fully responsible for the interscale transfer rate, i.e. $\langle T_r \rangle_I = \langle T_r^I \rangle_I$ (figure 5.17).

- Looking at the local 2D contour fields of $\langle D_t \rangle_I$, $\langle T_y \rangle_I$, $\langle T_r \rangle_I$ and $\langle T_p \rangle_I$ as functions of r_t and r_n (figure 5.18), a significant change in the field of $\langle T_y \rangle_I$ is observed for different locations along y_I/η. Despite $\langle T_y \rangle_I$ being completely negative at $y_I/\eta = 0$, it exhibits positive regions mostly associated with separation vectors in the interface normal direction at $y_I/\eta = -6$, $y_I/\eta = -10$. It suggests the advection of the kinetic energy associated with scales with an approximate size of 10η, towards the interface location, by the local velocity field.

- Again the contour fields in figure 5.18 show that the interscale transfer term $\langle T_r \rangle_I$ becomes more isotropic on the $(r_t - r_n)$ plane as we go to $y_I/\eta = -10$. For $y_I/\eta = 0$ and $y_I/\eta = -6$, $\langle T_r \rangle_I$ remains very small for separations in the tangential direction and it gets negative values (forward cascade) in the interface normal direction.

- Decomposition of $\langle T_r \rangle_I$ into irrotational and solenoidal parts shows that $\langle T_r^I \rangle_I$ remains similar in scale-space $(r_t - r_n)$ for various y_I/η locations. On the other hand, $\langle T_r^S \rangle_I$ change significantly, especially in the tangential direction. Going from $y_I/\eta = 0$ to $y_I/\eta = -10$, the contribution of $\langle T_r^S \rangle_I$ gets more and more significant in the direction of forward cascade in the tangential direction of the interface.

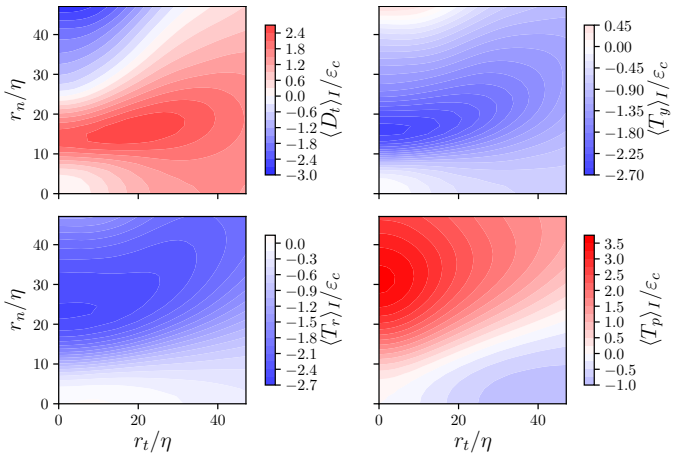

(a) $\boldsymbol{x}_0$ at $y_I/\eta = 0$

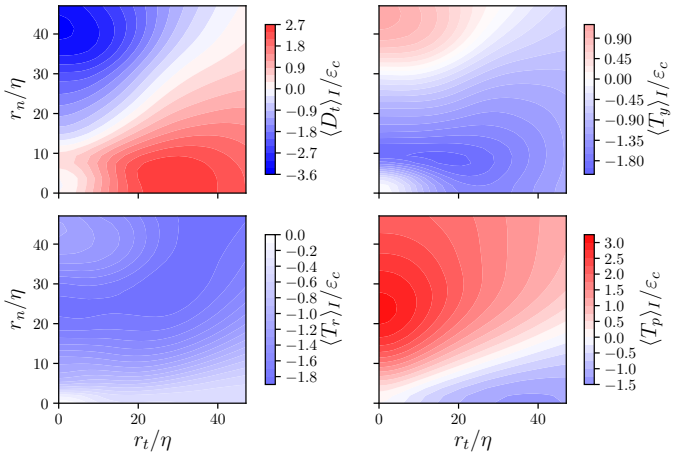

(b) $\boldsymbol{x}_0$ at $y_I/\eta = -6$

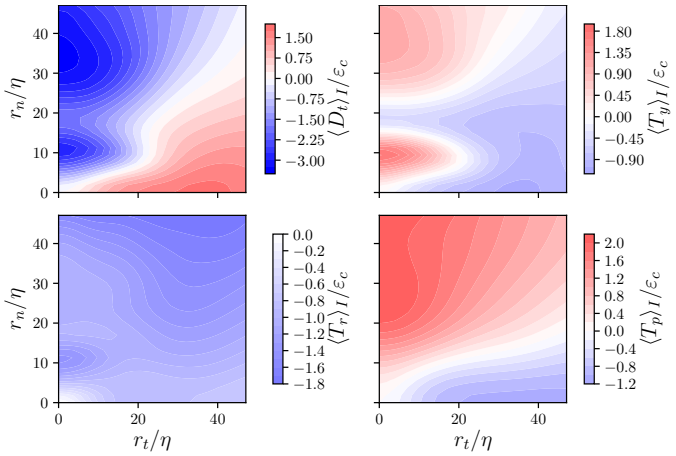

(c) $\boldsymbol{x}_0$ at $y_I/\eta = -10$

Fig. 5.18 TNTI-average local fields of KHMH terms, as a function of r_n/η and r_t/η. Computed with KHMH centered at $y_I/\eta = 0$, $y_I/\eta = -6$ and $y_I/\eta = -10$ for the IES of $\omega_{th}^2/\omega_{ref}^2 = 10^{-3}$, and normalized by ε_c.

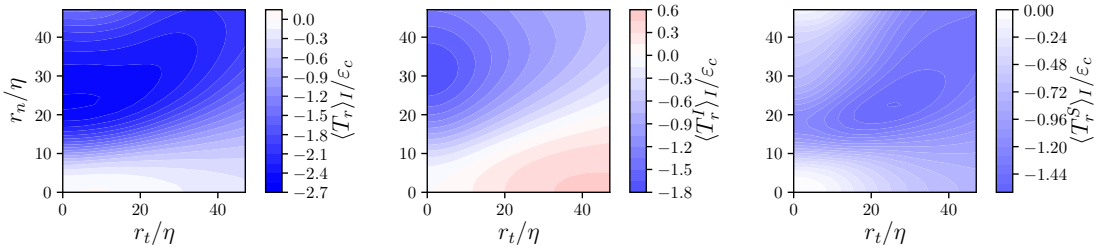

(a) $\boldsymbol{x}_0$ at $y_I/\eta = 0$

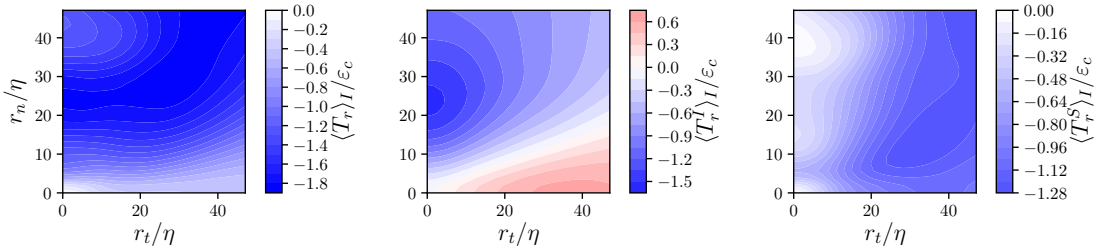

(b) $\boldsymbol{x}_0$ at $y_I/\eta = -6$

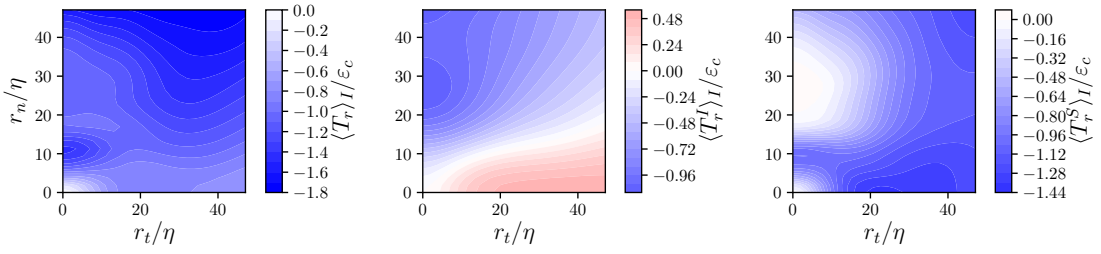

(c) $\boldsymbol{x}_0$ at $y_I/\eta = -10$

Fig. 5.19 TNTI-averaged fields of $\langle T_r \rangle_I$, $\langle T_r^S \rangle_I$ and $\langle T_r^I \rangle_I$, as functions of r_n/η and r_t/η. Computed with KHMH centered at $y_I/\eta = 0$, $y_I/\eta = -6$ and $y_I/\eta = -10$ for the IES of $\omega_{th}^2/\omega_{ref}^2 = 10^{-3}$, and normalized by ε_c.

5.5 Average compression/stretching-entrainment/detrainment conditions

In this section, we focus on the interscale transfer of the scale-by-scale kinetic energy $|\delta \boldsymbol{u}|^2$ at the location of the IES defined by $\omega_{th}^2/\omega_{ref}^2 = 10^{-3}$. Following the work of Zhou and Vassilicos (2020), we can define an average energy over scales smaller than $r \equiv |\boldsymbol{r}|$ as;

$$E(\boldsymbol{X},\boldsymbol{r}) = \frac{3}{\pi r^3}\int_{V(r)} |\delta \boldsymbol{u}|^2 d^3\boldsymbol{r}. \tag{5.9}$$

This relation is obtained by an application of a normalized 3D integration operation, $\frac{3}{4\pi r^3}\int_{V(r)} d^3\boldsymbol{r}$ where $V(r)$ is the volume of a sphere with radius r.

A relation for the evolution of $E(\boldsymbol{X},\boldsymbol{r})$ can be written by the application of the normalized integral operation to the eq. 5.3. Here, we specifically focus on the interscale energy flux term, which can be expressed as a flux across the bounding surface of the volume of the sphere $V(r)$ (making use of the divergence theorem) as follows;

$$\Pi(\boldsymbol{X},\boldsymbol{r}) = \frac{3}{\pi r^3}\int_{V(r)} \frac{\partial}{\partial r_i}[\delta u_i |\delta \boldsymbol{u}|^2] d^3\boldsymbol{r} = \frac{3}{\pi r^3}\int_{S(r)} \delta \boldsymbol{u}\cdot\hat{\boldsymbol{r}}|\delta \boldsymbol{u}|^2 d^2\boldsymbol{r} \tag{5.10}$$

where $S(r)$ denotes the surface of a sphere with radius r and $\hat{\boldsymbol{r}}$ is the unit vector in the direction of $\boldsymbol{r}$.

Upon integrating equation 5.3 and writing the interscale flux on the right-hand side, we can observe its contribution to the rate of change of $E(\boldsymbol{X},r)$ as follows;

$$\frac{\partial E}{\partial t} = -\frac{3}{\pi r^3}\int_{S(r)} \delta \boldsymbol{u}\cdot\hat{\boldsymbol{r}}(\delta \boldsymbol{u})^2 d^2\boldsymbol{r} + ..., \tag{5.11}$$

It is useful to note that, in this section, we focus on the interscale energy transfer rate at the TNTI location but the significant contributions of the other terms such as the pressure-velocity term, the term for the energy transfer in physical space in the vicinity of the TNTI should still be acknowledged as has been shown in previous sections and that these terms may be significant in the behaviour of E thus the "..." in eq. 5.11.

An important detail about eq. 5.10 is that the sign of the interscale energy flux is determined solely by the $\delta \boldsymbol{u}\cdot\hat{\boldsymbol{r}}$ term. Considering the relation between the rate of change of E and the interscale flux given by relation 5.11, it can be observed that E associated with scales smaller than r, increases over time when $(\delta \boldsymbol{u}\cdot\hat{\boldsymbol{r}}) < 0$, and it decreases when $(\delta \boldsymbol{u}\cdot\hat{\boldsymbol{r}}) > 0$ if all other terms are kept constant. It should be noted that these cases of

$(\delta \boldsymbol{u} \cdot \hat{\boldsymbol{r}}) < 0$ and $(\delta \boldsymbol{u} \cdot \hat{\boldsymbol{r}}) > 0$ correspond to compression and stretching events in the direction of $\boldsymbol{r}$, respectively.

In the case of compression events, $|\delta \boldsymbol{u}|^2$ is transported towards smaller scales, resulting in a positive contribution to kinetic energy at scales smaller than r. Stretching events, on the other hand, lead to the transfer of energy from scales smaller than r towards scales larger than r, manifesting as a negative contribution to E in equation 5.11.

We begin by examining figure 5.20, which presents $\langle \delta \boldsymbol{u} \cdot \boldsymbol{r} \rangle_I$ and $\langle \delta \boldsymbol{u} \cdot \boldsymbol{r} |\delta \boldsymbol{u}|^2 \rangle_I$ as functions of r_t/δ and r_n/δ. The TNTI-averaging operation is performed across the IES without applying any conditions on H_m and v_n^l.

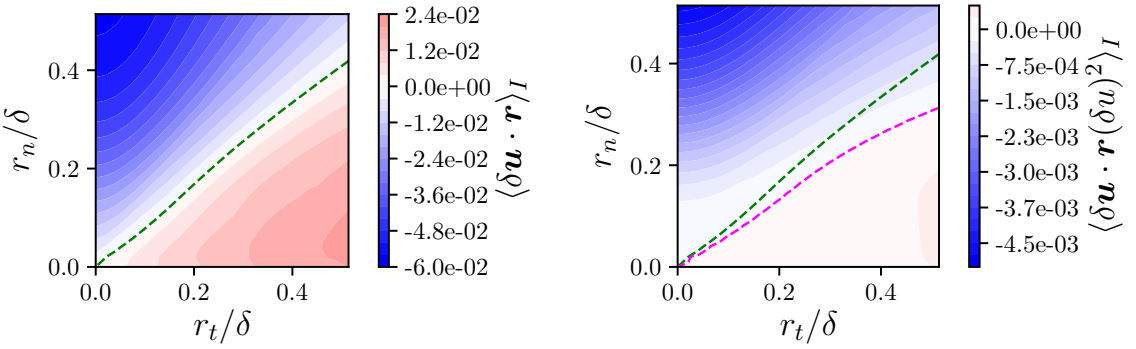

(a) (b)

Fig. 5.20 $\langle \delta \boldsymbol{u} \cdot \boldsymbol{r} \rangle_I$ and $\langle \delta \boldsymbol{u} \cdot \boldsymbol{r} (\delta u)^2 \rangle_I$ as a function of r_t/δ and r_n/δ, centered at the interface. Without any conditions applied for H_m and v_n^l and for the IES of $\omega_{th}^2/\omega_{ref}^2 = 10^{-3}$.

The current findings align with those presented in Zhou and Vassilicos (2020), where the same variables are obtained for the TNTI of a spatially developing turbulent wake. Figure 5.20a illustrates the presence of compressive motion on average, indicated by the negative values of $\langle \delta \boldsymbol{u} \cdot \boldsymbol{r} \rangle_I$, in the TNTI normal direction. The green dashed line demarcates the boundary between regions where this term is negative and positive. The angle between the face normal $\boldsymbol{e}_y$ and the vector $\boldsymbol{r}$, where the characteristics of the motion change from compressive to stretching on average, is found to be 50°, which is the exact same value that has been reported by Zhou and Vassilicos (2020) for the TNTI of a spatially developing wake.

Figure 5.20b displays $\langle \delta \boldsymbol{u} \cdot \hat{\boldsymbol{r}} (\delta \boldsymbol{u})^2 \rangle_I$ as a function of r_n/δ and r_t/δ, which directly represents the interscale energy flux. The magenta dashed line in figure 5.20b delineates the border between negative and positive values of $\langle \delta \boldsymbol{u} \cdot \hat{\boldsymbol{r}} |\delta \boldsymbol{u}|^2 \rangle_I$, while the green dashed line is taken from figure 5.20a for comparison.

Above the green dashed line, the local field exhibits compressive motion on average, and the average interscale transfer of energy is from large to small scales. Below the magenta line,

motion is predominantly stretching on average, and the energy transfer occurs from small to large scales. A region between these two exists, which corresponds to the area between the green and magenta dashed lines, where the motion is stretching on average but the average interscale transfer is nevertheless from large to small scales. This suggests significant contributions of the extreme events, as an average forward cascade is present where the motion is stretching on average. A more detailed analysis of this phenomenon is presented in Zhou and Vassilicos (2020) and a similar picture for $\langle \delta \boldsymbol{u} \cdot \boldsymbol{r} |\delta \boldsymbol{u}|^2 \rangle_I$ is presented for the spatially developing turbulent wake. There is a slight difference which is that the mid-zone between green and magenta dashed lines is larger in the flow of Zhou and Vassilicos (2020). This difference may be due to the fact that the expansion of the temporally developing turbulent jet analyzed in the present study is fundamentally different from its spatially developing counterpart and also from the spatially developing turbulent wake. Furthermore, the spatial development of the wake may have implications for the mean orientation of the $\boldsymbol{e}_y$, which affects the TNTI-averaged fields of velocity, thus affecting the $\langle \delta \boldsymbol{u} \cdot \boldsymbol{r} \rangle_I$ at the TNTI.

The results presented in figure 5.20 are also to be compared with the findings of Watanabe et al. (2020), where they employed a decomposition of the interscale energy flux term in the SGS budget equation (Watanabe et al., 2020) into contributions associated with the gradients of the different components of velocity in various directions. They observed that the terms containing the gradients in the interface normal direction (both for the interface normal and tangential components of the velocity) cause a transfer of energy from large to small scales (Watanabe et al., 2020). Similar to what has been observed in figure 5.20b, Watanabe et al. (2020) report that the terms containing the tangential gradient lead to an average energy transfer from small to large scales for a certain distance from the interface.

5.5.1 Average compression/stretching and the interscale energy flux at the entrainment/detrainment regions of the interface

In section 4.11.1, we have observed significant changes in the TNTI-averaged fields when conditioning was applied based on H_m and v_n^l in the regions of detrainment, entrainment, and fast entrainment. These variations in the TNTI-averaged local fields are likely to have direct implications for the statistics of compression and stretching events in the interface normal and tangential directions. To gain further insight, we will now examine the terms presented in figure 5.20 for the conditions D2, E2, E3, and E6.

Figure 5.21 displays $\langle \delta \boldsymbol{u} \cdot \boldsymbol{r} \rangle_I$ and $\langle \delta \boldsymbol{u} \cdot \boldsymbol{r} |\delta \boldsymbol{u}|^2 \rangle_I$ as functions of r_t/δ and r_n/δ for the D2, E2, E3, and E6 conditions. Comparison of figure 5.21a with figures 5.21c, 5.21e, and 5.21g, leads to a conclusion supporting the observations made in section 4.11.1 and highlights

the crucial difference between the local detrainment and entrainment regions as the different directions where the average compression/stretching events are observed. In the entraining regions, we observe an average compression in the TNTI normal direction and a stretching event in the tangential direction of the interface on average. In contrast, the detrainment regions exhibit compression on average in the tangential direction and an average stretching in the TNTI normal direction.

For the D2 condition, there is a significant stretching motion in the interface normal direction, indicated by positive values of $\langle \delta \boldsymbol{u} \cdot \boldsymbol{r} \rangle_I$ in figure 5.21a. The positive peak in $\langle \delta \boldsymbol{u} \cdot \boldsymbol{r} \rangle_I$ occurs at $r_n/\delta = 0.43$ ($r_n/\eta = 38.7$) in the normal direction of the interface. At this separation value, the point on the turbulent side of the interface is located at $y_I/\eta \approx 20$.

In figure 5.21e (E3 condition), for the convex regions ($H_m > 0$), both compression and stretching events in the interface normal and tangential directions do not appear to be as prominent for relatively small separations, such as $\boldsymbol{r} < 0.15\delta(13.5\eta)$. However, in the case of the E2 and E6 conditions, compression in the TNTI normal direction and stretching in the tangential direction are noticeable even at very small separation values (see figures 5.21c and 5.21g). It can be noted that when the centroid $\boldsymbol{X}$ is placed at $y_I/\eta = 0$, the scales associated with $r_n \approx 14\eta$ beyond the mean TNTI layer thickness δ_{ω^2}.

In addition to the significant differences in compression and stretching events on average, the interscale energy flux is observed to vary significantly between detrainment and entrainment regions when the figures 5.21b, 5.21d, 5.21f, and 5.21h are compared.

For the E2 and E6 conditions, a forward cascade is present in the interface normal direction, while an inverse cascade is observed in the tangential direction of the interface. A similar pattern can be seen for the E3 condition, although the interscale energy flux does not reach high magnitudes for scales smaller than $|\boldsymbol{r}|/\lambda \approx 0.2$. In the tangential direction, an inverse cascade is observed for scales $r_t/\lambda > 0.39(r_t > 35.3\eta)$.

The behaviour of $\langle \delta \boldsymbol{u} \cdot \boldsymbol{r} |\delta \boldsymbol{u}|^2 \rangle_I$ undergoes a significant change for the D2 condition (see figure 5.21b), where a forward cascade is present for tangential separations. However, the magnitudes of $\langle \delta \boldsymbol{u} \cdot \boldsymbol{r} |\delta \boldsymbol{u}|^2 \rangle_I$ remain lower compared to the other cases. A region where $\langle \delta \boldsymbol{u} \cdot \boldsymbol{r} |\delta \boldsymbol{u}|^2 \rangle_I$ acquires positive values can be observed for large separations in the TNTI normal direction, i.e., $r_n/\delta > 0.38$, which shows an energy transfer from small scales towards larger scales in the interface normal direction.

This observation is interesting as the predominant direction of the average interscale energy transfer changes radically in the regions of local detrainment, while the previous observations made in figure 5.20 mostly hold for the regions of local entrainment (apart from the slightly different picture in the convex regions which are discussed above). With the investigation of $\langle \delta \boldsymbol{u} \cdot \boldsymbol{r} \rangle_I$ and $\langle \delta \boldsymbol{u} \cdot \boldsymbol{r} |\delta \boldsymbol{u}|^2 \rangle_I$ at the location of the IES, without applying any

conditions on the statistics (see figure 5.20a), it has been observed that compression/stretching motions dominate, on average, in the interface normal/tangential directions respectively. The contour plot in figure 5.20b also shows that the direction and scales for which the mean compression/stretching is observed mostly align with the forward/backward cascade of energy in scale space. On the contrary, when the TNTI-average values of $\langle \delta \boldsymbol{u} \cdot \boldsymbol{r} \rangle_I$ and $\langle \delta \boldsymbol{u} \cdot \boldsymbol{r} | \delta \boldsymbol{u} |^2 \rangle_I$ is analyzed for the D2 condition (associated with the local detrainment), in the interface normal direction positive values of $\langle \delta \boldsymbol{u} \cdot \boldsymbol{r} \rangle_I$ shows stretching on average, and in the tangential direction, negative values of $\langle \delta \boldsymbol{u} \cdot \boldsymbol{r} \rangle_I$ shows compression on average. In addition to that, the mean interscale energy flux becomes large to small scales in the tangential direction, while an inverse cascade is observed on average in the interface normal direction. It can be noted that the average forward/backward cascade in various directions and scales does not correspond strictly to the average compression/stretching regions in the scale space for the D2 condition.

5.5.2 Main observations for the average compression/stretching motions and the interscale energy flux at the regions of ED conditions

In this section, we have focused on the contributions to the interscale energy transfer rate for various scales and directions at the location of the IES of $\omega_{th}^2/\omega_{ref}^2 = 10^{-3}$. The average compression/stretching events are also analyzed for the different regions of the IES as the $\delta \boldsymbol{u} \cdot \boldsymbol{r}$ term which determines the direction of the local cascade. The main observations presented in this section can be given as follows;

- Considering the TNTI-averaged results $\langle \delta \boldsymbol{u} \cdot \boldsymbol{r} \rangle_I$ and $\langle \delta \boldsymbol{u} \cdot \boldsymbol{r} | \delta \boldsymbol{u} |^2 \rangle_I$, average compression and stretching motions are present at the location of the IES but in different directions in $\boldsymbol{r}$ space i.e., compression in the interface normal direction and stretching in the tangential direction. These observations are compatible with the TNTI-average velocity fields analyzed in chapter 4 and the results obtained in the present study align with the findings in the literature for the TNTI of a spatially developing wake (Zhou and Vassilicos, 2020) and shear-free turbulence (Watanabe et al., 2020).

- Conditioning of the TNTI-averaged statistics allows us to see the average picture separately for the entrainment and detrainment regions of the interface (figure 5.21). For the regions of entrainment, compression ($\langle \delta \boldsymbol{u} \cdot \boldsymbol{r} \rangle_I < 0$) on average is observed in the interface normal direction and stretching ($\langle \delta \boldsymbol{u} \cdot \boldsymbol{r} \rangle_I > 0$) on average is observed in the tangential direction of the interface. Results are compatible with the observations made in chapter 4 for the TNTI-average velocity fields at the entrainment regions.

For the regions of detrainment, this picture is inverted and we observe stretching on average in the interface normal direction and compression on average in the tangential direction.

- The contribution to the total energy flux changes in various $\boldsymbol{r}$ directions with varying signs of $\langle \boldsymbol{\delta u} \cdot \boldsymbol{r} |\boldsymbol{\delta u}|^2 \rangle_I$. For the regions of entrainment, there is a dominantly forward cascade in the normal direction and a backward cascade in the tangential direction. On the other hand, for the regions of local detrainment, a forward cascade is present in the tangential direction, and a backward cascade is observed in the normal direction on average for a certain range of scales.

- The variation of $\langle \boldsymbol{\delta u} \cdot \boldsymbol{r} |\boldsymbol{\delta u}|^2 \rangle_I$ is observed to be affected less dramatically with the conditioning on the local mean curvature H_m. The main difference between the concave cases (E2 and E6 condition) and the convex cases (E3 condition) is at scales $r_t < 0.3\delta$ (27η), where the inverse cascade seen for concave cases is not present for the condition E3. However, the forward cascade in the interface normal direction remains unchanged between the concave and convex regions.

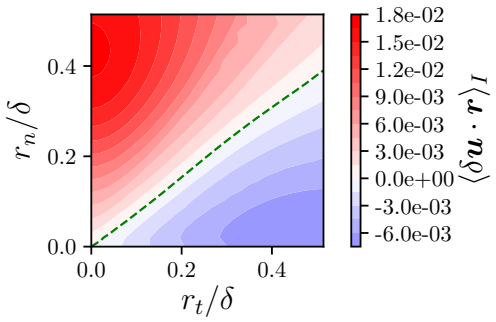

(a) D2 condition

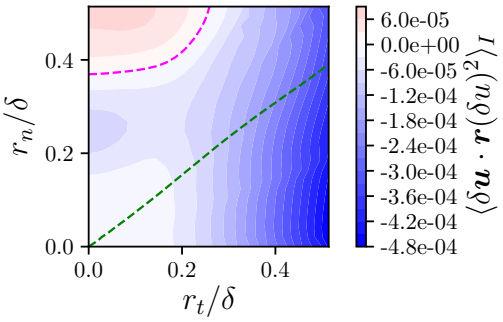

(b) D2 condition

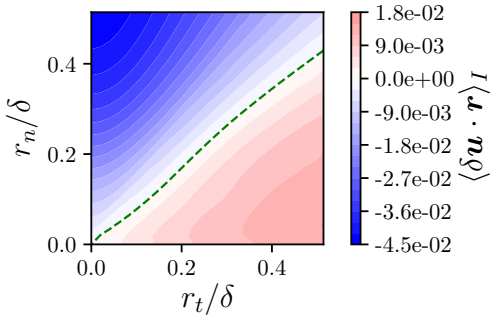

(c) E2 condition

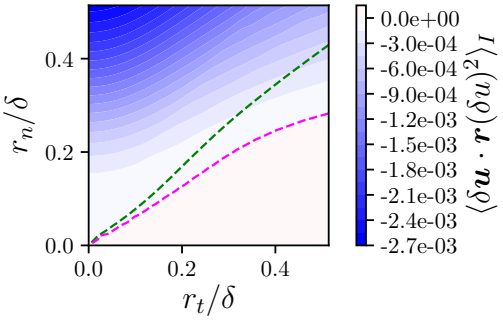

(d) E2 condition

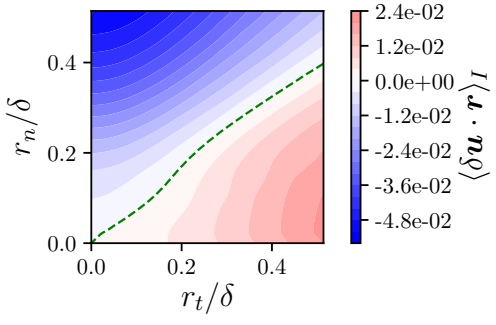

(e) E3 condition

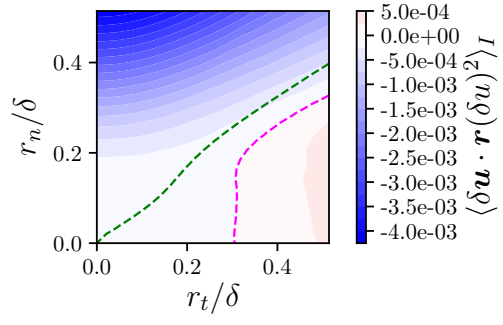

(f) E3 condition

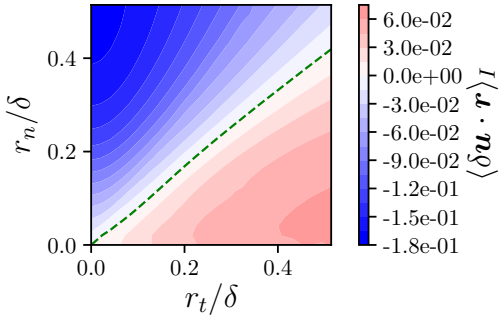

(g) E6 condition

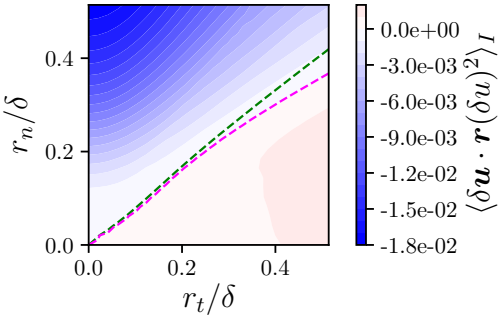

(h) E6 condition

Fig. 5.21 $\langle \delta \boldsymbol{u} \cdot \boldsymbol{r} \rangle_I$ and $\langle \delta \boldsymbol{u} \cdot \boldsymbol{r} |\delta \boldsymbol{u}|^2 \rangle_I$ as functions of r_t and r_n, for conditions D2, E2, E3 and E6. KHMH centroid placed on the IES defined by $\omega_{th}^2/\omega_{ref}^2 = 10^{-3}$.

5.6 Conclusions for the KHMH balance in the vicinity of the TNTI

In this chapter, we have investigated the KHMH balance at the TNTI location. The KHMH equation (eq. 5.3) provides insights into the interplay of various mechanisms affecting the balance of the turbulent kinetic energy at a given location for various scales such as the interscale transfer, transport in physical space, effects of pressure, viscous diffusion mechanisms in physical and scale space and the viscous dissipation.

Due to the various stages of the analysis being rather independent of each other, the conclusions are given separately in sections 5.2.7, 5.3.4, 5.4.5 and 5.5.2 in detail. In the current section, we give a general conclusion for the entire chapter, gathering the observations from previous sections.

We begin our analysis by looking at the scale-by-scale KHMH balance averaged along the IES of $\omega_{th}^2/\omega_{ref}^2 = 10^{-3}$ by placing the centroid $\boldsymbol{X}$ on the IES location. It has been shown that all terms of the KHMH equation (eq. 5.3) are active, on average, for most of the scales associated with various separations in the interface normal direction r_n. The kinetic energy associated with scales $r_n \lessapprox 10\eta$ is observed to increase in a reference frame moving with the flow i.e., $(\langle D_t \rangle_I + \langle T_y \rangle_I) > 0$.

The KHMH terms are also computed for the IES of $\omega_{th}^2/\omega_{ref}^2 = 10^{-6}$. The results show the robustness of the qualitative picture for the balance between various terms of the KHMH equation (eq. 5.3).

The TNTI-average results of the interscale transfer $\langle T_r \rangle_I$ and the transfer in physical space $\langle T_y \rangle_I$ analysed in the present study in the vicinity of the TNTI of a temporally developing jet, are observed to be qualitatively similar to the results obtained for the TNTI of spatially developing wakes by Zhou and Vassilicos (2020).

Following this, we performed an analysis by conditioning the KHMH statistics on local parameters along the IES i.e., local mean curvature H_m and the local propagation velocity v_n^l (ED conditions introduced in section 4.11). This conditioning revealed notable distinctions between entrainment and detrainment regions concerning various KHMH terms, as well as disparities between concave and convex regions in relation to the pressure-velocity term (see figure 5.11). The main observations are discussed below.

A very approximate balance between the TNTI-averaged interscale transfer and the dissipation terms ($\langle T_r \rangle_I \approx -\langle \varepsilon \rangle_I$) is observed for the conditions with the highest rate of occurrence along the IES i.e., E2 and E3 conditions (see figures 5.11b and 5.11c), which does not exist for the unconditioned case (figure 5.3b). This observation shows that the approximate balance between $\langle T_r \rangle_I$ and $\langle \varepsilon \rangle_I$ does not hold for the unconditioned statistics

due to the contribution from the regions where KHMH terms attain much higher values compared to the mean i.e., E6 condition (see figure 5.11d).

The effects of the pressure field vary significantly between the concave and convex regions. The direct relation between the pressure-velocity term T_p and the irrotational part of the interscale transfer rate T_r^I is given by the eq. 5.6. Considering this relation, $\langle T_p \rangle_I$ contributes in the direction of an inverse cascade i.e. $\langle T_r^I \rangle_I > 0$ in the interface normal direction at convex regions with local entrainment (see figure 5.12c for the E3 condition).

At the location of the IES of $\omega_{th}^2/\omega_{ref}^2 = 10^{-3}$, the solenoidal part of the interscale transfer $\langle T_r^S \rangle_I$ is observed to attain its maximal contribution at $r_n \approx \lambda$ for scales in the direction of the TNTI normal axis. Similar observations have been made in terms of the scales for which the contribution of T_r is highest in different flows, such as turbulent channel flow (Apostolidis et al., 2023) and forced homogeneous turbulence (Yasuda and Vassilicos, 2018) (where they apply an averaging over all the directions of $\boldsymbol{r}$) and decaying grid-generated turbulence (Obligado and Vassilicos, 2019) (where the isotropic form of interscale transfer rate is considered).

Moreover, we conducted an analysis of the KHMH balance at different locations along the TNTI normal axis, specifically at $y_I/\eta = -6$ and $y_I/\eta = -10$. These centroid locations were selected based on their significance in terms of the non-linear production of enstrophy P_{ω^2} for E2 and E6 conditions. A Kolmogorov-like balance has been observed ($\langle T_r \rangle_I \approx \langle \varepsilon \rangle_I$) at $y_I/\eta = -10$ for scales $r_n > 10\eta$.

Further examination of the solenoidal and irrotational parts, $\langle T_r^S \rangle_I$ and $\langle T_r^I \rangle_I$ at $y_I/\eta = -10$ revealed that, for scales fully contained within the turbulent side of the IES, $\langle T_r^S \rangle_I$ predominantly contributes to the total interscale transfer rate (see figure 5.17f). In contrast, for scales extending beyond the IES location, $\langle T_r \rangle_I$ is entirely attributed to the irrotational part, $\langle T_r^I \rangle_I$, which is directly linked to pressure effects as described by eq. 5.6. On the other hand, the contour fields of $\langle T_r^S \rangle_I$ and $\langle T_r^I \rangle_I$ in figure 5.19c show that in the tangential direction, the picture is much more different and there is a significant contribution from the $\langle T_r^S \rangle_I$ enhancing the energy transfer towards smaller scales i.e. forward cascade. The $\langle T_r^I \rangle_I$ contributes in the direction of an inverse cascade.

Finally, we focused on the interscale/interspace energy transfer terms. We analyzed the compression/stretching motions on average with the use of TNTI-averaged statistics $\langle \delta \boldsymbol{u} \cdot \boldsymbol{r} \rangle_I$ at the location of the interface, due to the direct relationship between the average compression/stretching and the direction of the local energy cascade across the scales for each direction. The unconditioned results obtained in the present study are observed to be qualitatively similar to the results obtained for the TNTI of spatially developing turbulent wake in the study of Zhou and Vassilicos (2020), where compression in the interface normal

direction and stretching in the tangential direction is reported. The TNTI-average statistics of the interscale energy flux $\langle \delta \boldsymbol{u} \cdot \boldsymbol{r} | \delta \boldsymbol{u} |^2 \rangle_I$ are observed to align with the findings by Zhou and Vassilicos (2020). These observations are also in parallel with the conclusions given by Watanabe et al. (2020), where they investigate the scale-by-scale energy transfer by applying a filtering operation and the analysis of the sub-grid scale energy budget equations near the TNTI of a turbulent front in shear-free turbulence.

Conditioning the TNTI-averaged statistics on the local propagation velocity v_n^I allows us to analyze the compression/stretching events separately for the entrainment and detrainment regions. The average compression and stretching motions in the interface normal and tangential directions are observed to change when the detrainment regions are considered. At the regions of local entrainment, compression motion is present in the interface normal direction on average, while stretching is observed in the tangential direction. Conversely, at the regions of detrainment, stretching is observed on average in the interface normal direction, and compression is observed in the tangential direction.

Similarly, the interscale energy flux is also shown to vary between the regions of local entrainment and detrainment across the interface. The average forward cascade in the normal direction and inverse cascade in the tangential direction observed for the unconditioned statistics are also present for the entrainment regions. On the other hand, in the detrainment regions, a forward cascade is present in the tangential direction, while an inverse cascade is observed for the scales associated with $r_n/\delta > 0.38$ in the interface normal direction. This difference between the entrainment/detrainment regions highlights the local nature of the interscale energy transfer in both scale space and the physical space.

Chapter 6

Conclusion

6.1 Conclusions

The TNTI is a highly localized phenomenon within the flow. Being a sharp boundary that separates the turbulent and non-turbulent regions, it is a subject of significant interest due to its complex structure, dynamics, and the intricate local processes responsible for entraining non-turbulent fluid into the turbulent region. In this study, we undertake a comprehensive examination of the TNTI of a temporally developing turbulent planar jet, employing both global and local approaches for the analysis.

We conducted highly resolved simulations of the temporally developing turbulent planar jet, aligning with the objectives outlined in section 1.2. The details of the simulations and discussions on the resolution have been given in chapter 2. Chapter 3 is based on a global approach, for the investigation of the propagation velocity and the inner structure of the TNTI. On the other hand chapters 4 and 5 focus more on localized analyses, utilizing a methodology based on TNTI-averaging. Additionally, chapter 5 employs the KHMH equation to explore various mechanisms acting on the kinetic energy balance at the TNTI location, considering the energy transfer in both physical and scale space.

The observations and conclusions at each stage of the analysis have been given at the end of each chapter. These concluding sections include various points, some being entirely novel, others being partially or thoroughly observed by previous studies in the literature. Some of the prominent novel conclusions of the entire thesis may be summarized as:

- The TNTI is a continuous layer containing various iso-enstrophy surfaces (IES) associated with a wide range of enstrophy values. In chapter 3 the variation of the geometrical properties of these IES has been demonstrated in terms of the fractal dimension D_f of the IESs which we have found to vary across the thickness of the TNTI layer. Going

towards the non-turbulent region, the TNTI becomes less and less contorted and D_f reduces to 2. A relationship has also been obtained for the average propagation velocity of the TNTI v_n in eq. 3.26, which accounts for the variation of v_n across the thickness of the TNTI. Eq. 3.26 exhibits a dependence of v_n on $\omega_{th}^2/\omega_{ref}^2$ through the dependence on $\omega_{th}^2/\omega_{ref}^2$ of the fractal dimension D_f of the associated IES.

- In the reference frame of the TNTI, a non-zero TNTI-average velocity exists in the normal direction $\langle v_l \rangle_I$. This observation is to be contrasted with the global cross-stream velocity, averaged across the homogeneous $(x-z)$ plane, V, which is zero at each y location along the cross-stream direction. The profile of $\langle v_l \rangle_I$ along the TNTI normal axis is found to be dominated by the correlation between the fluctuations of velocity $\boldsymbol{u}$ and the face-normal vector $\boldsymbol{e}_y$ with respect to their TNTI-averaged values i.e., $\langle \boldsymbol{u}'' \cdot \boldsymbol{e}_y'' \rangle_I$ (see figure 4.7b).

- A balance between interscale transfer and dissipation ($\langle T_r \rangle_I = \langle \varepsilon \rangle_I$) is observed for scales $r_n > 10\eta$ in the interface normal direction, for the centroid placed at $y_I/\eta = -10$ (see figure 5.16f). This balance holds for scales exceeding the TNTI extent in size (corresponds to $r_n > 20\eta$ in figure 5.16f). The decomposition of the interscale transfer term into irrotational/solenoidal parts shows that, for $r_n > 20\eta$, the solenoidal part $\langle T_r^S \rangle_I$ is zero, implying that $\langle T_r \rangle_I$ consists solely of the irrotational part i.e., $\langle T_r \rangle_I = \langle T_r^I \rangle_I$. It is shown by Larssen and Vassilicos (2023) that $\langle T_r^I \rangle_I$ is directly related to the pressure-velocity term by eq. 5.6. This highlights the importance of the pressure in the vicinity of the TNTI for the transfer of the kinetic energy in scale space. Conversely, at the IES location ($y_I/\eta = 0$), both the solenoidal and irrotational contributions $\langle T_r^S \rangle_I$ and $\langle T_r^I \rangle_I$ are comparable in magnitude for the entire range of scales analyzed (see figure 5.5).

- Conditioning the TNTI-average statistics on the local mean curvature H_m and the local propagation velocity v_n^l shows that the directions of the average compression/stretching differ in local entrainment and detrainment regions (see figure 5.21). In the regions of local entrainment, average compression is observed in the interface normal direction. Conversely, average stretching is present in the tangential direction of the interface. At the regions of local detrainment, this picture is inverted and the stretching motion is, on average, present in the normal direction while compression is, on average, present in the tangential direction.

  The direction of the interscale energy cascade also changes with entrainment/detrainment characteristics of the local regions of the interface. In figure 5.21, it has been shown

that forward/backward cascade is present for the normal/tangential directions respectively, at the regions of local entrainment. On the contrary, considering the regions of local detrainment, the cascade is backward/forward in the normal/tangential directions respectively.

In addition to the points given above, the current analysis has led to a number of more specific but significant results for certain aspects of the TNTI and/or the entrainment process. Moreover, the high-resolution dataset and the local methodology based on the TNTI-averaging operation have allowed us to confirm and support several observations made in the literature, some having been made for flows that differ from the present study because of their spatially developing nature or because of the absence of mean shear acting on the TNTI. These further conclusions can be summarized as follows:

- In the case of a temporally developing planar jet, it has been observed that the scalings of velocity and length scales in time remain unaffected for various turbulent dissipation scaling regimes, in contrast to the spatially developing planar jets (Cafiero and Vassilicos, 2019) and axisymmetric wakes (Obligado et al., 2016). The length scales δ, λ and η all exhibit the time dependency of $t^{1/2}$, while the velocities u_0, u_λ, u_η and v_n all vary with $t^{-1/2}$ and Re_λ remains constant in time, independent of the dissipation scaling regime being equilibrium or non-equilibrium.

- The importance of the high enough grid resolution is demonstrated for capturing accurately the PDF of the quantities containing high-order derivatives of the velocity/vorticity fields i.e., H_m and v_n^l, especially at the external regions of the TNTI. A difference of 50% is observed between the values of $\langle v_n^l \rangle_I$ obtained for the IES of $\omega_{th}^2/\omega_{ref}^2 = 10^{-3}$ with grid resolutions $dy/\eta = 1.4$ and $dy/\eta = 0.46$. This disparity is more significant for the IESs associated with lower ω_{th}^2 values.

- An average rotating motion, aligned in the local spanwise direction and rotating counter-clockwise, is observed in the turbulent side of the TNTI-averaged local fields. This average motion is found to be associated with the turbulent fluctuation field $\boldsymbol{u}'$ with respect to the $(x-z)$ averaging (see figure 4.16) and has been detected (figure 4.39a) in the reference frame of the TNTI, suggesting that it is linked with the shape of the interface. This rotating motion may be related to the vortical structures residing in the vicinity of the interface mentioned by da Silva and Taveira (2010), da Silva and dos Reis (2011), da Silva et al. (2011) and Watanabe et al. (2017).

- Analyzing the PDFs of scalar products of the face-normal vector $\boldsymbol{e}_y$ and the global streamwise, cross-stream, and spanwise unit vectors $\boldsymbol{i}$, $\boldsymbol{j}$, and $\boldsymbol{k}$ reveals that the local

entrainment regions predominantly face downstream. This observation suggests that these regions are positioned on the streamwise side of the concave surfaces formed around the vortical structures depicted in figure 4.39b. Conversely, the detrainment regions are located in the upstream-facing regions of the interface, likely on the upstream side of the concave surfaces. These observations align with the results presented by Watanabe et al. (2014a) considering the orientation of the local regions along the TNTI with different orientations.

- In the regions of fast local entrainment (E6 condition), a significant peak in $\langle P_{\omega^2} \rangle_I$ is observed near the IES location, at $y_I/\eta \approx -6$. Interestingly, in these same regions, the total TNTI thickness δ_I and TSL thickness δ_{ω^2} are halved compared to the unconditioned case, while the VSL thickness δ_ν does not decrease as significantly as the former two.

- In regions of local entrainment, the TNTI-average velocity field points towards the interface from the turbulent side i.e., $\langle v_l \rangle_I > 0$ (see figures 4.32c, 4.32d, and 4.32e). Conversely, in the local detrainment regions, the TNTI-average velocity field is directed towards the turbulent core i.e., $\langle v_l \rangle_I < 0$ (see figure 4.32b). Examination of the TNTI-averaged profiles of the terms of the enstrophy balance for different ED conditions highlights the crucial role of the $\langle v_l \rangle_I$ on the local enstrophy balance at the regions of entrainment and detrainment (see figure 4.34).

  The transport of vorticity/enstrophy by $\langle v_l \rangle_I$ towards the interface enhances the production of enstrophy P_{ω^2} close to the IES (figure 4.34d), resulting in much sharper enstrophy gradient and enhancing local propagation velocity towards the non-turbulent region v_n^l. Conversely, the transport of vorticity/enstrophy further away from the interface leads to less sharp regions of the interface, where the mechanisms of production and diffusion cannot overcome the viscous dissipation of enstrophy resulting in the IES retreating towards the turbulent core relative to the flow. These conclusions align with the findings presented in the literature for the TNTI of the spatially developing turbulent planar jet (Watanabe et al., 2014a) and temporally developing turbulent jet (Watanabe et al., 2017).

- The PDF of relative helicity $\hat{h}$ reveals that the orientation of $\boldsymbol{u}$ and $\boldsymbol{\omega}$ vectors tends to become more orthogonal as we move towards the non-turbulent region across the TNTI. This results in a slower decrease rate of the non-linear enstrophy production term $\langle P_{\omega^2} \rangle_I$ in the interface normal direction, compared to the case where the PDF of the relative orientation of $\boldsymbol{u}$ and $\boldsymbol{\omega}$ remains similar to the turbulent core. It is worth noting that $\langle P_{\omega^2} \rangle_I$ contributes at some locations to the propagation of the TNTI into

the non-turbulent region, by maintaining $\langle D\omega^2/Dt\rangle_I > 0$, even though the viscous dissipation is higher than the diffusion of the enstrophy i.e., $(\langle D_{\omega^2}\rangle_I - \langle \varepsilon_{\omega^2}\rangle_I) < 0$.

- The analysis of the local KHMH balance near the TNTI reveals significant contributions from all the different terms specified in eq. 5.3. This highlights the importance of considering all these mechanisms together to gain a complete understanding of the KHMH balance at the TNTI location. The KHMH balance is observed to be qualitatively similar at various IES locations associated with different threshold values $\omega^2_{th}/\omega^2_{ref}$ (see figures 5.3 and 5.4).

- In the interface normal direction, the kinetic energy associated with scales $r_n < 11.4\eta$ is observed to increase in a reference frame moving with the flow ($(\langle D_t\rangle_I + \langle T_y\rangle_I) > 0$) for the IES of $\omega^2_{th}/\omega^2_{ref} = 10^{-3}$ in figure 5.3b (the same observation holds for scales $r_n < 17.6\eta$ for the IES of $\omega^2_{th}/\omega^2_{ref} = 10^{-6}$, as seen in figure 5.4b). This is an interesting observation as $(D_t + T_y) < 0$ is observed for all ranges of scales (including the small scales) when the KHMH centroid point is moved towards the turbulent side of the IES. A possible relation might be suggested with the reporting of Cimarelli et al. (2021) that the kinetic energy is transferred from the internal region of the turbulent jet towards the interfacial region, meanwhile, the cascade in the scale space exhibits mainly a forward transfer towards the smaller cross-stream scales.

- The profile of $\langle v_l\rangle_I$ reveals a compressive motion in the normal direction, as illustrated in figure 4.4a. Additionally, a stretching motion on average in the tangential plane of the interface has been observed from the 3D TNTI-averaged velocity fields given in figure 4.14a. The variation of this compression/stretching behaviour, on average, in the normal/tangential directions at the interface location is further shown by the TNTI-averaged statistics of $\langle \delta\boldsymbol{u}\cdot\boldsymbol{r}\rangle_I$, as presented in figure 5.20a. This finding is similar to the observations made for the TNTI of shear-free turbulence (Watanabe et al., 2020) and spatially developing wakes (Zhou and Vassilicos, 2020).

- A forward cascade in the interface normal direction and an inverse cascade in the tangential direction is observed in figure 5.20b. This observation is largely in line with the overall trend of compression and stretching that has been discussed for the TNTI-average velocity fields locally at the TNTI location in chapter 4. The qualitative similarity has been noted between the results of the current study and the results presented for spatially developing wake by Zhou and Vassilicos (2020), suggesting that the observations made in the present study may be more general than just for the TNTI of temporally developing jets.

6.2 Perspectives

The current study has aimed to enhance our understanding of the TNTI layer's structure, the mechanisms influencing the kinetic energy balance in both physical and scale spaces near the TNTI, and the entrainment and detrainment processes. Even though various analyses have been conducted using global and local approaches, as well as different equations employed such as the one-point enstrophy balance equation and the KHMH equation, there are still numerous avenues for further research on the TNTI. Some perspectives concerning the directions for future studies include:

- The investigation of the KHMH balance in section 5.4 yields intriguing results. Notably, it reveals a balance between the interscale transfer $\langle T_r \rangle_I$ and the dissipation $\langle \varepsilon \rangle_I$ at $y_I/\eta = -10$, which resembles Kolmogorov equilibrium but is nevertheless very different for at least two reasons: it occurs in a very inhomogeneous region of the flow and it appears as account of pressure variations.

  Decomposing $\langle T_r \rangle_I$ into its solenoidal and irrotational parts reveals that both contributions are required for the balance between $\langle T_r \rangle_I$ and $\langle \varepsilon \rangle_I$, for scales inside the turbulent region. On the contrary, this balance exists solely due to $\langle T_r^I \rangle_I$ at scales extending to the non-turbulent region. Further investigation of these very large scales may thus be interesting in order to understand their role in the kinetic energy transfer across the TNTI and in the development of the jet.

- The 2D spectra presented in figure 2.3 and the visual inspection of enstrophy cut sections in figures 2.2c and 2.6 indicate that the scale separation between turbulent length scales is not very wide, primarily due to the limited Reynolds number (Re_G) of the PJx-HR simulations. To gain deeper insights into the distinct roles of each scale, it would be beneficial to utilize datasets with higher Re_G values. This would offer more room for comparisons with studies such as da Silva and dos Reis (2011); da Silva et al. (2011); da Silva and Taveira (2010), which discuss the roles of various scales in the TNTI phenomenon. However, as demonstrated in chapter 2, this would require much higher computational resources to keep an acceptable spatial resolution as required by the KHMH analysis and statistics conditioned on local mean curvature and local propagation velocity of the IES.

- The methodology employed in this study can be combined with coherent structure detection methods to further investigate the localized influence of specific structures on the TNTI and the local KHMH balance.

- Applying the local TNTI analysis to spatially developing jets and wakes could yield valuable insights into the connection between different dissipation scaling regimes and local scale-by-scale energy balance near the TNTI.
- Examining the spatially developing jet could also be intriguing because of the increase in mass flux while momentum is conserved along the streamwise direction. This is a fundamental difference from its temporally developing counterpart, where the mass flux is conserved over time. This unique characteristic of the temporally developing jet does impose limitations when addressing certain questions related to the entrainment of mass.
- In the present study, we have investigated the TNTI-average values of the terms related to the various mechanisms playing a role in the KHMH balance (eq. 5.3). As has been shown by Larssen and Vassilicos (2023); Yasuda and Vassilicos (2018); Yuvaraj (2021), the fluctuations of these terms can be high compared to their mean values. Thus the fluctuations can also be included in further analysis of the KHMH balance in the vicinity of the TNTI.

References

Alves Portela, F., Papadakis, G., and Vassilicos, J. C. (2018). Turbulence dissipation and the role of coherent structures in the near wake of a square prism. *Physical Review Fluids*, 3:124609.

Apostolidis, A., Laval, J. P., and Vassilicos, J. C. (2023). Turbulent cascade in fully developed turbulent channel flow. *Journal of Fluid Mechanics*, 967:A22.

Attili, A., Cristancho, J., C., and Bisetti, F. (2014). Statistics of the turbulent/non-turbulent interface in a spatially developing mixing layer. *Journal of Turbulence*, 15:555–568.

Balamurugan, G., Rodda, A., Philip, J., and Mandal, A. C. (2020). Characteristics of the turbulent non-turbulent interface in a spatially evolving turbulent mixing layer. *Journal of Fluid Mechanics*, 894:A4.

Bisset, D. K., Hunt, J. C. R., and Rogers, M. M. (2002). The turbulent/non-turbulent interface bounding a far wake. *Journal of Fluid Mechanics*, 451:383–410.

Borrell, G. and Jimenez, J. (2016). Properties of the turbulent/non-turbulent interface in boundary layers. *Journal of Fluid Mechanics*, 801:554–596.

Brown, G. L. and Roshko, A. (1974). On density effects and large structure in turbulent mixing layers. *Journal of Fluid Mechanics*, 64:775–816.

Cafiero, G. and Vassilicos, J. C. (2019). Non-equilibrium turbulence scalings and self-similarity in turbulent planar jets. *Proceedings of the Royal Society A*, 475(2225):20190038.

Cafiero, G. and Vassilicos, J. C. (2020). Non-equilibrium scaling of the turbulent-nonturbulent interface speed in planar jets. *Physical Review Letters*, 125(17):174501.

Catrakis, H. J. and Dimotakis, P. E. (1999). *Scale-Dependent Fractal Geometry*, pages 145–162. Springer.

Chauhan, K., Philip, J., De Silva, C. M., Hutchins, N., and Marusic, I. (2014). The turbulent/non-turbulent interface and entrainment in a boundary layer. *Journal of Fluid Mechanics*, 742:119–151.

Cimarelli, A., Cocconi, G., Frohnapfel, B., and Angelis, E. D. (2015). Spectral enstrophy budget in a shear-less flow with turbulent/non-turbulent interface. *Physics of Fluids*, 27:125106.

Cimarelli, A., Fregni, A., Mollicone, J.-P., van Reeuwijk, M., and Angelis, E. D. (2022). Structure of turbulence in temporal planar jets. *Physics of Fluids*, 34:045109.

Cimarelli, A., Mollicone, J. P., Reeuwijk, M. V., and Angelis, E. D. (2021). Spatially evolving cascades in temporal planar jets. *Journal of Fluid Mechanics*, 910:A19.

Corrsin, S. and Kistler, A. L. (1955). Free-stream boundaries of turbulent flows. Technical Report January, NACA.

Crow, S. C. and Champagne, F. H. (1971). Orderly structure in jet turbulence. *Journal of Fluid Mechanics*, 48:547–591.

da Silva, C. B. (2009). The behavior of subgrid-scale models near the turbulent/nonturbulent interface in jets. *Physics of Fluids*, 21:4–7.

da Silva, C. B. and dos Reis, R. J. N. (2011). The role of coherent vortices near the turbulent/non-turbulent interface in a planar jet. *Philosophical Transactions of the Royal Society A: Mathematical, Physical and Engineering Sciences*, 369:738–753.

da Silva, C. B., dos Reis, R. J. N., and Pereira, J. C. F. (2011). The intense vorticity structures near the turbulent/non-turbulent interface in a jet. *Journal of Fluid Mechanics*, 685:165–190.

da Silva, C. B., Hunt, J. C., Eames, I., and Westerweel, J. (2014). Interfacial layers between regions of different turbulence intensity. *Annual Review of Fluid Mechanics*, 46(1):567–590.

da Silva, C. B. and Pereira, J. C. F. (2004). The effect of subgrid-scale models on the vortices computed from large-eddy simulations. *Physics of Fluids*, 16:4506–4534.

da Silva, C. B. and Pereira, J. C. F. (2008). Invariants of the velocity-gradient, rate-of-strain, and rate-of-rotation tensors across the turbulent/nonturbulent interface in jets. *Physics of Fluids*, 20:1–18.

da Silva, C. B. and Taveira, R. R. (2010). The thickness of the turbulent/nonturbulent interface is equal to the radius of the large vorticity structures near the edge of the shear layer. *Physics of Fluids*, 22:1–4.

Dahm, W. J. and Dimotakis, P. E. (1987). Measurements of entrainment and mixing in turbulent jets. *AIAA Journal*, 25(9):1216–1223.

Dairay, T., Obligado, M., and Vassilicos, J. C. (2015). Non-equilibrium scaling laws in axisymmetric turbulent wakes. *Journal of Fluid Mechanics*, 781:166–195.

de Silva, C. M., Philip, J., Chauhan, K., Meneveau, C., and Marusic, I. (2013). Multiscale geometry and scaling of the turbulent-nonturbulent interface in high Reynolds number boundary layers. *Physical Review Letters*, 111:044501.

Dimotakis, P. E. and Catrakis, H. J. (1999). Turbulence, Fractals, and Mixing. In Chaté H., Villermaux E., C. J., editor, *Mixing: chaos and turbulence*, pages 59–143. Springer, Boston, MA.

Er, S., Laval, J.-P., and Vassilicos, J. (2023). Length scales and the turbulent/non-turbulent interface of a temporally developing turbulent jet. *Journal of Fluid Mechanics*, 970:A33.

Fiedler, H. (1988). Coherent structures in turbulent flows. *Progress in Aerospace Sciences*, 25:231–269.

Flohr, P. and Olivari, D. (1994). Fractal and multifractal characteristics of a scalar dispersed in a turbulent jet. *Physica D: Nonlinear Phenomena*, 76(1-3):278–290.

Gampert, M., Boschung, J., Hennig, F., Gauding, M., and Peters, N. (2014). The vorticity versus the scalar criterion for the detection of the turbulent/non-turbulent interface. *Journal of Fluid Mechanics*, 750:578–596.

Gauding, M., Bode, M., Brahami, Y., Varea, and Danaila, L. (2021). Self-similarity of turbulent jet flows with internal and external intermittency. *Journal of Fluid Mechanics*, 919:A41.

George, W. K. (1989). The Self-Preservation of turbulent flows and its relation to the initial conditions and coherent structures. In Arndt, W. K. G. and R., editors, *Advances in Turbulence*, pages 39–73, New York. Hemisphere.

Goto, S. and Vassilicos, J. C. (2016). Unsteady turbulence cascades. *Physical Review E*, 94:053108.

Gutmark, E. and Wygnanski, I. (1976). The planar turbulent jet. *Journal of Fluid Mechanics*, 73:465–495.

Hayashi, M., Watanabe, T., and Nagata, K. (2021). Characteristics of small-scale shear layers in a temporally evolving turbulent planar jet. *Journal of Fluid Mechanics*, 920:A38.

Hentschel, H. G. and Procaccia, I. (1984). Relative diffusion in turbulent media: The fractal dimension of clouds. *Physical Review A*, 29:1461–1470.

Hill, R. J. (2001). Equations relating structure functions of all orders. *Journal of Fluid Mechanics*, 434:379–388.

Hill, R. J. (2002). Exact second-order structure-function relationships. *Journal of Fluid Mechanics*, 468:317–326.

Holzner, M., Liberzon, A., Nikitin, N., Kinzelbach, W., and Tsinober, A. (2007). Small-scale aspects of flows in proximity of the turbulent/nonturbulent interface. *Physics of Fluids*, 19(7).

Holzner, M., Liberzon, A., Nikitin, N., Lüthi, B., Kinzelbach, W., and Tsinober, A. (2008). A Lagrangian investigation of the small-scale features of turbulent entrainment through particle tracking and direct numerical simulation. *Journal of Fluid Mechanics*, 598:465–475.

Holzner, M. and Lüthi, B. (2011). Laminar superlayer at the turbulence boundary. *Physical Review Letters*, 106:134503.

Howard, L. (1803). *On the Modification of Clouds: Essay to the Askesian Society*. J. Taylor.

Hunt, J. C. R., Eames, I., and Westerweel, J. (2008). Vortical interactions with interfacial shear layers. In Kaneda, Y., editor, *IUTAM Symposium on Computational Physics and New Perspectives in Turbulence*, pages 331–338, Dordrecht. Springer Netherlands.

Hunt, J. C. R., Rottman, J. W., and Britter, R. E. (1984). Some physical processes involved in the dispersion of dense gases. In Ooms, G. and Tennekes, H., editors, *Atmospheric Dispersion of Heavy Gases and Small Particles*, pages 361–395, Berlin, Heidelberg. Springer Berlin Heidelberg.

Jahanbakhshi, R. and Madnia, C. K. (2016). Entrainment in a compressible turbulent shear layer. *Journal of Fluid Mechanics*, 797:564–603.

Jahanbakhshi, R. and Madnia, C. K. (2018). The effect of heat release on the entrainment in a turbulent mixing layer. *Journal of Fluid Mechanics*, 844:92–126.

Jimenez, J., Wray, A. A., Saffman, P. G., and Rogallo, R. S. (1993). The structure of intense vorticity in isotropic turbulence. *Journal of Fluid Mechanics*, 255:65–90.

Jiménez, J. and Wray, A. A. (1998). On the characteristics of vortex filaments in isotropic turbulence. *Journal of Fluid Mechanics*, 373:255–285.

Kankanwadi, K. S. and Buxton, O. R. H. (2020). Turbulent entrainment into a cylinder wake from a turbulent background. *Journal of Fluid Mechanics*, 905:A35.

Kline, S. J., Reynolds, W. C., Schraub, F. A., and Runstadler, P. W. (1967). The structure of turbulent boundary layers. *Journal of Fluid Mechanics*, 30:741–773.

Krug, D., Chung, D., Philip, J., and Marusic, I. (2017). Global and local aspects of entrainment in temporal plumes. *Journal of Fluid Mechanics*, 812:222–250.

Lane-Serff, G. F. (1993). Investigation of the fractal structure of jets and plumes. *Journal of Fluid Mechanics*, 249:521–534.

Larssen, H. and Vassilicos, J. (2023). Spatio-temporal fluctuations of interscale and interspace energy transfer dynamics in homogeneous turbulence. *Journal of Fluid Mechanics*, 969:A14.

Liepmann, D. and Gharib, M. (1992). The role of streamwise vorticity in the near-field entrainment of round jets. *Journal of Fluid Mechanics*, 245:643–668.

Lovejoy, S. (1982). Area-perimeter relation for rain and cloud areas. *Science*, 216:185–187.

Mandelbrot, B. B. (1982). *The fractal geometry of the nature*. W. H. Freeman & Co., New York.

Mathew, J. and Basu, A., J. (2002). Some characteristics of entrainment at a cylindrical turbulence boundary. *Physics of Fluids*, 14(7):2065–2072.

Meldi, M. and Vassilicos, J. C. (2021). Analysis of Lundgren's matched asymptotic expansion approach to the Kármán-Howarth equation using the eddy damped quasinormal Markovian turbulence closure. *Physical Review Fluids*, 6:064602.

Miller, P. L. and Dimotakis, P. E. (1991). Stochastic geometric properties of scalar interfaces in turbulent jets. *Physics of Fluids A*, 3(1):168–177.

Mistry, D., Dawson, J. R., and Kerstein, A. R. (2018). The multi-scale geometry of the near field in an axisymmetric jet. *Journal of Fluid Mechanics*, 838:501–515.

Mistry, D., Philip, J., and Dawson, J. R. (2019). Kinematics of local entrainment and detrainment in a turbulent jet. *Journal of Fluid Mechanics*, 871:896–924.

Mistry, D., Philip, J., Dawson, J. R., and Marusic, I. (2016). Entrainment at multi-scales across the turbulent/non-turbulent interface in an axisymmetric jet. *Journal of Fluid Mechanics*, 802:690–725.

Nagata, R., Watanabe, T., and Nagata, K. (2018). Turbulent/non-turbulent interfaces in temporally evolving compressible planar jets. *Physics of Fluids*, 30(10):105109.

Neamtu-Halic, M. M., Krug, D., Haller, G., and Holzner, M. (2019). Lagrangian coherent structures and entrainment near the turbulent/non-turbulent interface of a gravity current. *Journal of Fluid Mechanics*, 877:824–843.

Neamtu-Halic, M. M., Krug, D., Mollicone, J.-P., van Reeuwijk, M., Haller, G., and Holzner, M. (2020). Connecting the time evolution of the turbulence interface to coherent structures. *Journal of Fluid Mechanics*, 898:A3.

Neamtu-Halic, M. M., Mollicone, J. P., van Reeuwijk, M., and Holzner, M. (2021). Role of vortical structures for enstrophy and scalar transport in flows with and without stable stratification. *Journal of Turbulence*, 22:393–412.

Nedić, J. (2013). *Fractal-generated wakes*. PhD thesis, Imperial College London.

Nedić, J., Vassilicos, J. C., and Ganapathisubramani, B. (2013). Axisymmetric turbulent wakes with new nonequilibrium similarity scalings. *Physical Review Letters*, 111:144503.

Obligado, M., Dairay, T., and Vassilicos, J. C. (2016). Nonequilibrium scalings of turbulent wakes. *Physical Review Fluids*, 1:044409.

Obligado, M. and Vassilicos, J. C. (2019). The non-equilibrium part of the inertial range in decaying homogeneous turbulence. *Europhysics Letters*, 127(6):64004.

Ortiz-Tarin, J., Nidhan, S., and Sarkar, S. (2021). High-Reynolds-number wake of a slender body. *Journal of Fluid Mechanics*, 918:A30.

Philip, J. and Marusic, I. (2012). Large-scale eddies and their role in entrainment in turbulent jets and wakes. *Physics of Fluids*, 24(5):055108.

Philip, J., Meneveau, C., de Silva, C. M., and Marusic, I. (2014). Multiscale analysis of fluxes at the turbulent/non-turbulent interface in high Reynolds number boundary layers. *Physics of Fluids*, 26:015105.

Phillips, O. M. (1955). The irrotational motion outside a free turbulent boundary. *Mathematical Proceedings of the Cambridge Philosophical Society*, 51(1):220–229.

Phillips, O. M. (1972). The entrainment interface. *Journal of Fluid Mechanics*, 51:97–118.

Prasad, R. R. and Sreenivasan, K. R. (1990). The measurement and interpretation of fractal dimensions of the scalar interface in turbulent flows. *Physics of Fluids A: Fluid Dynamics*, 2(5):792–807.

Ramaprian, B. R. and Chandrasekhara, M. S. (1985). LDA measurements in plane turbulent jets. *Journal of Fluids Engineering*, 107:264–271.

Reynolds, W. C. (1972). Large-scale instabilities of turbulent wakes. *Journal of Fluid Mechanics*, 54(3):481–488.

Sandham, N. D., Mungal, M. G., Broadwell, J. E., and Reynolds, W. C. (1988). Scalar entrainment in the mixing layer. In *Proceedings of the CTR Summer Program*, pages 69–76.

Silva, T. S., Zecchetto, M., and da Silva, C. B. (2018). The scaling of the turbulent/non-turbulent interface at high Reynolds numbers. *Journal of Fluid Mechanics*, 843:156–179.

Sreenivasan, K. R. (1991). Fractals and multifractals in fluid turbulence. *Annual Review of Fluid Mechanics*, 23(1):539–604.

Sreenivasan, K. R. and Meneveau, C. (1986). The fractal facets of turbulence. *Journal of Fluid Mechanics*, 173:357–386.

Sreenivasan, K. R., Ramshankar, R., and Meneveau, C. (1989). Mixing, Entrainment and Fractal Dimensions of Surfaces in Turbulent Flows. *Proceedings of the Royal Society A: Mathematical, Physical and Engineering Sciences*, 421(1860):79–108.

Taveira, R. R. and da Silva, C. B. (2013). Kinetic energy budgets near the turbulent/nonturbulent interface in jets. *Physics of Fluids*, 25:015114.

Taveira, R. R. and da Silva, C. B. (2014a). Characteristics of the viscous superlayer in shear free turbulence and in planar turbulent jets. *Physics of Fluids*, 26(8):021702.

Taveira, R. R. and da Silva, C. B. (2014b). Erratum: "characteristics of the viscous superlayer in shear free turbulence and in planar turbulent jets" [phys. fluids 26, 021702 (2014)]. *Physics of Fluids*, 26.

Taveira, R. R., Diogo, J. S., Lopes, D. C., and da Silva, C. B. (2013). Lagrangian statistics across the turbulent-nonturbulent interface in a turbulent plane jet. *Physical Review E*, 88:043001.

Tennekes, H. and Lumley, J. L. (1972). *A first course in turbulence*. MIT Press.

Townsend, A. A. (1949). The Fully Developed Turbulent Wake of a Circular. *Australian Journal of Scientific Research*, 2(4):451–468.

Townsend, A. A. (1976). *The structure of turbulent shear flow*. Cambridge University Press, 2nd edition.

Tritton, D. J. (1988). *Physical Fluid Dynamics*. Oxford University Press.

Turner, J., S. (1986). Turbulent entrainment: the development of the entrainment assumption, and its application to geophysical flows. *Journal of Fluid Mechanics*, 173:431–471.

Valente, P. C. and Vassilicos, J. C. (2015). The energy cascade in grid-generated non-equilibrium decaying turbulence. *Physics of Fluids*, 27:045103.

van Reeuwijk, M. and Holzner, M. (2014). The turbulence boundary of a temporal jet. *Journal of Fluid Mechanics*, 739:254–275.

Vassilicos, J. C. (2015). Dissipation in turbulent flows. *Annual Review of Fluid Mechanics*, 47(1):95–114.

Vela-Martín, A. (2022). Subgrid-scale models of isotropic turbulence need not produce energy backscatter. *Journal of Fluid Mechanics*, 937:A14.

Virtanen, P., Gommers, R., Oliphant, T. E., Haberland, M., Reddy, T., Cournapeau, D., Burovski, E., Peterson, P., Weckesser, W., Bright, J., van der Walt, S. J., Brett, M., Wilson, J., Millman, K. J., Mayorov, N., Nelson, A. R. J., Jones, E., Kern, R., Larson, E., Carey, C. J., Polat, İ., Feng, Y., Moore, E. W., VanderPlas, J., Laxalde, D., Perktold, J., Cimrman, R., Henriksen, I., Quintero, E. A., Harris, C. R., Archibald, A. M., Ribeiro, A. H., Pedregosa, F., van Mulbregt, P., and SciPy 1.0 Contributors (2020). SciPy 1.0: Fundamental Algorithms for Scientific Computing in Python. *Nature Methods*, 17:261–272.

Watanabe, T., da Silva, C. B., and Nagata, K. (2019). Non-dimensional energy dissipation rate near the turbulent/non-turbulent interfacial layer in free shear flows and shear free turbulence. *Journal of Fluid Mechanics*, 875:321–344.

Watanabe, T., da Silva, C. B., and Nagata, K. (2020). Scale-by-scale kinetic energy budget near the turbulent/nonturbulent interface. *Physical Review Fluids*, 5:124610.

Watanabe, T., da Silva, C. B., Nagata, K., and Sakai, Y. (2017). Geometrical aspects of turbulent/non-turbulent interfaces with and without mean shear. *Physics of Fluids*, 29:085105.

Watanabe, T., da Silva, C. B., Sakai, Y., Nagata, K., and Hayase, T. (2016a). Lagrangian properties of the entrainment across turbulent/non-turbulent interface layers. *Physics of Fluids*, 28:031701.

Watanabe, T., Riley, J. J., de Bruyn Kops, S. M., Diamessis, P. J., and Zhou, Q. (2016b). Turbulent/non-turbulent interfaces in wakes in stably stratified fluids. *Journal of Fluid Mechanics*, 797:R1.

Watanabe, T., Sakai, Y., Nagata, K., Ito, Y., and Hayase, T. (2014a). Enstrophy and passive scalar transport near the turbulent/non-turbulent interface in a turbulent planar jet flow. *Physics of Fluids*, 26:105103.

Watanabe, T., Sakai, Y., Nagata, K., Ito, Y., and Hayase, T. (2014b). Vortex stretching and compression near the turbulent/non-turbulent interface in a planar jet. *Journal of Fluid Mechanics*, 758:754–785.

Watanabe, T., Sakai, Y., Nagata, K., Ito, Y., and Hayase, T. (2015). Turbulent mixing of passive scalar near turbulent and non-turbulent interface in mixing layers. *Physics of Fluids*, 27(8):085109.

Westerweel, J., Fukushima, C., Pedersen, J. M., and Hunt, J. C. (2009). Momentum and scalar transport at the turbulent/non-turbulent interface of a jet. *Journal of Fluid Mechanics*, 631:199–230.

Westerweel, J., Fukushima, C., Pedersen, J. M., and Hunt, J. C. R. (2005). Mechanics of the turbulent-nonturbulent interface of a jet. *Physical Review Letters*, 95:174501.

Wolf, M., Holzner, M., Luthi, B., Krug, D., Wolfgang, K., and Tsinober, A. (2013a). Effects of mean shear on the local turbulent entrainment process. *Journal of Fluid Mechanics*, 731:95–116.

Wolf, M., Lüthi, B., Holzner, M., Krug, D., Kinzelbach, W., and Tsinober, A. (2012). Investigations on the local entrainment velocity in a turbulent jet. *Physics of Fluids*, 24(10):105110.

Wolf, M., Lüthi, B., Holzner, M., Krug, D., Kinzelbach, W., and Tsinober, A. (2013b). Erratum: "Investigations on the local entrainment velocity in a turbulent jet" [Phys. Fluids 24, 105110 (2012)]. *Physics of Fluids*, 25(1):019901.

Yasuda, T. and Vassilicos, J. C. (2018). Spatio-temporal intermittency of the turbulent energy cascade. *Journal of Fluid Mechanics*, 853:235–252.

Yuvaraj, R. (2021). *Analysis of energy cascade in wall-bounded turbulent flow*. PhD thesis, Centrale Lille.

Zecchetto, M. and da Silva, C. B. (2021). Universality of small-scale motions within the turbulent/non-turbulent interface layer. *Journal of Fluid Mechanics*, 916:A9.

Zhou, Y. and Vassilicos, J. C. (2017). Related self-similar statistics of the turbulent/non-turbulent interface and the turbulence dissipation. *Journal of Fluid Mechanics*, 821:440–457.

Zhou, Y. and Vassilicos, J. C. (2020). Energy cascade at the turbulent/nonturbulent interface. *Phys. Rev. Fluids*, 5:064604.